

UNIVERSITÀ  
DEGLI STUDI  
DI PADOVA

**UNIVERSITÀ DEGLI STUDI DI PADOVA**

**DIPARTIMENTO DI TECNICA E GESTIONE  
DEI SISTEMI INDUSTRIALI**

**SCUOLA DI DOTTORATO DI RICERCA IN  
INGEGNERIA MECCATRONICA E DELL'INNOVAZIONE  
MECCANICA DEL PRODOTTO**

**CICLO XXVIII**

**MULTI-SCALE MODELING OF THE FATIGUE  
BEHAVIOR FOR SHORT FIBER REINFORCED  
THERMOPLASTICS**

**Direttore della Scuola:** Ch.mo Prof. Alessandro Persona

**Supervisore:** Ch.mo Prof. Marino Quaresimin

**Dottorando:** Enrico Belmonte



*To my family Veronica and Pietro.*





# Abstract

This PhD thesis deals with the investigation of damage initiation in a short glass fiber reinforced polyamide under fatigue loading. This material belongs to Short Fiber Reinforced Plastics (SFRPs) and is widely used in load-bearing applications in the automotive sector. Lifetime prediction models represent a powerful tool for optimizing structural parts in the early stage of a project reducing the number of prototypes needed before the series production. Multi-scale predictive models aim to integrate the relevant damage mechanisms in order to obtain accurate estimation of the lifetime to failure reducing empirical parameters and assumptions. The aim of this PhD thesis is to gain insight into the conditions for damage initiation in a short glass fiber reinforced polyamide under fatigue loading in order to prepare the basis for the development of a multi-scale, mechanism-based lifetime prediction model. This objective was addressed through three main activities: 1) The quantification of the lifetime to crack initiation during fatigue tests (Chapter 4); 2) The investigation of the fatigue damage mechanisms (Chapter 5 - 6); 3) The study of the local stress concentrations at crack initiation (Chapter 7).

Chapter 4 describes the development of an optical method for the quantification of the lifetime to crack initiation during fatigue tests. Using the proposed experimental method, it was possible to generate a set of fatigue data to crack initiation for the calibration of a lifetime prediction model.

The investigation of the damage mechanisms constitutes a major part of the PhD. In Chapter 5 an extensive damage investigation on PA66-GF35 plain and notched specimens is presented. In Chapter 6 the influence of the fiber volume fraction on the damage mechanisms is investigated. Fatigue damage mechanisms were studied at multiple scales by means of Field Emission Scanning Electron Microscopy (FESEM). Damage investigation was carried out analyzing either the fracture surface of failed specimens or the polished side surface of specimens subjected to interrupted fatigue tests. Specific fractographic features were analyzed and compared with the results from the literature. These are: ductile / brittle matrix fracture behavior, fiber failure / pull-out, degree of fiber-matrix interfacial adhesion. Particular attention was devoted to the analysis of the fiber-matrix interface. Mirror-clean fibers on the

fracture surface indicate fiber-matrix debonding. By contrast, fibers covered by a resin layer suggest the damage occurs in form of matrix-cracking in the resin, at a certain distance from the interface.

In Chapter 7, the influence of the fiber distribution on the local stress concentrations at crack initiation is studied. Stress concentrations are potential locations for damage initiation. In SFRPs, fiber-fiber and fiber-matrix interactions lead to stress concentrations at micro-scale. X-Ray Computed Tomography (X-Ray CT) was used for the quantitative description of the fiber distribution around a molded notch, at crack initiation. For this purpose, a fatigue test of a notched specimen was interrupted before failure. A sample surrounding the notch and including a crack propagated during the fatigue test was scanned by means of X-Ray CT. A manual procedure for reconstructing the real fiber orientation distribution around the notch is proposed. The reconstructed volume was simulated with the FEM code ABAQUS with the aim to study the stress concentrations at crack initiation.

Finally, the findings of the experimental and modeling activities were used for the development of a preliminary multi-scale approach for the prediction of the crack initiation in a short glass fiber reinforced polyamide under fatigue loading. This activity is presented in Chapter 8.

# Sommario

Il tema del presente dottorato di ricerca è lo studio della nucleazione del danneggiamento in una poliammide rinforzata con fibre di vetro corte soggetta a un carico di fatica. La poliammide è un materiale termoplastico molto utilizzato nell'industria automobilistica per applicazioni strutturali sotto il cofano della vettura. Questo materiale è caratterizzato da ottime proprietà meccaniche e da un'elevata resistenza ad alte temperature e alla corrosione. Inoltre è leggero contribuendo in questo modo a ridurre il peso dell'autovettura. I componenti strutturali realizzati con questo materiale sono soggetti in esercizio a sollecitazioni cicliche di natura termica e meccanica che provocano una rottura a fatica. Lo sviluppo di modelli previsionali è pertanto di fondamentale importanza perché permette una stima della vita a fatica nella fase di progettazione riducendo il numero di prototipi necessari prima dell'avvio della produzione in serie. Lo sviluppo di questi modelli richiede la comprensione dei meccanismi di danneggiamento che causano l'innesco di una cricca e la sua propagazione fino alla rottura finale.

L'obiettivo che si pone questo dottorato di ricerca è la comprensione del fenomeno di nucleazione del danneggiamento in una poliammide rinforzata con fibre di vetro corte, soggetta a un carico di fatica al fine di porre le basi per lo sviluppo di un modello previsionale basato sui meccanismi di danneggiamento. Le tre principali attività svolte sono: 1) L'identificazione dell'inizio cricca durante test di fatica (Capitolo 4); 2) L'analisi dei meccanismi di danneggiamento (Capitolo 5 - 6); 3) Lo studio dei campi tensione locali a inizio cricca (Capitolo 7).

Il Capitolo 4 descrive lo sviluppo di un metodo ottico per l'identificazione dell'inizio cricca durante i test di fatica. È stata condotta una campagna sperimentale di test a fatica su provini lisci e intagliati. Lo sviluppo della tecnica sperimentale ha reso possibile lo studio dell'effetto della frazione di volume sulla vita a innesco della poliammide. In questo modo è stato generato un set di dati sperimentali per lo sviluppo di un modello previsionale a inizio cricca. L'analisi dei meccanismi di danneggiamento copre una parte importante del dottorato. Nel Capitolo 5 è presentata l'analisi del danneggiamento su provini lisci e intagliati per una poliammide rinforzata con il 35 % (in peso) di fibre. Nel Capitolo 6, l'analisi del danneggiamento è estesa a diverse frazioni di volume. È stato utilizzato un microscopio a

scansione ad alta risoluzione. L'analisi del danneggiamento è stata condotta analizzando o la superficie di frattura di provini giunti a rottura durante test di fatica o la superficie laterale di provini soggetti a test di fatica interrotti. I meccanismi di danneggiamento sono stati studiati analizzando specifiche evidenze frattografiche: il comportamento duttile / fragile della matrice; la presenza di fibre rotte o estratte intere dalla superficie di frattura; il grado di adesione fibra-matrice. In particolare, l'evidenza sulla superficie di frattura di fibre pulite o coperte da un strato di resina è importante nell'ottica di sviluppo modello. Nel primo caso il danneggiamento avviene all'interfaccia in forma di debonding. Nel secondo caso, il danneggiamento avviene fuori dall'interfaccia in uno strato di resina che potrebbe essere stato modificato chimicamente dal sizing usato durante il processo di formatura delle fibre per migliorarne l'adesione con la matrice.

Il Capitolo 7 tratta l'effetto dell'orientazione delle fibre sui campi di tensione locali a inizio cricca. Le concentrazioni di tensione rappresentano potenziali fonti di innesco di una cricca. Nei materiali plastici rinforzati, l'interazione tra fibre e matrice su scala microscopica dà luogo a concentrazioni di tensione. È stato condotto un test di fatica su un provino intagliato fino alla comparsa di una cricca. A questo punto, il test è stato interrotto e un volume di materiale attorno all'intaglio e comprendente la cricca è stato fresato dal provino e analizzato con un tomografo computerizzato. In seguito, la reale distribuzione delle fibre a bordo intaglio è stata riprodotta manualmente in un software agli elementi finiti con l'obiettivo di studiare i campi di tensione locali nella matrice che possono causare l'innesco di una cricca. Infine i risultati dell'attività sperimentale e di modellazione sono stati utilizzati per lo sviluppo di un approccio multi scala per la previsione della vita a innesco di cricca in una poliammide rinforzata soggetta a un carico di fatica. Quest'attività è presentata nel Capitolo 8.

# Acknowledgements

This PhD Thesis is the result of the collaboration between the University of Padova and Robert Bosch GmbH. I had the unique opportunity to do basic research in an industrial context. I've learnt how deeply basic research affects the development of innovative products. Working between university and industry has been a great experience.

I would like to express my special appreciation and thanks to Professor Quaresimin for his brilliant guidance. I was very fortunate to be supervised by one of the leading experts in the world in the field of durability of composite materials. During the whole PhD period he was always ready to give me his precious advice and feedback on my work. He steady encouraged me to improve the quality of my work inspiring me to give the best of myself.

I would express my gratitude to Dr. De Monte for his supervision at Robert Bosch. I enjoyed the freedom he gave me to explore new ideas and I appreciated our lively and constructive discussions. He taught me working in a structured way without losing the objectives of the PhD thesis.

I'm very grateful to Prof. Talreja for his insightful comments and the motivating suggestions.

I would also like to thank Mr. Moosbrugger and Mr. Trumpfheller for their support in carrying out fatigue tests. They were always available and kind to me supporting the continuous improvement of the experimental techniques.

My sincere thanks go to Mr. Hoffmann and Dr. Riedel. Without their expertise and patience, the results of the damage investigations would not have reached the current state.

My gratitude goes also to Dr. Giersbeck and Dr. Hornberger for giving me the opportunity to work as a PhD student at Robert Bosch and for their constant encouragement and support.

A special thank goes to my best friend Dominik for always being there for me since my first day as a master's student at Bosch.

I would like to thank the PhD students and researchers at Robert Bosch Alexander Schaaf, Patrick Zerbe, Andreas Wilmes and Camilo Cruz as well as those at university of Padova Alberto Campagnolo, Paolo Andrea Carraro, Pasquale Gallo, for their help and availability.

I'm very grateful to my parents. With their example they instilled in me determination, perseverance that enabled me to complete this long journey.

Finally I want to acknowledge my fiancè Veronica for her infinite patience and for having shared with me this experience. She only knows the time and energy I've invested in this PhD thesis. My thank goes also to our five month old son Pietro. His birth has brought new energy to my life. I enjoyed the final review of my PhD thesis with him in my arms.

# Table of contents

<b>Abstract</b> .....	I
<b>Sommario</b> .....	III
<b>Acknowledgments</b> .....	V
<b>1. Introduction</b> .....	1
1.1. Motivation .....	1
1.2. Current state of research .....	4
1.3. Goals and outline .....	6
References of Chapter 1 .....	7
<b>2. Short fiber reinforced plastic materials</b> .....	11
2.1. Preliminary remarks .....	11
2.2. Matrix material .....	11
2.3. Fibers material .....	14
2.4. Fiber-matrix interface .....	14
2.5. Injection molding process .....	17
2.6. Microstructure of SFRPs .....	19
2.6.1 Fiber orientation .....	19
2.6.2 Fiber volume fraction .....	24
2.6.3 Fiber aspect ratio .....	25
2.6.4 Defects in the microstructure .....	26
References of Chapter 2 .....	27
<b>3. Factors affecting the fatigue life of SFRPs</b> .....	33
3.1. Preliminary remarks .....	33
3.2. Fiber orientation .....	33
3.3. Fiber volume fraction .....	35
3.4. Frequency .....	35
3.5. Mean stress .....	36
3.6. Notch .....	38

3.7. Multiaxiality.....	39
3.8. Fluids.....	41
3.9. Temperature .....	42
References of Chapter 3 .....	43
<b>4. Life to crack initiation in notched specimens of unreinforced and short fiber reinforced polyamide under fatigue loading.....</b>	<b>49</b>
Abstract .....	49
4.1. Introduction.....	49
4.2. Experimental set up.....	51
4.3. Validation of the experimental method.....	57
4.4. Fatigue tests results .....	58
4.5. Conclusions.....	61
References of Chapter 4.....	62
<b>5. Damage mechanisms in a short glass fiber reinforced polyamide under fatigue loading .....</b>	<b>65</b>
Abstract .....	65
5.1. Introduction.....	65
5.2. Literature review on the damage mechanisms investigated by means of electron microscopy.....	67
5.3. Material, geometry and test equipment.....	71
5.4. Fatigue tests results .....	73
5.5. Damage investigation.....	74
5.5.1 Analysis of the failure mode of plain and notched specimens by means of IR thermography.....	74
5.5.2 Analysis of the fracture surface .....	75
5.5.3 Analysis of the crack path .....	83
5.6. Conclusions.....	87
References of Chapter 5.....	88
<b>6. Influence of fiber loading on the fatigue damage mechanisms in short glass fiber reinforced polyamide 6.6 .....</b>	<b>93</b>
Abstract .....	93



6.1. Introduction.....	93
6.2. Materials, geometry and test equipment .....	95
6.3. Fatigue tests results .....	97
6.4. Damage investigation.....	98
6.4.1 Analysis of the crack path .....	98
6.4.2 Analysis of the fracture surface .....	102
6.5. Conclusions.....	108
References of Chapter 6.....	109
<b>7. Local microstructure and stress distributions at the crack initiation site in a short fiber reinforced polyamide under fatigue loading .....</b>	<b>115</b>
Abstract .....	115
7.1. Introduction.....	115
7.2. Experimental .....	118
7.2.1 Material system.....	118
7.2.2 X-Ray Computed Tomography .....	119
7.3. Results and discussion .....	120
7.3.1 Quantitative analysis of the fiber distribution around the notch .....	120
7.3.2 Reconstruction of the material volume in the FEM Software ABAQUS.....	125
7.3.2.1 Geometry .....	125
7.3.2.2 Boundary conditions and mesh.....	127
7.3.2.3 Analysis of the results.....	128
7.4. Conclusions.....	132
References of Chapter 7.....	132
<b>8. Multi-scale modeling of the fatigue behavior of short glass fiber reinforced polyamide notched specimens .....</b>	<b>137</b>
Abstract .....	137
8.1. Introduction.....	137
8.2. Experimental .....	138
8.3. Equivalent description of the microstructure.....	141
8.4. Formulation of the failure criterion and analysis of the results .....	144

8.5. Conclusions.....	148
References of Chapter 8.....	148
<b>9. Concluding remarks.....</b>	<b>151</b>
<b>Appendix A. Damage investigation.....</b>	<b>153</b>
1. Analysis of the cryo-fracture surface of PA66-GF35 specimen.....	153
2. Fiber avoidance mode .....	155
3. Clusters of through-the-thickness oriented fibers .....	156
4. Fiber pull-out .....	157
5. Fiber failure.....	158
6. Degree of fiber-matrix adhesion .....	159
7. Matrix cracking.....	162
8. Voids and particles.....	164
<b>Appendix B - Use of Digital Image Correlation (DIC) for the crack initiation detection during fatigue tests of PA66-GF35 notched specimens.....</b>	<b>167</b>
1. Introduction.....	167
2. Experimental .....	167
3. Results and discussions.....	170
4. Conclusions.....	173
References of Appendix B .....	173
<b>List of publications .....</b>	<b>175</b>

# Chapter 1

## Introduction

### 1.1. Motivation

The interest for Short Fiber Reinforced Plastics (SFRPs) in structural applications is growing due to the need to balance increasing demands in terms of reliability and lightness with cost reduction and productivity improvements. SFRPs find applications in a wide range of fields as construction, electronics, packaging and automotive. Let us consider the automotive sector. According to a recent research [1], in the US, the polymer composites are 8.4 % of the total vehicle weight. The wide range of applications where SFRPs are used include: exterior body of the vehicle, interior design parts, under-the hood components (fuel systems and engine systems), electronic, electric and mechatronic systems. Around 25 % of the total plastics (100 - 200 kg depending on the vehicle) are located under the hood. Robert Bosch GmbH is a leading automotive supplier. One of the main Bosch businesses is the development of innovative mobility solutions. Fuel injection systems, exhaust systems, brake systems are located under the hood and have several parts made of SFRPs. Typical under-the-hood plastic components are plug-in connectors, sensor units (oil, position, tank), housings (battery, electrical motors), gears, fuse boxes, pumps, fuel rails, valve covers, air manifolds, filters. Size and weight of plastic parts vary from a few millimeters and grams (sealing elements) to some hundred millimeters and some kilograms (air intake manifold). Figure 1.1 shows some typical applications of SFRPs in Bosch automotive systems. In order to satisfy this large demand, several SFRPs are available on the market differing in terms of cost, mechanical properties but also compatibility with fluids, chemicals and high temperatures.

The success of SFRPs is connected to the advantages of the injection molding process. This technology enables complex geometries to be manufactured at high production rates, with low production waste and without the need for additional post-molding finishing operations. In fact, injection molded parts are generally ready to use after ejection from the mold. The possibility to inject multiple molds simultaneously makes the production particularly cost efficient.

Thanks to their advantages in comparison to standard materials, SFRPs offer new solutions being key enablers of product innovation. In particular, the design freedom has been very welcomed by designers becoming a key factor for the wide use of these materials. For example, threaded parts can be manufactured by injection molding without any post-molding machining operation.

Application of SFRPs enables a significant component weight saving, improving the fuel efficiency of the vehicle. In addition, these materials show outstanding mechanical properties. High strength to weight ratio, high temperature and chemical resistance make these materials excellent candidates for under the hood applications. For example in the 90s, the use of a short fiber reinforced polyamide instead of aluminum for an air intake manifold reduced significantly the manifold weight and improved its performance [2]. Recently, the increasing demand for SFRPs is also driven by the improvement of the Noise Vibration Harshness (NVH) properties of mechanical systems, due to their better sound absorption properties in comparison to metals. SFRPs also find several applications in gears by virtue of their inherent lubricity and wear resistance.

The mechanical parts mentioned in this chapter belong to the category “structural parts”. That means they have to fulfill a function under specific load conditions for a minimum expected lifetime. These parts have to be designed against mechanical and environmental loading. During the vehicle’s operation, engine compartment parts come in contact with fluids like water, diesel, gasoline and motor oil. They have to guarantee their functionalities for severe ranges of temperatures which arise from the engine warming up but also from the climatic condition in which the vehicle is operated. In addition, real injection molded parts are exposed to cyclic loading which leads to fatigue failure.

Lifetime prediction models aim to reduce the number of prototypes needed before the series production by virtually optimizing the product in the early stages of the project. This leads to a reduction of development costs and time to market. The formulation of accurate models implies the understanding of the mechanisms responsible for material degradation during the product lifetime. The development of mechanism-based models is not an easy route but represents the only way to reduce the number of assumptions and empirical parameters to be included in the model for accurate lifetime estimations.

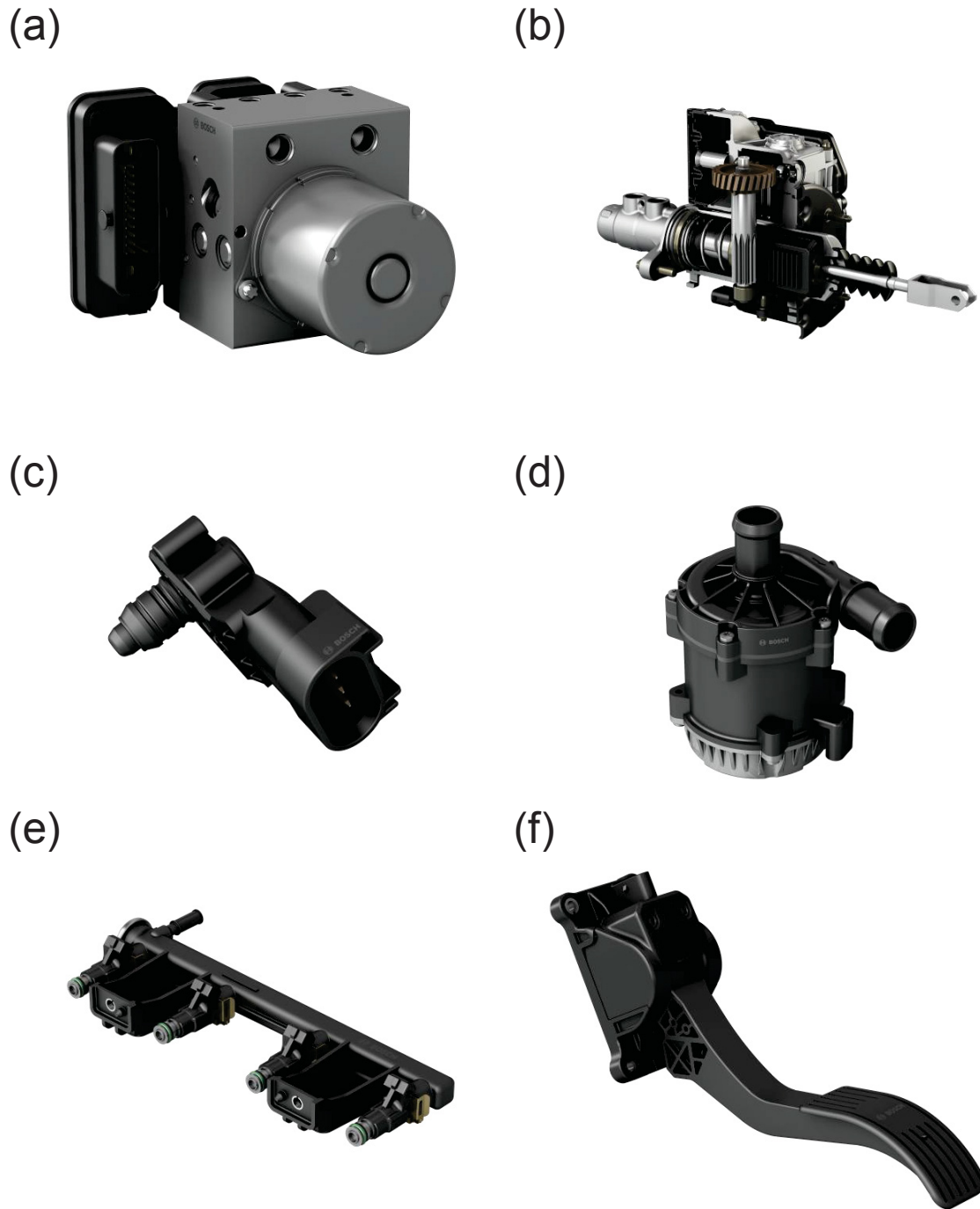


**Figure 1.1** Mechanical systems produced by Robert Bosch GmbH with SFRPs components. (a) ESP (b) iBooster; (c) Low pressure sensor for tank pressure; (d) Electrical coolant pump; (e) Fuel Rail; (f) Accelerator pedal.

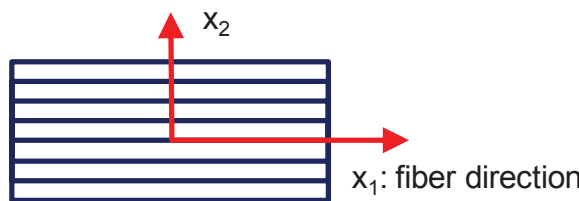
## 1.2 Current state of research

In the literature, some approaches for the lifetime prediction of SFRPs are available. However, most of them are extensions of models originally developed for homogeneous, isotropic materials and therefore are not based on the damage mechanisms occurring in SFRPs. An example is the Tsai-Hill criterion extended by De Monte et al. [3, 4] to predict the influence of the fiber orientation on the tensile and fatigue strength of PA66-GF35 specimens. The Hill's criterion [5] (eq. 1.1) is a generalization of the Von Mises criterion (eq. 1.2) for orthotropic metals. The Von-Mises criterion states that yielding occurs when the second invariant of the deviatoric stress tensor reaches a critical value (measured from uniaxial tensile test).

$$F(\sigma_x - \sigma_y)^2 + G(\sigma_y - \sigma_z)^2 + H(\sigma_x - \sigma_z)^2 + 2 \cdot L \cdot \tau_{yz}^2 + 2 \cdot M \cdot \tau_{xz}^2 + 2 \cdot N \cdot \tau_{xy}^2 = 1 \quad (1.1)$$

$$(\sigma_x - \sigma_y)^2 + (\sigma_y - \sigma_z)^2 + (\sigma_x - \sigma_z)^2 + 6 \cdot (\tau_{xy}^2 + \tau_{yz}^2 + \tau_{xz}^2) = 2 \cdot Y^2 \quad (1.2)$$

Hence, the six constant of the Hill's criterion refer to one physical phenomenon: yielding. In the 1968, Tsai applied the Hill's criterion to continuous fibers reinforced composite materials (eq. 1.3) [6].



$$\left(\frac{\sigma_1}{X}\right)^2 - \left(\frac{\sigma_1 \sigma_2}{X}\right)^2 + \left(\frac{\sigma_2}{Y}\right)^2 + \left(\frac{\tau_{12}}{T}\right)^2 = 1 \quad (1.3)$$

**Figure 1.2** Material coordinate system.

He replaced the six yield stress constants with six composite strength constants (four for plain stress conditions, eq. 1.3) obtained testing a unidirectional composite in different loading directions. In doing so, he implicitly assumed that the composite material fails as a homogeneous solid and that the main mechanism is yielding. Conversely, there is a growing body of evidence indicating that the damage mechanisms strongly depend on the relative orientation between fibers and loading direction. In particular, Asp and coworkers [7] observed that for unidirectional fiber composites under static loading, the mechanisms depend

on the stress state. If the stress state is mainly deviatoric, the mechanism is yielding while, if the stress state is equitriaxial (hydrostatic), failure occurs due to matrix cavitation. An equitriaxial stress state typically occurs in the matrix between parallel-aligned fibers if the loading direction is perpendicular to the fibers. Concluding, even if some lifetime prediction models can be successfully extended to SFRPs, particular caution must be exercised because some damage mechanisms may not have been taken into account.

Another example is the volume-based Strain Energy Density (SED) approach originally developed by Lazzarin et al. [8-10] for isotropic materials. This criterion was successfully extended by De Monte and coworkers [11] in order to predict the lifetime of PA66-GF35 specimens with notches. The SED model was further extended by Schaaf and coworkers [12] for the lifetime prediction of a PBT-GF30 under thermomechanical loading. A third example is the volume-based approach proposed by Sonsino and Moosbrugger [13] for the lifetime prediction of notched SFRP parts.

In the last years, the improvement of the damage investigation methods and the explosion of the computational power have prompted researchers to deeply investigate the damage mechanisms before formulating damage criteria. At the same time, there is a growing recognition that the accurate prediction of the material response requires the understanding of the manufacturing process. SFRPs are heterogeneous, anisotropic material. This means that the load transfer from the matrix (softer phase) to the fibers (stiffer phase) is higher if the fibers are aligned to the loading direction. The material microstructure is frozen during the process thus determining the mechanical response of the material. Recently, approaches have been proposed which reproduce the observed damage mechanisms. Huang and Talreja [14] presented the application of a ductile fracture model for the prediction of the crack propagation in the matrix between two fibers aligned with the loading direction. Horst et. al. [15] modeled the fiber-matrix debonding of a single fiber studying the role of the tensile stress at the fiber-matrix interface. Hoffmann [16] modeled the static behavior of a short glass fiber reinforced Polybutylene terephthalate (PBT-GF30) including the main dominant damage mechanisms (matrix damage, fiber-matrix debonding and fiber fracture). These models contribute to improve the understanding of damage evolution in SFRPs. However, they deal with the static behavior of SFRPs while the fatigue behavior remains to be explored. From a point of view of a reliability engineer, the understanding of the damage processes should be integrated in models for the lifetime prediction of real injection molded parts. This modeling strategy is referred to as multi-scale modeling.

### **1.3. Goals and outline**

The aim of this PhD thesis is to investigate damage nucleation in a short glass fiber reinforced polyamide 6.6 (PA66) under fatigue loading. This objective was addressed through three major activities: 1) The experimental quantification of the lifetime fraction spent in the crack initiation during fatigue tests; 2) The investigation of the fatigue damage mechanisms; 3) The investigation of typical stress distributions at crack initiation related to local fiber orientation distributions. The results of this work lay the foundation for the development of a multi-scale, mechanism-based, lifetime prediction model for SFRPs.

In Chapter 2, the material used in this work and the injection molding technology are introduced. The discussion focuses on the material constituents (fiber, matrix, interface) and the microstructural variables affecting the mechanical behavior of SFRPs. Chapter 3 is dedicated to the study of the fatigue behavior of SFRPs and the factors influencing it.

After necessary fundamentals on the investigated material, the PhD activities are discussed.

The PhD structure is depicted in Figure 1.2. In Chapter 4 an optical method for the quantification of the lifetime to crack initiation in fatigue tests is presented. An image acquisition system with a high resolution CCD camera was developed for detecting the crack onset. Fatigue curves up to crack initiation and until failure for specimens having different fiber loadings were compared to each other. In Chapter 5, Fatigue damage mechanisms in SFRPs discussed in literature were reviewed by reference to specific fractographic features: matrix fracture behavior (ductile / brittle), fiber failure / pull-out, fiber-matrix interfacial adhesion. Thereafter an extensive damage investigation by means of electron microscopy on plain and notched PA66-GF35 specimens is described. In Chapter 6 the damage investigation is extended for considering the effect of the fiber volume fraction on the fatigue damage mechanisms. Chapter 7 is dedicated to the quantitative analysis of the microstructure at crack initiation. For this purpose, a fatigue test was interrupted at crack initiation. A region surrounding the notch was analyzed by means of X-Ray Computed Tomography (X-Ray CT). The real fiber orientation was modeled with the Finite Element (FE) code ABAQUS in order to study the stress concentrations at crack initiation. In Chapter 8 the results of the experimental activities were used for the development of preliminary multi-scale, lifetime prediction model. The PhD closes with Chapter 9 with a summary of the most relevant results.



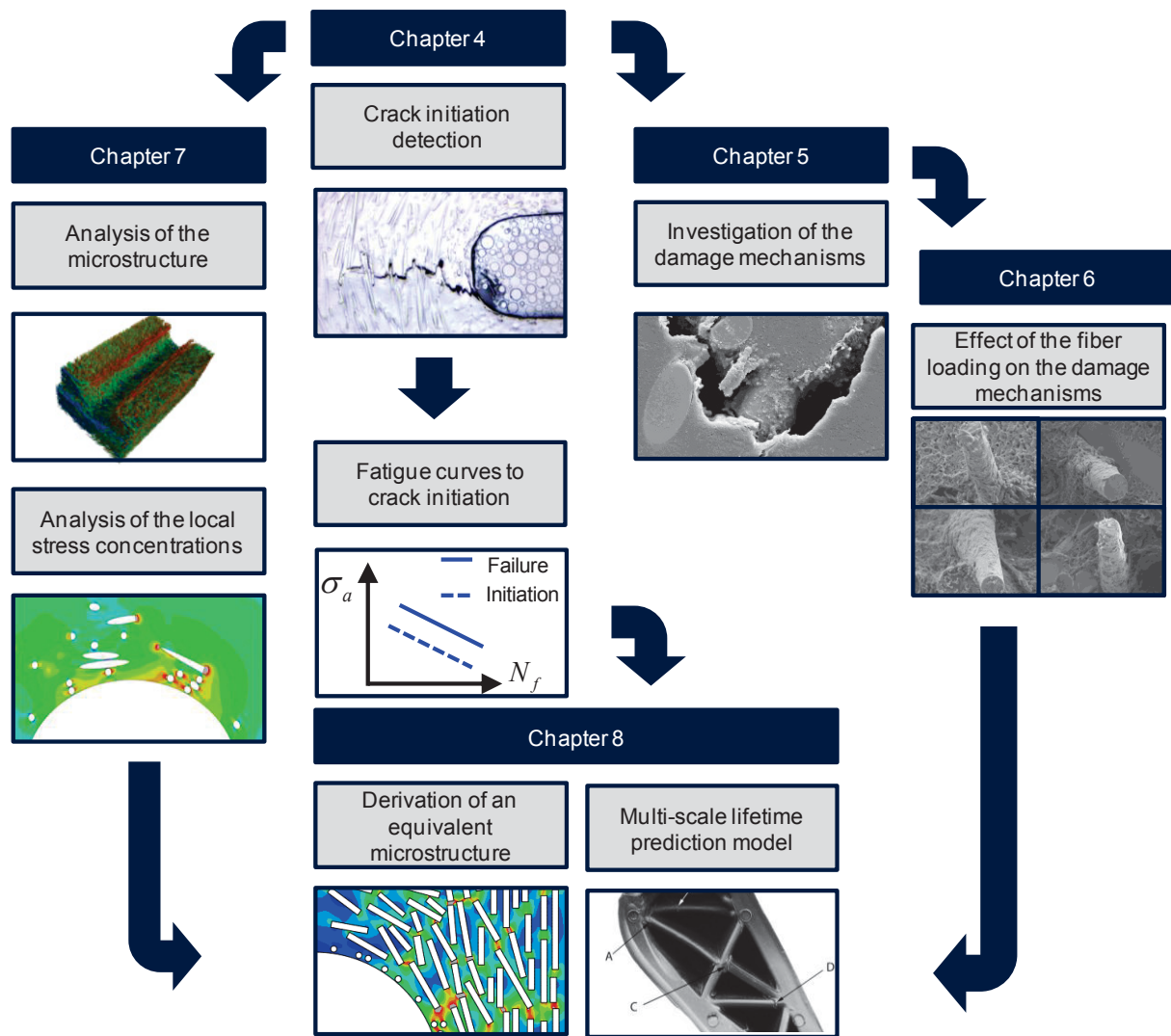


**Figure 1.2.** Schematic structure of the PhD Thesis.

## References of Chapter 1

- [1] American Chemistry Council, Economics and Statistics Department, *Plastics and Polymer Composites in Light Vehicles* (2014).
- [2] E. Carlson, K. Nelson, *Nylon Under-the-Hood: A History of Innovation*, *Automotive Engineering* (1996) 84-89.
- [3] M. De Monte, E. Moosbrugger, M. Quaresimin, Influence of temperature and thickness on the off-axis behaviour of short glass fibre reinforced polyamide 6.6 – Quasi-static loading, *Composites Part A: Applied Science and Manufacturing*. 41 (2010) 859-871.

- [4] M. De Monte, E. Moosbrugger, M. Quaresimin, Influence of temperature and thickness on the off-axis behaviour of short glass fibre reinforced polyamide 6.6 – cyclic loading, *Composites Part A: Applied Science and Manufacturing*. 41 (2010) 1368-1379.
- [5] R. Hill, *The mathematical Theory of Plasticity*, Oxford University Publications, Oxford, 1950.
- [6] S.W. Tsai, *Strength Theories of Filamentary Structures*, in: R.T. Schwartz, H.S. Schwartz (Eds.), *Fundamentals aspects of Fibre Reinforced Plastic Composites*, Wiley Interscience, New York, 1968, pp. 3-11.
- [7] L.E. Asp, L.A. Berglund, R. Talreja, A criterion for crack initiation in glassy polymers subjected to a composite-like stress state, *Composites Sci. Technol.* 56 (1996) 1291-1301.
- [8] P. Lazzarin, R. Zambardi :, A finite-volume-energy based approach to predict the static and fatigue behavior of components with sharp V-shaped notches, *International Journal of Fracture*. 12 (2001) 275-298.
- [9] P. Lazzarin, F. Berto, Some Expressions for the Strain Energy in a Finite Volume Surrounding the Root of Blunt V-notches, *International Journal of Fracture*. 135 (2005) 161-185.
- [10] B. Atzori, F. Berto, P. Lazzarin, M. Quaresimin, Multi-axial fatigue behaviour of a severely notched carbon steel, *Int. J. Fatigue*. 28 (2006) 485-493.
- [11] M. De Monte, M. Quaresimin, P. Lazzarin, Modelling of fatigue strength data for a short fiber reinforced polyamide 6.6 based on local strain energy density. *Proceedings of ICCM16, 16th International Conference on Composite Materials* (2007).
- [12] A. Schaaf, M. De Monte, E. Moosbrugger, M. Vormwald, M. Quaresimin, Life estimation methodology for short fiber reinforced polymers under thermo-mechanical loading in automotive applications, *Materialwissenschaft und Werkstofftechnik*. 46 (2015) 214-228.
- [13] C.M. Sonsino, E. Moosbrugger, Fatigue design of highly loaded short-glass-fibre reinforced polyamide parts in engine compartments, *Int. J. Fatigue*. 30 (2008) 1279-1288.

- [14] H. Huang, R. Talreja, Numerical simulation of matrix micro-cracking in short fiber reinforced polymer composites: Initiation and propagation, *Composites Sci. Technol.* 66 (2006) 2743-2757.
- [15] J.J. Horst, N.V. Salienko, J.L. Spoormaker, Fibre-matrix debonding stress analysis for short fibre-reinforced materials with matrix plasticity, finite element modelling and experimental verification, *Composites Part A: Applied Science and Manufacturing.* 29 (1998) 525-531.
- [16] S. Hoffmann, *Computational Homogenization of Short Fiber Reinforced Thermoplastic Materials* (2012).



## **Chapter 2**

# **Short fiber reinforced plastic materials**

### **2.1 Preliminary remarks**

SFRPs are composite materials. According to Jesson and Watts [1] a material which belongs to the category “composite materials” respects three conditions: 1) It is composed of at least two materials which are physically and mechanically distinguishable; 2) It can be manufactured by mixing two or more materials in such a way that the dispersion of one material into the other can be controlled; 3) Mixing the constituents, the mechanical properties of the composite material are higher than those of the constituents. In SFRPs fibers and matrix have complementary roles. The matrix provides the shape of the part and confers toughness and great elongation properties while the composite stiffness and strength is increased by the fibers. The fiber-matrix interaction occurs through the fiber-matrix interface. In order to improve the fiber-matrix adhesion, the surface of the fibers is subjected to a coating treatment called sizing.

A large range of thermoplastic materials is available on the market. However, the most used thermoplastic resins in the automotive sector are PA66, PA6, PBT, POM and PP. In the work at hand a short glass fiber reinforced polyamide (PA66) is investigated.

### **2.2 Matrix material**

Polyamide 66 is a semi-crystalline thermoplastic material. Under quasi-static cooling conditions the polymer melt solidifies with the formation of semi-crystalline spherical structures called spherulites. Spherulites grow radially as long as they do not touch each other. Spherulite diameter is strongly depending on cooling conditions and local molecular configuration. In injection molded parts, spherulite diameter is typically in the range 5-50 $\mu\text{m}$ . Spherulites consist of ordered lamellae (crystalline regions) linked to each other by amorphous regions. Lamellae are composed by folded polymer chains that align between them forming ordered structures. The crystalline regions enable the material to work at high temperature while the amorphous regions enhance the material-toughness characteristics.

When an idealized amorphous polymer is subjected to a mechanical load, the molecular chains uncoil and align into the loading direction. After removal of the load, the molecular chains coil again. If the load is held constant, the molecules slip over each other resulting in a viscous material behavior. This simplified description of the molecular behavior under an external load is the basis for understanding the viscoelastic material character of polymers. The material response of this class of materials is represented in Figure 2.1.

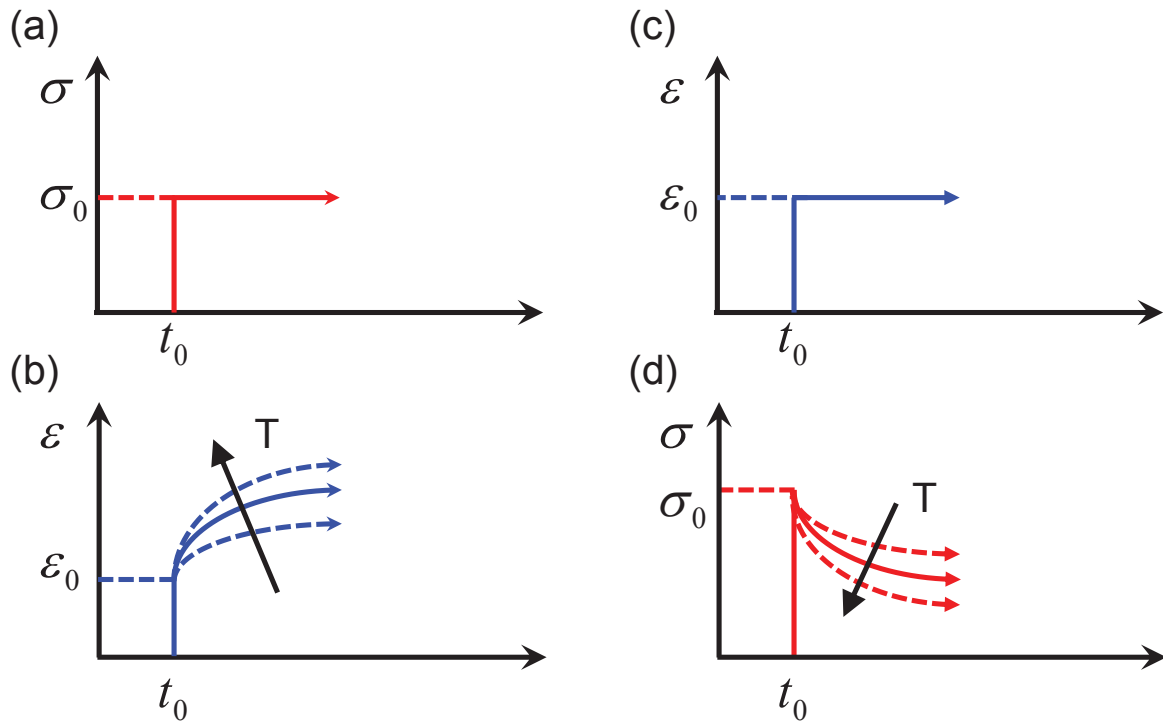


**Figure 2.1.** Schematic representation of the viscoelastic material behavior for various temperatures. (a)-(b) strain response under constant applied stress; (c)-(d) stress response under constant applied strain.

Figure 2.1 a-b shows the material response under constant stress. As the stress  $\sigma_0$  is applied ( $t = t_0$ ), the strain increases instantaneously showing an elastic material behavior. If the stress is held constant, the strain increases continuously due to the viscous material flow. This material behavior is known as creep. Figure 2.1 c-d shows the material response under constant deformation  $\epsilon_0$ . At  $t = t_0$ , the stress increases instantaneously exhibiting an elastic material behavior. If the applied strain is held constant, the stress in the material relaxes over the time. Creep and stress relaxation are two complementary aspects which reflect the viscoelastic nature of polymers. Both effects strongly depend on the stress level, temperature and time. Since the material response of polymers is time dependent, a durability analysis is

needed even under static loading. Creep and stress relaxation may lead to failure of plastic parts albeit in different ways. The strain increase due to the application of a constant tensile stress may result in an unacceptable stiffness decrease or, if the strain overcomes its critical value, in the breakage of the part.

The creep behavior can be divided in three parts (Figure 2.2a): Initially, strain hardening occurs. The second phase is characterized by a linear increase of the strain; strain hardening and softening balance each other. The final stage prior failure is characterized by an increase of the strain rate. In this phase, the strain softening is dominant. Creep rupture data are represented by plotting the stress level against the number of hours (Figure 2.2b).

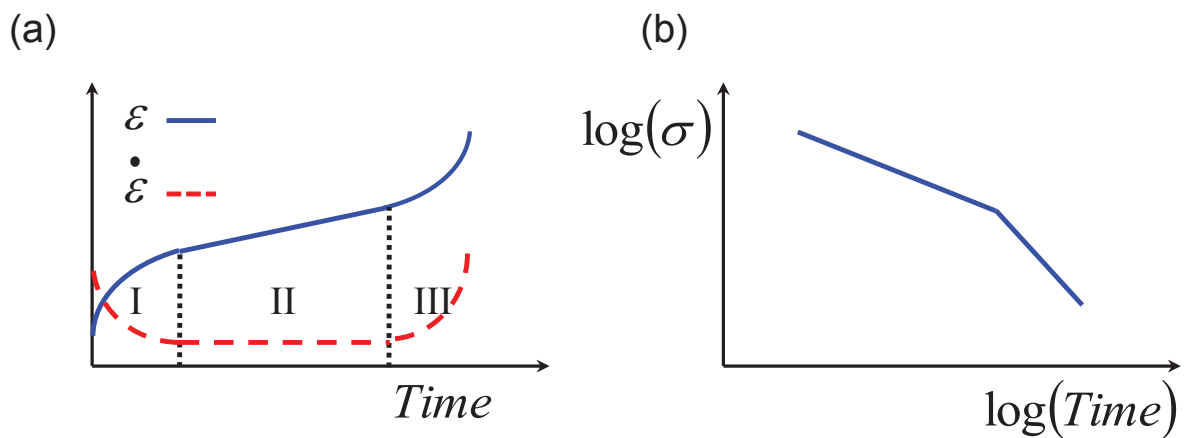


**Figure 2.2.** (a) Creep behavior divided in three stages [2]; (b) Schematic representation of creep rupture data.

Even though stress relaxation cannot cause failure in sense of part breakage, it may be critical for structural applications as well. Let us consider a plastic-to-metal friction connection. In such a case, the stress relaxation causes the reduction of the friction force and, hence, compromises the stress transfer through the connection.

As all other semi-crystalline polymers, the mechanical properties of polyamide exhibit strong variations across the glass transition temperature ( $T_g$ ). Above  $T_g$ , portions of the molecular chains in the amorphous regions have enough molecular mobility for enabling local rotations of atoms or group of atoms. The increase of the molecular mobility leads to a decrease of the Young's modulus [3] and increase of the impact strength [4]. For the material under study in this work (PA66-GF35), glass transition occurs around 70 °C.

## **2.3 Fibers material**

Injection molded materials are available on the market unreinforced and reinforced. Short glass and carbon fibers are the most widely used fillers but there are also different types of reinforcement like beads and minerals. Glass fibers are by far the most used. Carbon fibers are more expensive than glass fibers but lead to a better mechanical resistance (including fatigue resistance [5]). In particular, carbon fiber reinforced materials are used by virtue of their wear resistance [6]. The fiber stiffness and strength are generally assumed constant. Thomason [7] reported that annealing effects during the fiber forming process may cause a stiffness reduction of the fibers while the strength is generally reduced due to fiber-fiber and fiber-machine interaction during injection molding.

## **2.4 Fiber-matrix interface**

The mechanical properties of SFRPs strongly depend on the ability of the matrix to transfer the stress onto the fibers across the fiber-matrix interface. The “quality” of this transfer depends primarily on the fiber sizing.

During the fiber forming process, fibers are coated by a mixture of different chemicals (0.05 - 10 %) and water (> 85 %) called sizing. For a detailed description of the fiber forming process see [8-10]. The sizing formulation aims to improve the coating process itself and to promote the fiber-matrix adhesion. The sizing composition consists mainly of the following components: 1) Coupling agent which provides the fiber-matrix adhesion; 2) Film former for holding the filaments together in a strand and avoid the fiber damage during the process; 3) Lubricant to improve the abrasion resistance. If the material is susceptible to hydrolysis, sizing also contains anti-hydrolysis agents. Further agents are emulsifiers, wetting agents and anti-static agents. The high water fraction used in the sizing process has a twofold function: cooling down the fibers during the process and transporting homogeneously the chemicals on the fibers surface. Thomason and Schoolenberg [11] observed that the interfacial strength of a glass fiber reinforced polypropylene varies significantly depending on the sizing composition. In particular, if sizing is composed by only silane coupling agent, the improvement in terms of interface strength is low. Instead, in combination with other chemicals, the resulting interface strength is much higher. The performance of the interface is thus determined by the interaction between different chemicals.



Sizing covers the fiber surface with exception of the fiber extremities. Fiber breakage during injection molding process due to fiber-fiber and fiber-machine interaction results in the formation of new surfaces which are not covered by the sizing coating. From this evidence it may be assumed that at the extremities of each fiber there is a pre-existing crack. Starting from this consideration, Huang and Talreja [12] described the crack propagation between two aligned fibers under static loading, Horst and Spoomaker [13] modeled the debonding of a single fiber from the matrix material.

Sizing may affect the composite material at the interface between fibers and matrix. The interface is not simply a bi-dimensional border between fibers and matrix. Instead, it can be thought of as a region of a certain thickness, an additional phase having chemical and mechanical properties different from both matrix and fibers (Figure 2.3) [1, 14-16].

Lastly, studying the fiber-matrix interface, one should not neglect the effect of polymer shrinkage around the fibers during cooling down after injection molding. Due to the mismatch between the thermal expansion coefficient of matrix and fibers, a compressive radial stress is generated on the fiber surface contributing to increase the fiber-matrix interfacial strength.

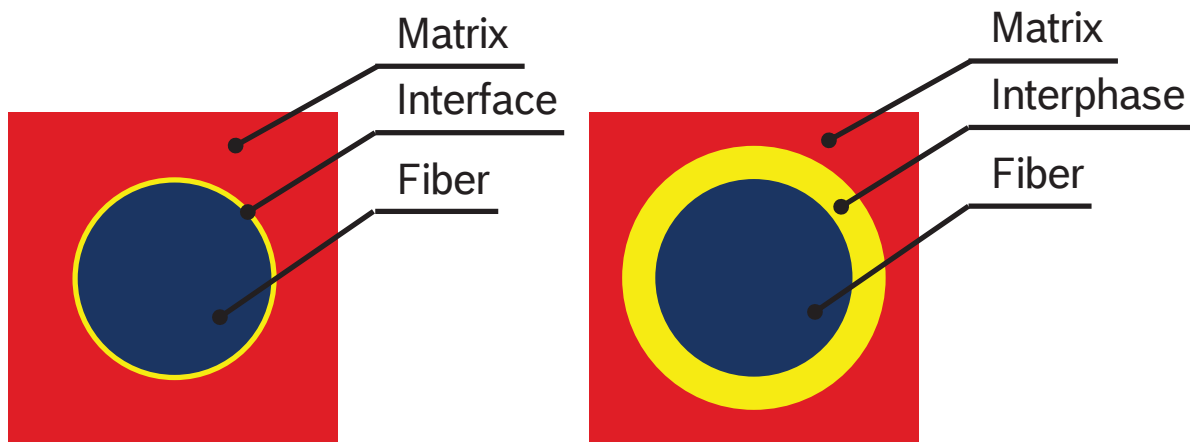


**Figure 2.3.** (a) Interface represented as a demarcation between fiber and matrix; (b) Interphase represented as a three-dimensional region surrounding the fibers.

The characterization of the fiber-matrix interface is still an open issue in the scientific community. A significant effort has been devoted over the years for the development of characterization methods of the fiber-matrix interface. The development of micromechanical tests for the interface characterization has been discussed in a certain number of papers during the last decades. These tests are based on the measurement of the resistance of a single fiber to be extracted from the matrix. Single fiber fragmentation test, push-out test, micro-bond test

and pull-out test are some of micromechanical tests shown in the literature [16-18]. For SFRPs the most used tests are the pull-out test and the micro-bond test [19, 20]. The differences between the two tests are shown in Figure 2.4. In the pull-out test the fiber is embedded in a matrix film, block or disk. In the micro-bond test, the specimen is prepared by laying a piece of a polymer fiber on a single glass fiber and curing the sample above the melting temperature of the polymer in order to obtain a droplet. The polymer droplet is characterized by the embedded length and the droplet diameter. The specimen is drawn through shearing blades. In both tests, the applied axial force generates a shear stress between the fiber and the polymer. The test ends with fiber-matrix separation.

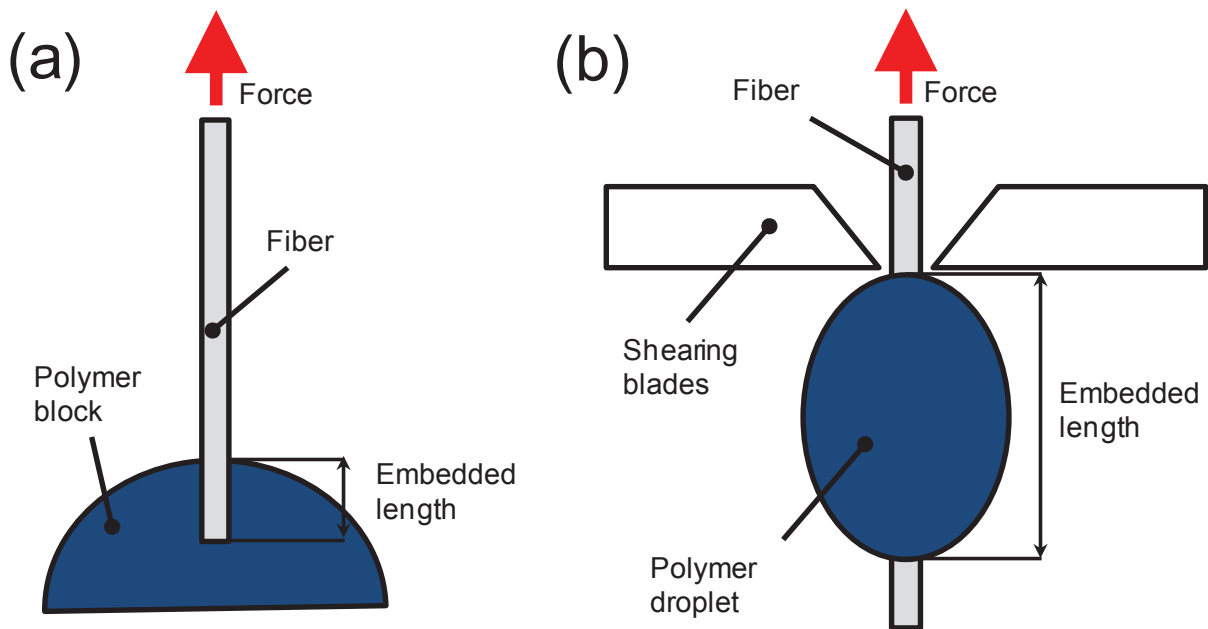


**Figure 2.4.** Schematic representation of micromechanical tests for measuring the fiber-matrix interface strength.; (a) Pull-out test; (b) Micro-bond test.

In [18] Zhandarov and Maeder reported that stress- and energy-based failure parameters can be used to measure the interfacial strength in a micro-mechanical test. Yang and Thomason [20] measured the value of the Interfacial Shear Strength (IFSS or  $\tau$ ).

$$\tau = \frac{F_{\max}}{\pi DL_e} \quad (2.1)$$

$l_e$  is the embedded length,  $D$  is the fiber diameter and  $F_{max}$  is the maximum force obtained during the test (Figure 2.4).

These micro-mechanical tests enable the investigation of different types of sizing on the interfacial strength. Moreover, the effect of environment [21, 22] and mechanical loading [23] on the fiber-matrix interface can be investigated. However, these methods encounter difficulties in finding industrial application due to the labor effort in preparing the samples and due to the fact that the composite system created in the laboratory may differ from the effective material system. For this reason, Thomason [24, 25] proposed an analytical method based on the residual fiber length distribution and the static values of stress and strain at failure for a first estimation of the IFSS in SFRPs.

## 2.5 Injection molding process

Injection molding is the most widespread technology in use today to manufacture plastic parts. The plastic material in form of pellets is firstly melted and then conveyed at high pressure into a mold cavity where it solidifies taking the design form. Finally, the mold opens and the part can be removed or ejected. In order to give a brief overview of the injection molding technology, this section describes only the reciprocating screw injection molding machine. For a more detailed overview, the interested reader is referred to e.g., [26]. The injection molding machine consists of injection system, mold and clamping system (Figure 2.5). The injection system comprises the screw, the hopper, the injection barrel, the motor and the injection cylinder. The material is fed to the injection barrel via a hopper. As the material is poured into the barrel, it is pushed forward by the screw which slides axially and rotates, powered by a hydraulic or electric motor. The plastic material melts since the screw drags it towards the nozzle. While flowing, the polymer molecules slide over each other leading to frictional heat. Heating bands surround the barrel to supply additional heat needed to melt the resin. The screw has three functions, namely: melting pellets, homogenizing resin molten flow, injecting melt into the mold cavity and finally press it. The three-section screw (also called universal screw) is the most widely used screw. The first zone of the screw from the hopper side has a constant flight depth and aims to homogenize the material. In the subsequent zone, the flight depth is decreasing resulting in a compression effect on the molten material. This increases the sliding between neighboring molecules causing an increment of the polymer melting process. In the last zone, the material must reach an adequate temperature and viscosity to properly fill the mold. This zone is characterized by a constant

flight depth but smaller than the other two zones. The molten flow leaves the barrel and moves into the mold through a nozzle. The mold can accommodate one or multiple cavities which are connected to each other via channels. The mold consists of two halves which are held together by the clamping system. The clamping system is composed by the support plate, the moving and stationary platens, the tie bars, and the ejector system. One half of the mold is fixed to the stationary platen while the second half is attached to the moving platen and thus it is allowed to slide. As the mold cavity is completely filled, the injection molding machine exerts an additional pressure (hold pressure) to compensate the loss of volume due to the material shrinkage. In this phase, the screw does not rotate but pushes the material forward as a plunger. After this step, the screw rotates backward in preparation for the next cycle. The injected part is cooled down in the mold so that it can be ejected when the mold is opened.

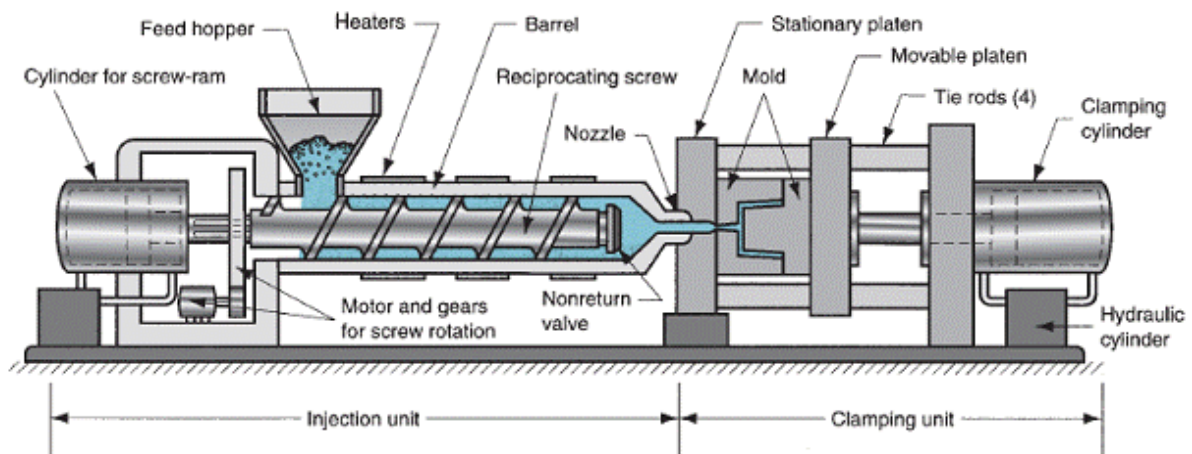


**Figure 2.5.** Injection molding machine (<http://www.mechscience.com/4922-injection-moldinginjection-molding-machineinjection-molding-processinjection-molding-on-plastics/>).

Several process parameters have to be optimized to obtain high-quality injection molded parts. Among the most important process parameters are resin and mold temperature, fill and hold pressure, injection speed, injection time. The optimization of the process parameters aims to achieve cost-efficient production. That means that a compromise should be found for obtaining the best quality for the required performances. For this reason, the constraints related to use of the injection molding process (dimensional tolerances, surface requirements, target cycle time) should be taken into account in the early stages of the development of a new product.

## 2.6 Microstructure of SFRPs

In any material, the microstructure is designed by the process. This is all the more true with regard to SFRPs. The material properties of composites depend primarily on the material properties of the constituents and how the stress is transferred from the softer phase (matrix) to the stiffer phase (fibers). This depends on the fiber distribution, on the relative orientation between fibers and loading direction, and finally on the fiber-matrix interface. In a first analysis, the SFRPs can be described as three-phase materials (fiber, matrix, fiber/matrix interface). The material microstructure is determined by three variables: fiber orientation, fiber volume fraction and fiber aspect ratio. The material properties of SFRPs vary from point to point depending on the microstructural variables. Ideally, it can be assumed that all the fibers are align in the injection direction, that they are uniformly distributed and have the same length, that the fiber-matrix interface ensures continuously the stress transfer from the matrix to the fibers and that the matrix is homogenous and devoid of any defect. The reality is that the microstructure is much more complex. In the following, a description of the microstructural factors is given.

### 2.6.1 Fiber orientation

Unlike continuous fiber reinforced composites where the fiber orientation is a design variable, in SFRPs it can be determined only to a limited extent. Fiber orientation depends on a combination of various factors: injection molding process (process parameters, injection gate position, mold cooling system), fiber volume fraction, geometry of the mold. If the mold contains any geometrical discontinuity, the molten flow of plastic is forced to change direction during the process resulting in a variation of the fiber orientation distribution. SFRPs are heterogeneous anisotropic materials. If the fibers are aligned to the loading direction, the Young's modulus and the static strength will be higher than if the fibers lie crosswise to this direction while the strain at failure will be lower [27-30]. In the literature, static and fatigue characterization of a SFRPs are carried out by testing specimens which are machined out of an injection molded plate at different angles with respect to the injection molding direction. However, the fiber orientation distribution has a layered structure along the thickness of an injection molded specimen [28, 29, 31-33]. This takes the name of "skin- shear-core" or more simply "shear-core or shell-core" depending on the number of layers which are identified (Figure 2.6).

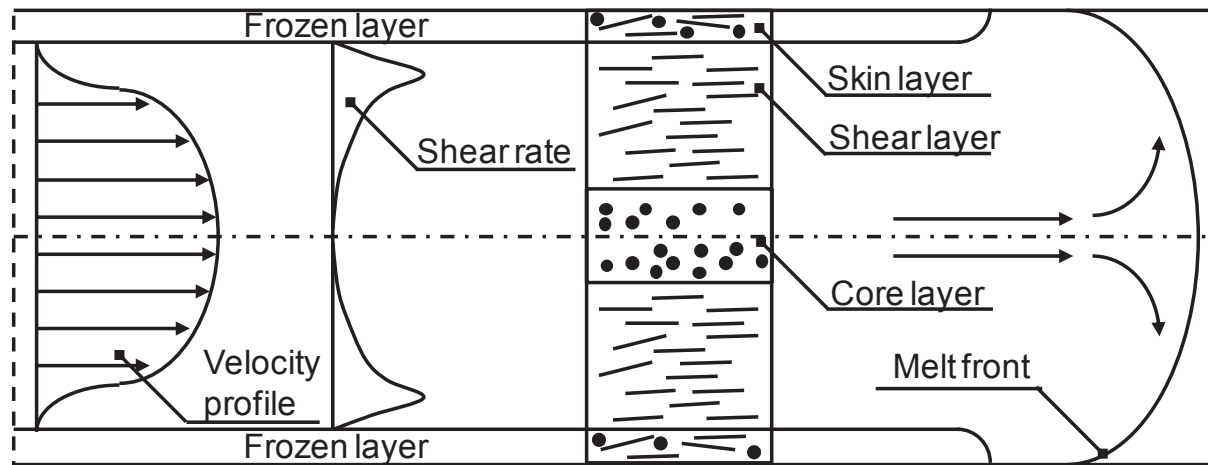


**Figure 2.6.** Velocity and shear rate profile resulting from polymer melt flow in a plate having rectangular section with constant thickness [34].

A molten plastic is a non-Newtonian fluid. The viscosity of the fluid increases with decreasing of temperature. The cooling down and consequently the material solidification in the mold cavity is not uniform. The perimeter surface gets cold before than the inner regions. This temperature gradient results in a viscosity gradient (higher viscosity close to the walls of the mold cavity and lower viscosity in the inner region). The fluid moves from the central region to the external surface and decelerates next to the walls of the mold cavity. This phenomenon is called fountain flow and it is schematically represented in Figure 2.6. The melt elements forced towards the mold walls are exposed to a high elongational deformation. As they come in contact with the cooler walls cavity, they solidify immediately. This layer is generally called skin layer and it is characterized by a random fiber orientation distribution. The molten plastic flowing between the surfaces is subjected to a shear loading which is higher near the solidified skins. Going towards the interior, fibers align to the shear lines. This layer is called shear layer. At the middle thickness, the shear deformation of the flow relaxes. Due to the divergent melt flow, fibers align transversally to the mean flow direction. Taken together, the described effects lead to a layered microstructure known as skin-shear-core microstructure. This structure is symmetric with respect to the mid-thickness plane of the specimen. The process parameters influence the shear and elongated flow affecting the resulting material microstructure. Karger-Kocsis [35] observed that the shear-core structure is strongly influenced by the injection speed. He reported that a slow injection speed results in the formation of a 5-layers structure, while a higher injection speed leads to a 3-layers structure. The shear-core effect also applies to unreinforced materials. Analyzing the microstructure of unfilled polymers (PA6, PBT), Friedrich and Karger-Kocsis [36] observed a

layered structure along the specimen thickness. They observed amorphous thin regions adjacent to the specimen surfaces and a more crystalline region at the mid-thickness. Analyzing the skin-core morphology along the thickness of a PA66 plate, Karger-Kocsis [35] observed that an increase of the mold temperature results in a reduction of the skin layer, an increase of the spherulite diameter and an increase of the crystallinity in the skin layer.

An essential contribution to the development of mathematical instruments for the quantitative description of the fiber orientation distribution has been provided by Advani and Tucker [37]. The authors presented a framework aimed to describe the fiber orientation in dilute systems without considering the mutual interaction between neighboring fibers. The assumptions underlying their theory are as follows: 1) Fibers have a cylindrical shape; 2) Length and diameter of the fibers are uniform; 3) Fiber volume fraction is constant. The orientation of a fiber in the three-dimensional space can be described by using two angles  $\theta$ ,  $\phi$  (Figure 2.7). One also can specify the fiber orientation through a unit vector. The two representations are related to each other by the following equations:  $p_1 = \sin \theta \cos \phi$ ;  $p_2 = \sin \theta \sin \phi$ ;  $p_3 = \cos \theta$ .

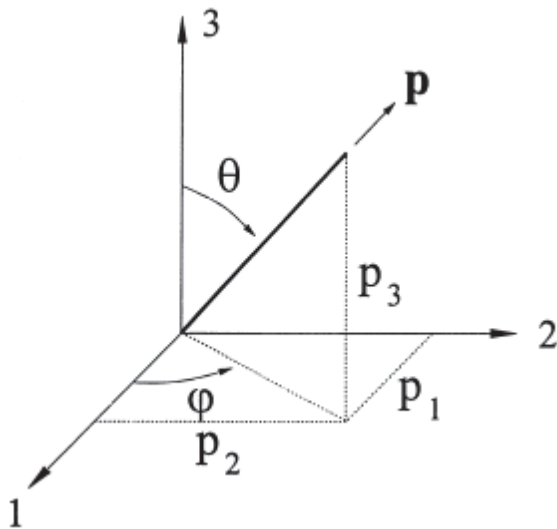


**Figure 2.7.** Cartesian coordinate system for the determination of the orientation vector.

Now if the discussion is extended to a larger number of fibers, one can introduce the probability distribution function  $\psi(\theta, \phi)$  or, equivalently,  $\psi(p)$ . This function identifies the probability to find a fiber between the angles  $\theta_1$  and  $\theta_1 + d\theta_1$  and  $\phi_1$  and  $\phi_1 + d\phi_1$ . The probability distribution function satisfies two conditions: 1) The fiber ends are indistinguishable from each other (periodic condition).



$$\psi(p) = \psi(-p) \quad (2.2)$$

2) The integral of the probability fiber distribution function over all possible directions is one (normalization condition).

$$\oint \psi(p) dp = 1 \quad (2.3)$$

For the sake of convenience, the origin of the Cartesian coordinate system shown in Figure 2.7 corresponds to one fiber extremity. If one would to extend the framework to another fiber,  $\psi(p)$  would be also a function of the fiber position.

Due to the difficulties in handling  $\psi(p)$ , the concept Fiber Orientation Tensor (FOT) was introduced by Advani and Tucker [37]. The expressions of the second and fourth-rank FOT are:

$$a_{ij} = \oint p_i p_j \psi(p) dp \quad (2.4)$$

$$a_{ijkl} = \oint p_i p_j p_k p_l \psi(p) dp \quad (2.5)$$

The FOT provides in a compact form a statistical description of the fiber orientation distribution in a material volume. The order of the FOT is arbitrary but must be even. In fact, due to the symmetry condition expressed for the probability distribution function, the FOTs of odd order are zero. The higher the order of the FOT the more accurate is the reproduction of the probability distribution function. However, the order of the FOT is related to the effective property that has to be homogenized. For example, for the calculation of the effective thermal conductivity tensor or thermal expansion tensor which are both second order tensors, the second order FOT is needed. Instead, since the elastic stiffness tensor is of the fourth order, the fourth order FOT is required. However, the fourth-order FOT is computationally more expensive than the second-order tensor and it is not outputted by the process simulation.

The process simulation returns the second order FOT for each element of the mesh. The second-order FOT can be mathematically described through an ellipsoid. The principal axes of the ellipsoid are the eigenvectors (V1, V2, V3). The eigenvalues (A1, A2, A3) indicate the magnitude of the fiber orientation along the three coordinate axes. The eigenvalue A1



indicates the portion of fibers aligned in the preferential direction V1. This direction corresponds to the direction of maximum stiffness for the composite material.

The fiber orientation tensor has the following properties which derive from the conditions imposed to the probability distribution function.

$$a = a^T \quad (2.6)$$

$$tr(a) = 1 \quad (2.7)$$

$$-\frac{1}{2} \leq a_{ij} \leq \frac{1}{2}, i \neq j \quad (2.8)$$

Therefore, only five of the nine components of the second-order FOT are independent. The fiber orientation distribution varies between two extremes: the full fiber alignment and the random fiber distribution. Actually neither of the two cases is representative of the real fiber orientation distribution. Instead, even for simple geometries, fiber orientation distribution is quite complex depending on the injection direction, the process parameters and the mold thickness (Figure 2.8).

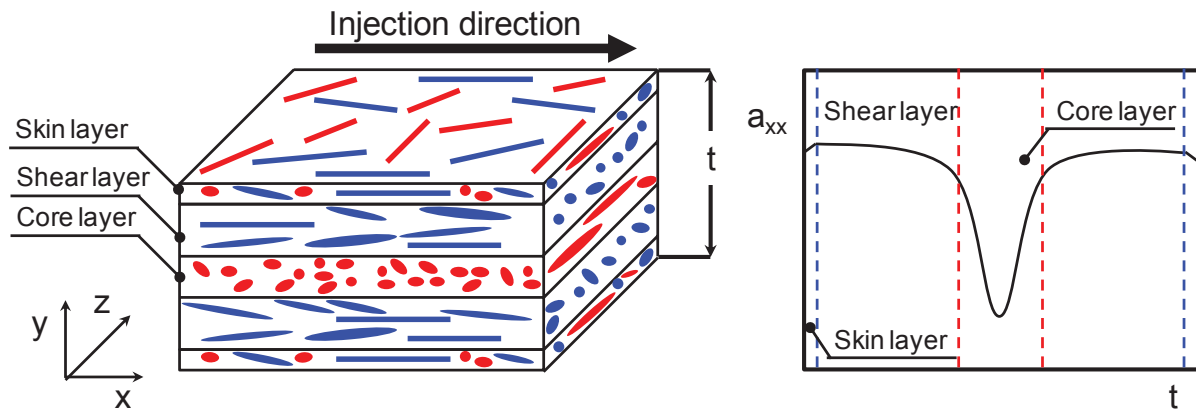


**Figure 2.8.** Three-dimensional representation of the skin-shear-core structure. (b) Schematic orientation of the  $a_{xx}$  trend along the specimen thickness.

Hoffmann [34] showed that different fiber orientation sets may result in the same second order FOT. The three fiber orientations analyzed by Hoffmann [34] are reported in Figure 2.9, lead to the same FOT:  $a = \text{diag}(0.5; 0.5; 0)$ .

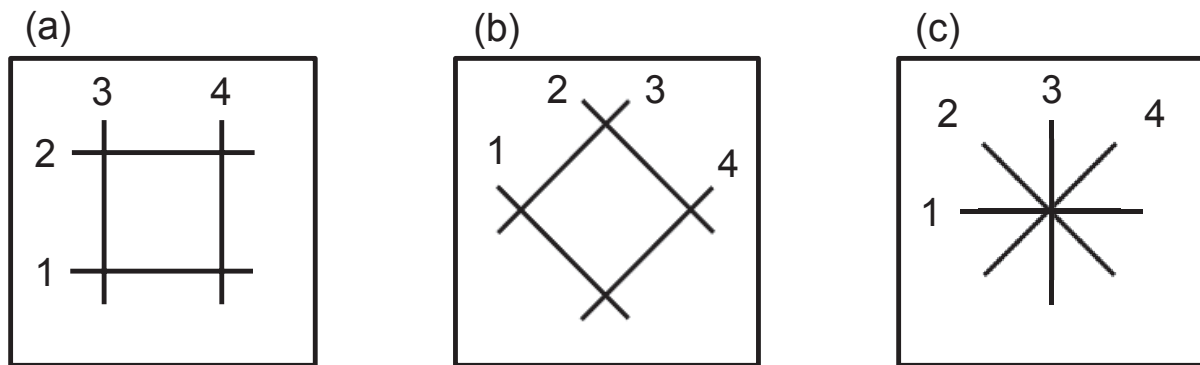


**Figure 2.9.** Three different fiber orientation distributions resulting from the same FOT  $a=\text{diag}(0.5; 0.5; 0)$  [34].

The matrix stiffness related to the three fiber orientations is different. Being aware of the inaccuracy deriving from the calculation of the second-rank FOT, it is worthwhile noting that the fiber configurations shown in Figure 2.9a and Figure 2.9b are rarely to be found in the reality. What is mostly occurring is a combination between them. Therefore, the error resulting from the derivation of the second-order FOT can be considered negligible. Nevertheless it should be pointed out that the adoption of the fourth-order FOT would remove this inaccuracy.

### 2.3.2 Fiber volume fraction

SFRPs are available on the market with different fiber contents. Typically, the fiber mass fraction varies between 15 and 50 % of the total weight. Fiber weight fraction  $W_f$  and fiber volume fraction  $V_f$  are related to each other by the following equation:

$$V_f = \frac{\rho_m \cdot W_f}{(\rho_m - \rho_f) \cdot W_f + \rho_f} \quad (2.9)$$

Where  $\rho_m$  is the density of the matrix,  $\rho_f$  is the density of the fibers.

Fiber fraction influences the other microstructural variables (fiber orientation, fiber aspect ratio). In [24, 38], it was found that an increase in fiber fraction results in a higher alignment of the fibers in the MFD. Friedrich and Karger-Kocsis [36] observed that the ratio between the core and the shear layer increases with increasing fiber fraction.

The higher the fiber content, the higher the elastic modulus and the tensile strength, and the lower the toughness of the material system will be [34, 38-40]. Testing short glass fiber reinforced PA66 specimens having different fiber volume fractions under quasi-static loading, Thomason [3] and Bernasconi [38] showed that a small addition of short glass fibers results in a marked decrease of the strain to failure. With fiber contents in the range of 10 to 35 wt. % the strain to failure is pretty constant and it decreases again for  $W_f > 35$  wt. %.

## 2.6.2 Fiber aspect ratio

Fiber aspect ratio ( $a_f$ ) is the ratio of fiber length over fiber diameter. During the injection molding process, the average fiber length is reduced due to the fiber-fiber and fiber-machine contact. Fiber breakage also occurs during the previous chopping and compounding steps (Figure 2.10a) [41, 42].

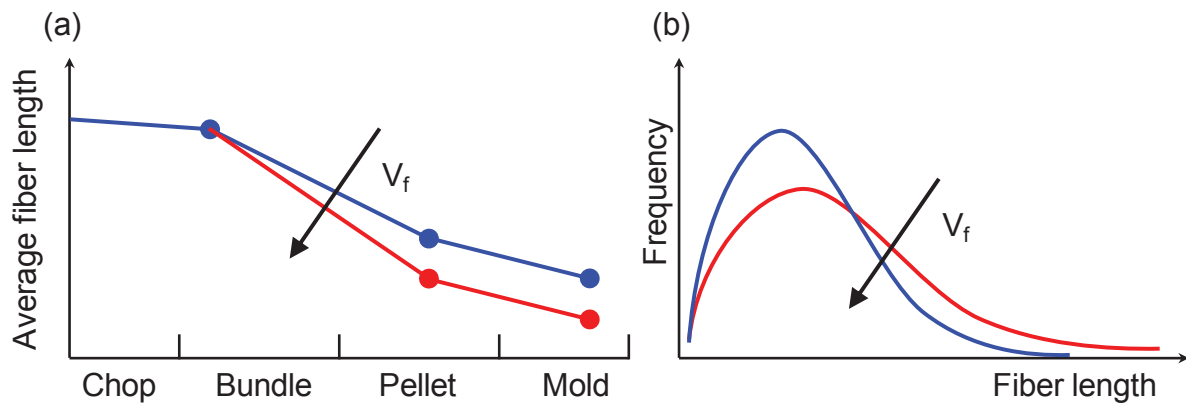


**Figure 2.10.** (a) Fiber shortening during fiber production process and injection molding; (b) fiber length distribution with different fiber contents.

The amount of fiber breakage depends on several factors as process parameters, fiber volume fraction, and complexity of the mold geometry. Figure 2.10b shows typical fiber length distributions varying the fiber volume fraction. The fiber length distribution is obtained using optical microscopy or image analysis after high temperature ashing [43-45]. However, as reported by Pyrz [46] the pyrolysis can also introduce some fiber breakage.

In [3], Thomason measured the fiber length in short glass fiber reinforced polyamide specimens having different fiber volume fractions. He observed that with low fiber loadings ( $W_f < 10$  wt. %), the average fiber length is almost independent of the fiber content. For  $W_f < 10$  wt. %, the resulting average fiber length is 0.7 mm; almost 6 times lower than the initial value ( $l_f = 4$  mm). For higher fiber fractions (10 – 40 wt. %), the residual fiber length

scales inversely with the fiber fraction. A reduction of the fiber length with the increase of the fiber fraction was also reported in [35, 38, 47]. Comparing the fiber length distribution in a plain specimen and in an injection molded clutch pedal, Bernasconi and coworkers [48] observed that the average length is lower in the latter case probably due to the complexity of the mold geometry. In [7], Thomason studied the effect of fiber diameter on stiffness and strength properties of injection molded PA66-GF30 specimens. He observed that while the composite stiffness is not directly affected by the fiber diameter, the tensile and flexural strength as well as the strain at failure increase with increasing the fiber diameter.

### **2.6.3 Defects in the microstructure**

As in all other manufacturing processes, the microstructure resulting from injection molding is not homogeneous and defect free. Among the most important defects, weld lines, fiber breakage, voids, air traps and fiber clusters are briefly discussed in this section.

Weld lines are regions where two or more streams of molten plastic join together. A weld line represents a weak point of a composite structure since it exhibits lower mechanical properties. Testing PA66-GF33 specimens milled out of plates in three different configurations: 1) MFD aligned to the loading direction; 2) MFD crosswise to the loading direction 3) Specimens characterized by a central weld line which is oriented perpendicularly with respect to the loading direction, Zhou and Mallick [49] showed that the mechanical properties (Young's modulus, static stress and strain to failure, fatigue resistance) at the weld line are the lowest.

Fiber breakage occurs during the injection molding process due to fiber-fiber and fiber-machine contacts. This phenomenon leads to two considerations: 1) The stress transfer between matrix and fibers is reduced since the average fiber length is lower; 2) New free surfaces due to the fiber breaking are formed which are not covered by any sizing treatment.

Voids and entrapped air are different types of cavities occurring in injection molded parts. Voids are vacuum cavities forming due to material shrinkage, while entrapped air refers to the occurrence of air bubbles in the material. These defects can be mitigated by adjusting the geometry and the process parameters. They represent structural discontinuities inside the material and thus potential location of damage initiation.

Fiber clusters should be included in the microstructural defects since they reflect the inhomogeneity of the fiber distribution. Segurado and Llorca [50] performed a stress analysis on matrix material reinforced by spherical particles, for different clustering configurations of the particles. Yang and Qin [51] studied the effect of fiber clusters in relation to the

mechanical properties of a unidirectional fiber composite. In both cases, it was observed that fibers clusters do not significantly influence the stiffness properties of the composite material but the local stresses in the matrix. Therefore, fiber clusters may represent preferential locations for damage initiation and should be considered in a lifetime prediction model.

## **References of Chapter 2**

- [1] D.A. Jesson, J.F. Watts, *The Interface and Interphase in Polymer Matrix Composites: Effect on Mechanical Properties and Methods for Identification*, - *Polymer Reviews*. 52 (2012) 321-354.
- [2] W.N. Findley, J.S. Lai, K. Onaran, *Creep and relaxation of nonlinear viscoelastic materials with an introduction to linear viscoelasticity*, Amsterdam : New York :North-Holland Pub. Co. ; American Elsevier Pub. Co., 1978.
- [3] J.L. Thomason, Structure-property relationships in glass-reinforced polyamide, part 1: The effects of fiber content, *Polymer Composites*. 27 (2006) 552-562.
- [4] L.E. Nielsen, R.F. Landel, *Mechanical Properties of Polymers and Composites*, Second Edition, Marcel Dekker, New York, 1994.
- [5] J.F. Mandell, F.J. McGarry, D.D. Huang, C.G. Li, Some effects of matrix and interface properties on the fatigue of short fiber-reinforced thermoplastics, *Polymer Composites*. 4 (1983) 32-39.
- [6] H. Voss, K. Friedrich, On the wear behaviour of short-fibre-reinforced peek composites, *Wear*. 116 (1987) 1-18.
- [7] J.L. Thomason, The influence of fibre properties of the performance of glass-fibre-reinforced polyamide 6,6, *Composites Sci. Technol*. 59 (1999) 2315-2328.
- [8] J.L. Thomason, L.J. Adzima, Sizing up the interphase: an insider's guide to the science of sizing, *Composites Part A: Applied Science and Manufacturing*. 32 (2001) 313-321.
- [9] J.L. Thomason, Interfaces and interfacial effects in glass reinforced thermoplastics - Keynote Presentation (2007).

- [10] J.L. Thomason, *Glass Fibre Sizing : A Review of Size Formulation Patents* (2015).
- [11] J.L. Thomason, G.E. Schoolenberg, An investigation of glass fibre/polypropylene interface strength and its effect on composite properties, *Composites*. 25 (1994) 197-203.
- [12] H. Huang, R. Talreja, Numerical simulation of matrix micro-cracking in short fiber reinforced polymer composites: Initiation and propagation, *Composites Sci. Technol.* 66 (2006) 2743-2757.
- [13] J.J. Horst, N.V. Salienco, J.L. Spoomaker, Fibre-matrix debonding stress analysis for short fibre-reinforced materials with matrix plasticity, finite element modelling and experimental verification, *Composites Part A: Applied Science and Manufacturing*. 29 (1998) 525-531.
- [14] L.E. Asp, L.A. Berglund, L. Talreja, Effects of fiber and interphase on matrix-initiated transverse failure in polymer composites, *Composites Sci. Technol.* 56 (1996) 657-665.
- [15] A. Bergeret, M.P. Bozec, J.-. Quantin, A. Crespy, J.-. Gasca, M. Arpin, Study of interphase in glass fiber-reinforced poly(butylene terephthalate) composites, *Polymer Composites*. 25 (2004) 12-25.
- [16] L. Yang, J.L. Thomason, Interface strength in glass fibre–polypropylene measured using the fibre pull-out and microbond methods, *Composites Part A: Applied Science and Manufacturing*. 41 (2010) 1077-1083.
- [17] P.J. Herrera-Franco, L.T. Drzal, Comparison of methods for the measurement of fibre/matrix adhesion in composites, *Composites*. 23 (1992) 2-27.
- [18] S. Zhandarov, E. Mäder, Characterization of fiber/matrix interface strength: applicability of different tests, approaches and parameters, *Composites Sci. Technol.* 65 (2005) 149-160.
- [19] L. Yang, J.L. Thomason, Development and application of micromechanical techniques for characterising interfacial shear strength in fibre-thermoplastic composites, *Polym. Test*. 31 (2012) 895-903.

- [20] L. Yang, J.L. Thomason, Interface strength in glass fibre–polypropylene measured using the fibre pull-out and microbond methods, *Composites Part A: Applied Science and Manufacturing*. 41 (2010) 1077-1083.
- [21] A. Bergeret, L. Ferry, P. Ienny, Influence of the fibre/matrix interface on ageing mechanisms of glass fibre reinforced thermoplastic composites (PA-6,6, PET, PBT) in a hygrothermal environment, *Polym. Degrad. Stab.* 94 (2009) 1315-1324.
- [22] J.L. Thomason, L. Yang, Temperature dependence of the interfacial shear strength in glass–fibre polypropylene composites, *Composites Sci. Technol.* 71 (2011) 1600-1605.
- [23] H.M. Brodowsky, W. Jenschke, E. Mäder, Characterization of interphase properties: Microfatigue of single fibre model composites, *Composites Part A: Applied Science and Manufacturing*. 41 (2010) 1579-1586.
- [24] J.L. Thomason, Micromechanical parameters from macromechanical measurements on glass reinforced polyamide 6,6, *Composites Sci. Technol.* 61 (2001) 2007-2016.
- [25] J.L. Thomason, Interfacial strength in thermoplastic composites - at last an industry friendly measurement method?, *Composites Part A: Applied Science and Manufacturing*. 33 (2002) 1283-1288.
- [26] D.V. Rosato, D.V. Rosato, M.G. Rosato, *Injection Molding Handbook*, 3 ed., Springer US, 2000.
- [27] A. Bernasconi, P. Davoli, A. Basile, A. Filippi, Effect of fibre orientation on the fatigue behaviour of a short glass fibre reinforced polyamide-6, *Int. J. Fatigue*. 29 (2007) 199-208.
- [28] M. Laspalas, C. Crespo, M.A. Jiménez, B. García, J.L. Pelegay, Application of micromechanical models for elasticity and failure to short fibre reinforced composites. Numerical implementation and experimental validation, *Comput. Struct.* 86 (2008) 977-987.
- [29] M. De Monte, E. Moosbrugger, M. Quaresimin, Influence of temperature and thickness on the off-axis behaviour of short glass fibre reinforced polyamide 6.6 – Quasi-static loading, *Composites Part A: Applied Science and Manufacturing*. 41 (2010) 859-871.

- [30] M.F. Arif, N. Saintier, F. Meraghni, J. Fitoussi, Y. Chemisky, G. Robert, Multiscale fatigue damage characterization in short glass fiber reinforced polyamide-66, *Composites Part B: Engineering*. 61 (2014) 55-65.
- [31] J.J. Horst, J.L. Spoormaker, Mechanisms of fatigue in short glass fiber reinforced polyamide 6, *Polymer Engineering & Science*. 36 (1996) 2718-2726.
- [32] Y. Zhou, P.K. Mallick, A non-linear damage model for the tensile behavior of an injection molded short E-glass fiber reinforced polyamide-6,6, *Materials Science and Engineering: A*. 393 (2005) 303-309.
- [33] M.F. Arif, F. Meraghni, Y. Chemisky, N. Despringre, G. Robert, In situ damage mechanisms investigation of PA66/GF30 composite: Effect of relative humidity, *Composites Part B: Engineering*. 58 (2014) 487-495.
- [34] S. Hoffmann, *Computational Homogenization of Short Fiber Reinforced Thermoplastic Materials* (2012).
- [35] J. Karger-Kocsis, Effects of processing induced microstructure on the fatigue crack propagation of unfilled and short fibre-reinforced PA-6, *Composites*. 21 (1990) 243-254.
- [36] K. Friedrich, J. Karger-Kocsis, Fracture and fatigue of unfilled and reinforced polyamides and polyesters, in: J.M. Schultz, S. Fakirov (Eds.), *Solid state behavior of linear polyesters and polyamides*, Prentice Hall Inc., Englewood Cliffs, 1990, pp. 249-322.
- [37] S.G. Advani, C.L. Tucker, The Use of Tensors to Describe and Predict Fiber Orientation in Short Fiber Composites, *Journal of Rheology* (1978-present). 31 (1987) 751-784.
- [38] A. Bernasconi, F. Cosmi, Analysis of the dependence of the tensile behaviour of a short fibre reinforced polyamide upon fibre volume fraction, length and orientation, *Procedia Engineering*. 10 (2011) 2129-2134.
- [39] A. Pegoretti, T. Riccò, Fatigue crack propagation in polypropylene reinforced with short glass fibres, *Composites Sci. Technol*. 59 (1999) 1055-1062.



- [40] B. Mouhmid, A. Imad, N. Benseddiq, S. Benmedakhène, A. Maazouz, A study of the mechanical behaviour of a glass fibre reinforced polyamide 6,6: Experimental investigation, *Polym. Test.* 25 (2006) 544-552.
- [41] J.L. Thomason, G. Kalinka, A technique for the measurement of reinforcement fibre tensile strength at sub-millimetre gauge lengths, *Composites Part A: Applied Science and Manufacturing.* 32 (2001) 85-90.
- [42] S. Wilberforce, S. Hashemi, Effect of fibre concentration, strain rate and weldline on mechanical properties of injection-moulded short glass fibre reinforced thermoplastic polyurethane, *Journal of Materials Science.* 44 (2009) 1333-1343.
- [43] J.F. Mandell, D.D. Huang, F.J. McGarry, Fatigue of glass and carbon fiber reinforced engineering thermoplastics, *Polymer Composites.* 2 (1981) 137-144.
- [44] S.Y. Fu, B. Lauke, Y.H. Zhang, Y.-. Mai, On the post-mortem fracture surface morphology of short fiber reinforced thermoplastics, *Composites Part A: Applied Science and Manufacturing.* 36 (2005) 987-994.
- [45] K. Tanaka, T. Kitano, N. Egami, Effect of fiber orientation on fatigue crack propagation in short-fiber reinforced plastics, *Eng. Fract. Mech.* 123 (2014) 44-58.
- [46] R. Pyrz, Microstructural Description of Composites, Statistical Methods, in: H.J. Böhm (Ed.), *Mechanics of Microstructured Materials*, Springer Vienna, 20014, pp. 173-233.
- [47] K. Friedrich, R. Walter, H. Voss, J. Karger-Kocsis, Effect of short fibre reinforcement on the fatigue crack propagation and fracture of PEEK-matrix composites, *Composites.* 17 (1986) 205-216.
- [48] A. Bernasconi, P. Davoli, C. Armani, Fatigue strength of a clutch pedal made of reprocessed short glass fibre reinforced polyamide, *Int. J. Fatigue.* 32 (2010) 100-107.
- [49] Y. Zhou, P.K. Mallick, Fatigue performance of an injection-molded short E-glass fiber-reinforced polyamide 6,6. I. Effects of orientation, holes, and weld line, *Polymer Composites.* 27 (2006) 230-237.

[50] J. Segurado, J. LLorca, Computational micromechanics of composites: The effect of particle spatial distribution, *Mech. Mater.* 38 (2006) 873-883.

[51] Q. Yang, Q. Qin, Modelling the effective elasto-plastic properties of unidirectional composites reinforced by fibre bundles under transverse tension and shear loading, *Materials Science and Engineering: A.* 344 (2003) 140-145.

## **Chapter 3**

# **Factors affecting the fatigue material behavior of SFRPs**

### **3.1. Preliminary remarks**

In this chapter, a review of the most important factors affecting the fatigue behavior of SFRPs is presented. Firstly, the microstructural variables (fiber orientation and fiber volume fraction) are discussed. This is followed by an analysis of the testing parameters (frequency, load ratio, mean stress). The discussion continues on the effect of geometrical discontinuities (notches) and multiaxiality. Since SFRPs find applications in harsh environments (like under the hood) the influence of temperature and fluids on the fatigue behavior is analyzed.

### **3.2. Fiber orientation**

In literature, the most common approach for studying the influence of the fiber orientation on the mechanical properties of SFRPs has been to test specimens machined from injection molded plates at different angles with respect to the Mold Flow Direction (MFD). This approach was also used for studying the effect of the fiber orientation on the fatigue strength of plain and notched specimens [1-3] and on the fatigue crack propagation using CT specimens [4-7]. Bernasconi and coworkers [1] observed a marked decrease of the fatigue strength of PA66-GF35 plain specimens with increasing off-axis angle. De Monte and coworkers [2] carried out a similar analysis but varying the plate thickness. For 1 mm thick specimens, a marked decrease of the fatigue strength with increasing off-axis angle was observed. The same fatigue tests carried out on 3 mm thick specimens showed that the fatigue data fall into a narrow band irrespective of the machining direction indicating a more isotropic material behavior. The analysis of the fiber orientation distribution revealed that 3 mm thick specimens are characterized by a thicker core layer than 1 mm thick specimens. Hence, the load portion carried by the shear layers varies with the specimen thickness. This result shows the limits of such a procedure. In particular, the assumption that the dominant fiber orientation coincides with the MFD is strongly dependent on specimen thickness.

Horst and Spoormaker [8], milled five parallel specimens from the same plate and tested them under static and cyclic loading. They showed that both the static and fatigue strength vary depending on the machining position. Specimens located at the plate sides exhibited higher static and fatigue strength than those machined out from the center of the plate. At the side walls of the mold the fibers are oriented in the MFD (shear layer). The specimens machined out from the center of the plate are thus characterized by a more pronounced core effect. Similar results were also shown by Laspalas et al. [9] who tested specimens under quasi-static loading which were machined at different positions in the plate. However, they reported that only specimens machined longitudinally with respect to the MFD are sensitive to the position on the plate. Instead, specimens machined transversally to the MFD exhibited similar stress-strain curves independently of the machining position.

The knowledge of the MFD is not sufficient to understand the effect of the fiber orientation on the fatigue behavior of SFRPs. Instead a three-dimensional analysis of the fiber orientation is needed. Moreover, in the real world components, the fiber orientation is much more complex than in plain specimens. Thickness variations and geometrical discontinuities strongly influence the fiber orientation distribution. A possible approach to deal with these cases is to analyze the fiber orientation around a molded notch. The insert used to create the notch is an obstacle for the molten flow. Hence, it is representative of geometrical discontinuities in injection molded real parts. Bernasconi et al. [10] studied the fatigue strength of notched specimens injected at different positions (longitudinally and laterally). They found that the specimens injected laterally exhibit lower fatigue strength than those injected longitudinally. However, they did not observe any significant variation of the fiber orientation at the notch tips. In both cases the fibers were mainly found to be aligned in the longitudinal direction of the specimen.

The effect of the fiber orientation on FCP was investigated in [4-7]. It has been noted that fiber orientation affects the threshold for fatigue crack propagation with lower values if the fibers are aligned to the crack propagation direction. Moreover it was found that Paris's curves referring to different fiber orientations fall within a scatter band if the crack propagation rate is reported as a function of the strain energy release rate.

### 3.3. Fiber volume fraction

The addition of fibers to the pure matrix leads to an increase of both the lifetime to failure (plain specimens) [11, 12] and the fatigue crack propagation resistance (CT specimens) [6, 13-19]. In Chapter 6 the influence of the fiber volume fraction on the fatigue strength of notched specimens will be analyzed focusing on the damage mechanisms.

### 3.4. Frequency

In a viscoelastic material, loading and unloading processes are not reversible. The energy loss per cycle is represented by the area enclosed by the hysteresis loop in a stress-strain diagram (Figure 3.1a). In an equilibrium state, the amount of dissipated energy per cycle is released to the environment. If the testing frequency is too high, part of the energy is stored in the material causing an increase of the specimen temperature (self-heating).

Testing specimens machined from injection molded plates in the MFD, at  $R = 0$ , at room temperature, Zhou and Mallick [20] showed that, the acceleration of the testing frequency up to 2 Hz results in an increase of the fatigue life. A further increase of the testing frequency leads to a reduction of the fatigue life (Figure 3.1b). For  $f < 2$  Hz the decrease of the fatigue life is due to the increase of the cycle time. In fact, the lower the frequency, the longer the stress is applied during the cycle. For viscoelastic materials, the application of a constant stress results in material creep. The creep effect becomes increasingly important as the testing frequency diminishes. For  $f > 2$  Hz, the dominant effect accelerating material failure is the storage of energy in form of temperature increase. The decrease of the fatigue life with increasing the testing frequency was also observed in [21, 22].

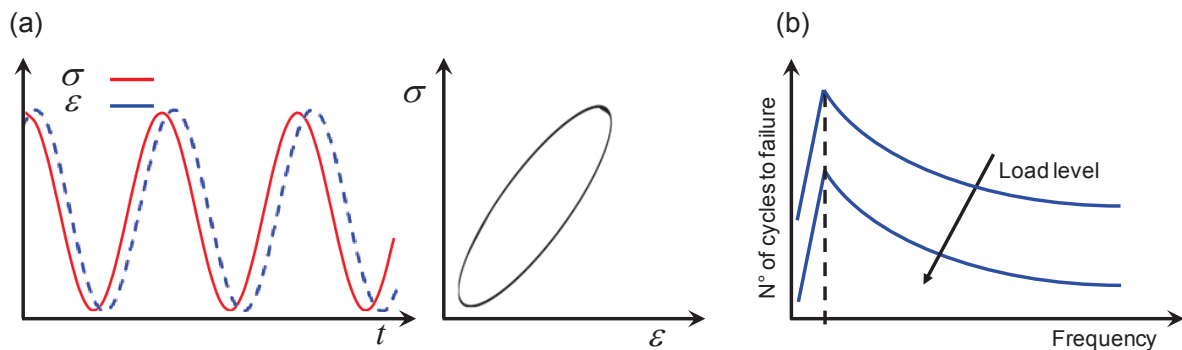


**Figure 3.1.** (a) Phase delay between stress and strain signal and hysteresis loop; (b) Effect of the frequency on the fatigue life [20].

Bernasconi and Kulin [22] showed that fatigue data at different frequencies can be synthesized in a unique scatter band if plotted in terms of cyclic creep rate (defined as the variation of the mean strain over the cycles) against the number of cycles to failure. Wyzgoski et al. [23] studied the effect of the testing frequency on the crack propagation of CT polyamide specimens. He reported that low frequency leads to higher crack propagation rate. Both investigations on plain and CT specimens published in the literature have shown that the fatigue behavior of plastic materials is strongly influenced by the testing frequency. Hence, care should be taken when determining the testing frequency in a fatigue test to avoid the material self-heating.

### 3.5. Mean stress

Except for the case  $R = -1$ , every fatigue stress can be described as the sum of a mean stress  $\sigma_m$  and a stress amplitude  $\sigma_a$ . Due to the viscoelastic material behavior exhibited by SFRPs, the application of a constant stress leads to a gradual increase of the strain over the time. Under tension-tension loading mean strain is not zero (Figure 3.2a). In this case, one can observe a progressive shift of the hysteresis loop throughout the test (Figure 3.2b) [2, 19, 22, 24]. This means that, for tension-tension cyclic loading the material undergoes a combination of creep and fatigue loading.

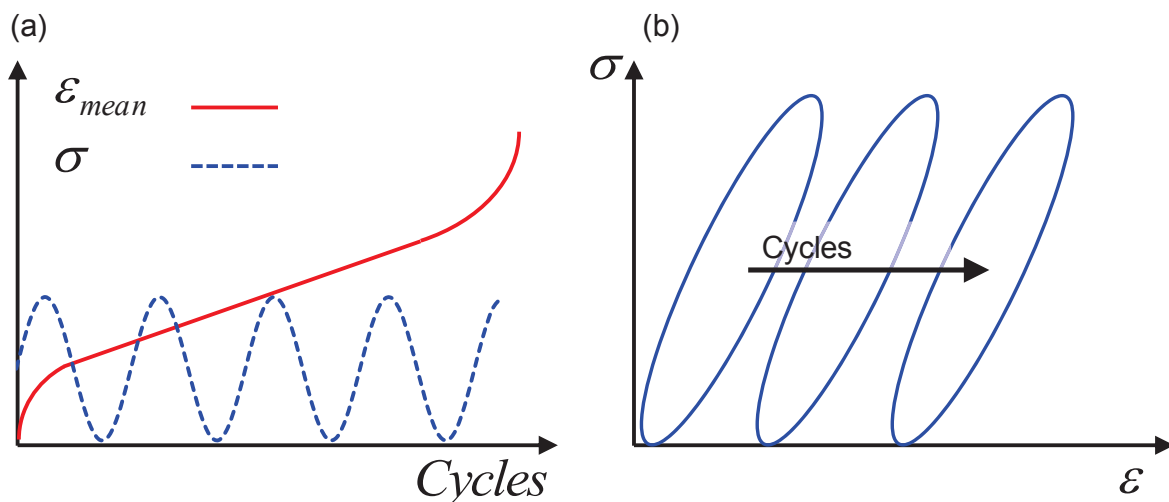


**Figure 3.2.** (a) Strain increase due to cyclic loading; (b) Shift of the hysteresis loops due to increasing mean stress.

Mallick and Zhou [20] carried out fatigue tests on PA66-GF33 plain specimens for different load ratios. Comparing two fatigue tests characterized by the same stress amplitude but different load ratios, they showed that fatigue strength diminishes with increasing the mean stress. If the comparison is made between two fatigue tests characterized by the same maximum stress but different load ratios, the higher the stress amplitude, the lower the fatigue strength will be (Figure 3.3).

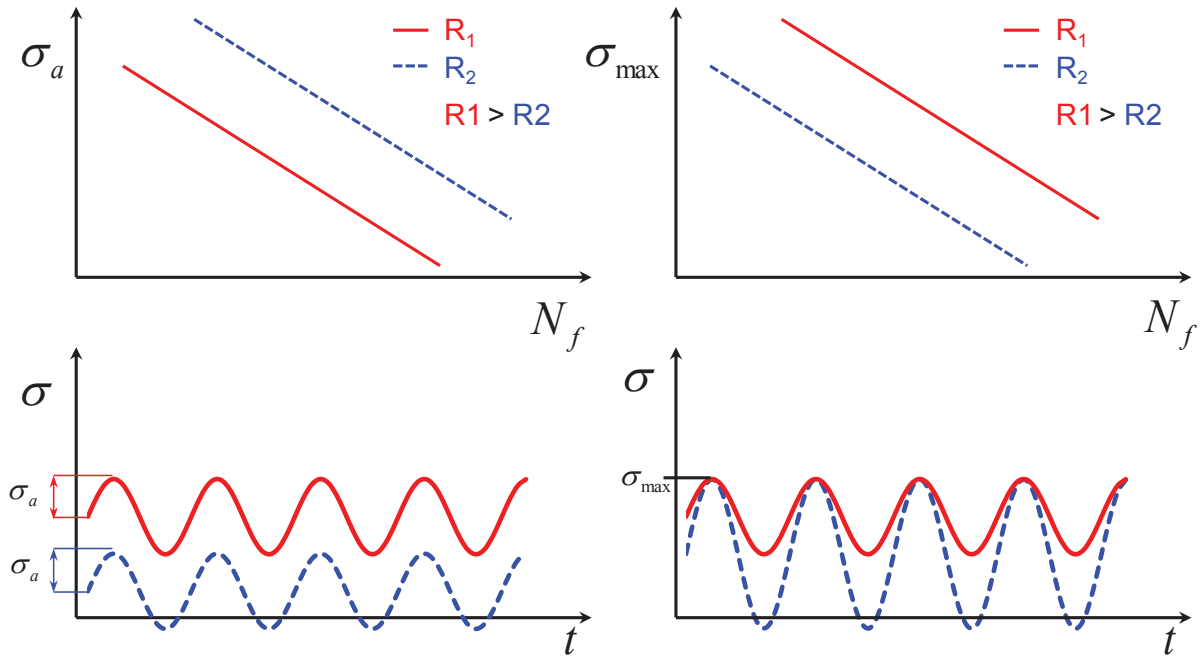


**Figure 3.3.** Effect of the mean stress on the fatigue behavior of PA66-GF35 plain specimens [20].

Mallick and Zhou also showed that a modified Gerber equation can be used to relate the mean stress with the stress amplitude for a specific number of cycles (Figure 3.4).

$$\frac{\sigma_a}{S_f} + \left( \frac{\sigma_m}{S_{rupture}} \right)^2 = 1 \quad (3.1)$$

Where  $S_{rupture}$  is the creep rupture strength and  $S_f$  is the fatigue strength for  $R = -1$ . Unlike for metals, the intercept with the x axis ( $\sigma_a = 0$ ) is the creep strength and not the static strength.

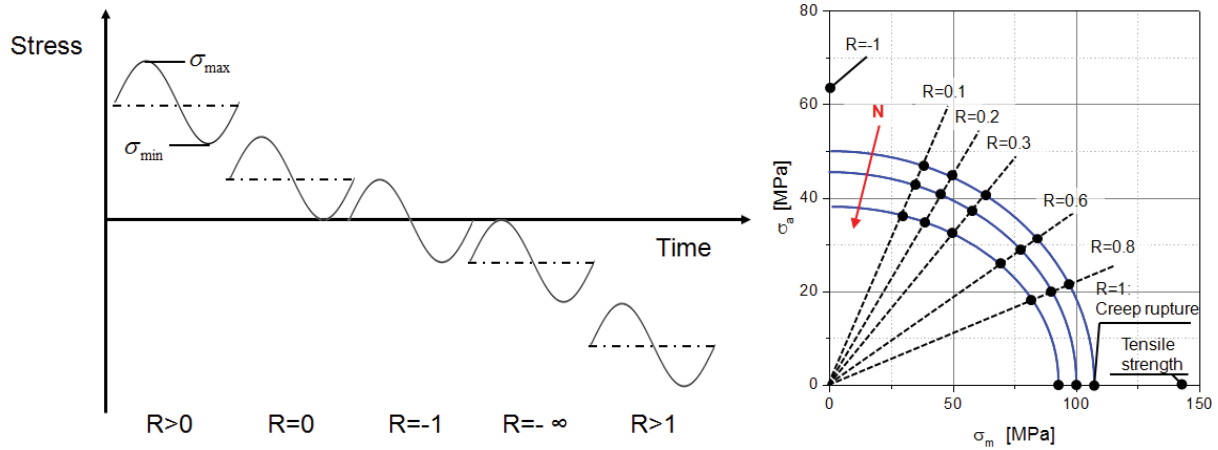


**Figure 3.4.** Effect of the mean stress on the fatigue strength [20].

The results reported by Zhou and Mallick [20] were confirmed in [2, 25]. In [2], De Monte and coworkers tested plain specimens made of PA66-GF35 under tension-compression loading ( $R = -1$ ) and tension-tension loading ( $R = 0$ ) reporting a lower fatigue strength in the second case. Sonsino and Moosbrugger [25] confirmed the detrimental effect of a positive mean stress for specimens with holes.

### 3.6 Notch

Injection molded parts are characterized by several geometric discontinuities. These regions represent stress concentrations and therefore are potential locations for the damage initiation. Examples of failure of real parts at notches are reported by Sonsino and Moosbrugger [25] and by Bernasconi et al. [26]. In order to investigate the notch effect on the fatigue strength of SFRPs, Sonsino and Moosbrugger [25] tested specimens with different notch geometries under uniaxial cyclic loading. They reported a significant decrease of the fatigue resistance with decreasing notch radius.

Zhou and Mallick [20] tested specimens with holes varying the hole diameter. They plotted the fatigue data in terms of gross and net cross-sectional area against the number of cycles to failure. In the former case, they observed a reduction of the fatigue strength increasing the hole radius, while in the latter case all the fatigue data fell within a scatter band so that they could be fitted by a unique S-N line.

De Monte and coworkers [27] reanalyzed fatigue data on notched specimens with different notch radius, for  $R = 0$  and  $R = -1$ , in terms of local Strain Energy Density (SED) range showing the fatigue data can be summarized in a single scatter band. The SED model was



originally developed by Lazzarin et al. [28-30]. The criterion was applied to weld joints [31, 32] and it was used for predicting the static failure of quasi-brittle materials [33]. One of its main advantages is that singular stress fields can be analyzed. In fact the energy averaged over a material volume surrounding the notch tip has a finite value even if the radius at the notch tip tends towards zero (crack). The energy is averaged over a volume of radius  $R$  which is a material property. Only two fatigue curves are needed for calibrating the model namely one for plain specimens and one for cracked specimens.

Basing on the same fatigue data reported by De Monte [27], Sonsino and Moosbrugger [25] proposed a volume based method originally developed for metallic materials [34]. The failure variable is the material volume included in the range  $(\sigma_{\text{peak}} - 80 \% \sigma_{\text{peak}})$ . The fatigue analysis can be carried out using a calibration curve which is derived experimentally from fatigue tests on notched specimens. This curve correlates the maximum peak stress for a given number of cycles with the material volume in the range  $\sigma_{\text{peak}}$  and  $80 \% \sigma_{\text{peak}}$ .

### 3.7 Multiaxiality

Quaresimin and coworkers [35] distinguished between external and internal multiaxiality depending upon whether a multiaxial stress state is generated by an external load or due to the material anisotropy. Local stress fields depend on the mutual orientation between external load and on fiber-matrix and fiber-fiber interactions. In the literature, the effect of external multiaxiality on the fatigue behavior of SFRPs was investigated in [36-40]. De Monte et al. [40] investigated the effect of multiaxial loading on the fatigue life of hollow tubular specimens made of PA66-GF35. They also considered the effect of load ratio, temperature and shifting phase. It was observed that for both tension-tension ( $R = 0$ ) and tension-compression ( $R = -1$ ) loading, at room temperature, the fatigue strength under pure torsion loading is lower than under pure tensile loading (Figure 3.5). However, the most severe case is represented by the combination, in equal parts, of tensile and torsion loading. The combination of tension and torsion loading is expressed by the biaxiality factor  $\lambda = \tau/\sigma$ . A lower biaxiality factor  $\lambda = 1/3$  resulted in a higher fatigue resistance. A slight beneficial effect of the out-of-phase loading ( $\delta = 90^\circ$ ) on the fatigue resistance was observed for both  $\lambda = 1$  and  $\lambda = 0.3$ . The same considerations apply in the case  $R = -1$ . However, for  $R = -1$ , the beneficial effect of the phase shifting is negligible. At high temperature, ( $T = 130^\circ\text{C}$ ) the fatigue strength is lower for all the considered cases. In particular, for  $R = -1$ , pure torsion,  $\lambda = 1$  and

$\lambda = 0.3$  fatigue data fall in an unique scatter band revealing that the shear stress is controlling the fatigue life.

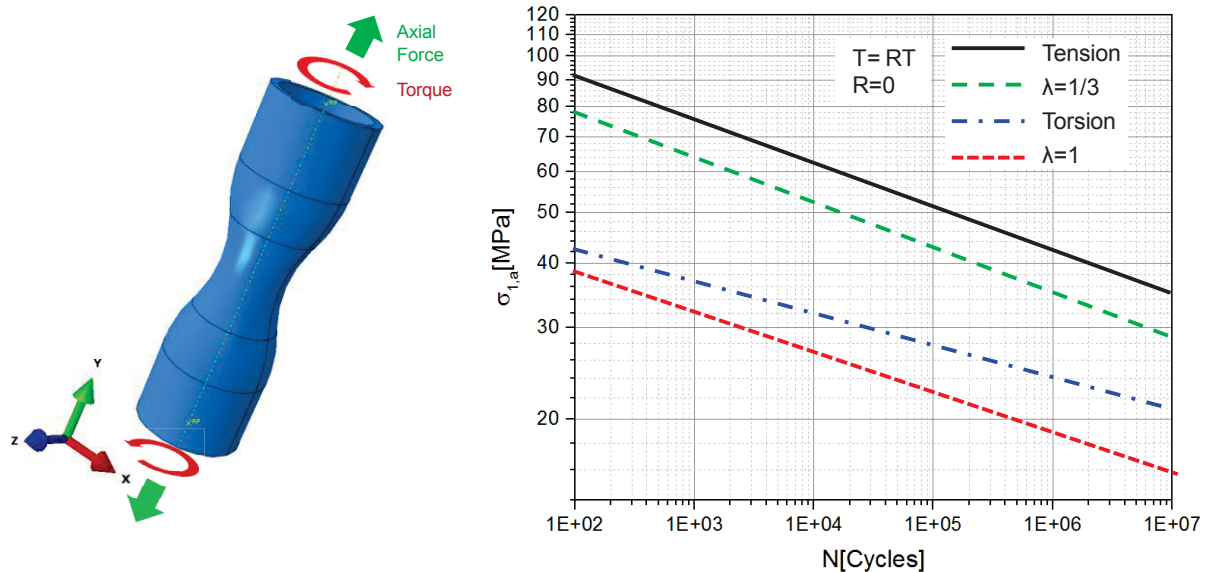


**Figure 3.5.** Effect of multiaxial loading on the fatigue resistance of tubular specimens [40]

In a subsequent work, De Monte et al. [37] studied the effect of the notch on the fatigue resistance of PA66-GF35 tubular specimens under multiaxial loading. Firstly tubular specimens characterized by a molded-in V-shaped notch ( $R_{\text{notch root}} = 0.2 \text{ mm}$ ) were manufactured by injection molding. These specimens were tested at  $R = 0$  and  $R = -1$  under the four testing conditions already reported in the previous work (pure tensile loading, pure torsion loading,  $\lambda = 1$  and  $\lambda = 0.3$ ). Unlike for plain tubular specimens tested at  $R=0$ , no significant difference in terms of fatigue strength was observed between specimens tested under pure torsion and pure tensile loading. Instead, the combination in equal parts of tension and torsion loading resulted in a decrease of the fatigue strength. For tension-compression loading ( $R = -1$ ), pure torsion resulted in a slight reduction of the fatigue resistance in comparison to pure axial loading. S-N lines of plain and notched tubular specimens under pure torsion loading, were found to overlap each other. This result suggested that the material is notch insensitive when subjected to pure torsion. The second step was to drill a circular hole of radius ( $R = 1 \text{ mm}$ ) in the central part of the plain tubular specimens. The hole was obtained at  $90^\circ$  with respect to the weld line which resulted from the injection molding process. Fatigue tests of these specimens under pure torsion revealed a significant decrease of the fatigue strength when compared to plain tubular specimens. This occurs in spite of the fact that the notch radius is 5 times larger than the tip radius of the molded V-shaped notch. This

result indicates that the fatigue material behavior exhibited by specimens with molded-in notches is affected by the fiber orientation distribution at the notch tip. The multiaxial fatigue behavior of SFRPs was also investigated by Klimkeit and coworkers [38, 39]. Tubular and plain specimens made of PBT-GF30 were tested under multiaxial fatigue loading. The authors confirmed that the fatigue strength of tubular specimens is really sensitive to shear stress. In particular, they observed that the fatigue strength of tubular specimens under multiaxial fatigue loading with biaxiality ratio  $\lambda = 0.5$  is between the pure tensile and the pure torsion S-N lines confirming the results shown by De Monte et al. [40].

### **3.8 Fluids**

The choice of polymer for under-the-hood applications is driven by the compatibility of the material with automotive fluids such as gasoline, diesel, brake fluid, motor coolant. Polyamides are known to absorb a significant amount of water and other polar fluids. Water content in PA66-GF35 at ambient temperature and 50 % relative humidity is typically 2.5 % by weight. Fluid absorption by the composite leads to volume increase (swelling). Thomason and coworkers [41-44] investigated the mass and volume change of short fiber reinforced polyamide after conditioning in three different fluids: water, ethylene glycol and water-glycol mixture. They observed that swelling is anisotropic being lower in the fiber direction since fibers prevent matrix to deform. They also showed that 1) Water-absorption rate increases with temperature; 2) water uptake at equilibrium is almost temperature independent but fluid dependent, being higher for water-ethylene glycol antifreeze than for water alone.

The fluid uptake leads to chemical and mechanical changes in the material. It is well known that the glass transition temperature of polyamides strongly decrease with increasing water content [43-47]. This means that some polyamide parts that have been exposed to water or other polar fluids could be found in the rubbery state at room temperature. The fluid absorption has normally a plasticizing effect on polyamides leading to a decrease of both Young's modulus tensile strength [48, 49], an increase of the notch impact [44] and strain at failure [50].

The influence of the media on the fatigue behavior of SFRPs was studied, although in lower extent than for quasi-static loading. Karger-Kocsis and Friedrich [51] performed FCP tests on dry and water saturated unfilled polyamide specimens. They found that conditioned specimens exhibit a lower  $\Delta K_{th}$  and a higher crack propagation rate. The same results were confirmed by Günzel and coworkers [52]. They performed FCP tests on DAM and

conditioned (water content: 2.1 wt. %) PA66-GF30 specimens and observed a shift of the Paris curve to the left due to the water absorption. Brodowsky et al. [53] performed fatigue tests on single-fiber specimens (matrix: PA, fiber: Glass) in DAM condition and after water conditioning. In the latter case they reported for the same applied displacement a lower resulting force due to the mollifying effect of water.

### **3.9 Temperature**

The temperature under the hood depends mainly on the following factors: Motor and exhaust systems, external temperature, cooling system. A typical temperature range for under-the-hood component goes from -40 to 120 °C. -40 °C is typically the temperature experienced by mechanical and electro-mechanical systems when motor starts in extremely cold ambient conditions. On the other hand, just after motor switch off, when the cooling system ceases to function, temperature under the hood can reach up to 120 °C. Thermal loading affects both the stiffness and the strength of SFRPs and represents challenging requirements for SFRPs in automotive applications. Mechanical properties of SFRPs vary significantly through  $T_g$ .

The detrimental effect of the temperature on the fatigue strength of short glass fiber reinforced polyamide was reported in [2, 25, 48, 54]. Jia and Kagan [48] observed that fatigue data at different temperatures fall within a scatter band if the stress amplitude is divided by the corresponding tensile strength.

Heating is non-negligible ahead of the crack tip during crack propagation [23, 55]. Lang and Manson [55] studied heating at crack tip during crack propagation on CT specimens of PA and PS systems. They identified two mechanisms which lead to temperature increase at the crack tip: hysteretic heating and frictional heating. The hysteretic heating is the mechanical energy supplied during one cycle and corresponds to the area enclosed by the hysteresis loop. The frictional contribution is due to the damage mechanisms such as friction between crack surfaces during the unloading part of a fatigue cycle and the fiber matrix friction occurring when fibers are pulled out from matrix.

In some applications failure is not caused by cyclic loading at a specific temperature, but rather due to cyclic temperature variation. When the cyclic stress is caused by temperature variations we refer to Thermomechanical Fatigue (TMF). The TMF test developed at the Department of Management and Engineering-University of Padova and presented in [56, 57] consists firstly in the application of a constant pre-strain to the specimen (which is held constant throughout the test) and then in a cyclic temperature variation between two extreme

temperatures (i.e.  $-40\text{ }^{\circ}\text{C} < T < +120\text{ }^{\circ}\text{C}$ ) within a short span of time (for example, 5 min). The resulting stress profile follows the temperature profile where maximum stress corresponds to the minimum temperature and the minimum stress to the maximum temperature. The application of the previously described test to plain and notched specimens leads to earlier failure when compared with displacement controlled fatigue tests carried out at constant temperature [57].

### **References of Chapter 3**

- [1] A. Bernasconi, P. Davoli, A. Basile, A. Filippi, Effect of fibre orientation on the fatigue behaviour of a short glass fibre reinforced polyamide-6, *Int. J. Fatigue*. 29 (2007) 199-208.
- [2] M. De Monte, E. Moosbrugger, M. Quaresimin, Influence of temperature and thickness on the off-axis behaviour of short glass fibre reinforced polyamide 6.6 – cyclic loading, *Composites Part A: Applied Science and Manufacturing*. 41 (2010) 1368-1379.
- [3] S. Mortazavian, A. Fatemi, Fatigue behavior and modeling of short fiber reinforced polymer composites including anisotropy and temperature effects, *Int. J. Fatigue*. 77 (2015) 12-27.
- [4] K. Friedrich, Microstructure and fracture mechanical properties of short fiber reinforced thermoplastic P.E.T., *Colloid and Polymer Science*. 259 (1981) 808-811.
- [5] M.G. Wyzgoski, G.E. Novak, Fatigue fracture of nylon polymers: Part II. Effect of glass-fibre reinforcement, *Journal of Materials Science*. 26 (1991) 6314-6324.
- [6] W.J. Evans, D.H. Isaac, K.S. Saib, The effect of short carbon fibre reinforcement on fatigue crack growth in PEEK, *Composites Part A: Applied Science and Manufacturing*. 27 (1996) 547-554.
- [7] K. Tanaka, T. Kitano, N. Egami, Effect of fiber orientation on fatigue crack propagation in short-fiber reinforced plastics, *Eng. Fract. Mech*. 123 (2014) 44-58.
- [8] J.J. Horst, J.L. Spoomaker, Mechanisms of fatigue in short glass fiber reinforced polyamide 6, *Polymer Engineering & Science*. 36 (1996) 2718-2726.

- [9] M. Laspalas, C. Crespo, M.A. Jiménez, B. García, J.L. Pelegay, Application of micromechanical models for elasticity and failure to short fibre reinforced composites. Numerical implementation and experimental validation, *Comput. Struct.* 86 (2008) 977-987.
- [10] A. Bernasconi, F. Cosmi, E. Zappa, Combined Effect of Notches and Fibre Orientation on Fatigue Behaviour of Short Fibre Reinforced Polyamide, *Strain.* 46 (2010) 435-445.
- [11] J.F. Mandell, F.J. McGarry, D.D. Huang, C.G. Li, Some effects of matrix and interface properties on the fatigue of short fiber-reinforced thermoplastics, *Polymer Composites.* 4 (1983) 32-39.
- [12] A. Avanzini, G. Donzella, D. Gallina, Fatigue damage modelling of PEEK short fibre composites, *Procedia Engineering.* 10 (2011) 2052-2057.
- [13] J.F. Mandell, D.D. Huang, F.J. McGarry, Fatigue of glass and carbon fiber reinforced engineering thermoplastics, *Polymer Composites.* 2 (1981) 137-144.
- [14] K. Friedrich, R. Walter, H. Voss, J. Karger-Kocsis, Effect of short fibre reinforcement on the fatigue crack propagation and fracture of PEEK-matrix composites, *Composites.* 17 (1986) 205-216.
- [15] H. Voss, J. Karger-Kocsis, Fatigue crack propagation in glass-fibre and glass-sphere filled PBT composites, *Int. J. Fatigue.* 10 (1988) 3-11.
- [16] J. Karger-Kocsis, K. Friedrich, Fatigue crack propagation in short and long fibre-reinforced injection-moulded PA 6.6 composites, *Composites.* 19 (1988) 105-114.
- [17] K. Friedrich, J. Karger-Kocsis, Fracture and fatigue of unfilled and reinforced polyamides and polyesters, in: J.M. Schultz, S. Fakirov (Eds.), *Solid state behavior of linear polyesters and polyamides*, Prentice Hall Inc., Englewood Cliffs, 1990, pp. 249-322.
- [18] J. Karger-Kocsis, Effects of processing induced microstructure on the fatigue crack propagation of unfilled and short fibre-reinforced PA-6, *Composites.* 21 (1990) 243-254.
- [19] A. Pegoretti, T. Riccò, Fatigue crack propagation in polypropylene reinforced with short glass fibres, *Composites Sci. Technol.* 59 (1999) 1055-1062.

- [20] Y. Zhou, P.K. Mallick, Fatigue performance of an injection-molded short E-glass fiber-reinforced polyamide 6,6. I. Effects of orientation, holes, and weld line, *Polymer Composites*. 27 (2006) 230-237.
- [21] V. Bellenger, A. Tcharkhtchi, P. Castaing, Thermal and mechanical fatigue of a PA66/glass fibers composite material, *Int. J. Fatigue*. 28 (2006) 1348-1352.
- [22] A. Bernasconi, R.M. Kulin, Effect of frequency upon fatigue strength of a short glass fiber reinforced polyamide 6: A superposition method based on cyclic creep parameters, *Polymer Composites*. 30 (2009) 154-161.
- [23] M.G. Wyzgoski, G.E. Novak, Fatigue fracture of nylon polymers Part 1 Effect of frequency, *Journal of Materials Science*. 25 (1990) 4501-4510.
- [24] M.F. Arif, N. Saintier, F. Meraghni, J. Fitoussi, Y. Chemisky, G. Robert, Multiscale fatigue damage characterization in short glass fiber reinforced polyamide-66, *Composites Part B: Engineering*. 61 (2014) 55-65.
- [25] C.M. Sonsino, E. Moosbrugger, Fatigue design of highly loaded short-glass-fibre reinforced polyamide parts in engine compartments, *Int. J. Fatigue*. 30 (2008) 1279-1288.
- [26] A. Bernasconi, P. Davoli, C. Armani, Fatigue strength of a clutch pedal made of reprocessed short glass fibre reinforced polyamide, *Int. J. Fatigue*. 32 (2010) 100-107.
- [27] M. De Monte, M. Quaresimin, P. Lazzarin, Modelling of fatigue strength data for a short fiber reinforced polyamide 6.6 based on local strain energy density. *Proceedings of ICCM16, 16th International Conference on Composite Materials* (2007).
- [28] P. Lazzarin, R. Zambardi :, A finite-volume-energy based approach to predict the static and fatigue behavior of components with sharp V-shaped notches, *International Journal of Fracture*. 12 (2001) 275-298.
- [29] P. Lazzarin, F. Berto, Some Expressions for the Strain Energy in a Finite Volume Surrounding the Root of Blunt V-notches, *International Journal of Fracture*. 135 (2005) 161-185.



- [30] B. Atzori, F. Berto, P. Lazzarin, M. Quaresimin, Multi-axial fatigue behaviour of a severely notched carbon steel, *Int. J. Fatigue*. 28 (2006) 485-493.
- [31] F. Berto, P. Lazzarin, A review of the volume-based strain energy density approach applied to V-notches and welded structures, *Theor. Appl. Fract. Mech.* 52 (2009) 183-194.
- [32] F. Berto, P. Lazzarin, Fatigue strength of structural components under multi-axial loading in terms of local energy density averaged on a control volume, *Int. J. Fatigue*. 33 (2011) 1055-1065.
- [33] P. Lazzarin, F. Berto, M. Eleices, J. Gomez, Brittle failures from U- and V-notches in mode I and mixed, I + II, mode: a synthesis based on the strain energy density averaged on finite-size volumes, *Fatigue & Fracture of Engineering Materials & Structures*. 32 (2009) 671-684.
- [34] C.M. Sonsino, Evaluating the fatigue behaviour of components with consideration of local stresses, *Konstruktion*. 45 (1993) 25-33.
- [35] M. Quaresimin, L. Susmel, R. Talreja, Fatigue behaviour and life assessment of composite laminates under multiaxial loadings, *Int. J. Fatigue*. 32 (2010) 2-16.
- [36] E. Moosbrugger, M. DeMonte, K. Jaschek, J. Fleckenstein, A. Bütter, Multiaxial fatigue behaviour of a short-fibre reinforced polyamide - experiments and calculations, *Materialwissenschaft und Werkstofftechnik*. 42 (2011) 950-957.
- [37] M. De Monte, E. Moosbrugger, K. Jaschek, M. Quaresimin, Multiaxial fatigue behaviour of a short-fibre reinforced polyamide 6.6 in the presence of notches. *ECCM - 13th European Conference on Composite Materials* (2008).
- [38] B. Klimkeit, Y. Nadot, S. Castagnet, C. Nadot-Martin, C. Dumas, S. Bergamo, C.M. Sonsino, A. Bütter, Multiaxial fatigue life assessment for reinforced polymers, *Int. J. Fatigue*. 33 (2011) 766-780.
- [39] B. Klimkeit, S. Castagnet, Y. Nadot, A.E. Habib, G. Benoit, S. Bergamo, C. Dumas, S. Achard, Fatigue damage mechanisms in short fiber reinforced PBT+PET GF30, *Materials Science and Engineering: A*. 528 (2011) 1577-1588.



- [40] M. De Monte, E. Moosbrugger, K. Jaschek, M. Quaresimin, Multiaxial fatigue of a short glass fibre reinforced polyamide 6.6 – Fatigue and fracture behaviour, *Int. J. Fatigue*. 32 (2010) 17-28.
- [41] H.K. Reimschuessel, Relationships on the effect of water on glass transition temperature and young's modulus of nylon 6, *Journal of Polymer Science: Polymer Chemistry Edition*. 16 (1978) 1229-1236.
- [42] J.L. Thomason, J.Z. Ali, The dimensional stability of glass–fibre reinforced polyamide 66 during hydrolysis conditioning, *Composites Part A: Applied Science and Manufacturing*. 40 (2009) 625-634.
- [43] J.L. Thomason, J.Z. Ali, J. Anderson, The thermo-mechanical performance of glass-fibre reinforced polyamide 66 during glycol–water hydrolysis conditioning, *Composites Part A: Applied Science and Manufacturing*. 41 (2010) 820-826.
- [44] J.L. Thomason, G. Porteus, Swelling of glass-fiber reinforced polyamide 66 during conditioning in water, ethylene glycol, and antifreeze mixture, *Polymer Composites*. 32 (2011) 639-647.
- [45] U.T. Kreibich, H. Batzer, Influence of water on thermal transitions in natural polymers and synthetic polyamides, *Polymer Bulletin*. 5 (1981) 585-590.
- [46] N. Jia, H.A. Fraenkel, V.A. Kagan, Effects of Moisture Conditioning Methods on Mechanical Properties of Injection Molded Nylon 6, *Journal of Reinforced Plastics and Composites*. 23 (2004) 729-737.
- [47] S. Barbouchi, V. Bellenger, A. Tcharkhtchi, P. Castaign, T. Jollivet, Effect of water on the fatigue behaviour of a PA66/glass fibers composite material, *Journal of Materials Science*. 42 (2007) 2181-2188.
- [48] N. Jia, V. Kagan, Mechanical Performance of Polyamides with Influence of Moisture and Temperature – Accurate Evaluation and Better Understanding, in: *Plastics Failure: Analysis and Prevention*, Plastic Design Library, New York, 2001, pp. 95-104.

- [49] M.F. Arif, F. Meraghni, Y. Chemisky, N. Despringre, G. Robert, In situ damage mechanisms investigation of PA66/GF30 composite: Effect of relative humidity, *Composites Part B: Engineering*. 58 (2014) 487-495.
- [50] D. Ferreño, I. Carrascal, E. Ruiz, J.A. Casado, Characterisation by means of a finite element model of the influence of moisture content on the mechanical and fracture properties of the polyamide 6 reinforced with short glass fibre, *Polym. Test*. 30 (2011) 420-428.
- [51] J. Karger-Kocsis, K. Friedrich, Skin-core morphology and humidity effects on the fatigue crack propagation of PA-6.6, *Plastics and Rubber Processing and Applications*. 12 (1989) 63-68.
- [52] S. Günzel, S. Hickmann, C. Wittemeyer, V. Trappe, Effects of Fiber Orientation and Moisture on the Crack Growth in Short Glass Fiber Reinforced Polyamide, *Advanced Engineering Materials*. 14 (2012) 867-872.
- [53] H.M. Brodowsky, W. Jenschke, E. Mäder, Characterization of interphase properties: Microfatigue of single fibre model composites, *Composites Part A: Applied Science and Manufacturing*. 41 (2010) 1579-1586.
- [54] K. Noda, A. Takahara, T. Kajiyama, Fatigue failure mechanisms of short glass-fiber reinforced nylon 66 based on nonlinear dynamic viscoelastic measurement, *Polymer*. 42 (2001) 5803-5811.
- [55] R.W. Lang, J.A. Manson, Crack tip heating in short-fibre composites under fatigue loading conditions, *Journal of Materials Science*. 22 (1987) 3576-3580.
- [56] M. Pierantoni, M. De Monte, D. Papathanassiou, N. De Rossi, M. Quaresimin, Viscoelastic material behaviour of PBT-GF30 under thermo-mechanical cyclic loading, *Procedia Engineering*. 10 (2011) 2141-2146.
- [57] A. Schaaf, M. De Monte, E. Moosbrugger, M. Vormwald, M. Quaresimin, Life estimation methodology for short fiber reinforced polymers under thermo-mechanical loading in automotive applications, *Materialwissenschaft und Werkstofftechnik*. 46 (2015) 214-228.

## **Chapter 4**

# **Life to crack initiation in notched specimens of unreinforced and short fiber reinforced polyamide under fatigue loading**

**Keywords:** Short Fiber Reinforced Plastics, Fatigue, Polyamide, Crack initiation

### **Abstract**

An optical method was developed to quantify the lifetime to crack initiation during fatigue tests of unreinforced and short glass fiber reinforced polyamide notched specimens. During the fatigue test execution, pictures of the region surrounding the notch were captured using a CCD camera. The image acquisition system was synchronized with the testing machine. The crack initiation detection is based on the variation of the grey value distribution along a straight path tangent to the notch tip due to the crack occurrence.

The contribution of the crack initiation and growth phase to the total lifetime was studied for different load levels and fiber volume fractions. S-N lines to failure and to crack initiation were compared against each other. The proposed experimental methodology is validated by interrupting fatigue tests before failure and measuring the crack length by means of optical microscope.

### **4.1 Introduction**

Short Fiber Reinforced Plastics (SFRPs) find an increasing number of applications in the automotive sector. Thanks to their high strength to weight ratio, high temperature and chemical resistance, SFRPs are excellent candidates for under-the-hood applications. Under-the-hood parts are exposed to cyclic loading due to vibrations, pulsating pressure, temperature variations [1, 2]. When subjected to fatigue loading, the typical failure scenario of an injection molded part is the crack initiation at a geometric discontinuity [3] and its propagation until separation into two or more parts.

In the last decades, the research on the fatigue behavior of SFRPs has proceeded on separate tracks. On one side, the derivation of fatigue curves for plain specimens, on the other side, the Fatigue Crack Propagation (FCP) tests using Compact Tension (CT) specimens. The specimen geometries in the two cases reflect the two extremes of the fatigue material behavior. As shown in [4], failure of plain specimens is not preceded by any observed stable crack propagation. On the other hand, the use of CT specimens aims to study only the crack propagation. Fatigue failure of injection molded parts is likely to stand in the middle of these two scenarios. Cracks are expected to initiate at structural discontinuities such as notches or section changes and to propagate until final failure.

In certain structural components such as fuel rails, failure corresponds to the onset of a crack. According to the definition by Talreja [5], failure is the inability of a material system to perform its design function. The function of the fuel rail, is to convey fuel under high pressure to the injectors. If a crack occurs, the function of the fuel rail is lost. In other applications (i.e. plastic cases of power tools), injection molded parts may fulfill the design function even after the nucleation of a crack. The use of a model able to predict the crack initiation or the total lifetime should be related to the application. Nevertheless, “no-crack” is the dominant criterion in the durability analysis of SFRP parts. This is primarily due to the lack of models able to distinguish between the two phases of the total lifetime (initiation and propagation). In [2] thermo-mechanical fatigue tests of short glass fiber reinforced polybutylene terephthalate (PBT-GF30) notched specimens were interrupted when a 0.5 mm crack was observed. The distinction between crack initiation and crack propagation has been investigated more extensively for continuous fiber reinforced composites. Quaresimin et al. [7, 8] used two different representations (S-N lines and Paris-like curves) for illustrating the initiation and the propagation phase of Glass/Epoxy tubes undergoing multiaxial fatigue loading.

The aim of this work is to quantify the fraction of the total fatigue life of notched specimens spent in the initiation of a crack. An experimental optical method was developed for the crack initiation detection. The present work is part of the long-term collaboration between the University of Padova and the corporate research of Robert Bosch GmbH aimed to develop lifetime prediction models for SFRPs.

## 4.2 Experimental set up

Unreinforced and short glass fiber reinforced polyamides (PA66) were used in this work. Five material systems were considered: PA66, PA66-GF15, PA66-GF25, PA66-GF35, PA66-GF50 which correspond to 0 %, 15 %, 25 %, 35 %, 50 % weight fiber fraction respectively. Injection molded specimens characterized by a central slit ( $R_{\text{notch}} = 0.2$  mm) were used. The Mold Flow Direction (MFD) corresponds to the horizontal direction in Figure 4.1. Fiber length as well as the fiber orientation varies with the fiber fraction. In [9, 10] it was observed that an increase of fiber fraction results in an increase of the fiber alignment to the MFD and a decrease of the average fiber length.

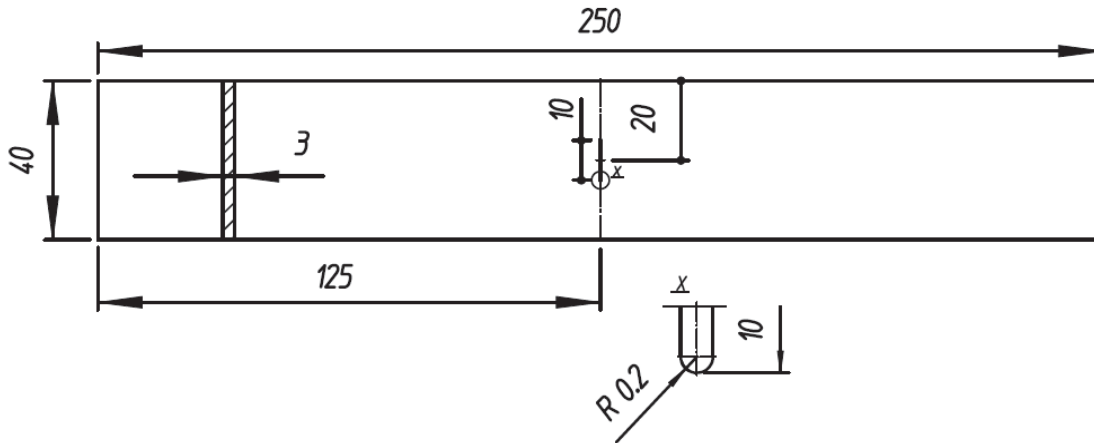


**Figure 4.1.** Specimen geometries and dimensions (in mm).

The notch was molded in and not machined afterwards. This configuration is closer to real injection molded parts which, in most cases, do not require any post-molding finishing operation since they are ready to use after ejection from the mold. Each geometric discontinuity in the mold represents a stress concentration but also a perturbation for the plastic molten flow which locally affects the fiber orientation distribution. The effect of molded-in and machined notch on the torsional fatigue resistance of PA66-GF35 hollow tubular specimens was studied by De Monte and coworkers in [11, 12]. In [11] it was found that the torsional fatigue resistance of plain and notched (molded-in V-shaped notch,  $R_{\text{notch}} = 0.2$  mm) hollow tubular specimens is similar. In another work [12], a strong decrease of the torsional fatigue resistance was observed when drilling a hole ( $R = 1$  mm) in the central part of plain tubular specimens. Even if the drilled hole has a larger diameter than the molded

notch, it strongly affects the torsional fatigue strength of the composite material. This is due to the reinforcement effect of the fiber orientation distribution at the notch tip.

The optical method for the determination of the lifetime to crack initiation was developed in two phases. An automated picture capturing system based on NI Labview® was developed at DTG-University of Padova (Figure 4.2a). This method was used by Schaaf and coworkers [2] for interrupting thermo-mechanical fatigue tests of notched specimens when a 0.5 mm crack was observed. Uniaxial load-controlled fatigue tests were carried out on a 25 kN hydraulic test system. Some fatigue tests were interrupted for studying the effect of various lighting techniques on the picture quality (Figure 4.2b-d). A 600 x 800 analog CCD Camera with optical magnification was used for this purpose. Firstly, indirect halogen lamps were used to illuminate the specimen (Figure 4.2b) revealing cracks departing from the tips of the notch. Figure 4.2c-d shows pictures of the region surrounding the notch when the specimen is illuminated using LED lamps. The orientation of the LED lamps strongly affects the quality of the pictures. In Figure 4.2c the illumination is horizontal. The specimen is cracked at both the sides of the notch but the cracks are hard to see. Instead, the vertical scratches on the specimen surface due injection molding are highlighted due to the horizontal direction of the luminous flux. Figure 4.2d shows the picture when the luminous flux of the LED lamps is vertical. Cracks at both the tips of the notch are easier to see. Hence, by comparing the three pictures to each other, it can be concluded that LED lamps oriented parallel to the crack opening direction enable the best possible crack detection.



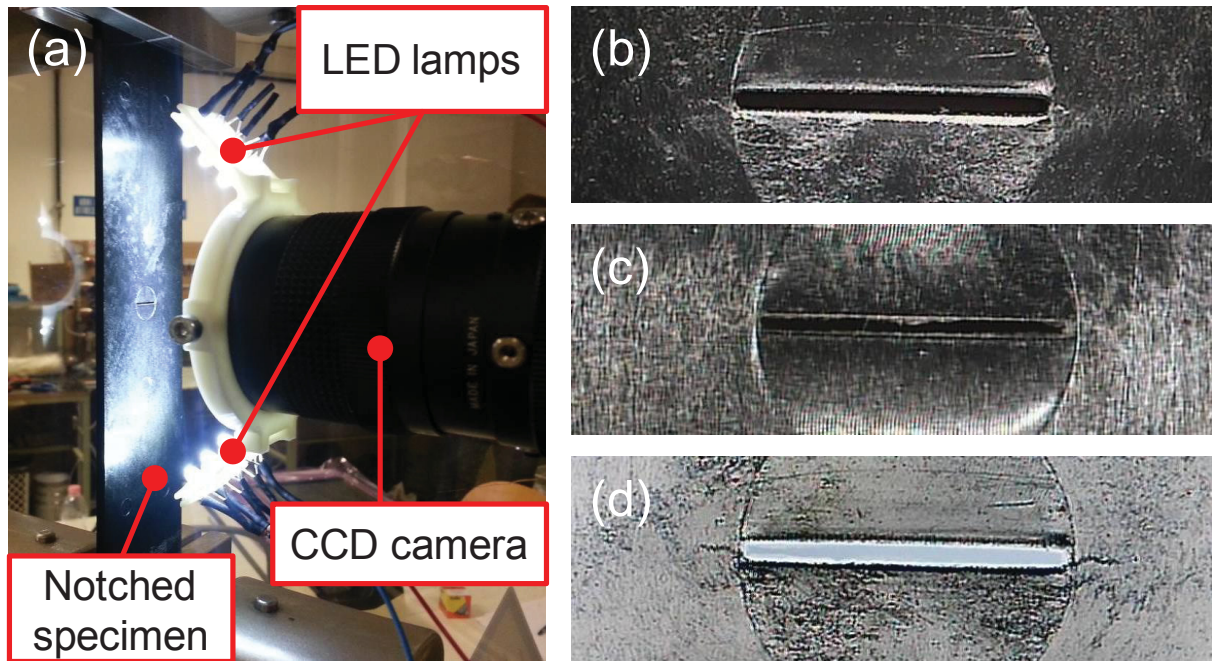


**Figure 4.2.** (a) Experimental set up at DTG; (b) Indirect halogen lamps, homogeneous illumination; (c) Direct led lamps, horizontal illumination; (d) Direct led lamps, vertical illumination and inverted colors. The circle around the notch is the mark left by the insert on the specimen surface.

The proposed methodology was further developed at Robert Bosch GmbH (Figure 4.3a). A 2 Megapixels CCD camera was used. According to the work done in the set-up phase of the initial investigation, two high-performance LED lamps were mounted on the framework to illuminate the specimen surface. To improve the image contrast, the specimen surface was sprayed in white (Figure 4.3b). The image acquisition system was synchronized with the testing machine. The system takes a picture when the 90 % of the maximum applied load is reached. The image acquisition rate was adapted to the testing frequency. Since only the specimen surface was investigated, it was assumed that the crack front is homogeneous through the thickness. This was verified by dedicated through-the-thickness analyses.

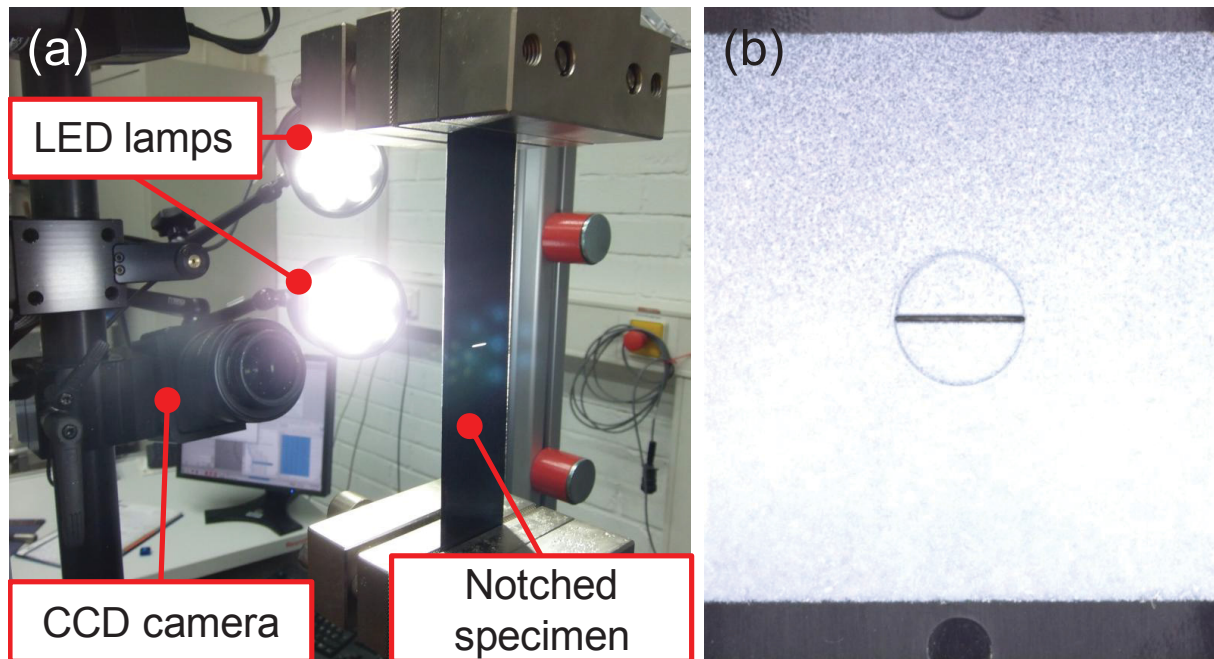


**Figure 4.3.** (a) Experimental set up at Robert Bosch GmbH; (b) White spray pattern applied to the specimen surface.

Uniaxial load-controlled fatigue tests were carried out on a 10 kN servo-hydraulic testing machine, under tension-tension loading (load ratio:  $R = 0$ ). The fatigue tests were carried out at room temperature; variations of ambient relative humidity were not controlled. The specimens were tested in dry-as-molded conditions. Right after the injection molding, they were stored in a drum containing a drying agent (silica gel pearls). The test frequency was chosen in order to avoid the self heating of the specimen and varies inversely with the load level. Fatigue tests were carried out until the separation of the specimen into two parts. Data were post processed using Matlab® after completion of the test. The procedure for the data analysis is summarized in Figure 4.4. A segment tangent to notch tip was superimposed to the picture taken before starting a fatigue test (Figure 4.4a-b). Each pixel has a grey value between 0 and 255. Before crack onset, the grey value distribution along the path is roughly constant (Figure 4.4b). The crack occurrence appears as a discontinuity on the white pattern. A negative peak in the grey value distribution indicates the onset of a crack (Figure 4.4e). This procedure is applied through a loop operation to all the pictures taken during the fatigue test. Figure 4.4c-f shows the trend of the minimum grey value along the path, throughout the fatigue test. The trend remains approximately constant during the first part of the test. At a certain point, a sudden drop of the minimum grey value is noticed. This point corresponds to the crack initiation. The cracks at the right and the left of the notch may not occur at the same



time. In this work, the criterion for determining the crack initiation is based on the first detectable crack.

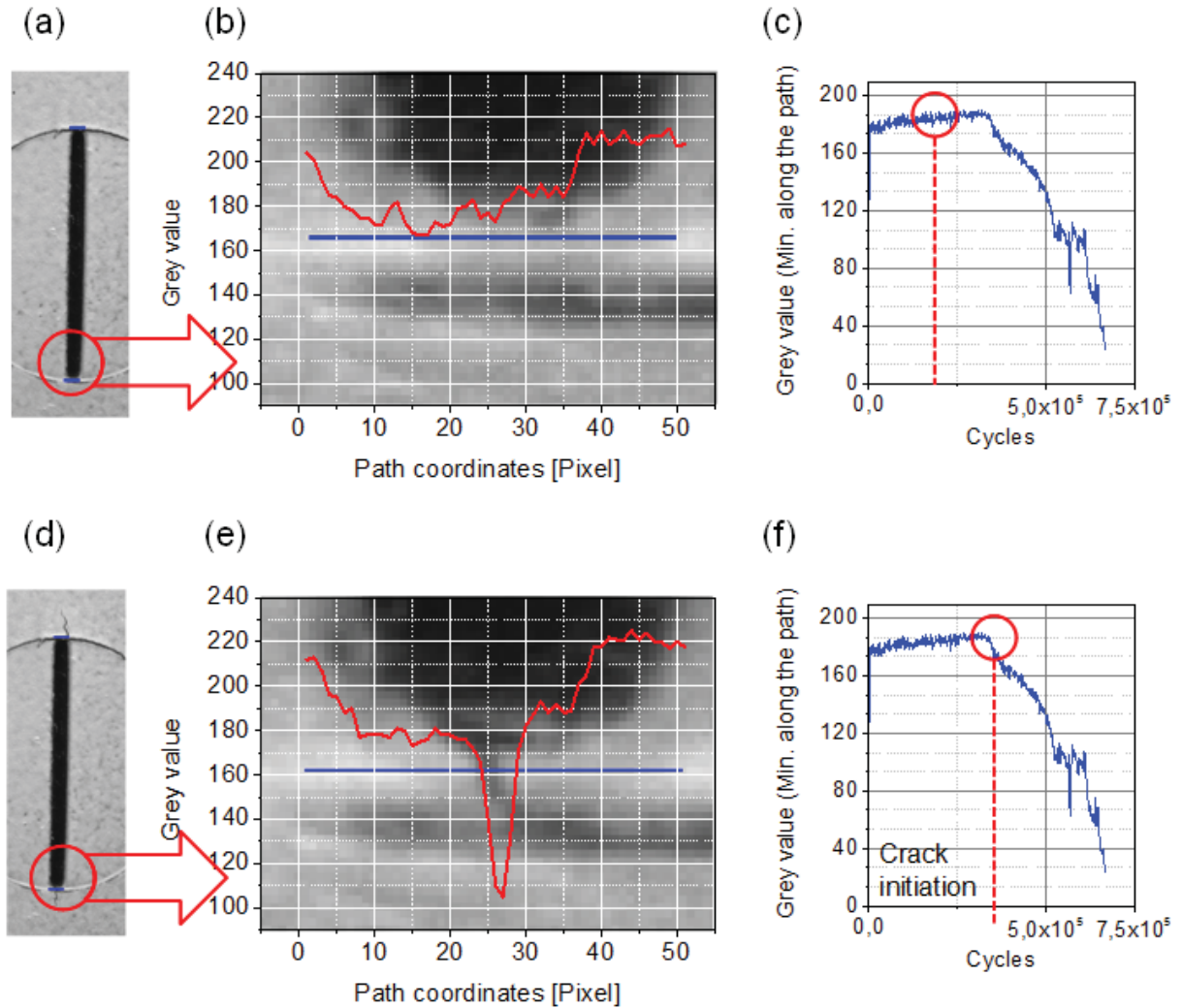


**Figure 4.4.** (a) Sprayed surface around the notch; (b) Grey value profile along the defined path; (c) Trend of the minimum gray value during the fatigue test. (a)-(c) Before the crack onset; (d)-(f) After crack onset.

The minimum grey value along the path decreases even after crack initiation. This is due to the increasing distance between the crack surfaces (Figure 4.5).

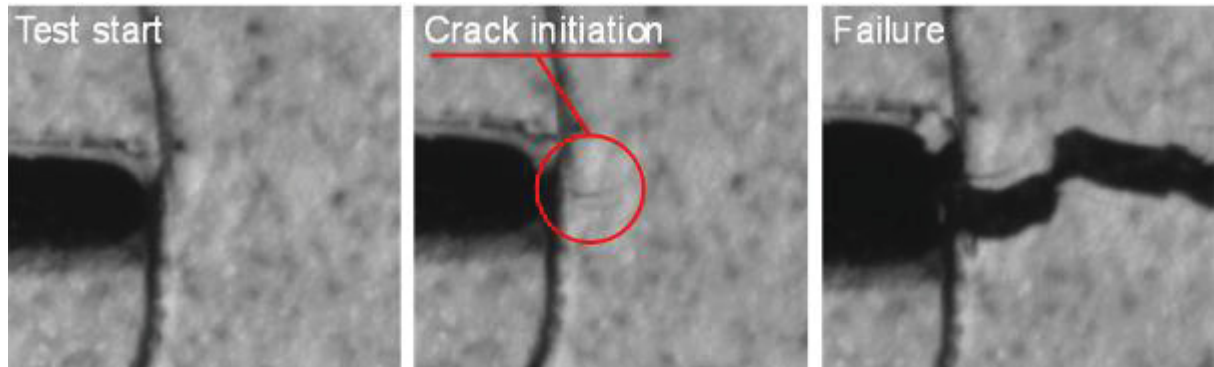


**Figure 4.5.** Crack initiation and propagation during fatigue test of notched specimens.

### 4.3 Validation of the experimental method

For the validation of the proposed method, some fatigue tests on PA66-GF35 specimens were interrupted at 50 % of the expected total lifetime. In this way, it was possible to compare the real crack length with the values measured according to the optical method. Once a fatigue test was interrupted, a sample around the notch was machined from the specimen and prepared for microscopic investigations. For the measure of the crack length, an optical microscope (Axio Scope.A1) was used. Figure 4.6 shows a comparison between the crack length measured by the optical method (on the left) and the real crack length measured by means of the optical microscope after polishing the specimen surface (on the right). The measure of the crack length is based on the distance between the two crack extremities.

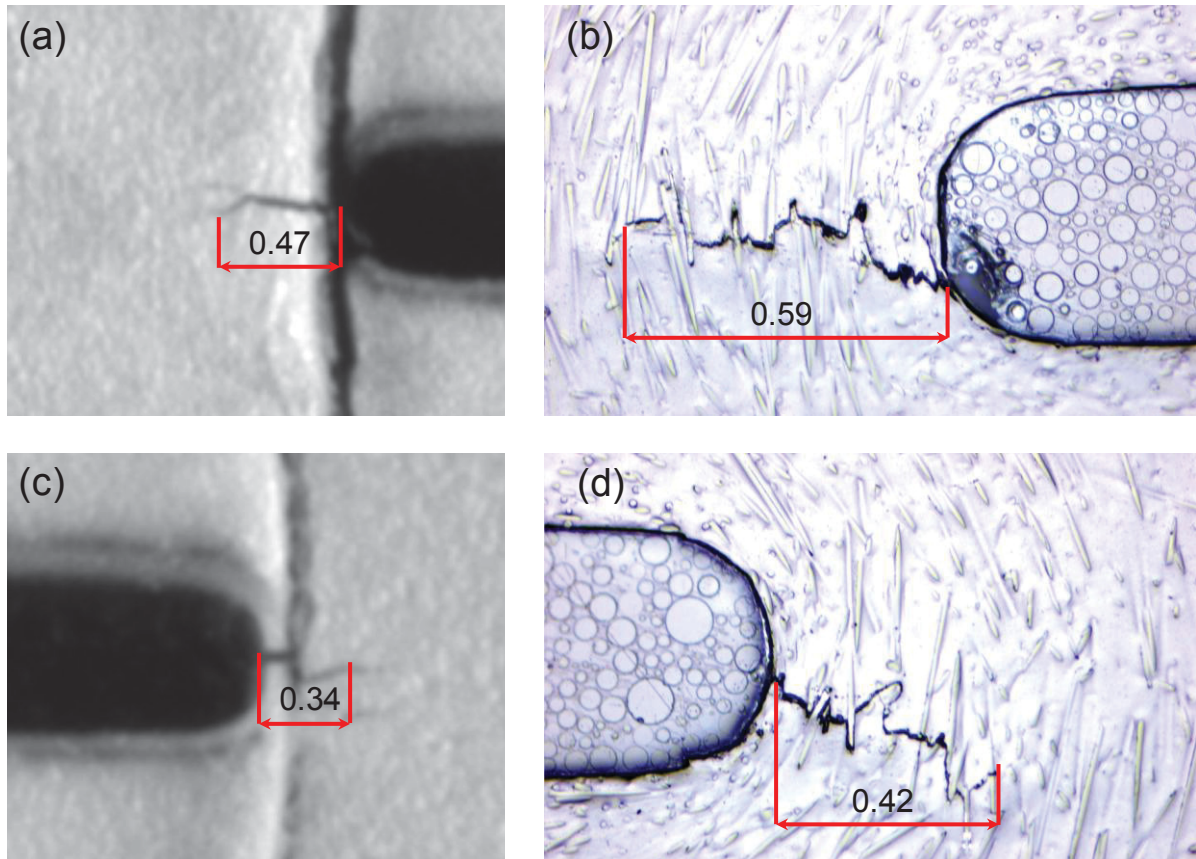


**Figure 4.6.** Comparison between the crack length measured by the optical method (on the left) and the real crack length measured by optical microscopy (on the right).

The results of the comparative analysis are summarized in Table 4.1. Due to sample preparation for the microscopic analysis, a layer of about 0.5 mm is removed from the specimen thickness. This may have an effect on the results of the measurements. Excluding

the test n°6 for which the crack on the left side was not noted using the optical method, for all the other tests, the maximum deviation between the measurements by the two techniques is on the order of 0.1 mm.

**Table 4.1.** Comparison between the crack length measured using the optical method and the crack length measured by optical microscopy after specimen preparation.

Test n°	$\sigma_a(\text{net})$ [MPa]	Frequency [Hz]	Cycles at interruption [Cycles]	Crack measure: CCD camera		Crack measure: Microscope		Deviation	
				Left [mm]	Right [mm]	Left [mm]	Right [mm]	Left [mm]	Right [mm]
1	31	8	7080	0.30	0.22	0.29	0.27	0.01	0.05
2	31	8	7080	0.26	0.40	0.23	0.25	0.03	0.15
3	23	10	65000	0.47	0.34	0.59	0.42	0.12	0.08
4	23	10	65000	0.53	0.44	0.56	0.33	0.03	0.11
5	18	20	392000	0.66	0.72	0.61	0.80	0.05	0.09
6	18	20	392000	0.00	0.53	0.40	0.57	0.40	0.03

#### 4.4 Fatigue tests results

Life to crack initiation and to final failure (specimen separation) are compared in Figure 4.7. Fatigue data were fitted by power laws using eq. 4.1 assuming a log-normal statistical distribution.

$$\sigma_a^k \cdot N = \text{const} \quad (4.1)$$

The values of  $\sigma_A(N = 1E6 \text{ cycles})$ , for 50 % survival probability, k and the scatter index  $T_\sigma = \sigma_{a,10\%}/\sigma_{a,90\%}$  are summarized in Table 4.2. Although the amount of data is limited, it is worthwhile noting that the fatigue data to failure have lower scatter than fatigue data to crack initiation. Fatigue resistance increases with increasing fiber fraction. A similar result was reported for other material systems in [13, 14]. For neat polyamide specimens, it was observed that the contribution of the crack propagation to the total lifetime is negligible. In

this case, only the fatigue curve to failure was drawn. The fatigue curve of the unreinforced polyamide is significantly flatter than the others. A similar result was reported by Mandell et al. [13, 15] for PPS, PA66 and PEEK based materials. The fatigue curves to failure and to crack initiation are nearly parallel except for PA66-GF50. According to the proposed optical method, the fraction of the lifetime spent for the crack initiation remains the same irrespective of the load level.

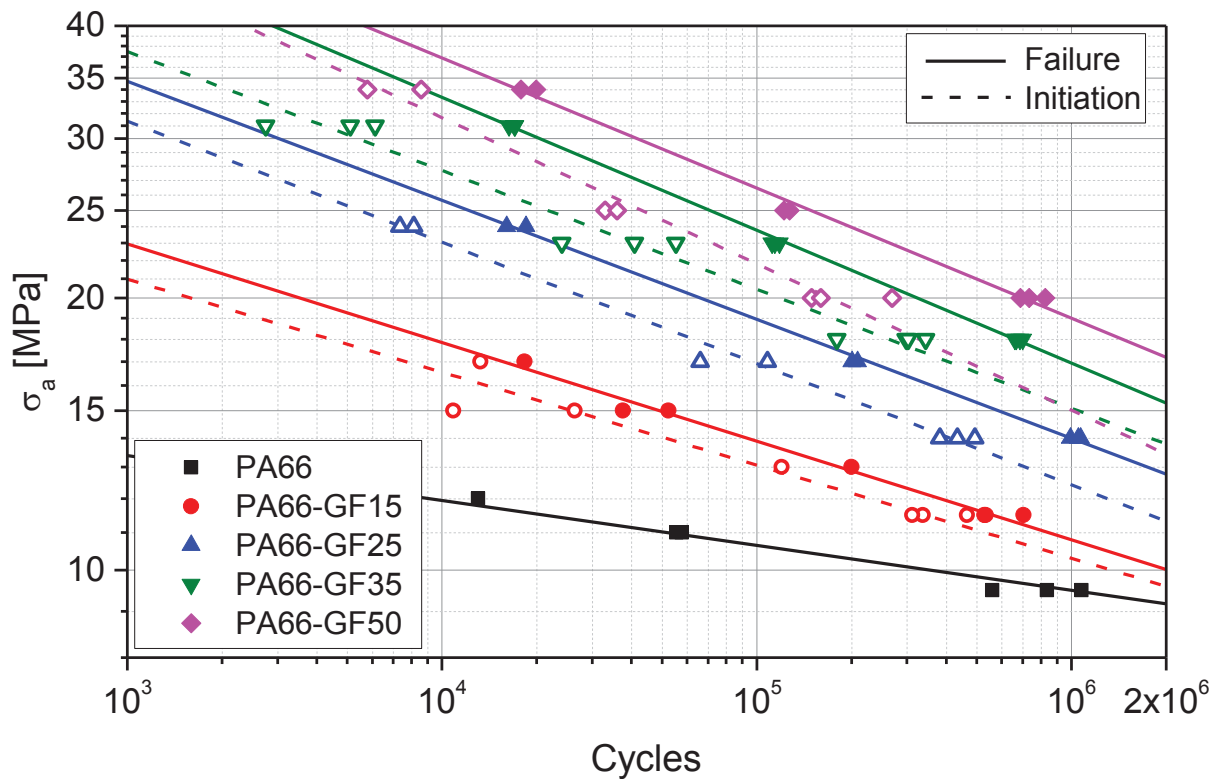
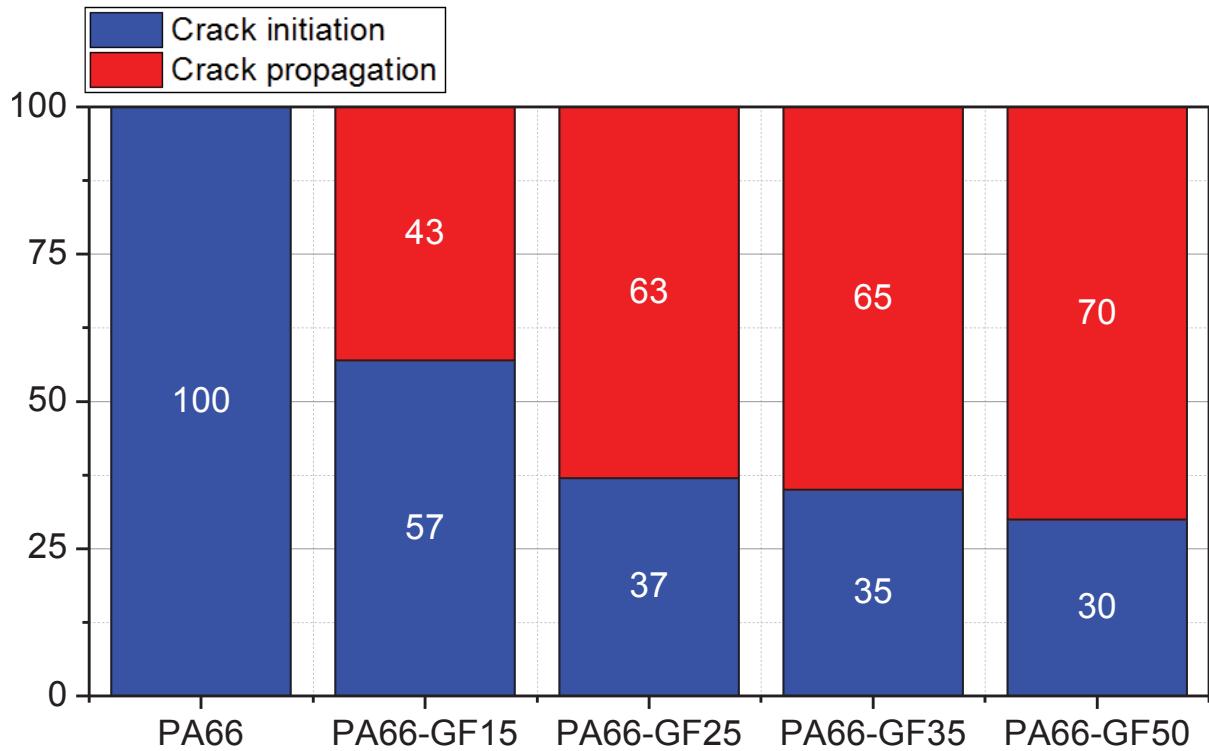


Figure 4.7. Fatigue curves to failure and to crack initiation for different fiber volume fractions.

**Table 4.2.** Summary of the fatigue curve parameters for each test series.

Material	Initiation			Failure		
	$\sigma_A$ [MPa]	k	$T_\sigma$ -	$\sigma_A$ [MPa]	k	$T_\sigma$ -
PA66	9.50	20.12	1.051	9.50	20.12	1.051
PA66-GF15	10.31	9.72	1.136	10.80	9.17	1.052
PA66-GF25	12.42	7.46	1.073	13.99	7.59	1.032
PA66-GF35	15.10	7.60	1.124	16.94	6.81	1.022
PA66-GF50	15.03	6.18	1.128	18.99	6.95	1.056

Figure 4.8 shows the average fraction of the total lifetime spent in the crack initiation for the various fiber contents analyzed in this work. With low fiber fractions ( $V_f = 15$  wt. %) the crack initiation and propagation phases are almost equal. Instead, with high fiber fractions, the lifetime spent for the crack initiation is lower than the crack propagation. Friedrich et al. [16] observed that the crack propagation rate slows down with increasing fiber fraction. These results were confirmed by Karger Kocsis [17] for a short glass fiber reinforced polyamide (PA6), by Evans et al. [18] for a Polyether ether ketone (PEEK) reinforced by short glass fibers, by Voss and Karger Kocsis [19] for a long glass fiber reinforced polybutylene terephthalate (PBT) and finally by Pegoretti and Riccò [20] for a short glass fiber reinforced polypropylene (PP).



**Figure 4.8.** Contribution of the crack initiation and growth phase to the total lifetime for various fiber fractions.

## 4.5 Conclusions

An optical method for the quantification of the life to crack initiation in unreinforced and short glass fiber polyamide notched specimens has been presented. The easy set up and high degree of automation make the method particularly suitable for large experimental testing campaigns. The proposed methodology was validated by carrying out interrupted fatigue tests and measuring the crack length by optical microscopy. It was found that the maximum deviation between crack length measured with the optical method and the real crack length measured by means of optical microscope is on the order of 0.1 mm. The analysis shows that the fraction of the total lifetime spent in the crack initiation diminishes with increasing fiber fraction. For unreinforced materials, the crack propagation phase is negligible.



## **References of Chapter 4**

- [1] C.M. Sonsino, E. Moosbrugger, Fatigue design of highly loaded short-glass-fibre reinforced polyamide parts in engine compartments, *Int. J. Fatigue*. 30 (2008) 1279-1288.
- [2] A. Schaaf, M. De Monte, E. Moosbrugger, M. Vormwald, M. Quaresimin, Life estimation methodology for short fiber reinforced polymers under thermo-mechanical loading in automotive applications, *Materialwissenschaft und Werkstofftechnik*. 46 (2015) 214-228.
- [3] A. Bernasconi, P. Davoli, C. Armani, Fatigue strength of a clutch pedal made of reprocessed short glass fibre reinforced polyamide, *Int. J. Fatigue*. 32 (2010) 100-107.
- [4] B. Klimkeit, S. Castagnet, Y. Nadot, A.E. Habib, G. Benoit, S. Bergamo, C. Dumas, S. Achard, Fatigue damage mechanisms in short fiber reinforced PBT+PET GF30, *Materials Science and Engineering: A*. 528 (2011) 1577-1588.
- [5] R. Talreja, Multi-scale modeling in damage mechanics of composite materials, *Journal of Materials Science*. 41 (2006) 6800-6812.
- [6] M. De Monte, M. Quaresimin, P. Lazzarin, Modelling of fatigue strength data for a short fiber reinforced polyamide 6.6 based on local strain energy density. *Proceedings of ICCM16, 16th International Conference on Composite Materials (2007)*.
- [7] M. Quaresimin, P.A. Carraro, Damage initiation and evolution in glass/epoxy tubes subjected to combined tension–torsion fatigue loading, *Int. J. Fatigue*. 63 (2014) 25-35.
- [8] M. Quaresimin, P.A. Carraro, L.P. Mikkelsen, N. Lucato, L. Vivian, P. Brøndsted, B.F. Sørensen, J. Varna, R. Talreja, Damage evolution under cyclic multiaxial stress state: A comparative analysis between glass/epoxy laminates and tubes, *Composites Part B: Engineering*. 61 (2014) 282-290.
- [9] A. Bernasconi, F. Cosmi, Analysis of the dependence of the tensile behaviour of a short fibre reinforced polyamide upon fibre volume fraction, length and orientation, *Procedia Engineering*. 10 (2011) 2129-2134.



- [10] J.L. Thomason, Micromechanical parameters from macromechanical measurements on glass reinforced polyamide 6,6, *Composites Sci. Technol.* 61 (2001) 2007-2016.
- [11] M. De Monte, E. Moosbrugger, K. Jaschek, M. Quaresimin, Multiaxial fatigue of a short glass fibre reinforced polyamide 6.6 – Fatigue and fracture behaviour, *Int. J. Fatigue.* 32 (2010) 17-28.
- [12] M. De Monte, E. Moosbrugger, K. Jaschek, M. Quaresimin, Multiaxial fatigue behaviour of a short-fibre reinforced polyamide 6.6 in the presence of notches. *ECCM - 13th European Conference on Composite Materials* (2008).
- [13] J.F. Mandell, F.J. McGarry, D.D. Huang, C.G. Li, Some effects of matrix and interface properties on the fatigue of short fiber-reinforced thermoplastics, *Polymer Composites.* 4 (1983) 32-39.
- [14] A. Avanzini, G. Donzella, D. Gallina, Fatigue damage modelling of PEEK short fibre composites, *Procedia Engineering.* 10 (2011) 2052-2057.
- [15] J.F. Mandell, D.D. Huang, F.J. McGarry, Fatigue of glass and carbon fiber reinforced engineering thermoplastics, *Polymer Composites.* 2 (1981) 137-144.
- [16] K. Friedrich, R. Walter, H. Voss, J. Karger-Kocsis, Effect of short fibre reinforcement on the fatigue crack propagation and fracture of PEEK-matrix composites, *Composites.* 17 (1986) 205-216.
- [17] J. Karger-Kocsis, Effects of processing induced microstructure on the fatigue crack propagation of unfilled and short fibre-reinforced PA-6, *Composites.* 21 (1990) 243-254.
- [18] W.J. Evans, D.H. Isaac, K.S. Saib, The effect of short carbon fibre reinforcement on fatigue crack growth in PEEK, *Composites Part A: Applied Science and Manufacturing.* 27 (1996) 547-554.
- [19] H. Voss, J. Karger-Kocsis, Fatigue crack propagation in glass-fibre and glass-sphere filled PBT composites, *Int. J. Fatigue.* 10 (1988) 3-11.

[20] A. Pegoretti, T. Riccò, Fatigue crack propagation in polypropylene reinforced with short glass fibres, *Composites Sci. Technol.* 59 (1999) 1055-10.

## **Chapter 5**

# **Damage mechanisms in a short glass fiber reinforced polyamide under fatigue loading**

**Keywords:** Short Fiber Reinforced Plastics, Damage Mechanisms, Fatigue, Interface / Interphase

### **Abstract**

This paper presents a damage investigation on a short glass fiber reinforced polyamide (PA66-GF35) under fatigue loading. Plain and notched specimens were tested at room temperature and humidity with load ratio  $R = 0$ . Electron microscopy was used to analyze the fracture surface of failed specimens and the crack path of specimens subjected to interrupted fatigue tests. Damage mechanisms were studied investigating the following fractographic features: matrix fracture behavior (ductile / brittle), fiber failure / pull-out, degree of fiber-matrix interfacial adhesion. The aim of the present paper is to understand the nature of damage initiation and propagation in order to lay the foundations for the development of a multi-scale, mechanism-based lifetime prediction model for short fiber reinforced plastics.

### **5.1. Introduction**

In the car engine compartment, Short Fiber Reinforced Plastics (SFRPs) are increasingly replacing metals in structural applications. High strength to weight ratio, high temperature and chemical resistance make these materials excellent candidates for under-the-hood applications. The competitiveness of SFRPs is also related to the advantages offered by the injection molding process. This technology enables complex geometries to be manufactured at high production rates without the need for additional post-molding machining operations. The durability assessment of SFRPs plays a key role in the design of injection molded structural parts. Typical under-the-hood parts such as fuel rails, pump housings and sealing elements are exposed to cyclic loading due to vibrations, pulsating forces, temperature variations. Often, in the automotive industry, several prototypes are needed before beginning the series production. Lifetime prediction models aim to reduce the number of recursions

before the series production by virtually optimizing the product in the early stages of the project. Lifetime predictions are accurate when the damage mechanisms are understood and properly integrated in the model. In SFRPs, damage mechanisms occur at a length scale below the macroscopic scale due to the interactions between the material constituents (fiber, matrix, fiber-matrix interface). Multi-scale models aim to bridge the scale at which the damage mechanisms occur and the macro-scale of structural applications. The first step in developing such a model is an extensive damage investigation.

The aim of this work is to investigate the fatigue damage mechanisms in plain and notched short glass fiber reinforced polyamide specimens in order to lay the basis for the development of a multi-scale lifetime prediction model. In the last 30 years, many papers were dedicated to the investigation of damage and failure mechanisms of SFRPs under fatigue loading. Considering the first works in this field in the 1970s [1, 2], the investigation techniques have taken huge steps in terms of accuracy of observation, image quality and development of new methodologies. Fractographic examinations by means of Field Emission Scanning Electron Microscope (FESEM) on a short fiber reinforced PBT were shown recently by Hoffmann [3]. Comparing the micrographs in [1, 2, 4, 5] with those in [3], the improvement of the microscopy technique in terms of resolution, magnification, image quality becomes immediately evident.

In Section 5.2, the authors reviewed the damage mechanisms from literature and sorted them based on specific fractographic features: matrix fracture behavior (ductile / brittle), fiber failure, fiber pull-out and degree of fiber-matrix interfacial adhesion. The results from the literature were compared with the results of an extensive damage investigation carried out at Robert Bosch GmbH on plain and notched short fiber reinforced polyamide specimens (Section 5.5). The damage investigation was conducted by means of three methods: 1) Infrared (IR) Thermography (Section 5.5.1); 2) Microscopic investigation of the fracture surface (Section 5.5.2); 3) Microscopic investigation of the crack path (Section 5.5.3). Damage mechanisms were investigated at multiple scales. Macro- meso- micro- nano-scale are frequently referred in the literature. Macro-scale is the scale of the specimen. At this scale, SFRPs are treated as homogeneous materials. The objectives of the macroscopic damage analysis are: 1) Localization of the crack initiation; 2) Investigation of the failure mode of plain and notched specimens. The meso-scale is the scale of the Representative Volume Element (RVE) [6]. At this scale, fibers and matrix are treated discretely, whereas the microstructural variables (fiber orientation, fiber volume fraction, fiber aspect ratio) are used

to globally describe the RVE [7]. The analysis at the meso-scale aims to study the influence of the fiber orientation on the crack initiation / propagation. The micro-scale is determined by the fiber diameter. At this scale SFRPs are described as three-phase materials (fiber, matrix, fiber-matrix interface). Particular attention is given to the analysis of the fiber-matrix interface after the application of cyclic loading. Fracture in composite materials can be either cohesive or adhesive depending upon whether a layer of matrix adheres to the fibers or not. Modern electron microscopes allow the investigation of the fiber-matrix interface at such a level of detail that was impossible just a few years ago. The issue whether damage occurs at the fiber-matrix interface or in the resin, at a certain distance from the interface, is crucial for the development of a damage-based model. Mirror-clean fibers on the fracture surface indicate fiber-matrix debonding. Otherwise, the mechanism is matrix cracking and the analysis should be focused on the resin layer covering the fibers. During the fiber forming process, fibers are coated by a mixture of chemicals and water called sizing in order to improve the fiber-matrix adhesion. Fiber sizing can chemically and mechanically affect the resin layer at the fiber-matrix interface leading to the formation of an interphase layer with different mechanical properties from the bulk matrix. Finally, a preliminary analysis of the damage mechanisms preceding the initiation of micro-cracks is presented.

## **5.2. Literature review on the damage mechanisms investigated by means of electron microscopy**

The first works on the damage investigation of SFRPs under fatigue loading date back to the 1970s and were motivated by the following reasons: 1) Comparing the fatigue behavior of different material systems; 2) Improving the mechanical properties varying the material microstructure; 3) Finding quantitative relationships between material failure modes and macroscopic material response. Historically, the damage investigation by means of electron microscopy has been based on two techniques: analysis of the fracture surface or of the crack path [1, 2, 4, 8-10]. In the former case, specimens are tested until failure. In the latter case, fatigue tests are interrupted before failure and the side surface of the specimen is polished for microscopic investigations. These two analyses offer complementary and mutually enriching points of view. The degree of fiber-matrix adhesion, the pull-out length, the amount of broken fibers can be examined through both analyses. Instead, the observation of the fracture surface is better for investigating the matrix fracture behavior (ductile / brittle) while the analysis of

the side surface of the specimen enables the study of the influence of the fiber distribution on the crack path. Both methodologies present some disadvantages. The analysis of the fracture surface requires the specimen separation into two parts limiting the access to the mechanisms responsible for the first event of damage. The observation of the side surface of a specimen limits the damage analysis to one planar section of the crack without any information on the damage mechanisms along the specimen thickness. A comprehensive analysis should consider multiple sections along the specimen thickness increasing the effort in the samples preparation.

Through the traces left by the crack on the fracture surface, it is possible to study the damage mechanisms occurring due to cyclic loading in a fatigue test. The damage mechanisms reported in literature were reviewed by reference to specific fractographic features: matrix fracture behavior (ductile / brittle), fiber failure / pull-out, degree of fiber-matrix interfacial adhesion. Finally, the effect of the fiber distribution on the damage mechanisms was also reviewed.

#### *1) Matrix fracture behavior*

Evidence of ductility / brittleness on the fracture surface reflects the local mode of crack advance. Ductile matrix behavior was observed on the fracture surface caused by initiation and stable Fatigue Crack Propagation (FCP) [4, 11-15]. Brittle matrix behavior indicates unstable crack propagation. Ductile matrix fracture indicates matrix yielding and appears in form of polymer filaments. The degree of matrix ductility on the fracture surface is related to the length of the polymer filaments. It depends on the material system, testing conditions (temperature, humidity), load level. Analyzing PA6-GF30 Compact Tension CT specimens under fatigue loading, Karger-Kocsis [16] observed a higher ductile matrix behavior at the end than at the beginning of the stable FCP. Horst and Spoormaker [15] compared the fracture surface of conditioned PA66-GF35 plain specimens, failed under static and fatigue loading. They observed a much larger ductile area in the latter case. Horst and Spoormaker [15] also compared the fracture surface of conditioned and dry-as-molded fatigued specimens, reporting a higher degree of the matrix ductility in the former case. Karger-Kocsis and Friedrich [17] observed that the degree of matrix ductility on the fracture surface of PA66-GF30 specimens failed under fatigue loading increases with testing temperature. The same result was reported by Noda et al. [18] for a short glass fiber reinforced polyamide

(PA66-GF33) tested under fatigue loading below and above the glass transition temperature of the material and by Schaaf and coworkers [19] testing a short fiber reinforced polybutylene terephthalate (PBT-GF30) under strain controlled fatigue loading at different temperatures ( $T = -40; 23; 120$  °C).

### 2) *Fiber failure / fiber pull-out*

The amount of broken fibers on the fracture surface depends on the loading type. In [4] it was found that the fracture surface of specimens failed under fatigue loading shows a higher amount of broken fibers than the fracture surface caused by static loading. According to Lang [4, 20] fiber failure is due crack closure effects. During the unloading part of the cycle, fibers fail by buckling and bending. Sato [21] observed more pulled-out fibers than broken fibers on the fracture surface of PA66-GF30 specimens failed under static loading. Testing PA66-GF33 plain specimens under fatigue loading, Noda et al. [18] observed pulled-out and broken fibers depending upon whether the temperature is above or below the glass transition temperature. Lang et al. [4, 20] noticed that the pull-out length is shorter on the fracture surface caused by stable FCP than unstable FCP. Horst and Spoomaker [15] observed that the pull-out length is shorter for specimens failed under fatigue loading than under static loading.

### 3) *Fiber-matrix adhesion*

The quality of fiber-matrix adhesion strongly affects the fatigue strength of SFRPs. Friedrich [22] analyzed the crack propagation behavior for a short glass fiber reinforced Polyethylene terephthalate (PET) in case of good (commercial) and very poor sizing. The poorly bonded material system exhibited higher crack propagation rate. Friedrich observed mirror-clean fibers on the fracture surface of the poorly bonded material system and high interfacial fiber-matrix adhesion on the fracture surface of the commercial material. The degree of fiber-matrix adhesion strongly depends on the material system and the testing conditions. Horst [15] and Bernasconi [13] observed mirror-clean fibers analyzing the fracture surface of conditioned short glass fiber reinforced polyamide specimens failed under fatigue loading. The same result was reported by De Monte [23] testing PA66-GF35 tubular specimens under multi-axial loading in Dry As Molded (DAM) condition. Contrary to previous results,

Karger-Kocsis noticed very good fiber-matrix bonding in a short fiber reinforced PA66 [24] and in a short glass fiber reinforced PBT [25] under fatigue loading.

Mirror-clean fibers on the fracture surface indicate fiber-matrix debonding. Instead, fibers covered by a resin layer suggest that damage occurs at certain distance from the interface in form of matrix cracking. Sizing can affect the resin layer surrounding the fibers leading to the formation of the interphase. Mechanical properties of the interphase differ from those of the bulk polymer and the fibers. Hence, the transition between the fiber and the matrix should be described as a region with a specific thickness. The interphase in short glass fiber reinforced thermoplastics was investigated by Thomason in [26]. Recently, Brodowsky and coworkers [27] developed an experimental technique to characterize the interphase of single fiber specimens under fatigue loading.

#### *4) Summary of the literature review*

The literature review demonstrated general agreement between different authors on the effect of failure mode (stable / unstable FCP), testing parameters (temperature, humidity) and material systems (matrix, fiber-matrix bonding) on matrix fracture behavior and fiber failure / pull-out. Instead, the degree of fiber-matrix interfacial adhesion remains a contentious issue with little agreement in the scientific community. This is due to the fact that only a few years ago microscopes did not allow researchers to study the fiber-matrix adhesion with high accuracy. In Section 5.5 a comprehensive damage investigation on plain and notched short glass fiber reinforced polyamide specimens is presented. A high resolution FESEM microscope was used to study the effect of fatigue loading on the mentioned fractographic features. Particular attention was devoted to the analysis of the fiber-matrix interfacial adhesion.

#### *5) Fiber distribution at crack initiation*

To complete the damage investigation, the role of the microstructure on the damage initiation / propagation should be taken into account. In fact, the worst combination of the weakest location due to local material microstructure and the local stress state creates the condition for crack initiation. The microstructure of the SFRPs is characterized by three main variables: fiber orientation, fiber aspect ratio and fiber volume fraction. The influence of the



fiber orientation on the fatigue behavior of SFRPs is generally studied by machining specimens from an injection molded plate at different orientations with respect to the injection direction [4, 10, 25, 28-30]. If the fibers are aligned to the loading direction, damage was found to initiate at the fiber ends, where no sizing is expected [14, 18, 19, 28, 31, 32].

The scenario changes if the fibers are aligned transversely with respect to the loading direction. Analyzing the fracture surface of CT specimens machined from injection molded plate crosswise to the mold flow direction (MFD), Lang et al. [4] reported that pre-existent micro-regions of poor adhesion along the fiber-matrix interface are sites for crack initiation.

The fiber orientation also varies along the thickness showing a typical shell-core structure [15, 29, 32-34]. Arif and coworkers [32] observed fiber-matrix debonding in the shell layers and matrix micro-cracks in the core layer. Analyzing tubular specimens under torsional fatigue loading, De Monte et al. [14] observed cracks nucleating in the core region where the fibers exhibit a lower alignment to the axial direction than in the skin layers. In [14, 23] De Monte and coworkers, studied the combined effect of the local microstructure and the notch on the torsional fatigue strength of short glass fiber reinforced polyamide tubular specimens. In [14] it was found that the torsional fatigue strength of plain and notched (molded-in V-shaped notch,  $R_{\text{notch}} = 0.2 \text{ mm}$ ) is similar. In another work [23], it was found that the torsional fatigue strength of plain tubular specimens decreases when drilling a hole ( $R = 1 \text{ mm}$ ) in the central part of the specimen. Even if the drilled hole has a larger diameter than the molded V-shaped notch, it affects more strongly the torsional fatigue strength. This is due to the local microstructure which, in case of molded notch, locally increases the material strength. The mutual position of the fibers affects the crack initiation. Dally and Carrillo [2] observed that for a long fiber reinforced polyamide under fatigue loading, clusters of fibers perpendicularly oriented to the load direction are preferred sites for crack initiation. By studying a PA66-GF30 Arif and coworkers [35] reported that the distance between two neighboring fibers affects the damage initiation area.

### **5.3. Material, geometry and test equipment**

The material investigated in the present work is a short fiber reinforced polyamide containing 35 wt. % glass fibers (designation: PA66-GF35). Plain and notched specimens were injected along the longitudinal axis, which corresponds to the loading direction. Geometries and dimensions of the specimens are reported in Figure 5.1. The notch is a central slit of 10 mm with notch radius of 0.2 mm. The net stress concentration factor, calculated using isotropic

material model, is  $K_{t_{net}} = 9.81$ . The notch was created with an insert in the mold cavity in order to reproduce the local fiber orientation at structural discontinuities in real injection molded parts. In fact, the majority of real plastic parts manufactured by injection molding are ready to use after ejection from the mold. Structural discontinuities in the mold perturb the melt flow affecting the local fiber orientation and consequently the material strength.

Relative humidity in the samples was kept under 0.1 wt. % by storing them before testing, in a container with a drying agent (silica gel parts). Hence, specimens were tested in Dry As-Molded (DAM) conditions.

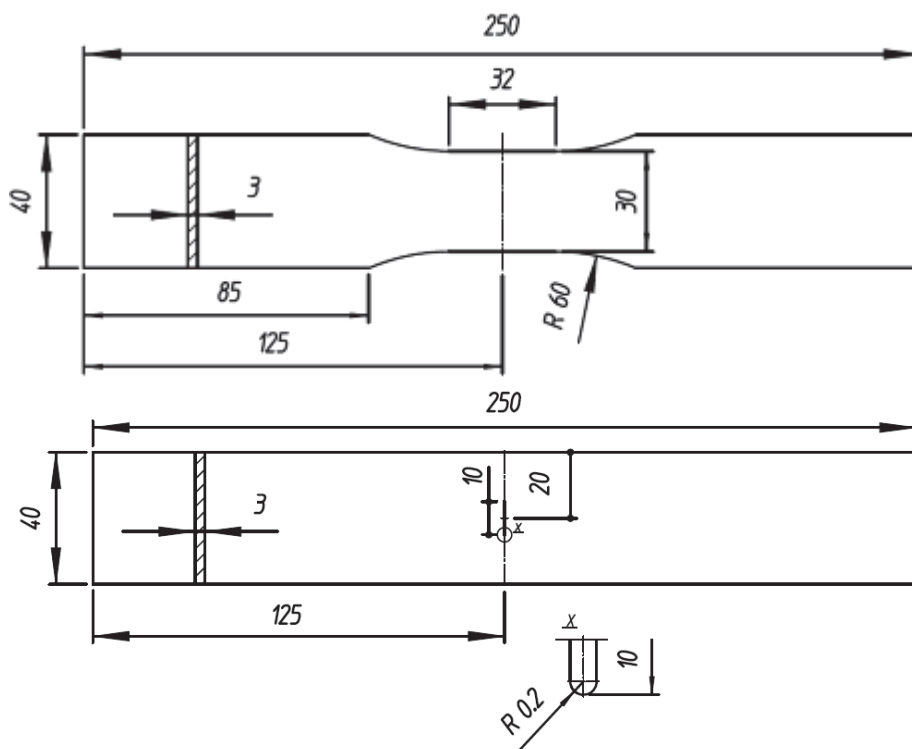


**Figure 5.1.** Specimen geometries and dimensions (in mm).

Uniaxial fatigue tests were carried out on a 10 kN servo-hydraulic testing machine. The fatigue tests were carried out under load control, applying a sinusoidal load with constant amplitude. Load ratio was kept constant and equal to zero for all the performed tests. All the specimens were tested at room temperature. Relative humidity in the room was not controlled during the fatigue tests. Testing frequency was chosen so as to avoid self-heating.

Fatigue tests were carried out until specimen separation. An optical method presented by the authors in [36] was used to quantify the contribution of the crack initiation to the total lifetime. An Infrared (IR) camera (FLIR ThermoCAM SC500) was used to monitor the

macroscopic damage evolution in plain and notched specimens during the fatigue tests. Optical and electron microscopy were used. The optical microscope is a Zeiss Axioplan 1. The FESEM microscope is a Zeiss Supra 55 VP with 7 kV accelerating voltage equipped with a EDAX X-Ray Si(Li)-Detector. The specimens analyzed through the FESEM microscope were gold sputtered in order to improve the quality of the micrographs.

Cryogenic fracture tests on specimens previously tested until crack initiation were carried out to study the damage mechanisms ahead of the crack tip. The specimens were cooled down to  $T = -196\text{ }^{\circ}\text{C}$  and broken by using two pliers.

## 5.4. Fatigue tests results

S-N curves up to crack initiation and up to failure (specimen separation) are shown in Figure 5.2. Fatigue data are represented in a double logarithmic diagram, plotting the net stress amplitude ( $\sigma_a$ ) against the number of cycles (N) to crack initiation / failure for a survival probability of 50 %. Fatigue curves are plotted using eq. 5.1.

$$N \cdot \sigma_a^k = N_A \cdot \sigma_A^k \quad (5.1)$$

Where  $N_A = 1\text{E}6$  cycles and  $\sigma_A = \sigma_a(1\text{E}6)$ . The values of  $\sigma_A$ , k and the scatter index  $T_\sigma = \sigma_{a,10\%}/\sigma_{a,90\%}$  are reported in Table 5.1. Plain specimens failed suddenly by unstable crack propagation. Hence, life to failure corresponds to life to crack initiation. Instead, notched specimen exhibit stable FCP. In [36] it was found that the amount of lifetime spent in the crack initiation depends on the fiber volume fraction. For PA66-GF35 notched specimens, the crack initiation takes some 35 % of the total lifetime. The rest of the lifetime is spent in stable FCP.

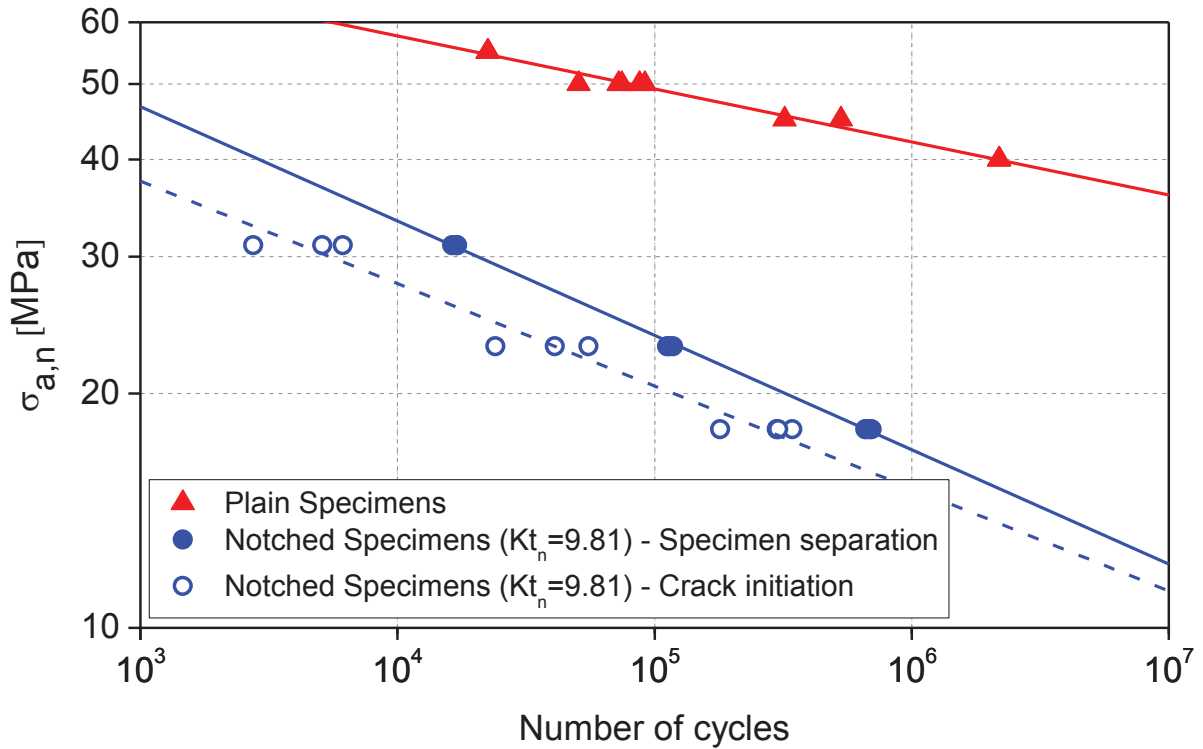


**Figure 5.2.** S-N curves up to crack initiation and up to failure of plain and notched specimens,  $T = RT$ ,  $R = 0$ .

**Table 5.1.** Summary of the fatigue curve parameters for each test series.

Geometry	Initiation			Failure		
	$\sigma_A$ [MPa]	k	$T_\sigma$	$\sigma_A$ [MPa]	k	$T_\sigma$
Plain	42.12	14.69	1.041	42.12	14.69	1.041
Notched	15.10	7.60	1.124	16.94	6.81	1.022

## 5.5. Damage investigation

### 5.5.1. Analysis of the failure mode of plain and notched specimens by means of IR thermography

The IR camera was used to monitor the temperature field on the specimen surface during the fatigue tests. This experimental method makes the macroscopic damage evolution before failure particularly evident (Figure 5.3). Plain specimens fail due to the unstable propagation of a crack. Failure is preceded by a localized temperature spot at one of the four stress

concentrations at the shoulder tips (Figure 5.3a). The temperature spot can be observed just few cycles before the separation of the specimen in two parts. Similar results were reported by Klimkeit et al.[37]. Instead, the notched specimens show stable FCP at both the sides of the notch (Figure 5.3b). The peaks of temperature, observable at a certain distance from the notch tips, indicate the crack front (Figure 5.3b).

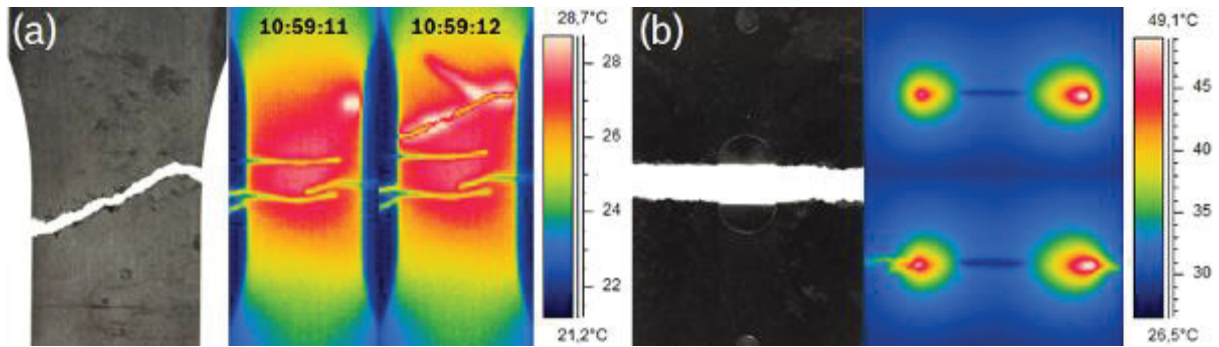


**Figure 5.3.** Crack path and temperature distribution at failure in (a) Plain specimens; (b) Notched specimens.

### 5.5.2. Analysis of the fracture surface

The microscopic analysis of the fracture surface of plain specimens reveals two different areas. At crack initiation, where the temperature spot was observed (Figure 5.3a), the matrix exhibits a ductile behavior (Figure 5.4b). The rest of the fracture surface is comparatively brittle (Figure 5.4c).

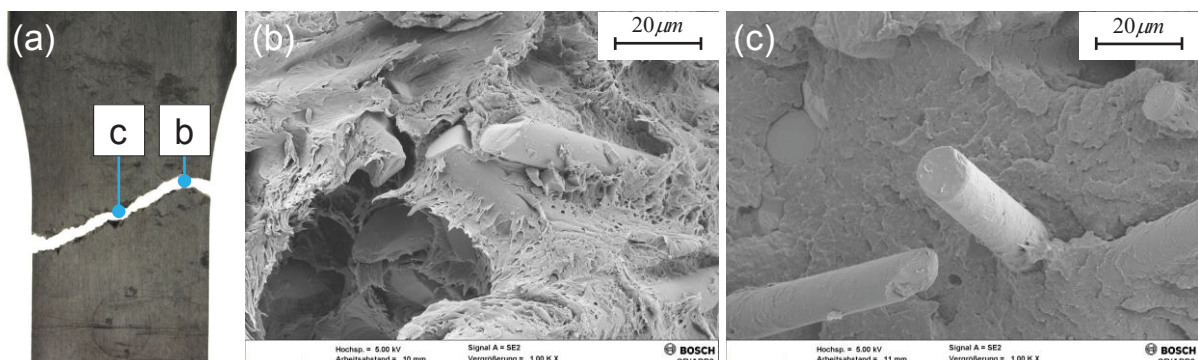


**Figure 5.4.** Fracture surface morphology of a plain specimen; (a) Investigated specimen; (b) Fracture surface at crack initiation; (c) Fracture surface caused by unstable crack propagation.



The examination of the fracture surface at high magnifications provides valuable insight into the state of the fiber-matrix interfacial adhesion (Figure 5.5). On both ductile and brittle areas, fibers are covered by a resin layer. Evidence of local matrix yielding in form of polymer fibrils is shown in Figure 5.5a. The high stress carried by the fibrils can cause either their failure or their detachment from the fiber surface. This second mechanism may be the reason of some clean regions on the fiber surface (Figure 5.5a). Conversely, on the brittle zone of the fracture surface, fibers are covered uniformly by a resin layer (Figure 5.5b).

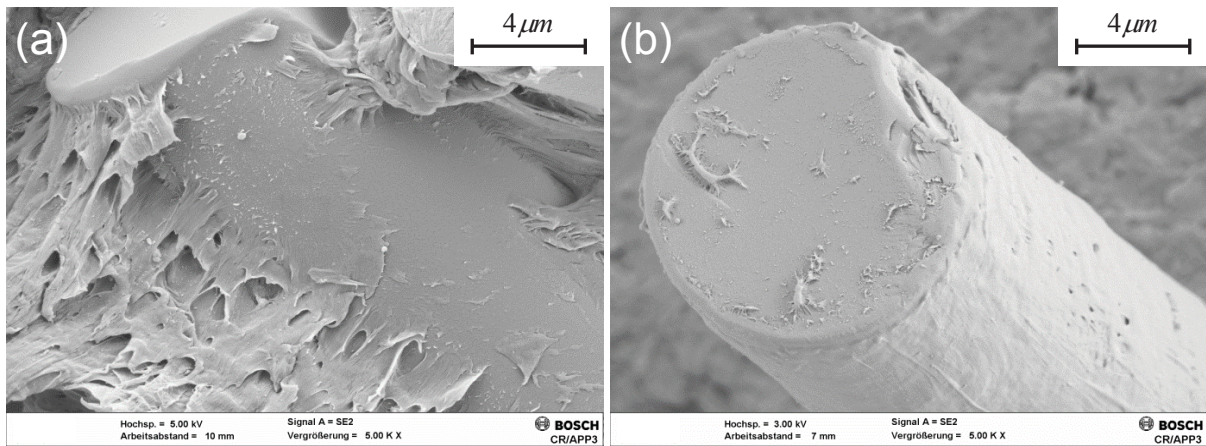


**Figure 5.5.** Degree of fiber-matrix interfacial adhesion on the fracture surface of a plain specimen; (a) Fracture surface at crack initiation; (b) Fracture surface caused by unstable crack propagation.

Failure of notched specimens occurs in three steps: crack initiation, stable and unstable fatigue crack propagation. Fracture surface caused by stable and unstable FCP can be identified with unaided eye. The fracture surface caused by stable FCP is stress whitened and smooth (Figure 5.6a). Instead, fracture surface caused by unstable FCP has a comparatively more irregular morphology (Figure 5.6a). This result was also reported in [4, 23, 38] for similar material systems. In Figure 5.6a, the stable FCP is indicated by the letter “s”, while the unstable FCP is indicated by the letter “u”. The fracture surface morphology varies according to the crack propagation mode. Near the notch tip, no evidence of ductile matrix deformation was observed (Figure 5.6b). At the end of the FCP, higher degree of matrix ductility was observed (Figure 5.6c). However, as indicated in Figure 5.6a, this region is very small. Next to this area, the fracture surface is brittle (Figure 5.6d). This region is caused by unstable FCP and it is similar to that observed in Figure 5.4c. Hence, unstable FCP leads to brittle fracture surface regardless of the specimen geometry. Comparing Figure 5.6b with Figure 5.6c-d, the

matrix material behavior can be described neither as ductile nor as brittle. A similar description was provided in [16, 24, 38, 39], although there is no full agreement on the terminology to be used. Hereinafter, the term “microductility” is associated with the evidence of ductile deformation at micro-scale only. The degree of the matrix ductility depends in fact on the scale of observation. An example is provided in Figure 5.7. Figure 5.7a shows a low magnifications FESEM micrograph of the fracture surface caused by stable FCP. The micrograph shown in Figure 5.7b is an enlargement of Figure 5.7a. In this case, the ductile matrix response is evident. Moreover, matrix cavitation around particles is observed.

The pull-out length on the fracture surface caused by unstable FCP is longer when compared with stable FCP. This result confirms the observations in [4, 15, 40]. During the stable FCP, crack propagates in a fiber avoidance mode. This mechanism was also observed in [5, 14, 19, 22, 40, 41]. Therefore, either the fibers are slightly below the free surface of the crack, or just a small portion of them is visible from the observation of the fracture surface. On the fracture surface caused by unstable FCP, the high amount of released energy leads to a more irregular crack path. Fibers are extracted from the fracture surface. Few broken fibers are observed on both the fracture surfaces caused by stable and unstable FCPs. This indicates that fiber failure is not the dominant mechanism.

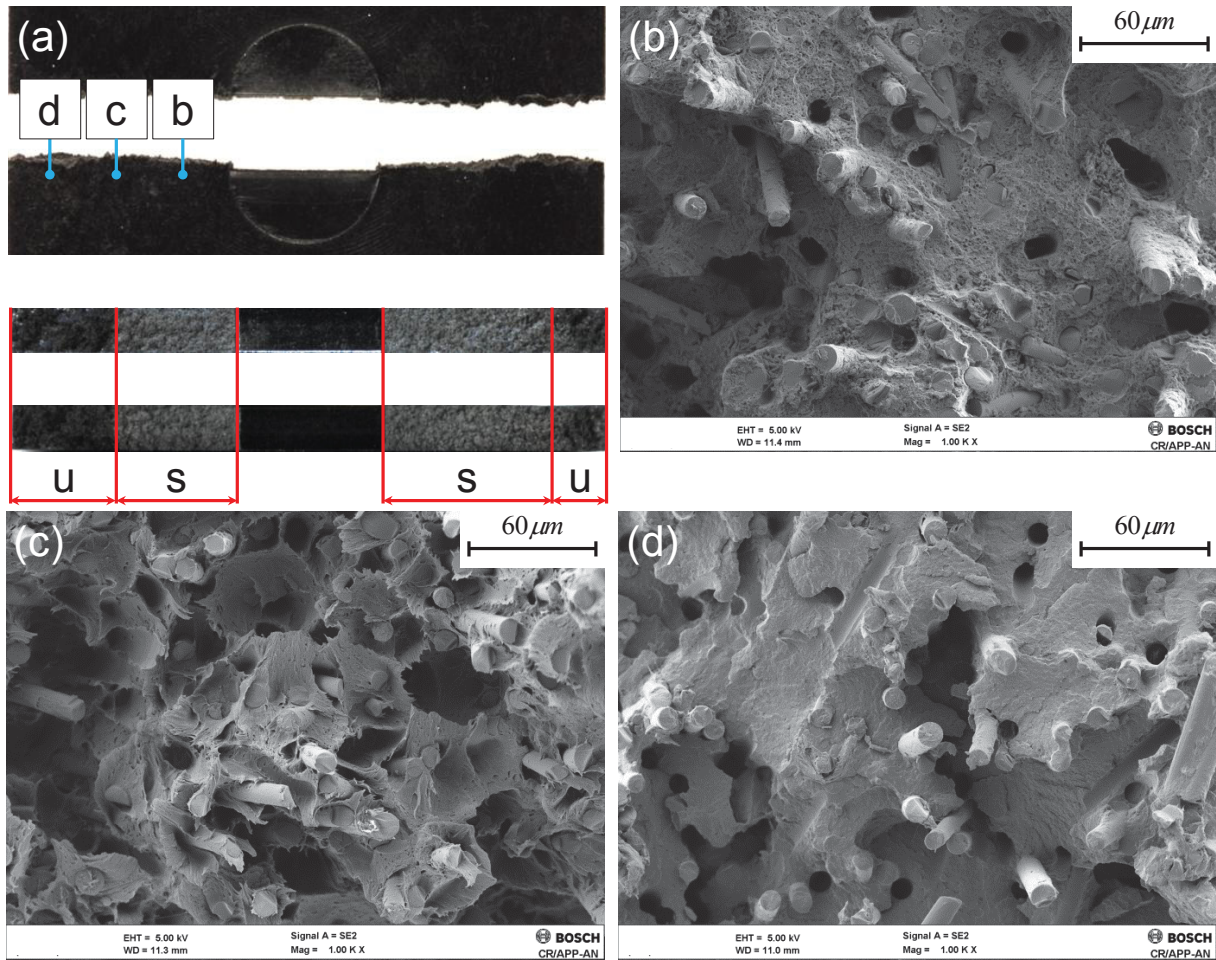


**Figure 5.6.** Fracture surface morphology of a notched specimen; (a) Failed specimen; “s” and “u” indicate the fracture surface caused by stable and unstable FCP respectively; (b) Fracture surface at crack initiation; (c) Fracture surface at the end of the stable FCP; (d) Fracture surface caused by unstable FCP.

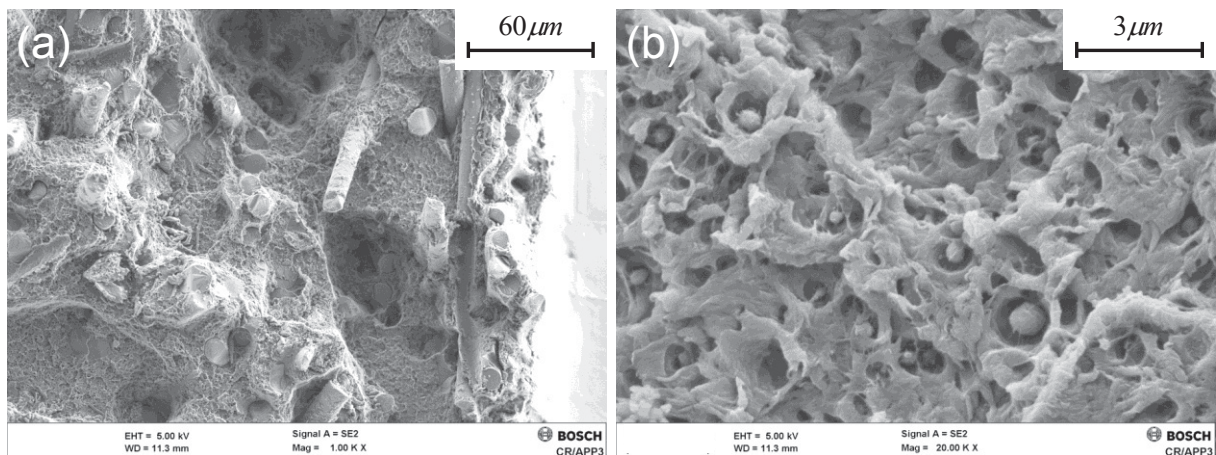


**Figure 5.7.** Fracture surface caused by stable FCP (notched specimen); (a) Low magnification; (b) High magnification.



So far, it is not clear if cavities observed on the fracture surface precede or follow the crack onset. In order to study this mechanism, a fatigue test of a notched specimen was interrupted at crack initiation (Figure 5.8a). Then the specimen was cryo-fractured at  $T = -196\text{ }^{\circ}\text{C}$  (Figure 5.8b). This test has a twofold aim: 1) Investigate whether the cavities can be observed also in the region ahead of the crack tip. 2) Investigate if there are pre-existing foreign particles in the material. If so, evidence of particles should be provided also on the cryo-fractured surface. Figure 5.8c-d shows the fracture surface caused by stable FCP and the cryo-fractured surface. Cryo-fracture leads to brittle fracture surface.

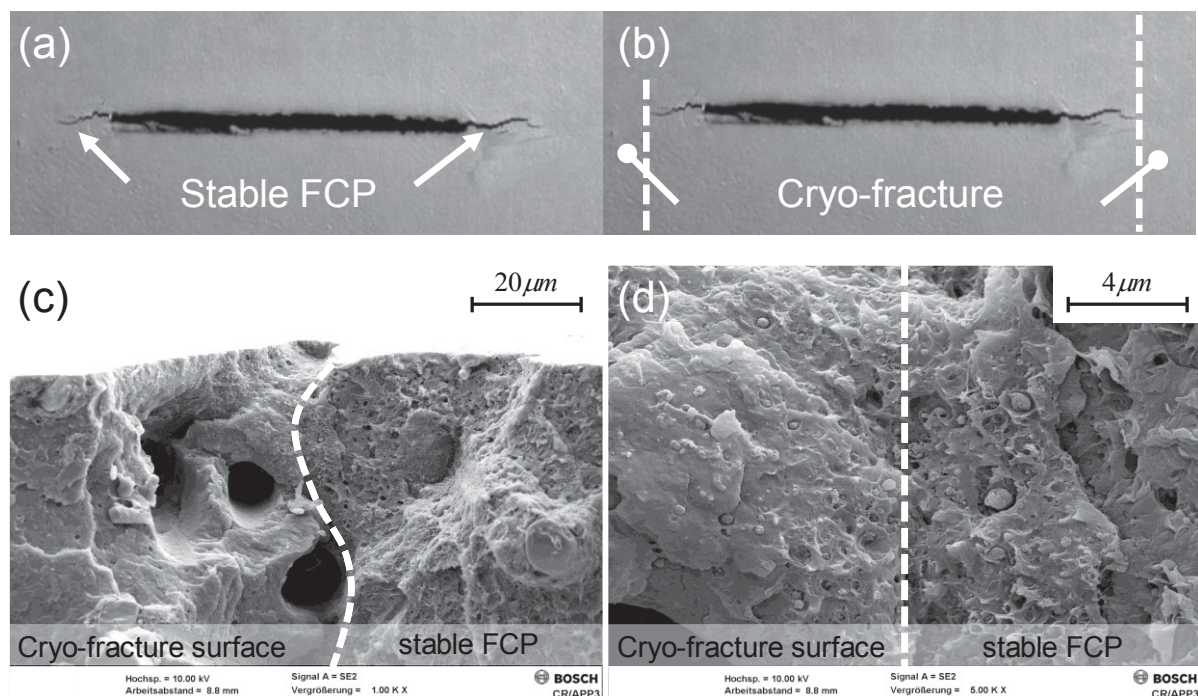


**Figure 5.8.** Stable FCP and the cryo-fractured surface; (a) Fatigue test was interrupted at crack initiation; (b) Cryo-fracture; (c) Fracture surface, low magnification; (d) Fracture surface, high magnification.

Figure 5.9 shows FESEM micrographs of different regions on the fracture surface of the cryo-fractured specimen shown in Figure 5.8. Cavities and particles are observed on the fracture surface caused by stable FCP (Figure 5.9b). On the region immediately ahead of the crack tip, a certain amount of cavities is observed (Figure 5.9c). Cavities can also be observed on the cryo-fractured surface (Figure 5.9d), far away from the crack tip. However they are few in number and also smaller. This preliminary investigation suggests that coalescence of voids precedes the formation of a micro-crack. The result would confirm some experimental

evidence of voids in a short fiber reinforced polyamide under static loading, recently provided in [11, 42].

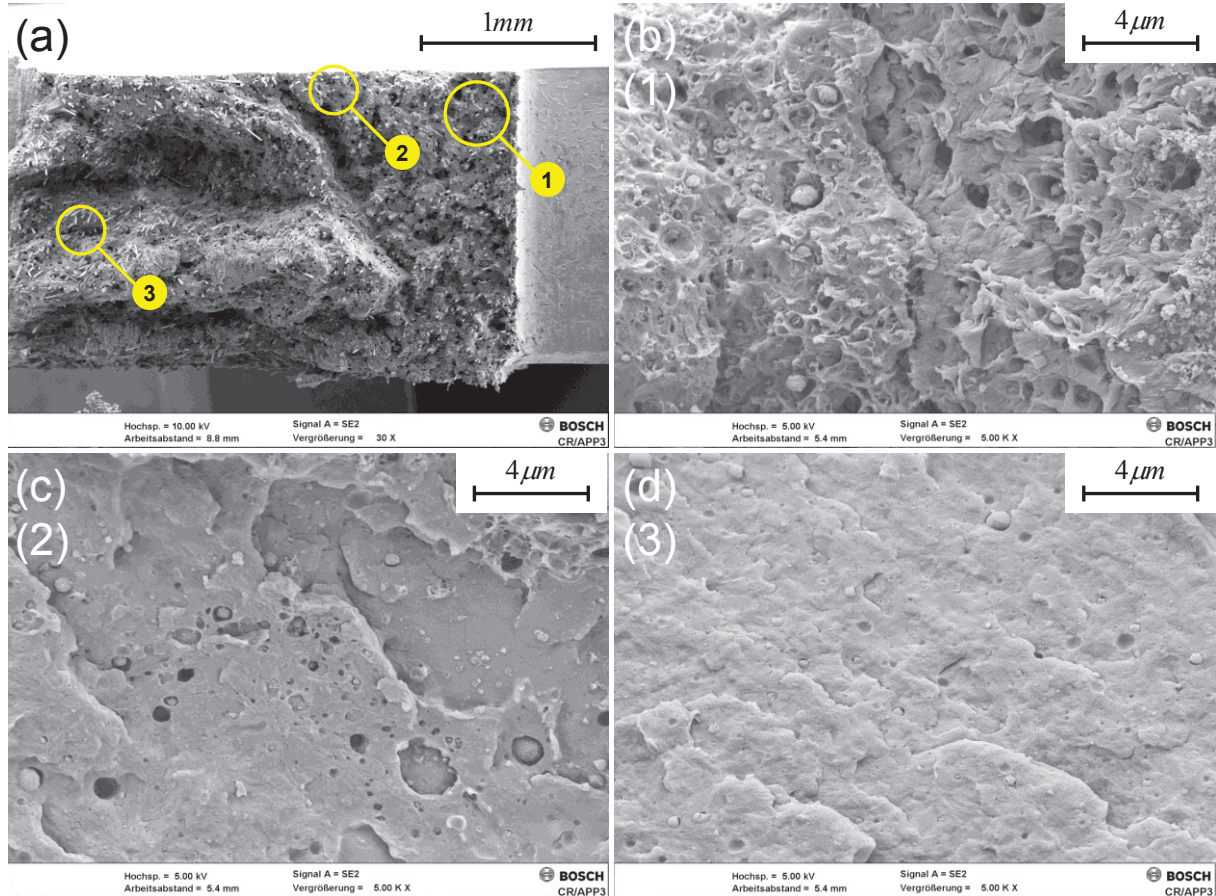


**Figure 5.9.** Fracture surface of notched specimen. Fatigue test was interrupted at crack initiation and then cryo-fractured. (a) Overview of the fracture surface; (b) Fracture surface caused by stable FCP region; (c) Cryo-fractured surface ahead the crack tip; (d) Cryo-fractured surface far from the crack tip.

Figure 5.10 shows examples of particles on the cryo-fracture surface, immediately ahead of the crack tip. The smooth fracture surface is interrupted by cavities of different sizes. Some cavities are filled by particles, some others are instead empty. A difference in terms of surface appearance between the particle and the matrix around it can be also appreciated in Figure 5.10b. This experimental evidence seems to suggest that the particles are not made by the same material of the matrix.



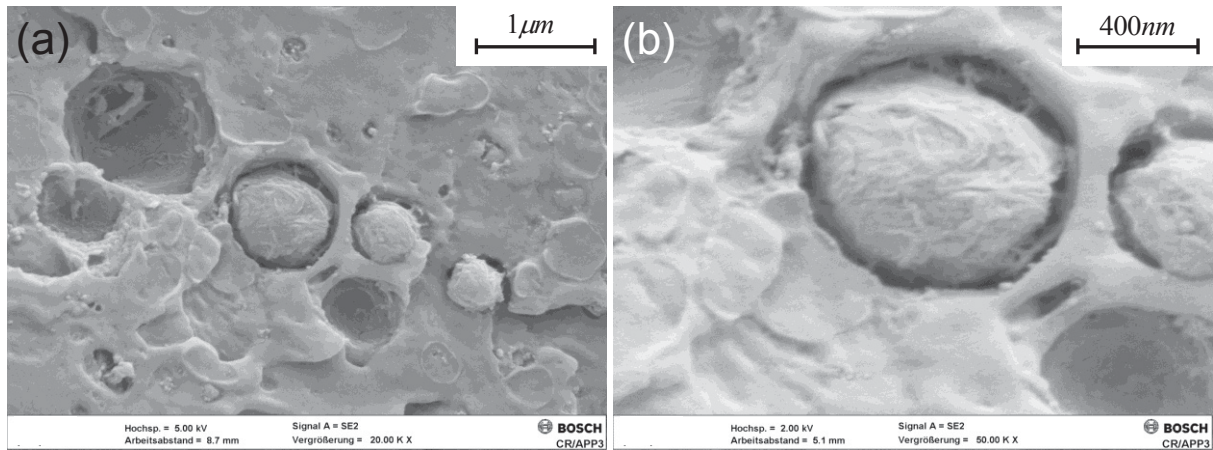


**Figure 5.10.** Particles on the cryo-fractured surface ahead the crack tip.

Energy-dispersive X-ray spectroscopy (EDX) analyses of the particles were also performed to study their elemental composition (Figure 5.11). The EDX analysis was performed with an excitation voltage of 15 kV. The peaks of carbon, oxygen and nitrogen (between the first two elements) are attributed to the polymer. A peak of gold is due to gold-sputtering. Smaller peaks of Silicon and Calcium were also noticed and may be related to the occurrence of a fiber fragment in the analyzed volume. Hence, the EDX analysis did not provide clear indication on the nature of the observed particles. It is worthwhile noting that the spatial resolution of the EDX detector is on the order of 3  $\mu\text{m}$  and it is probably too coarse for the elemental analysis of particle of diameter 0.1 - 0.3  $\mu\text{m}$ . The aim of this preliminary analysis was to highlight a new damage mechanism occurring below the micro-scale and preceding the formation of a micro-crack. For better understanding of this mechanism, further investigations are needed using more accurate experimental techniques.

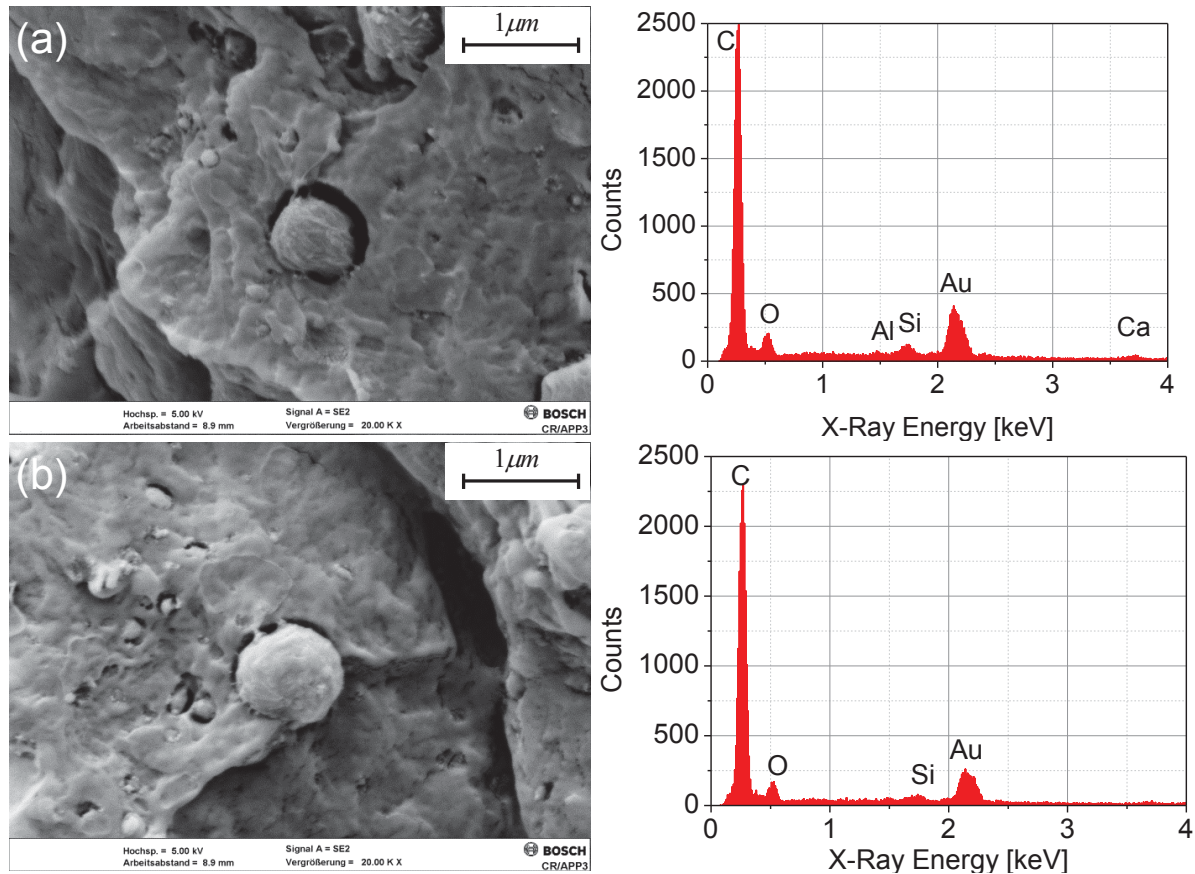


**Figure 5.11.** EDX analysis of particles found on the cryo-fractured surface ahead the crack tip.

The fracture surface shown in Figure 5.6b is caused by stable FCP. Therefore, between the three areas described in Figure 5.6, the area shown in Figure 5.6b was examined at high magnifications in order to observe the state of the fiber-matrix interfacial adhesion. Figure 5.12 shows two fibers (one perpendicular to fracture surface, (Figure 5.12a) and the other lying on the fracture surface, (Figure 5.12b) near the free surface of the notch. In both cases, fibers are covered by a resin layer. The microscopic examination suggests that damage occurs at a certain distance from the fiber-matrix interface. A thorough examination reveals that the resin layer is thicker for the fiber perpendicularly oriented to the fracture surface than for the fiber lying on the fracture surface.

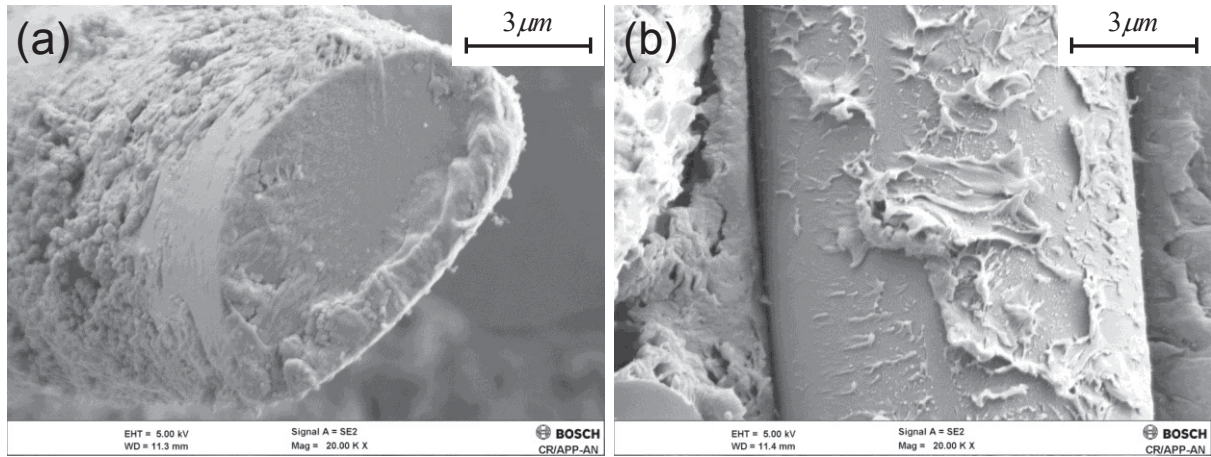


**Figure 5.12.** Fiber-matrix adhesion on the fracture surface of a notched specimen caused by stable FCP; (a) Fiber perpendicular to the fracture surface; (b) Fiber lying on the fracture surface.

### 5.5.3. Analysis of the crack path

In this Section, damage mechanisms were investigated on the side surface of the specimens. Fatigue tests were interrupted before failure using the IR camera (Section 5.5.1). Samples at crack initiation were machined from the specimens and analyzed by means of optical and field emission scanning electron microscope. The goals of this Section are: 1) To analyze the damage mechanisms at crack initiation in plain and notched specimens; 2) To study the fiber orientation distribution at crack initiation.

Figure 5.13 shows the damage analysis on the side surface of a plain specimen. Evidence of damage was found using the reflected light microscope (Figure 5.13a). This region was thoroughly investigated by means of FESEM. Figure 5.13 shows typical mechanisms occurring just before the specimen failure. Several micro-cracks were observed indicating that a macro-crack forms due to the coalescence of micro-cracks. An example of fiber failure is shown in Figure 5.13b. Figure 5.13c shows a small crack occurring between the matrix and a fiber fragment. Figure 5.13d shows a crack at the end of a longitudinally oriented fiber. Here the crack propagates at a distance of some tens of micrometers from the fiber surface. Figure 5.13e-f represent two high magnification pictures of the region 4. Voids can be observed close the fiber (Figure 5.13f). Coalescence of voids seems to represent the damage stage preceding the formation of a micro-crack in the matrix. If one compares Figure 5.13f with Figure 5.9b-c, it can be deduced that the size of the voids is comparable.



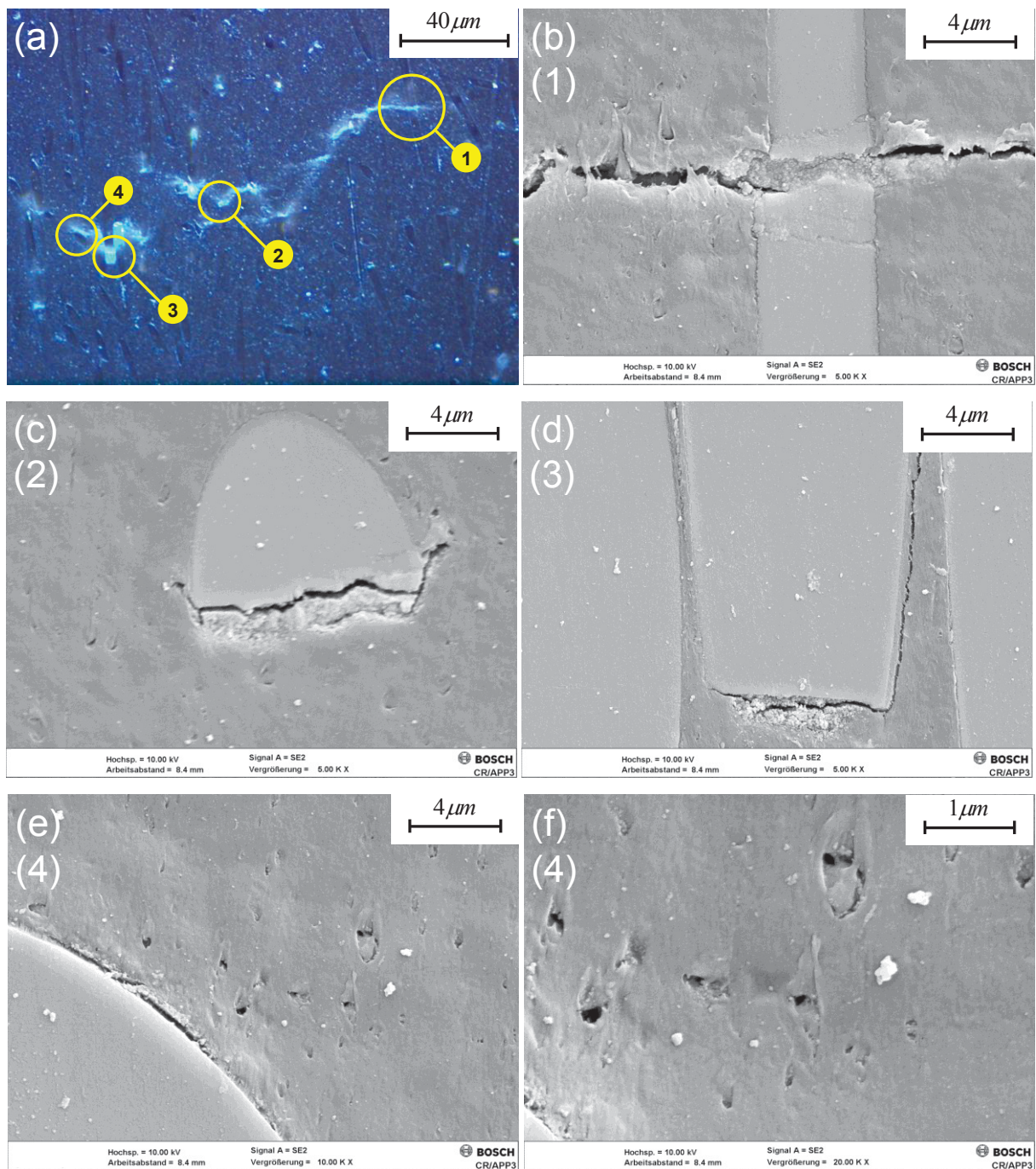


**Figure 5.13.** Damage investigation on the side surface of a plain specimen, interrupted fatigue test; (a) Damage zone observed through optical microscopy; (b) Fiber failure; (c) Crack at fiber fragment; (d) Crack at the fiber end; (e),(f) Voids in the matrix.

Figure 5.14 shows the side surface of a notched specimen subjected to interrupted fatigue test. The crack does not initiate at the notch tip as it would be expected if the material was homogeneous. At higher magnifications (Figure 5.14b-c), it is possible to examine the fiber

orientation distribution around the notch. At the close vicinity of the free surface of the notch, fibers are oriented through the thickness. This is deduced observing the circular footprints left by the fibers on the polished section. Few tens of millimeters from the free surface of the notch, the fibers are mostly in-plane oriented. Around the notch, fibers are unevenly distributed. They tend to agglomerate and form clusters. It is worthwhile noting that the location of crack initiation corresponds with a cluster of through-the-thickness oriented fibers (Figure 5.14c-d). The analysis of the side surface of other specimens confirmed the occurrence of fiber clusters around the notch. As well as being a geometric discontinuity, the insert also represents an obstacle for the melt stream during injection molding affecting the local fiber orientation. The analysis of the crack propagation shows that the crack exhibits a zig-zag path (Figure 5.14a). As soon as the effect of the insert vanishes, the crack follows the direction imposed by the in-plane fibers growing in a fiber avoidance mode (Figure 5.14b).

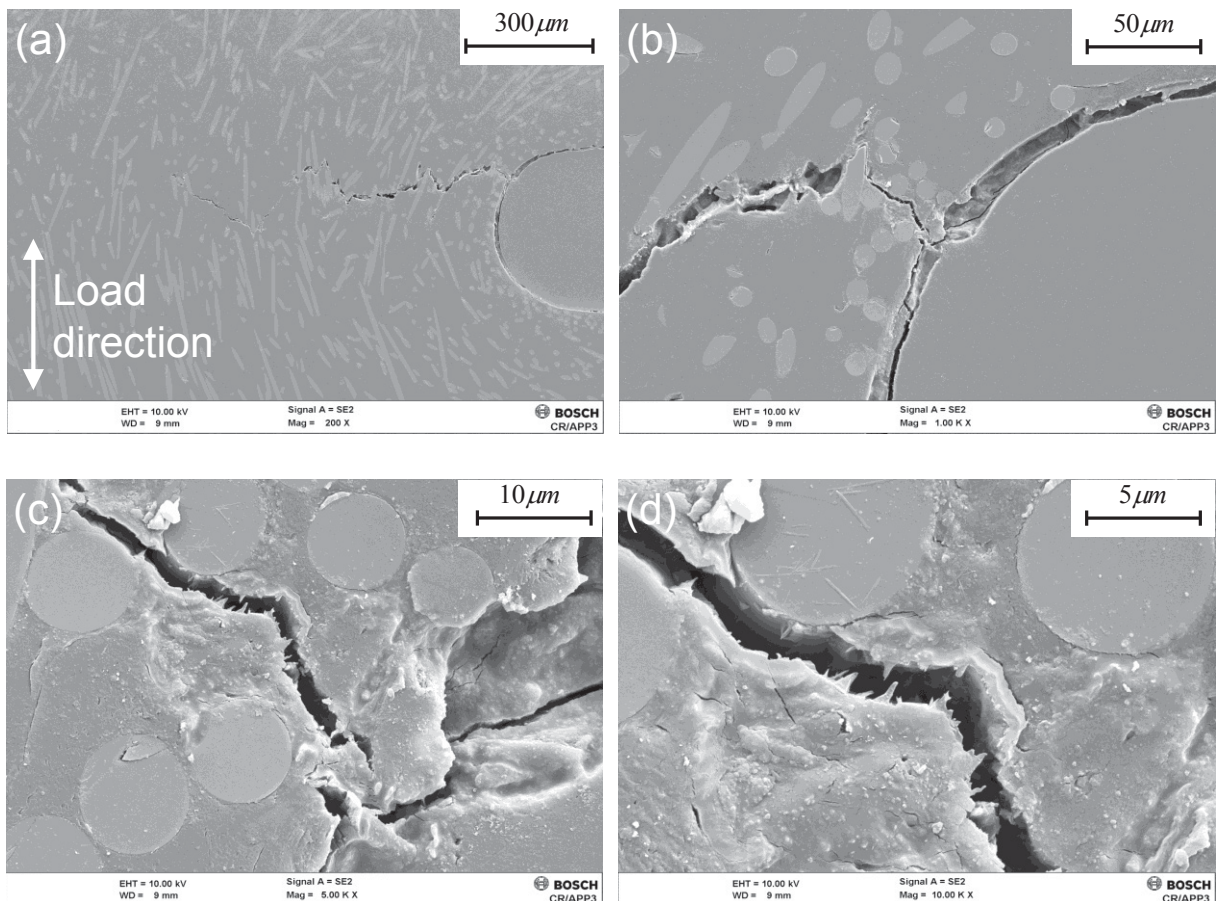


**Figure 5.14.** Fiber distribution at crack initiation for a notched specimen, interrupted fatigue test.



Figure 5.15 shows damage mechanisms along the crack path in different specimens. Crack propagates in a fiber avoidance mode (Figure 5.15a-b). Fibers are covered by a resin layer. Figure 5.15c provides an example of fiber pull-out in which the fiber extracted from the fracture surface is completely covered by a resin layer. This layer is around half a micrometer thick (Figure 5.15d). The FESEM micrographs shown in Figure 5.15 indicate that damage occurs at a certain distance from the fiber matrix interface in form of matrix cracking and not in form of fiber-matrix debonding. Hence, the lifetime prediction model should be able to reproduce the damage initiation and propagation at the resin layer covering the fibers. These results confirm the observations of the fracture surface in Section 5.5.2. They are valid for the material system and for the testing conditions reported in this paper.

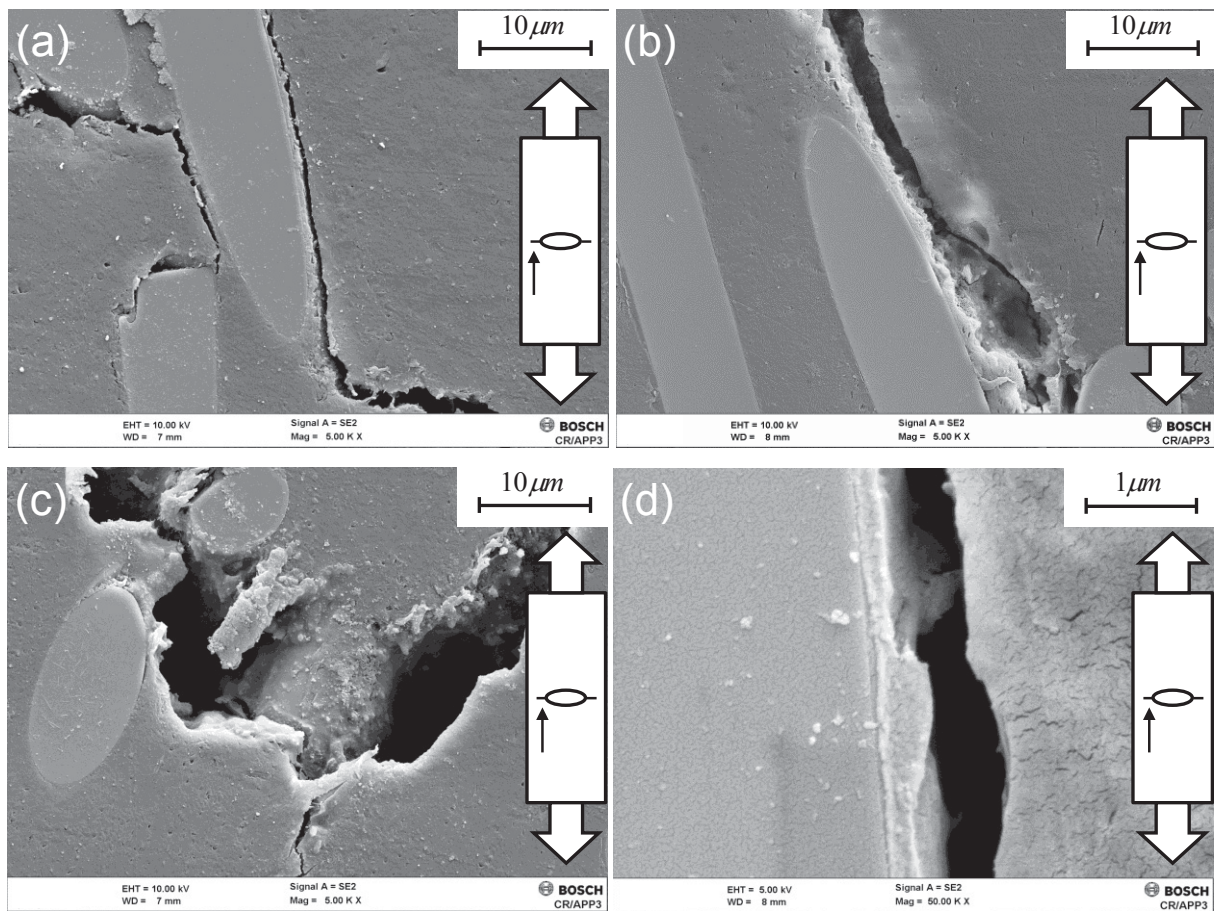


Figure 5.15. Damage mechanisms along the crack path (notched specimen).



## 5.6. Conclusions

In this work a damage investigation on a short glass fiber reinforced polyamide under fatigue loading is presented. The use of IR thermography enabled the localization of the damage initiation site. The damage mechanisms were studied by means of optical and electron microscopy investigating the following fractographic evidences: matrix fracture behavior (ductile / brittle), fiber failure / pull-out, degree of fiber-matrix interfacial adhesion. The results can be summarized as follows.

1. *Failure modes.* Plain and notched specimens exhibit different failure modes. Plain specimens fail due to unstable FCP preceded by a local temperature spot at shoulder tips. Failure scenario of notched specimens follows three steps: 1) Crack initiation; 2) Stable crack propagation; 3) Unstable crack propagation.
2. *Damage mechanisms.* The analysis of the fracture surface reveals that the material response varies according to the crack propagation mode (stable / unstable FCP). Matrix fracture behavior is micro-ductile on the fracture surface caused by stable FCP and brittle on the fracture surface caused by unstable FCP. FESEM fractographic analysis showed that fibers are mostly covered by a resin layer. This result, valid for the material system and the testing conditions presented in this work, indicates that damage does not occur at the fiber-matrix interface in form of fiber-matrix debonding but in the resin, at a certain distance from the interface in form of matrix cracking. A better understanding of the effect of sizing on the matrix at the fiber-matrix interface would be required to determine to what extent sizing affects the resin layer around the fibers leading to the formation of the interphase.  
  
Cavities were found on the fracture surface caused by stable FCP. With the aim to investigate this damage mechanism, fatigue tests of a notched specimens were interrupted at crack initiation and then cryo-fractured. Cavities were observed on the cryo-fracture surface immediately ahead of crack tip. Far from the crack tip, cavities are fewer and smaller. This preliminary analysis suggests that coalescence of voids in the matrix precedes the formation of a micro-crack. Evidence of voids was also proved analyzing the side surface of a plain specimen subjected to interrupted fatigue test.
3. *Fiber distribution at crack initiation.* The insert used in the mold for creating the notch affects the fiber orientation at crack initiation. Clusters of through-the-thickness oriented

fibers characterize the fiber orientation distribution around the notch. The crack was found to initiate in the matrix between through-the-thickness oriented fibers.

In plain specimens, micro-cracks were found at the end of fibers aligned to the loading direction. Some evidence of fractured fibers (longitudinally oriented with respect to the loading direction) was also provided.

## **References of Chapter 5**

- [1] A.T. Dibenedetto, G. Salee, R. Hlavacek, A study of the fatigue behavior of fiber reinforced nylons, *Polymer Engineering & Science*. 15 (1975) 242-251.
- [2] J.W. Dally, D.H. Carrillo, Fatigue behavior of glass-fiber fortified thermoplastics, *Polymer Engineering & Science*. 9 (1969) 434-444.
- [3] S. Hoffmann, Computational Homogenization of Short Fiber Reinforced Thermoplastic Materials (2012).
- [4] R.W. Lang, J.A. Manson, R.W. Hertzberg, Mechanisms of fatigue fracture in short glass fibre-reinforced polymers, *Journal of Materials Science*. 22 (1987) 4015-4030.
- [5] J.F. Mandell, D.D. Huang, F.J. McGarry, Crack propagation Modes in Injection Molded Fiber Reinforced Thermoplastics, in: *Short Fiber Reinforced Composite Materials*, B.A. Sanders, Philadelphia, 1982, pp. 3-32.
- [6] R. Talreja, Multi-scale modeling in damage mechanics of composite materials, *Journal of Materials Science*. 41 (2006) 6800-6812.
- [7] R. Pyrz, J. Schjødt-Thomsen, Bridging the length-scale gap-short fibre composite material as an example, *Journal of Materials Science*. 41 (2006) 6737-6750.
- [8] R.W. Hertzberg, J.A. Manson, *Fatigue of engineering plastics*, Academic Press, New York, 1980.
- [9] J.F. Mandell, D.D. Huang, F.J. McGarry, Fatigue of glass and carbon fiber reinforced engineering thermoplastics, *Polymer Composites*. 2 (1981) 137-144.

- [10] S. Mortazavian, A. Fatemi, Effects of fiber orientation and anisotropy on tensile strength and elastic modulus of short fiber reinforced polymer composites, *Composites Part B: Engineering*. 72 (2015) 116-129.
- [11] F. Cosmi, A. Bernasconi, Micro-CT investigation on fatigue damage evolution in short fibre reinforced polymers, *Composites Sci. Technol.* 79 (2013) 70-76.
- [12] A. Bernasconi, E. Conrado, P. Hine, An experimental investigation of the combined influence of notch size and fibre orientation on the fatigue strength of a short glass fibre reinforced polyamide 6, *Polym. Test.* 47 (2015) 12-21.
- [13] A. Bernasconi, P. Davoli, C. Armani, Fatigue strength of a clutch pedal made of reprocessed short glass fibre reinforced polyamide, *Int. J. Fatigue*. 32 (2010) 100-107.
- [14] M. De Monte, E. Moosbrugger, K. Jaschek, M. Quaresimin, Multiaxial fatigue of a short glass fibre reinforced polyamide 6.6 – Fatigue and fracture behaviour, *Int. J. Fatigue*. 32 (2010) 17-28.
- [15] J.J. Horst, J.L. Spoomaker, Fatigue fracture mechanisms and fractography of short-glassfibre-reinforced polyamide 6, *Journal of Materials Science*. 32 (1997) 3641-3651.
- [16] J. Karger-Kocsis, Effects of processing induced microstructure on the fatigue crack propagation of unfilled and short fibre-reinforced PA-6, *Composites*. 21 (1990) 243-254.
- [17] J. Karger-Kocsis, K. Friedrich, Fracture behavior of injection-molded short and long glass fiber—polyamide 6.6 composites, *Composites Sci. Technol.* 32 (1988) 293-325.
- [18] K. Noda, A. Takahara, T. Kajiyama, Fatigue failure mechanisms of short glass-fiber reinforced nylon 66 based on nonlinear dynamic viscoelastic measurement, *Polymer*. 42 (2001) 5803-5811.
- [19] A. Schaaf, M. De Monte, E. Moosbrugger, M. Vormwald, M. Quaresimin, Life estimation methodology for short fiber reinforced polymers under thermo-mechanical loading in automotive applications, *Materialwissenschaft und Werkstofftechnik*. 46 (2015) 214-228.
- [20] R.W. Lang, Roughness-induced crack closure in short fibre-reinforced plastics, *Journal of Materials Science Letters*. 4 (1985) 1391-1396.

- [21] N. Sato, T. Kurauchi, S. Sato, O. Kamigaito, Microfailure behaviour of randomly dispersed short fibre reinforced thermoplastic composites obtained by direct SEM observation, *Journal of Materials Science*. 26 (1991) 3891-3898.
- [22] K. Friedrich, Microstructure and fracture mechanical properties of short fiber reinforced thermoplastic P.E.T., *Colloid and Polymer Science*. 259 (1981) 808-811.
- [23] M. De Monte, E. Moosbrugger, K. Jäschek, M. Quaresimin, Multiaxial fatigue behaviour of a short-fibre reinforced polyamide 6.6 in the presence of notches. *ECCM - 13th European Conference on Composite Materials* (2008).
- [24] J. Karger-Kocsis, K. Friedrich, Fatigue crack propagation in short and long fibre-reinforced injection-moulded PA 6.6 composites, *Composites*. 19 (1988) 105-114.
- [25] H. Voss, J. Karger-Kocsis, Fatigue crack propagation in glass-fibre and glass-sphere filled PBT composites, *Int. J. Fatigue*. 10 (1988) 3-11.
- [26] J.L. Thomason, Interfaces and interfacial effects in glass reinforced thermoplastics - Keynote Presentation (2007).
- [27] H.M. Brodowsky, W. Jenschke, E. Mäder, Characterization of interphase properties: Microfatigue of single fibre model composites, *Composites Part A: Applied Science and Manufacturing*. 41 (2010) 1579-1586.
- [28] K. Friedrich, R. Walter, H. Voss, J. Karger-Kocsis, Effect of short fibre reinforcement on the fatigue crack propagation and fracture of PEEK-matrix composites, *Composites*. 17 (1986) 205-216.
- [29] M. De Monte, E. Moosbrugger, M. Quaresimin, Influence of temperature and thickness on the off-axis behaviour of short glass fibre reinforced polyamide 6.6 – cyclic loading, *Composites Part A: Applied Science and Manufacturing*. 41 (2010) 1368-1379.
- [30] S. Mortazavian, A. Fatemi, Fatigue behavior and modeling of short fiber reinforced polymer composites including anisotropy and temperature effects, *Int. J. Fatigue*. 77 (2015) 12-27.

- [31] K. Friedrich, Microstructural efficiency and fracture toughness of short fiber/thermoplastic matrix composites, *Composites Sci. Technol.* 22 (1985) 43-74.
- [32] M.F. Arif, N. Saintier, F. Meraghni, J. Fitoussi, Y. Chemisky, G. Robert, Multiscale fatigue damage characterization in short glass fiber reinforced polyamide-66, *Composites Part B: Engineering.* 61 (2014) 55-65.
- [33] A. Bernasconi, P. Davoli, A. Basile, A. Filippi, Effect of fibre orientation on the fatigue behaviour of a short glass fibre reinforced polyamide-6, *Int. J. Fatigue.* 29 (2007) 199-208.
- [34] M. De Monte, E. Moosbrugger, M. Quaresimin, Influence of temperature and thickness on the off-axis behaviour of short glass fibre reinforced polyamide 6.6 – Quasi-static loading, *Composites Part A: Applied Science and Manufacturing.* 41 (2010) 859-871.
- [35] M.F. Arif, F. Meraghni, Y. Chemisky, N. Despringre, G. Robert, In situ damage mechanisms investigation of PA66/GF30 composite: Effect of relative humidity, *Composites Part B: Engineering.* 58 (2014) 487-495.
- [36] E. Belmonte, E. Moosbrugger, N. De Rossi, M. De Monte, M. Quaresimin, Life to crack initiation in notched specimens of unreinforced and short fiber reinforced polyamide under fatigue loading, to appear.
- [37] B. Klimkeit, S. Castagnet, Y. Nadot, A.E. Habib, G. Benoit, S. Bergamo, C. Dumas, S. Achard, Fatigue damage mechanisms in short fiber reinforced PBT+PET GF30, *Materials Science and Engineering: A.* 528 (2011) 1577-1588.
- [38] S. Günzel, S. Hickmann, C. Wittemeyer, V. Trappe, Effects of Fiber Orientation and Moisture on the Crack Growth in Short Glass Fiber Reinforced Polyamide, *Advanced Engineering Materials.* 14 (2012) 867-872.
- [39] W.J. Evans, D.H. Isaac, K.S. Saib, The effect of short carbon fibre reinforcement on fatigue crack growth in PEEK, *Composites Part A: Applied Science and Manufacturing.* 27 (1996) 547-554.
- [40] R.W. Lang, Roughness-induced crack closure in short fibre-reinforced plastics, *Journal of Materials Science Letters.* 4 (1985) 1391-1396.

[41] K. Friedrich, R. Walter, H. Voss, J. Karger-Kocsis, Effect of short fibre reinforcement on the fatigue crack propagation and fracture of PEEK-matrix composites, *Composites*. 17 (1986) 205-216.

[42] H. Rolland, N. Saintier, G. Robert, Damage mechanisms into short glass fibre reinforced thermoplastic during in situ microtomographic tensile tests. 16th European Conference on Composite Materials, ECCM16 (2014).

## **Chapter 6**

# **Influence of fiber loading on the fatigue damage mechanisms in short glass fiber reinforced polyamide**

**Keywords:** Short Fiber Reinforced Composites, Damage Mechanisms, Fatigue, Polyamide

### **Abstract**

This paper investigates the influence of the fiber volume fraction on the damage mechanisms in a short glass fiber reinforced polyamide (PA66) under tension-tension fatigue loading. Uniaxial fatigue tests were carried out on notched specimens characterized by different fiber contents (0 %, 15 %, 25 %, 35 %, 50 % in weight). The notch was molded-in in order to reproduce a typical fiber orientation distribution at structural discontinuities in real injection molded parts. The damage investigation was performed by using Field Emission Scanning Electron Microscopy (FESEM). Interrupted fatigue tests were carried out to analyze the influence of the fiber volume fraction on the crack path. Fracture surfaces of specimens failed in the high cycle regime were also examined. Specific fractographic features (ductile/brittle appearance of the fracture surface, pulled-out/broken fibers, degree of fiber-matrix interfacial adhesion) were examined with the aim to study the effect of the fiber volume fraction on the fatigue damage mechanisms.

### **6.1. Introduction**

Due to the increasing use of SFRPs in structural applications, lifetime prediction models play an important role in the durability estimation of real injection molded parts. This is the topic of a long term collaboration between the University of Padova and the corporate research of Robert Bosch GmbH. The effect of anisotropy and temperature on tensile and fatigue behavior of SFRPs was studied by De Monte and coworkers in [1, 2]. The study was extended to include the effect of notch [3], multiaxial loading [4, 5] and recently thermomechanical loading [6, 7] on the fatigue behavior of SFRPs. A comprehensive literature review recently published by Mortazavian and Fatemi [8] shows that several studies have been conducted to

analyze the factors affecting the fatigue behavior of SFRPs. In spite of that, lifetime prediction models found in the literature are extensions of phenomenological models originally developed for isotropic materials [3, 9]. In the last years, the improvement of the damage investigation methods and the explosion of the computational power have prompted researchers to deeply investigate the damage mechanisms in SFRPs. Mechanisms-based lifetime prediction models aim to integrate the relevant damage mechanisms in order to obtain an accurate estimation of the lifetime to failure reducing empirical parameters and assumptions.

Recently in [10], the authors studied the damage mechanisms in plain and notched PA66-GF35 specimens under fatigue loading. In the present paper, the damage investigation is extended to consider the effect of the fiber volume fraction on the fatigue damage mechanisms in notched specimens. With this work, the authors aim to lay the foundations for the development of a multi-scale lifetime prediction model taking into account the material microstructure. In literature, the influence of the fiber volume fraction on the fatigue damage mechanisms in SFRPs was studied mainly with regard to crack propagation using Compact Tension (CT) specimens [11-14]. A study of the influence of the fiber volume fraction on the damage mechanisms at crack initiation is missing. A comparison between the fatigue life to crack initiation and to failure for short glass fiber reinforced polyamide notched specimens has been recently published by the authors in [15]. In the present paper, the fatigue behavior to crack initiation and to failure was studied by investigating the damage mechanisms. In literature, more emphasis has been given to the influence of fiber orientation on the lifetime of SFRPs rather than fiber volume fraction. In fact, a change in fiber content results in a variation of the other microstructural variables. The higher the fiber volume fraction the shorter the average fiber length will be due to fiber-fiber and fiber-machine interaction during injection molding [11, 16-18]. The fiber volume fraction also influences the fiber orientation. Bernasconi [18] and Thomason [19] observed that the higher the fiber volume fraction the more the fibers are aligned in the Mold Flow Direction (MFD). Instead, the analysis of the influence of the fiber orientation on fatigue behavior of SFRPs can be conducted cutting specimens out of injection molded plates at different orientations with respect to the injection molding direction [1, 2, 20-23]. Such approach keeps the other microstructural variables unchanged. However, the fiber orientation distribution also varies along the thickness affecting the material behavior. In [1, 2], De Monte and coworkers reported higher anisotropic tensile and fatigue strength for thinner specimens. Moreover, this method is not suitable for



studying the effect of the local fiber distribution on the crack initiation. In real injection molded parts, cracks occur at geometrical discontinuities [9, 24]. At these locations, fiber orientation is far from being unidirectional. Fiber orientation at critical locations strongly affects the fatigue strength of SFRPs. In [4] it was found that the torsional fatigue strength of hollow tubular specimens with V-shaped molded notch ( $R_{\text{notch}} = 0.2 \text{ mm}$ ) is higher than that of the same specimens with a drilled hole ( $R = 1 \text{ mm}$ ). This result was explained as a compensation of notch geometry and fiber orientation distribution at crack initiation. In [10, 15], the authors used rectangular specimens with a central molded-in notch with the aim to reproduce the fiber orientation at structural discontinuities in real injection molded parts. The MFD was parallel to the long dimension of the specimen. The insert used for creating the notch represents an obstacle for the melt flow affecting the local fiber orientation distribution. The authors observed that around the notch, fibers are oriented through-the-thickness.

In this work, the damage investigation is divided in two parts. Section 6.4.1 is dedicated to the analysis of the crack path. For this purpose, fatigue tests were interrupted before specimen separation. Then the side surface of the specimens was polished for microscopic investigations. Section 6.4.2 is dedicated to the analysis of the fracture surface. For this purpose, fatigue tests were carried out until failure which corresponds to specimen separation into two parts. The damage analysis was carried out at multiple scales. The influence of the fiber volume fraction on the specimen failure mode (stable/unstable Fatigue Crack Propagation (FCP)) was primarily investigated with unaided eye on the fracture surface of failed specimens. Meso- and micro-scale investigations were carried out by means of Field Emission Scanning Electron Microscopy (FESEM). At meso-scale, the effect of the fiber volume fraction on the crack path was investigated. At micro-scale, damage mechanisms were studied examining the following fractographic features: matrix fracture behavior (ductile/brittle), fiber failure/ pull-out and degree of fiber-matrix interfacial adhesion.

## **6.2. Materials geometry and test equipment**

The material investigated in the present paper is a short glass fiber reinforced polyamide (PA66). Five material systems were tested varying the fiber content ( $V_f = 0 \%, 15 \%, 25 \%, 35 \%, 50 \%$  by weight).

Uniaxial fatigue tests were carried out on a 10 kN servo-hydraulic testing machine. The fatigue tests were performed under load control, applying a sinusoidal load with constant amplitude. A specimen where the notch is created through an insert within the mold was

preferred to a specimen where the notch is machined afterwards. This geometry reflects the real injection molded parts, which are ready to use after ejection from the mold without any need of post-molding machining operation. Specimen geometry and dimensions are reported in Figure 6.1. The notch is a central slit of 10 mm with notch radius of 0.2 mm. Stress concentration factor (referring to the net section) calculated using isotropic material model is  $K_{t_{net}} = 9.81$ . Specimens were injected along the longitudinal direction which coincides with the loading direction.

The fatigue data were already published by the authors in [15]. Fatigue tests were carried out until specimen separation. An optical method was used to quantify the contribution of the crack initiation to the total lifetime of the specimen. Moreover, some fatigue tests were interrupted before failure in order to investigate the effect of the fiber volume fraction on the crack path. The load ratio  $R (= \sigma_{min}/\sigma_{max})$  was set to 0 for all the performed fatigue tests. The fatigue tests were carried out at room temperature. Relative humidity in the room was not controlled during the fatigue tests. The specimens were tested in dry-as-molded conditions since right after injection molding, they were stored in a drum containing a drying agent (silica gel pearls).

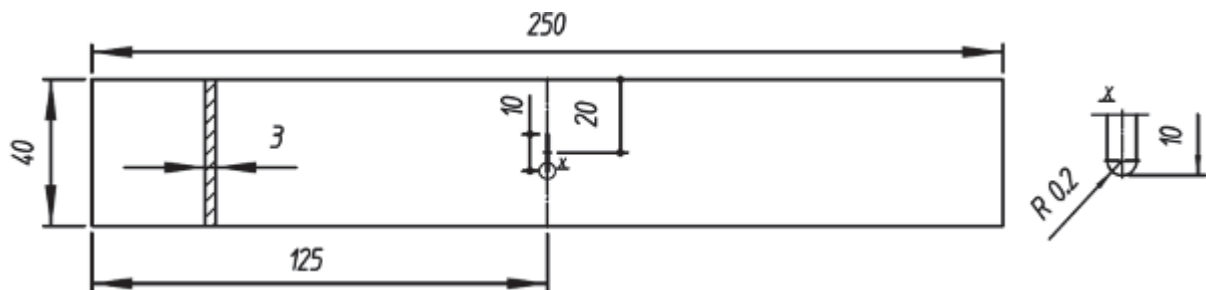


**Figure 6.1.** Specimen geometry and dimensions (in mm).

The damage investigation was performed by means of Zeiss Supra 55VP Field Emission Scanning Electron Microscope (FESEM) with 7kV accelerating voltage and equipped with a EDAX X-Ray Si(Li)-Detector. For improving the quality of the analysis, the samples analyzed by means of FESEM were gold sputtered. Energy-dispersive X-ray spectroscopy (EDX) was used for the elemental characterization of particles observed on the fracture surface caused by stable FCP.

### 6.3. Fatigue tests results

Figure 6.2 summarizes the S-N curves up to crack initiation and up to failure of the notched specimens for reinforced and unreinforced polyamide specimens. Fatigue data are represented in a double logarithmic diagram, plotting the net stress amplitude ( $\sigma_a$ ) against the number of cycles (N) to crack initiation / failure. Fatigue curves with 50 % failure probability are plotted using eq. 6.1.

$$N \cdot \sigma_a^k = N_A \cdot \sigma_A^k \quad (6.1)$$

Where  $N_A = 1E6$  cycles and  $\sigma_A = \sigma_a(1E6)$ . The values of  $\sigma_A$ ,  $k$  and the scatter index  $T_\sigma = \sigma_{a,10\%}/\sigma_{a,90\%}$  are reported in Table 6.1. With the same applied stress amplitude, an increase in fiber fraction results in an increase of both the lifetime to crack initiation and to failure. The beneficial effect of the fibers amount on the fatigue life to failure was also reported by Avanzini et al. [25] for plain specimens of short carbon fiber reinforced PEEK. The fatigue curve of unreinforced polyamide notched specimens is flatter than those of reinforced material systems.

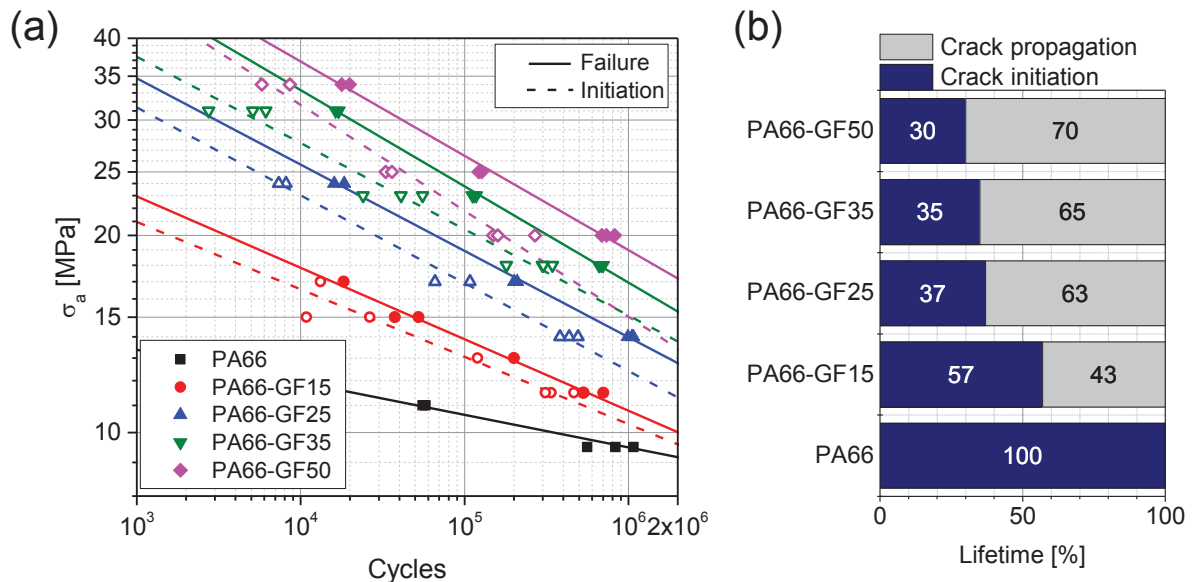


**Figure 6.2.** (a) S-N curves up to crack initiation and up to failure of notched specimens,  $T = RT$ ,  $R = 0$ , for different fiber volume fractions; (b) Contribution of the crack initiation / propagation to the total lifetime.

As reported in [10] failure of notched specimens under fatigue loading occurs in three phases: crack initiation, stable crack propagation, unstable crack propagation. The contribution of the crack initiation/crack propagation to the total lifetime changes with varying fiber volume fraction. The higher the fiber volume fraction the higher the contribution of the crack propagation to the total lifetime will be (Figure 6.2b). In fact, as reported in [11, 13, 14, 26] an increase in fiber content results in a reduced crack propagation rate. For unreinforced polyamide specimens, life to failure corresponds to life to crack initiation. Moreover, the life spent in crack propagation depends on the geometry of the notch. The sharper the notch, the longer the contribution of the crack propagation to the total lifetime will be [27]. In the next Section the effect of the fiber volume fraction on the fatigue material behavior will be investigated by analyzing the damage mechanisms.

**Table 6.1.** Summary of the fatigue curve parameters for each test series.

Material	Initiation			Failure		
	$\sigma_A$	k	$T_\sigma$	$\sigma_A$	k	$T_\sigma$
	[MPa]	-	-	[MPa]	-	-
PA66	9.50	20.12	1.051	9.50	20.12	1.051
PA66-GF15	10.31	9.72	1.136	10.80	9.17	1.052
PA66-GF25	12.42	7.46	1.073	13.99	7.59	1.032
PA66-GF35	15.10	7.60	1.124	16.94	6.81	1.022
PA66-GF50	15.03	6.18	1.128	18.99	6.95	1.056

## 6.4. Damage investigation

### 6.4.1 Analysis of the crack path

Fatigue tests were interrupted before failure with the aim to study the influence of the fiber volume fraction on the crack path. The crack path was analyzed on the side surface of the specimens. In literature, similar analyses were carried out to study the influence of different material systems [28, 29] and fiber orientations [30, 31] on the fatigue crack propagation using CT specimens.

Figure 6.3 shows FESEM micrographs of the crack path for different fiber volume fractions. Cracks show a zig-zag pattern. As reported by many authors [5, 28, 30, 32, 33], in SFRPs a crack grows avoiding fibers. This mechanism is called fiber avoidance mode. The higher the fiber content, the more irregular the path of the crack is. With low fiber fraction (15 wt. %), the crack grows perpendicularly to the loading direction (Figure 6.3a). The fibers along the crack path represent isolated obstacles which lead to a local variation of the crack direction. An increase in fiber fraction leads to the reduction of the interfiber distance. Fibers agglomerate forming clusters which force the crack to change direction in a far more effective way than isolated fibers. A similar observation was made by Mandell et al. [28]. They showed that fiber clusters have a stronger influence on the crack path than isolated fibers. Each variation of the crack direction imposed by the fibers causes an energy dissipation and, as a consequence, a slowing down of the crack. An increase in fiber fraction results therefore in the reduction of the crack growth rate.

Figure 6.3 shows the location of crack initiation for different fiber volume fractions. Apart of Figure 6.3b, the observed cracks do not initiate from the notch tip as it would be expected if the material was homogeneous. This evidence indicates that the crack initiation site is affected by the fiber distribution around the notch.

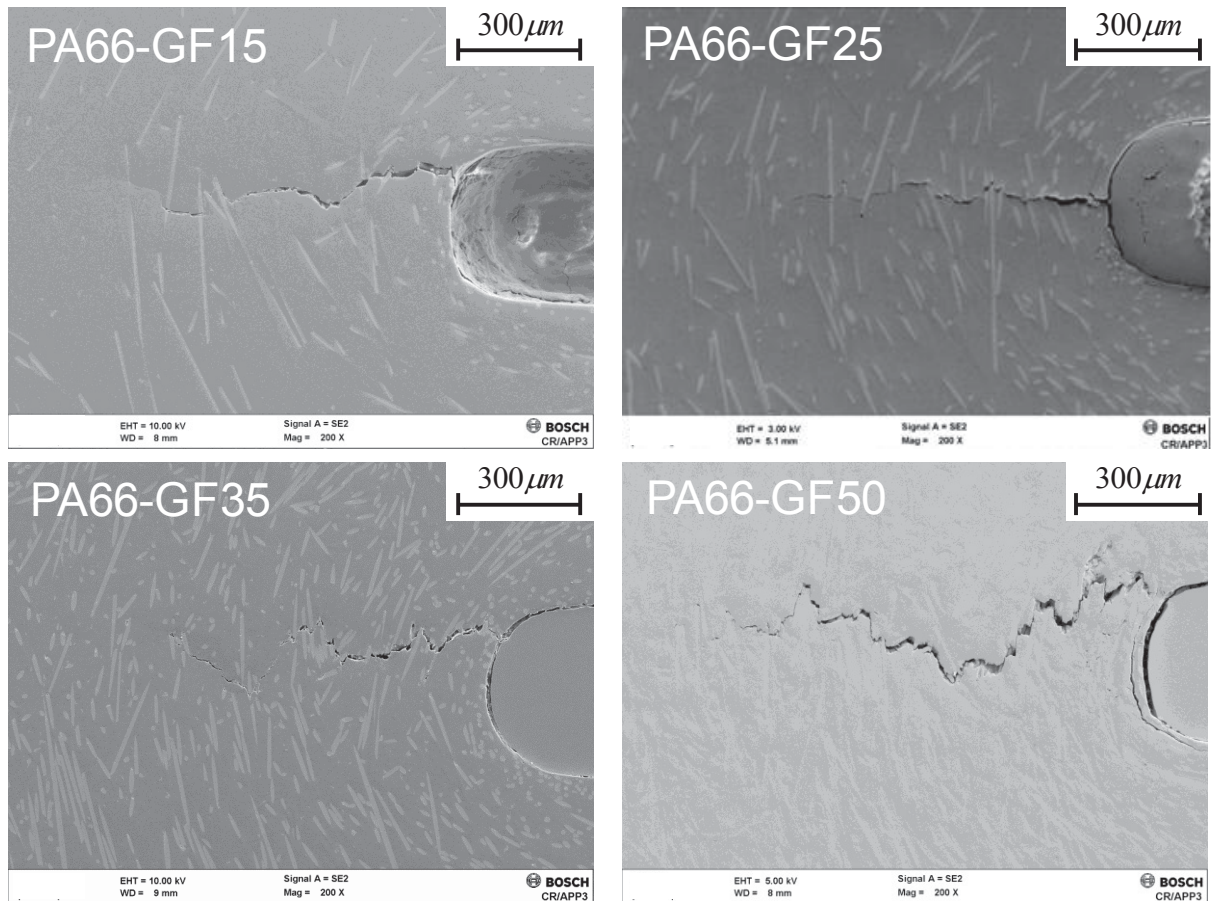


**Figure 6.3.** Crack path on the side surface of the specimens.

Two examples of damage mechanisms observed on the side surface of the PA66-GF25 specimen are shown in Figure 6.4a-b. Figure 6.4a shows an example of fiber pull-out. A significant portion of the fiber is pulled out from the matrix since the fiber ends are far from the crack plane. The fiber represents an isolated obstacle to the crack growth which does not cause any significant deviation of the crack plane. Figure 6.4b provides an example of fiber failure. Even in this case, the fiber is crossing the crack plane. This mechanism is far less frequent than fiber pull-out.



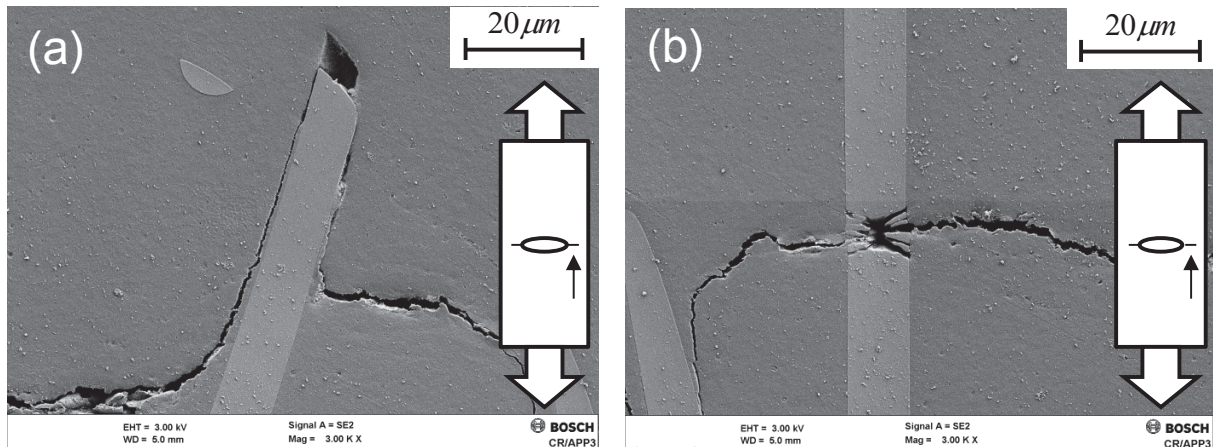


**Figure 6.4.** Damage mechanisms along the crack path, PA66-GF25 specimen (a) Fiber pull-out; (b) Broken fiber.

With higher fiber volume fraction (50wt. %), fractured fibers are noticed ahead of the main crack tip (Figure 6.5). Some fibers are broken into fragments which are still close to each other (Figure 6.5b). A similar analysis (not shown in this paper) was carried out for virgin specimens with the aim to see if fiber breakage occurs due to cyclic loading or during injection molding. No evidence of fiber breakage was found indicating that the broken fibers observed in Figure 6.5 are due to cyclic loading. Instead, the occurrence of many isolated fiber fragments is due to fiber breakage during injection molding. Analogously to the fiber ends, the new surfaces generated by fiber breakage during injection molding can be identified as being preferential locations for the crack propagation since are not covered by any sizing. While propagating, the crack is continuously forced to change direction by the fibers. With high fiber fractions, the crack plane is not perpendicularly oriented to longitudinal fibers as observed in Figure 6.4b. As a result, with high fiber volume fractions, the pull-out length is shorter.

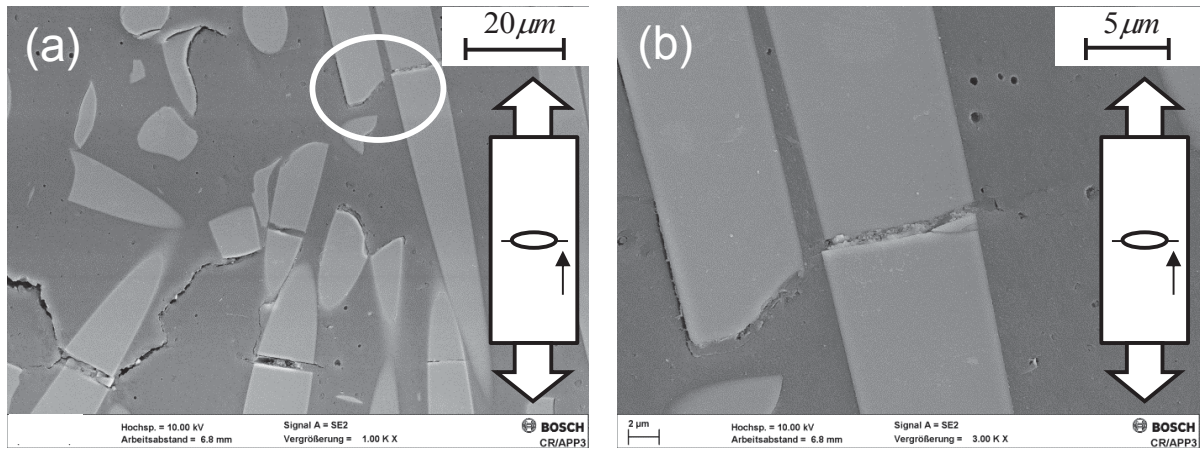


**Figure 6.5.** Damage mechanisms along the crack path, PA66-GF50 specimen; (a) Fractured fibers ahead of the crack tip; (b) Crack at the fiber end and fiber failure.

### 6.4.2. Analysis of the fracture surface

In this Section the influence of the fiber volume fraction on the fatigue damage mechanisms was studied by means of microscopic analysis of the fracture surface of failed specimens. Firstly the influence of the fiber volume fraction on the specimen failure mode (crack initiation, stable and unstable crack propagation) was investigated. As reported in [5], the distinction between the fracture surface caused by stable FCP and unstable FCP is evident to the unaided eye. The fracture surface caused by stable FCP is stress whitened and smooth. Instead, the fracture surface caused by unstable FCP is more irregular reflecting the sudden failure mode typical of quasi-static tensile tests. Table 6.2 reports the applied stress amplitude and the fatigue life to failure of each analyzed specimen.

**Table 6.2.** Stress amplitude and number of cycles to failure of the specimens used for the analysis of the fracture surface morphology.

Material designation	$\sigma_a$ [MPa]	$N_f$
PA66	9	1784240
PA66-GF15	11	877157
PA66-GF25	14	1027310
PA66-GF35	17	2182042
PA66-GF50	18	3334750



Figure 6.6 shows the fracture surfaces of the analyzed specimens. The stress whitened area corresponds to the fracture surface caused by stable FCP. The fracture surfaces of the reinforced polyamides are similar to each other. Conversely, there is a significant difference between the unreinforced and the reinforced material systems. The fracture surface caused by stable FCP in the neat matrix specimen is noticed only at the left of the notch. Instead, for the reinforced materials, it is observed at both sides of the notch. In PA66 and PA66-GF15 specimens, the area caused by stable FCP is smaller if compared with the other materials indicating a lower contribution of the crack propagation to the total lifetime. Fracture surfaces of unreinforced and reinforced polyamides also differ in the unstable FCP. Markings in form of curved lines converging to the middle thickness are noticed on the fracture surface of unreinforced polyamide specimens. According to Herzberg [34], they are called “chevron markings” and are characteristics of brittle failure. These markings were also observed by Lang et al. [35] on the fracture surface of a polystyrene matrix failed under fatigue loading.

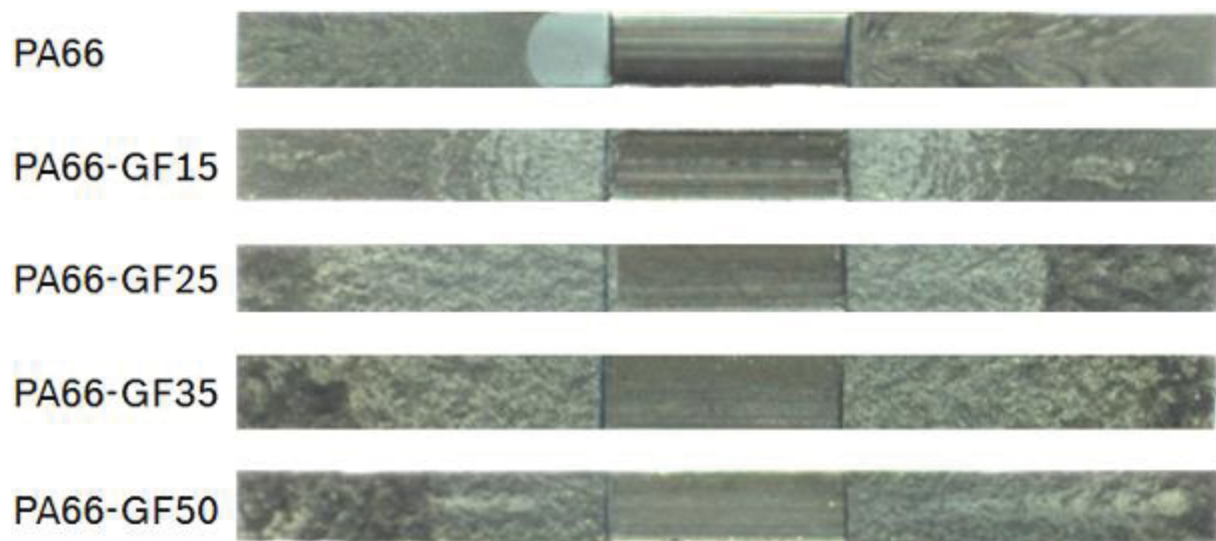
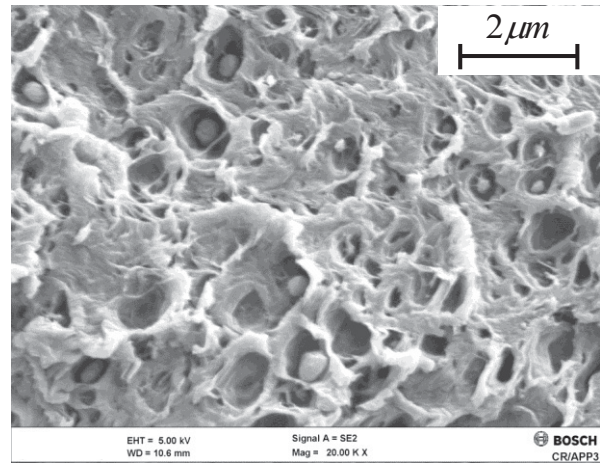
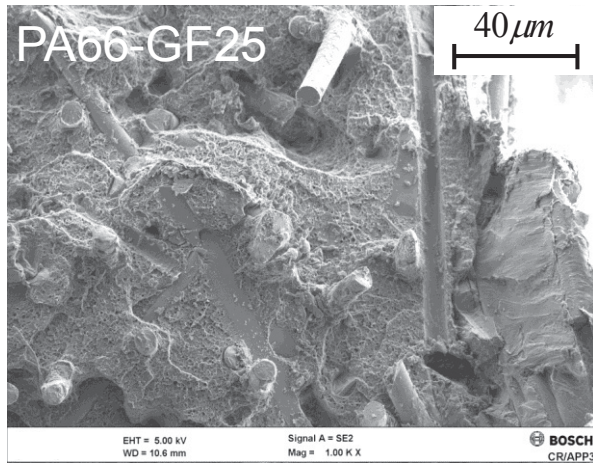
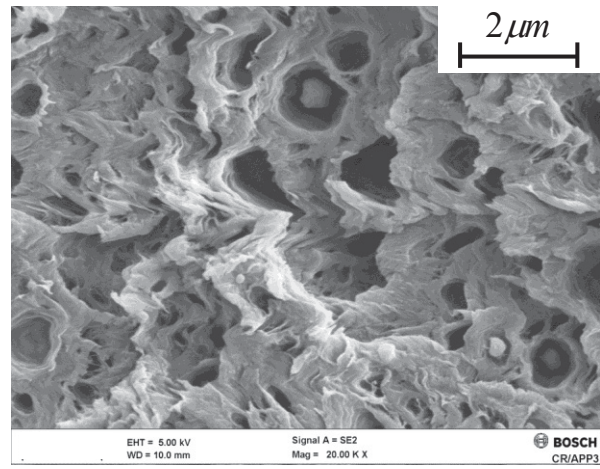
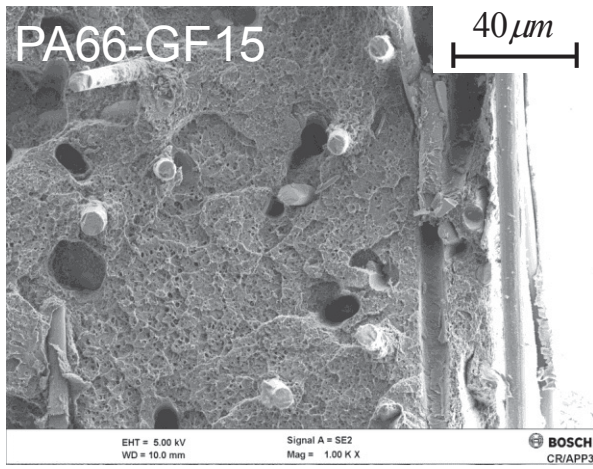
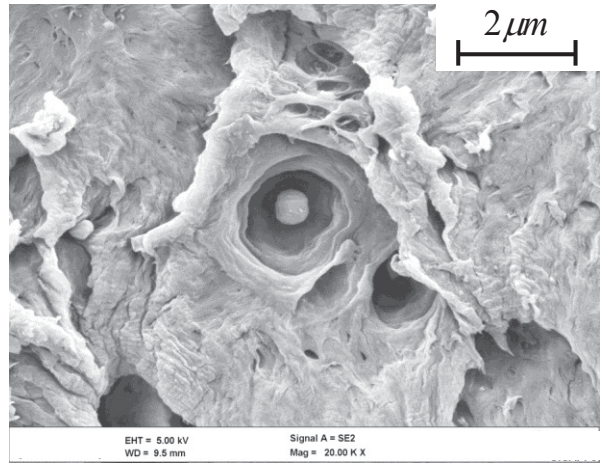
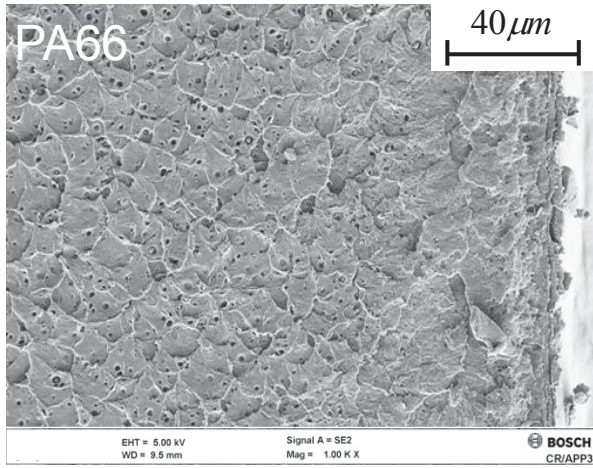


**Figure 6.6.** Fatigue crack surfaces of the analyzed specimens.

As reported by Hertzberg [34], terms which have a descriptive function but not the scientific agreement are used to describe the fracture surface morphology. This is the case of the term “micro-ductile” used to describe evidence of ductile fracture behavior on the fracture surface. In the following, the term “micro-ductility” will be used if a clear evidence of ductile matrix behavior can be provided only at micro-scale. In fact, by increasing the magnification at which the fracture surface is analyzed, some evidence of ductile matrix deformation can be

provided which was not visible at low magnifications. An example is given in Figure 6.7. On the left column of Figure 6.7, low magnifications FESEM micrographs (5000X) of the fracture surfaces are shown. For each picture on the left column, there is the corresponding high magnification enlargement (20000X) on the right column. All the FESEM micrographs are taken close to the notch. Apart from the unreinforced polyamide (Figure 6.7a), the observation of the fracture surface at low magnifications does not give any clear evidence of ductile matrix behavior. Instead, by observing the fracture surface at high magnification (Figure 6.7b), ductile matrix deformation is evident. Therefore, the matrix on the stable FCP of reinforced material systems shows a micro-ductile behavior. Instead, the unfilled matrix exhibits a macro-ductile matrix behavior. Referring to Figure 6.7 (left column) it was found that the higher the fiber volume fraction, the more peaks and valleys characterize the morphology of the fracture surface (Figure 6.7e). This result is consistent with the previous observation of the crack path (Section 6.4.1). Fiber clusters are obstacles which the crack avoids, leading to an irregular fracture surface. Isolated fibers have not the same effect. When not broken, they are pulled out leaving holes on the fracture surface (Figure 6.7b). The observation of the fracture surface also confirms that the pull-out length decreases with increasing fiber fraction. With high fiber fractions, fiber clusters force the crack plane to kink towards the fiber ends. Hence, the fracture surface of specimens characterized by high fiber fraction reveals only the ends or small portions of the fibers (Figure 6.7e).

Chapter 6. Influence of fiber loading on the fatigue damage mechanisms in short glass fiber reinforced polyamide





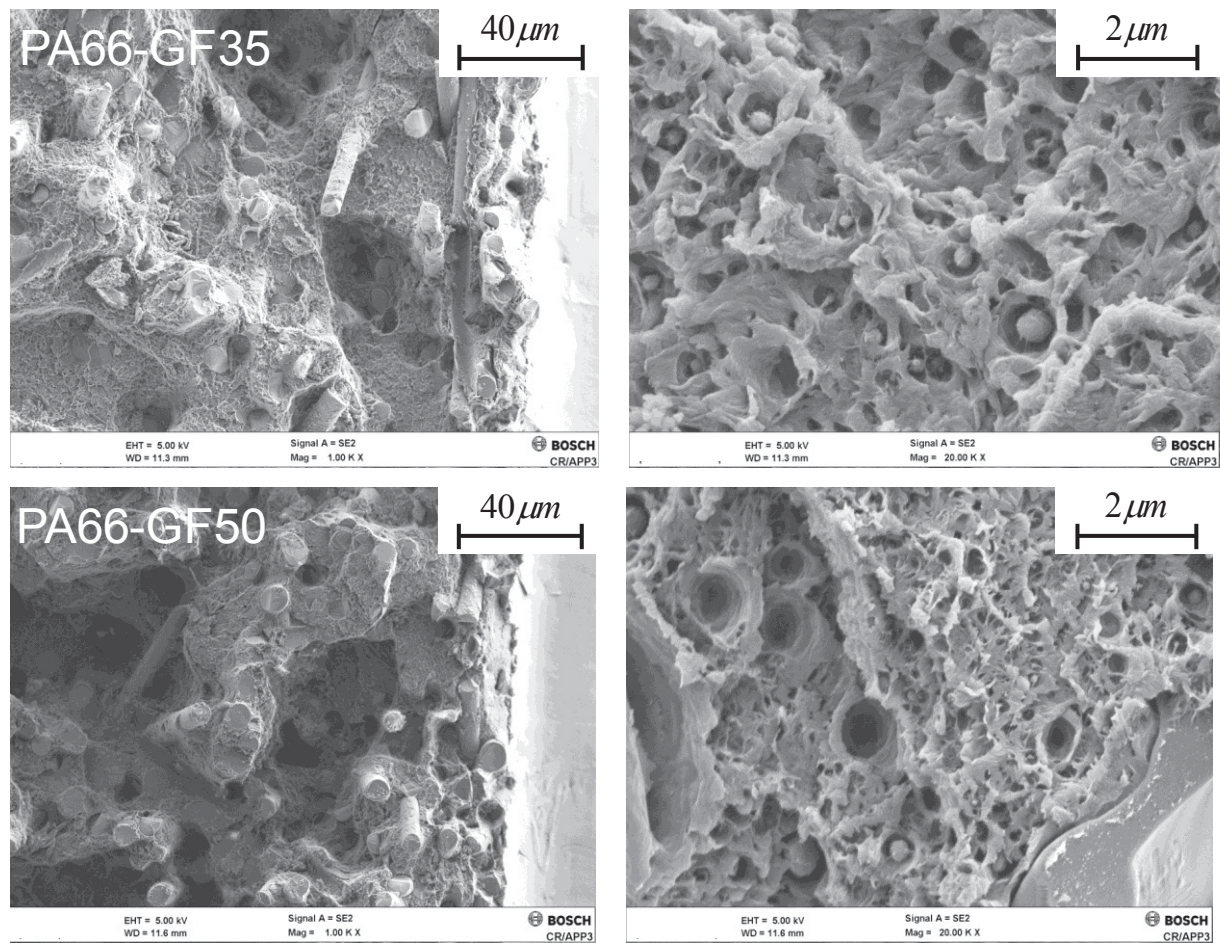


**Figure 6.7.** Fracture surface near the notch; low magnification micrographs on the left column; high magnifications micrographs on the right column (crack grows from the right to the left).

High-magnification FESEM micrographs in Figure 6.7 show evidence of matrix cavitation around particles. The same mechanism was recently reported by the authors in [10]. In [10] EDX analyses were carried out to study the elemental composition of the observed particles on the fracture surface of a PA66-GF35 specimen failing to capture their nature. The same particles observed in [10] were found on the fracture surface of the other short glass fiber reinforced polyamide specimens. Instead, the particles observed on the fracture surface of the neat polymer shall be distinguished by their shape and dimension. In fact, they are bigger and have a crystal-like form. Figure 6.8 shows high magnification FESEM micrographs of the investigated particles and the corresponding EDX maps. Gold peaks observed in Figure 6.8 are due to gold sputtering of the sample surface. Carbon and oxygen peaks are related to the polymer. Aluminum peaks are noticed which should not be related to the polymer. Hence the particles may be aluminum oxide.

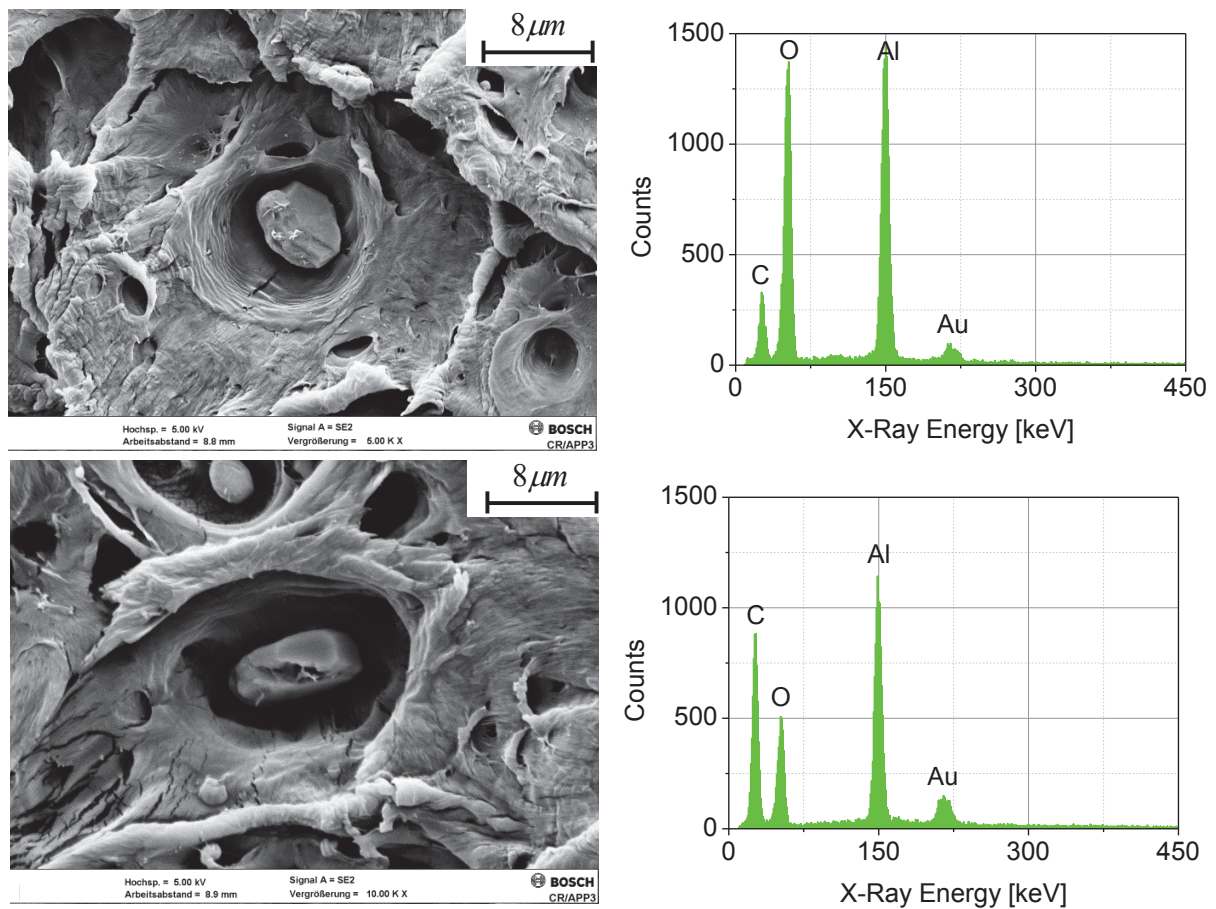


**Figure 6.8.** EDX analysis of particles on the fracture surface caused by stable FCP of unreinforced PA66 notched specimens.

Figure 6.9 shows the analysis of the degree of fiber-matrix adhesion for different fiber volume fractions. Fracture in composite materials can be either cohesive or adhesive depending upon whether a layer of matrix adheres to the fibers or not. The fibers shown in Figure 6.9 are completely covered by a resin layer. This experimental evidence indicates that damage occurs in form of matrix cracking at a certain distance from the interface. Accordingly, for the material system and the testing conditions analyzed in this work, damage mechanisms in the resin layer covering the fibers should be taken into account in a lifetime prediction model while fiber-matrix debonding should be excluded.



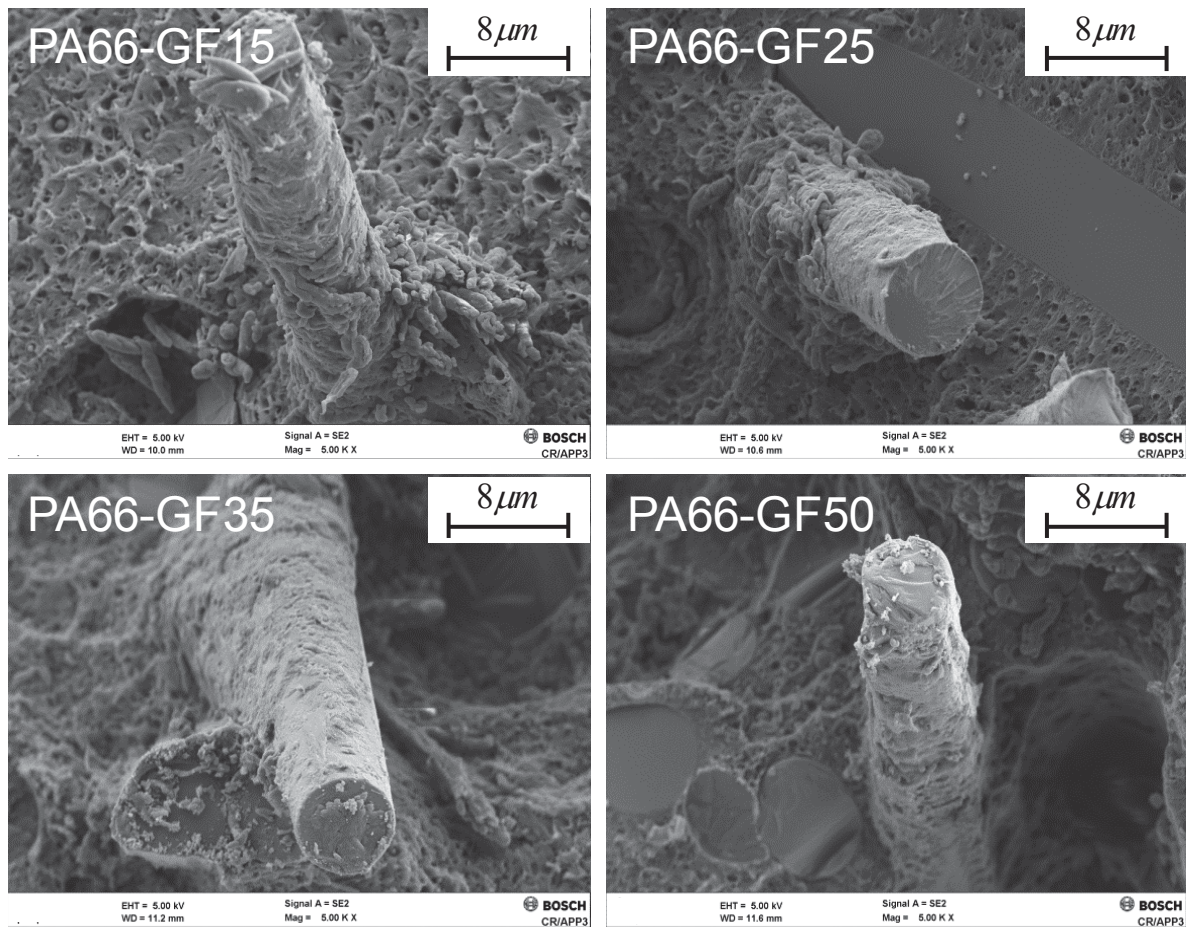


Figure 6.9. Analysis of the fiber-matrix adhesion on the fracture surface near the notch.

## 6.5. Conclusions

The effect of the fiber volume fraction on the fatigue behavior and the damage mechanisms of a short glass fiber reinforced polyamide were studied in this paper. Specimens with molded notch were used in order to reproduce the fiber orientation at structural discontinuities in real injection molded parts. An increase in fiber content improves both the fatigue strength to crack initiation and to failure of the composite material. The relative contribution of the crack propagation to the total lifetime increases with increasing fiber volume fraction. The results of the damage investigation are summarized according to the length-scale at which the analysis was performed.

*Macro-scale:* Fatigue failure of notched specimens occurs in three phases: crack initiation, stable FCP, unstable FCP. The fracture surface caused by stable FCP can be identified with

unaided eye. In fact, it is stress whitened and smoother than the fracture surface caused by unstable FCP.

*Meso-scale:* The crack path is strongly influenced by the fiber volume fraction. With high fiber contents, fibers tend to agglomerate forming clusters deviating the crack plane more effectively than isolated fibers and thereby reducing the crack propagation rate.

*Micro-scale:* At this scale, the following fractographic features were studied: matrix fracture behavior (ductile/brittle), fiber failure/pull-out, degree of the fiber-matrix interfacial adhesion.

- *Matrix fracture behavior:* The degree of matrix ductility observed on the fracture surface caused by stable FCP in the unfilled polyamide is higher compared to reinforced polyamides. The fracture surface of short glass fiber reinforced polyamide specimens show similar micro-ductile matrix behavior independently of the fiber volume fraction.
- *Fiber failure/pull-out:* Fiber pull-out is dominant compared to fiber failure. Fiber failure was found to be more relevant for higher fiber volume fractions.
- *Degree of fiber-matrix interfacial adhesion:* The analysis of fracture surface near the notch revealed that the fibers are completely covered by a resin layer. This result indicates that damage occurs in form of matrix-cracking at a certain distance from the interface.

Lastly, the analysis of the fracture surface revealed evidence of matrix cavitation around particles irrespective of whether the material is reinforced or not. A preliminary EDX analysis revealed aluminum oxide particles on the fracture surface of unreinforced polyamide specimens. Instead no clear understanding of the particles on the fracture surface of short glass fiber reinforced polyamide specimens was achieved.

## References of Chapter 6

[1] M. De Monte, E. Moosbrugger, M. Quaresimin, Influence of temperature and thickness on the off-axis behaviour of short glass fibre reinforced polyamide 6.6 – Quasi-static loading, Composites Part A: Applied Science and Manufacturing. 41 (2010) 859-871.

[2] M. De Monte, E. Moosbrugger, M. Quaresimin, Influence of temperature and thickness on the off-axis behaviour of short glass fibre reinforced polyamide 6.6 – cyclic loading, Composites Part A: Applied Science and Manufacturing. 41 (2010) 1368-1379.

- [3] M. De Monte, M. Quaresimin, P. Lazzarin, Modelling of fatigue strength data for a short fiber reinforced polyamide 6.6 based on local strain energy density. Proceedings of ICCM16, 16th International Conference on Composite Materials (2007).
- [4] M. De Monte, E. Moosbrugger, K. Jaschek, M. Quaresimin, Multiaxial fatigue behaviour of a short-fibre reinforced polyamide 6.6 in the presence of notches. ECCM - 13th European Conference on Composite Materials (2008).
- [5] M. De Monte, E. Moosbrugger, K. Jaschek, M. Quaresimin, Multiaxial fatigue of a short glass fibre reinforced polyamide 6.6 – Fatigue and fracture behaviour, Int. J. Fatigue. 32 (2010) 17-28.
- [6] M. Pierantoni, M. De Monte, D. Papathanassiou, N. De Rossi, M. Quaresimin, Viscoelastic material behaviour of PBT-GF30 under thermo-mechanical cyclic loading, Procedia Engineering. 10 (2011) 2141-2146.
- [7] A. Schaaf, M. De Monte, E. Moosbrugger, M. Vormwald, M. Quaresimin, Life estimation methodology for short fiber reinforced polymers under thermo-mechanical loading in automotive applications, Materialwissenschaft und Werkstofftechnik. 46 (2015) 214-228.
- [8] S. Mortazavian, A. Fatemi, Fatigue behavior and modeling of short fiber reinforced polymer composites: A literature review, Int. J. Fatigue. 70 (2015) 297-321.
- [9] C.M. Sonsino, E. Moosbrugger, Fatigue design of highly loaded short-glass-fibre reinforced polyamide parts in engine compartments, Int. J. Fatigue. 30 (2008) 1279-1288.
- [10] E. Belmonte, M. De Monte, C. Hoffmann, M. Quaresimin, Damage mechanisms in a short glass fiber reinforced polyamide under fatigue loading, to appear.
- [11] K. Friedrich, R. Walter, H. Voss, J. Karger-Kocsis, Effect of short fibre reinforcement on the fatigue crack propagation and fracture of PEEK-matrix composites, Composites. 17 (1986) 205-216.
- [12] W.J. Evans, D.H. Isaac, K.S. Saib, The effect of short carbon fibre reinforcement on fatigue crack growth in PEEK, Composites Part A: Applied Science and Manufacturing. 27 (1996) 547-554.



- [13] H. Voss, J. Karger-Kocsis, Fatigue crack propagation in glass-fibre and glass-sphere filled PBT composites, *Int. J. Fatigue*. 10 (1988) 3-11.
- [14] A. Pegoretti, T. Riccò, Fatigue crack propagation in polypropylene reinforced with short glass fibres, *Composites Sci. Technol.* 59 (1999) 1055-1062.
- [15] E. Belmonte, E. Moosbrugger, N. De Rossi, M. De Monte, M. Quaresimin, Life to crack initiation in notched specimens of unreinforced and short fiber reinforced polyamide under fatigue loading, to appear.
- [16] J.L. Thomason, The influence of fibre length, diameter and concentration on the impact performance of long glass-fibre reinforced polyamide 6,6, *Composites Part A: Applied Science and Manufacturing*. 40 (2009) 114-124.
- [17] J.L. Thomason, The influence of fibre properties of the performance of glass-fibre-reinforced polyamide 6,6, *Composites Sci. Technol.* 59 (1999) 2315-2328.
- [18] A. Bernasconi, F. Cosmi, Analysis of the dependence of the tensile behaviour of a short fibre reinforced polyamide upon fibre volume fraction, length and orientation, *Procedia Engineering*. 10 (2011) 2129-2134.
- [19] J.L. Thomason, Micromechanical parameters from macromechanical measurements on glass reinforced polyamide 6,6, *Composites Sci. Technol.* 61 (2001) 2007-2016.
- [20] A. Bernasconi, P. Davoli, A. Basile, A. Filippi, Effect of fibre orientation on the fatigue behaviour of a short glass fibre reinforced polyamide-6, *Int. J. Fatigue*. 29 (2007) 199-208.
- [21] S. Mortazavian, A. Fatemi, Effects of fiber orientation and anisotropy on tensile strength and elastic modulus of short fiber reinforced polymer composites, *Composites Part B: Engineering*. 72 (2015) 116-129.
- [22] S. Mortazavian, A. Fatemi, Fatigue behavior and modeling of short fiber reinforced polymer composites including anisotropy and temperature effects, *Int. J. Fatigue*. 77 (2015) 12-27.

- [23] M.F. Arif, N. Saintier, F. Meraghni, J. Fitoussi, Y. Chemisky, G. Robert, Multiscale fatigue damage characterization in short glass fiber reinforced polyamide-66, *Composites Part B: Engineering*. 61 (2014) 55-65.
- [24] A. Bernasconi, P. Davoli, C. Armani, Fatigue strength of a clutch pedal made of reprocessed short glass fibre reinforced polyamide, *Int. J. Fatigue*. 32 (2010) 100-107.
- [25] A. Avanzini, G. Donzella, D. Gallina, Fatigue damage modelling of PEEK short fibre composites, *Procedia Engineering*. 10 (2011) 2052-2057.
- [26] M.G. Wyzgoski, G.E. Novak, Fatigue fracture of nylon polymers: Part II. Effect of glass-fibre reinforcement, *Journal of Materials Science*. 26 (1991) 6314-6324.
- [27] G. Meneghetti, M. Quaresimin, Fatigue strength assessment of a short fiber composite based on the specific heat dissipation, *Composites Part B: Engineering*. 42 (2011) 217-225.
- [28] J.F. Mandell, D.D. Huang, F.J. McGarry, Crack propagation Modes in Injection Molded Fiber Reinforced Thermoplastics, in: *Short Fiber Reinforced Composite Materials*, B.A. Sanders, Philadelphia, 1982, pp. 3-32.
- [29] J.W. Dally, D.H. Carrillo, Fatigue behavior of glass-fiber fortified thermoplastics, *Polymer Engineering & Science*. 9 (1969) 434-444.
- [30] K. Friedrich, Microstructure and fracture mechanical properties of short fiber reinforced thermoplastic P.E.T., *Colloid and Polymer Science*. 259 (1981) 808-811.
- [31] K. Tanaka, T. Kitano, N. Egami, Effect of fiber orientation on fatigue crack propagation in short-fiber reinforced plastics, *Eng. Fract. Mech*. 123 (2014) 44-58.
- [32] K. Friedrich, R. Walter, H. Voss, J. Karger-Kocsis, Effect of short fibre reinforcement on the fatigue crack propagation and fracture of PEEK-matrix composites, *Composites*. 17 (1986) 205-216.
- [33] R.W. Lang, Roughness-induced crack closure in short fibre-reinforced plastics, *Journal of Materials Science Letters*. 4 (1985) 1391-1396.

[34] R.W. Hertzberg, *Deformation and Fracture Mechanics of Engineering Materials*, 3rd ed., New York, 1989.

[35] R.W. Lang, J.A. Manson, R.W. Hertzberg, Mechanisms of fatigue fracture in short glass fibre-reinforced polymers, *Journal of Materials Science*. 22 (1987) 4015-4030.



## **Chapter 7**

# **Local microstructure and stress distributions at the crack initiation site in a short fiber reinforced polyamide under fatigue loading**

**Keywords:** Short Fiber Reinforced Composites, Damage Mechanisms, Fatigue, Polyamide, Micro-tomography

### **Abstract**

This work aims to study the influence of the fiber distribution on the damage onset in a short glass fiber reinforced polyamide under fatigue loading. A fatigue test of a notched specimen was interrupted at crack initiation, then a small sample around the notch was machined from the specimen and analyzed by means of X-Ray Computed Tomography (X-Ray CT) for the quantitative description of the fiber distribution. The real microstructure was reconstructed and then simulated in the Finite Element Method (FEM) code ABAQUS. The analysis gives an insight into the typical local matrix stress distributions at the notch tip.

### **7.1. Introduction**

Short Fiber Reinforced Plastics (SFRPs) are extensively used in the automotive industry as load bearing materials. Major advantages are offered by the injection molding technology in terms of design of complex geometries, high production output rates, low production waste, good reproducibility. The increasingly use of these materials in structural applications has driven the development of lifetime prediction models. The advantage of using predictive models is that lifetime estimation is possible in the design phase of the product project, thus reducing the number of prototypes before the series production. Accurate lifetime prediction models depend on their ability to reproduce the damage mechanisms which lead to material failure. Nowadays, the improvement of the investigation techniques enables a deeper understanding of the damage mechanisms. In addition, with the increase in computational power, it is possible to model the observed damage mechanisms and to integrate them in a

lifetime prediction model. In [1, 2] the authors investigated the damage mechanisms in short glass fiber reinforced polyamide under fatigue loading using specimens with molded notch.

It was found that the crack initiation position is not at the notch tip as for homogenous materials but at clusters of through-the-thickness oriented fibers located around the notch. In this paper, the real microstructure around the notch was investigated by means of X-Ray CT and simulated using a FEM software with the aim to investigate the local matrix stress distributions at crack initiation.

The microstructure of SFRPs is characterized by three variables: fiber volume fraction, fiber aspect ratio and fiber orientation. Only fiber volume fraction is known beforehand. Fiber aspect ratio and fiber orientation depend on many factors such as process parameters, mold geometry, fiber volume fraction. Typically, the influence of the fiber orientation on the mechanical behavior of SFRPs has been studied by machining specimens from an injected plate at different orientations with respect to the Mold Flow Direction (MFD) [3-12]. In the mentioned works, the fiber orientation is assumed constant and corresponds to the angle between the longitudinal axis of the specimen and the MFD. However, even for plain specimens, fiber orientation has a complex structure since it varies through the specimen thickness. Close to the surface of the specimen, fibers are well aligned to the MFD, whereas at the mid-plane region, fibers are aligned transversely to the MFD. This structure is better known by the name shell-core where shell indicates the material layer adjacent to the specimen surfaces, and core indicates the layer at the middle thickness. This effect is to be ascribed to the dynamics of the melt flow and makes the material characterization for well defined fiber orientations difficult if not impossible. De Monte et al. [9, 10] showed that for specimens milled out from injection molded plates, the higher the specimen thickness, the larger the core layer is with an increasing isotropic response both under quasi-static and fatigue loading. Hine et al. [13] reported that the thickness of the shell and core layers is not constant in an injection molded transverse ribbed plate but varies along the injection direction. In real injection molded parts, geometric discontinuities within the mold make the fiber orientation distribution even more complex. They represent in fact, from a fluid-dynamic point of view, locations where the melt flow changes direction and from a structural point of view, typical areas for crack initiation [14, 15]. Hence, the study of the fiber orientation distribution at potentially critical locations such as geometric discontinuities is considered to be highly relevant for the lifetime prediction of real injection molded parts. Testing hollow plain tubular specimens under multiaxial (tension + torsion) fatigue loading, De Monte and

coworkers [16] observed cracks within the specimen thickness where fibers are transversely oriented with respect to the loading direction. In another work, De Monte and coworkers [17] compared the torsional fatigue strength of hollow plain tubular specimens, hollow tubular specimens with molded V-shaped notch ( $R_{\text{notch}} = 0.2 \text{ mm}$ ), and hollow tubular specimens with drilled hole ( $R = 1 \text{ mm}$ ). They found that in the first two cases the torsional fatigue strength is similar. Instead, specimens with drilled hole exhibited lower torsional fatigue strength even though the stress concentration in this case is lower than that of V-shaped notch. This result can be explained as an effect of the local microstructure at the crack initiation site. Bernasconi and coworkers [18] investigated the fatigue behavior of rectangular PA6-GF30 specimens characterized by lateral molded notches ( $R = 7.5 \text{ mm}$ ) varying the position of the injection gate. Specimens were injected either longitudinally or laterally. The fatigue strength of laterally injected specimens was found to be lower than that of longitudinally injected specimens. Nevertheless, they reported similar fiber orientation distributions at the notch tips in the two cases. As a continuation of this work, Bernasconi and coworkers [19] investigated the fiber orientation at the notch tip of longitudinally injected specimens for three different notch geometries ( $R = 0.5, 1.0 \text{ and } 2.0 \text{ mm}$ ) reporting a significant decrease of the fiber alignment in the longitudinal direction only for the sharpest notch ( $R = 0.5 \text{ mm}$ ).

Over the last decade, new methods were developed to analyze the fiber orientation distribution. An established technique is based on the analysis by means of optical or electron microscopy of the footprints left by the fibers on a polished section [20, 21]. Nowadays, this method is largely applied due to the easy set-up but allows the analysis of the fiber orientation distribution on a single section. Inaccuracies in measurement may arise when the fibers cross the plane almost perpendicularly. In this case, small ellipticity changes of the footprints result in a strong variation of the measured angles [22].

The use of the X-Ray CT has been on the rise in recent years. This technique, although it requires an expensive facility, enables a three dimensional description of the microstructure without the need of polishing the sample. Unlike the optical method, X-Ray CT does not need the destruction of the sample which can be thus analyzed a second time. However, in order to reach high resolution, a small sample has to be machined from a specimen / part. X-Ray CT can be thus considered a semi-destructive method. The continuous improvement of this investigation technique in terms of resolution and image contrast provides support for the investigation of the damage mechanisms [23-25].



This paper is organized as follows: In Section 7.3.1, the quantitative description of the microstructure around a molded notch is presented. For this purpose, a sample surrounding the notch tip and containing a crack propagated due to fatigue loading was analyzed by means of X-Ray CT. In Section 7.3.2 a procedure for the reconstruction of the volume analyzed by means of X-Ray CT is described and the local stress distributions around the notch are studied with the FEM software ABAQUS (Version 6.11/Standard) [26].

A step-wise approach would have required to separate the effects of the notch (stress gradient) and the fiber orientation. However, they are intrinsically linked to each other. As observed in [1], the possibility to study the crack path is limited to notched specimens. For plain specimens, a distinction between crack initiation and final failure is usually not possible. The present analysis aims to study the microscopic matrix stress distribution in a case representative of real injection molded parts and therefore represents a preliminary step for the development of a multi-scale lifetime prediction model for SFRPs.

## 7.2. Experimental

### 7.2.1. Material system

The material studied in the present investigation is a short glass fiber reinforced polyamide containing 35 wt. % glass fibers (designation PA66-GF35). The dimensions of the specimen are shown in Figure 7.1.

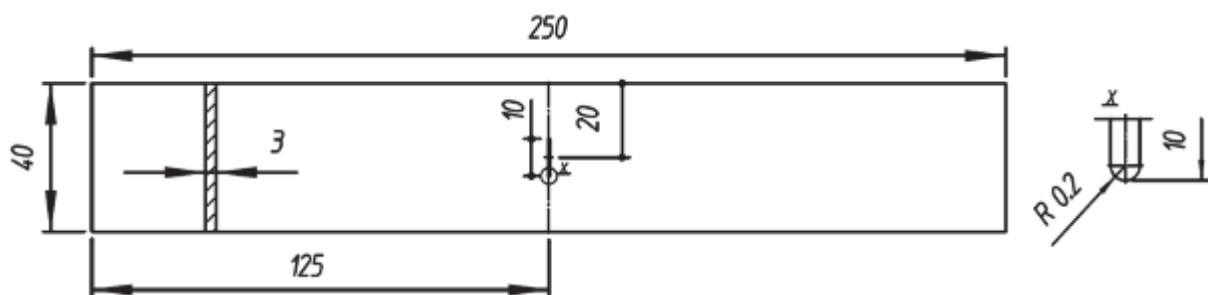


**Figure 7.1.** Specimen geometry and dimensions (in mm).

The specimen was injected along the longitudinal axis. The notch is molded-in and not machined after injection molding. This configuration is typical of the real injection molded parts where all the geometrical discontinuities are already within the mold in order to avoid post-molding machining operations. Some of the fatigue tests on notched specimens

performed in [1] were interrupted to study the fatigue damage mechanisms along the crack path. One of the specimens used for these tests was investigated by means of X-Ray CT with the aim to quantitatively analyze the fiber orientation distribution around the notch, at crack initiation. The testing parameters used in this case are: ( $\sigma_a = 23$  MPa;  $N_{\text{interruption}} = 71000$  Cycles;  $f = 20$  Hz, room temperature and humidity). When the test was interrupted, two cracks of circa 0.4 mm length were observed at the notch tips. A sample surrounding one of the two notch tips was machined from the specimen and analyzed by means of X-Ray CT (Figure 7.2). The dimensions of the analyzed sample are (1.2 x 1.2 x 3 mm). A smaller volume (0.41 x 0.36 x 0.21 mm), extracted from the machined sample at the middle thickness was reconstructed in the FEM software (ABAQUS/CAE).

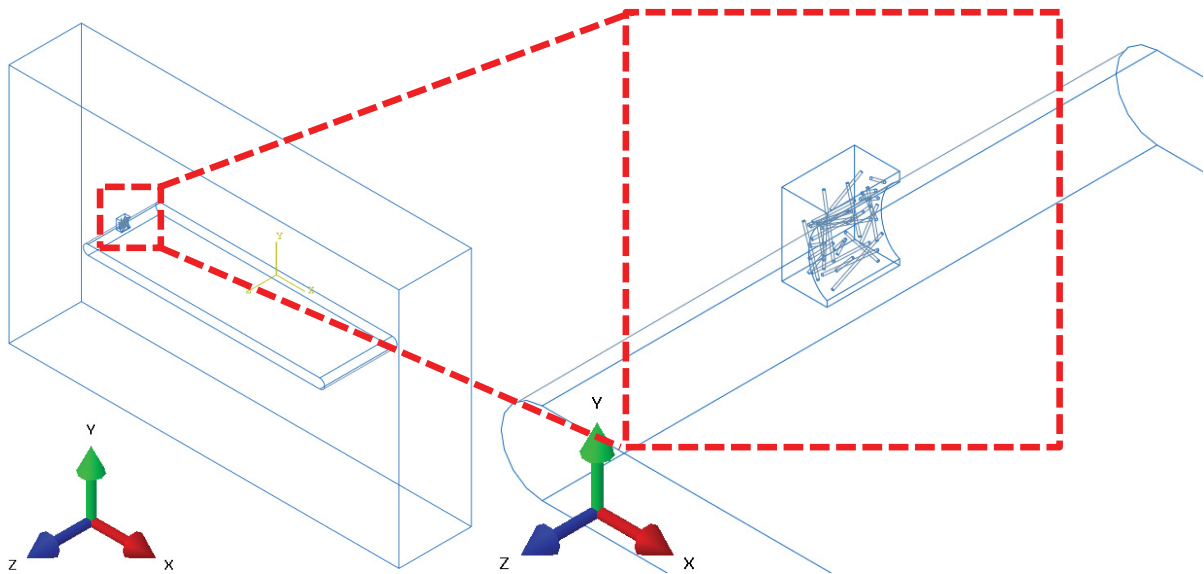


Figure 7.2. Location of the volume analyzed by means of X-Ray CT.

## 7.2.2. X-Ray Computed Tomography

A phoenix v|tome|x s 3D computed tomography system was used. The scans were carried out with these parameters: Tube voltage: 80 kV, Current intensity: 190  $\mu$ A, Integration time 1600 ms. The three-dimensional volume is obtained by stacking a set of CT slices. A standard PC with a videocard AMD Radeon HD7900 was used. The sample was rotated by 360°. The number of the projections which compose the volume is 720. Pixels are cubics. Pixel pitch is 200 $\mu$ m. One picture is composed by 1000 x 1000 pixels which become 2000 x 1000 due to the shift of the detector. The X-Ray CT device is equipped with a high dynamic temperature-

stabilized GE DXR digital detector with 30 frames per second. X-Ray CT resolution is 1.6  $\mu\text{m}$  (voxel edge size). The software VGStudio Max 2.2 of the company Volume Graphics was used for the analysis of the X-Ray CT dataset. The algorithm for the quantitative analysis of the fiber distribution is based on the grey value analysis. With this technique, the fibers are identified since they have a higher image contrast than the matrix. The threshold grey value between matrix and fibers was set by the operator. The choice of this threshold value aims to reproduce the global fiber fraction and the single fibers as they look like. For example, a too high threshold value would lead to too thin fibers. Such algorithms are not limited to the identification of the fibers but can also be used to distinguish other bodies in the material volume. The method implemented by the company Volume Graphics for the analysis of the fiber orientation was validated by Riedel in [27].

## **7.3. Results and discussion**

### **7.3.1. Quantitative analysis of the fiber distribution around the notch**

Figure 7.3 shows the fiber orientation plotted as color-coded overlay on the real material microstructure. The y-axis is the reference axis. The MFD is aligned to the y-axis but in the opposite direction. Off-axis fibers are oriented either in the x- or z-axis. In [1] it was found that crack initiates at clusters of fibers oriented in the through-the-thickness direction which corresponds to the z-axis in Figure 7.3. On the right side of Figure 7.3 the fiber orientation distribution around the notch tip is shown. A mix of longitudinally and through-the-thickness oriented fibers can be noticed. Even if the specimen was injected in the longitudinal direction, not all the fibers around the notch are aligned in the MFD. This result suggests that a more thorough investigation of the fiber orientation distribution should be carried out.

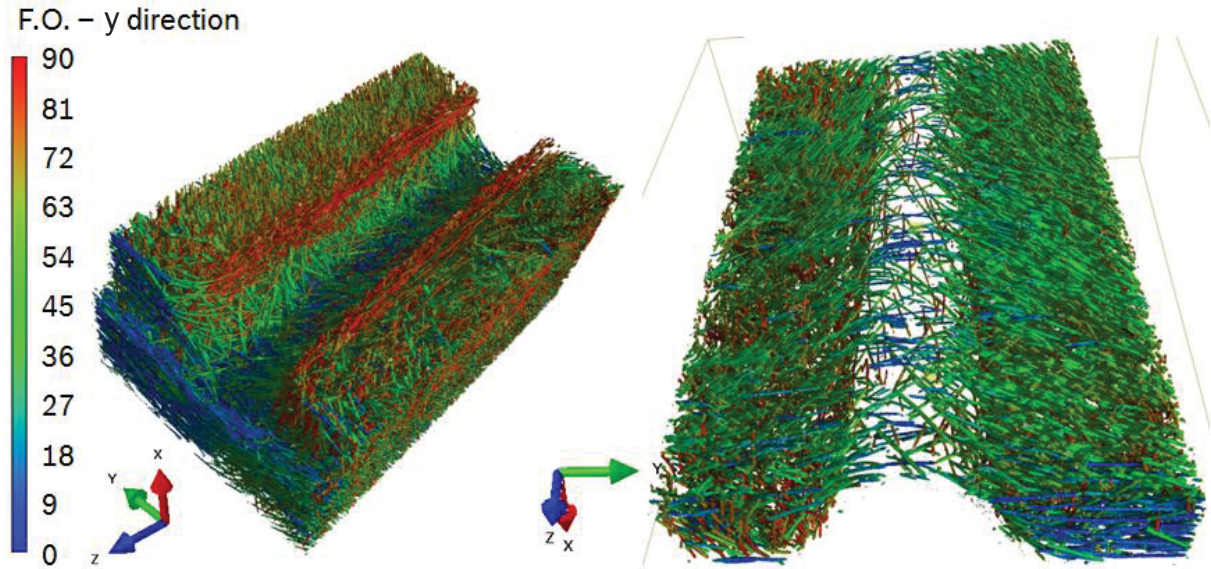


**Figure 7.3.** Fiber orientation distribution in the material volume analyzed by means of X-Ray CT.

The sample shown in Figure 7.3 was discretized into cubic elements (Figure 7.4) for the quantitative analysis of the fiber orientation distribution in such a way that all the components of the Fiber Orientation Tensor (FOT) are equally weighted. The number of elements and the element dimension for each analysis are reported in Table 7.1.

**Table 7.1.** Number of elements used in the quantitative analysis of the fiber distribution by means of X-Ray CT.

Analysis	N° of elements	Element size (mm)
1x1x1	1	1.2
2x2x2	8	0.6
4x4x4	64	0.3
8x8x8	512	0.15

In Figure 7.4, the values of the fiber content for each element are displayed as color-coded overlays on the X-Ray CT micrographs. The average second order FOT calculated by the software in each element can be geometrically represented as an ellipsoid. The ellipses observed within the elements are the projections on the x-y plane of these ellipsoids. The principal axes of the ellipsoids correspond to the eigenvectors of the tensor. The major axis indicates the main fiber orientation in the corresponding element. The orientation of the

ellipsoids shown in Figure 7.4 reproduces the curved path of the melt flow around the notch. Since only the projections of the ellipsoids on the x-y plane are shown, the magnitude of eigenvectors aligned in the z-axis (thickness direction) are not visible in Figure 7.4 but will be analyzed later on in this paper. The aim of the quantitative analysis of the fiber orientation distribution by means of X-Ray CT is to investigate how fine the discretization should be to capture local microstructural effects at the notch tip (such as clusters of through-the-thickness oriented fibers).

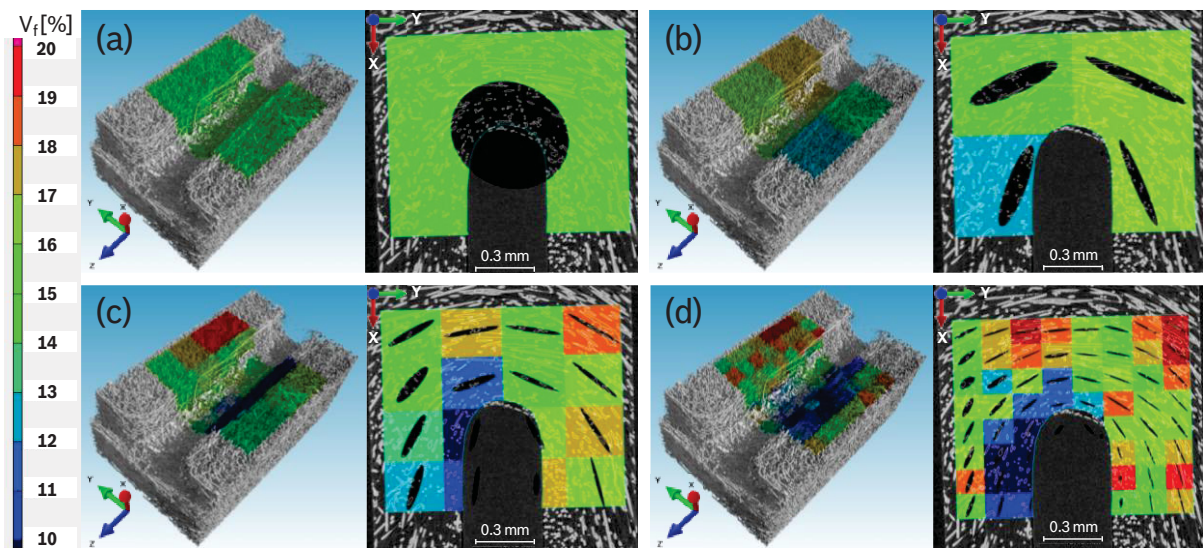


**Figure 7.4.** Discretization of the analyzed volume; (a) One single element of length 1.2 mm; (b) 8 elements of length 0.6 mm; (c) 64 elements of length 0.3 mm; (d) 512 elements of length 0.15 mm.

The one element analysis is shown in Figure 7.4a. The software provides the average FOT and fiber volume fraction over the whole volume. The FOT is almost two-dimensional ( $a_{xx} = 0.40$ ;  $a_{yy} = 0.44$ ;  $a_{zz} = 0.16$ ). The through-the-thickness component is lower than the other two diagonal components. The evaluation of the fiber volume fraction ( $V_f$ ) gives  $V_f = 15\%$  which is lower than the nominal value  $V_f = 19.7\%$ . However, the fiber volume fraction strongly depends on the threshold grey value set to distinguish between fibers and matrix. The curved path of the plastic molten flow is already noticeable in the  $2 \times 2 \times 2$  discretization scheme. Figure 7.4b also shows that the elements at the left side of the notch are characterized by lower fiber content when compared with the elements at the right side. The reason is that the MFD is parallel to the y-axis but in the opposite direction. As the melt front approaches the insert, it splits into separated streams which rejoin after the notch leading to a



weld line. The majority of the fibers are pushed toward the end of the mold cavity leaving the region immediately downstream of the notch with fewer fibers. The 4 x 4 x 4 discretization and especially the 8 x 8 x 8 discretization results in a more accurate description of the local fiber distribution around the notch.

Figure 7.5 shows the analysis of the three diagonal components of the FOT and the fiber volume fraction for six sections along the thickness. The fiber orientation distribution is planar (x-y plane) with the exception of the layer surrounding the notch (see Figure 7.5, first row,  $a_{zz}$ ). Here, high values of the  $a_{zz}$  component are observed. The occurrence of through-the-thickness oriented fibers at the notch tip is particularly relevant since this region corresponds to the crack initiation site. The distribution of the  $a_{yy}$  and  $a_{xx}$  are complementary to each other reflecting the curvature of the melt flow around the insert.

Figure 7.5 shows that fiber volume fraction varies in each element of the discretization. The maximum variation of the fiber volume fraction is by a factor 3. Fiber rich zones alternate with matrix rich zones without a precise scheme except for the elements downstream of the notch which are characterized by a lower fiber volume fraction. Examining the layer surrounding the curved part of the notch (see Figure 7.5, first row,  $V_f$ ), for the six sections along the specimen thickness shown in Figure 7.5, the fiber volume fraction varies by almost a factor 2 having a minimum value of 10.8 % and a maximum value of 17.7 %. The average value is 12.95 %, lower than the average fiber volume fraction over the entire analyzed volume.



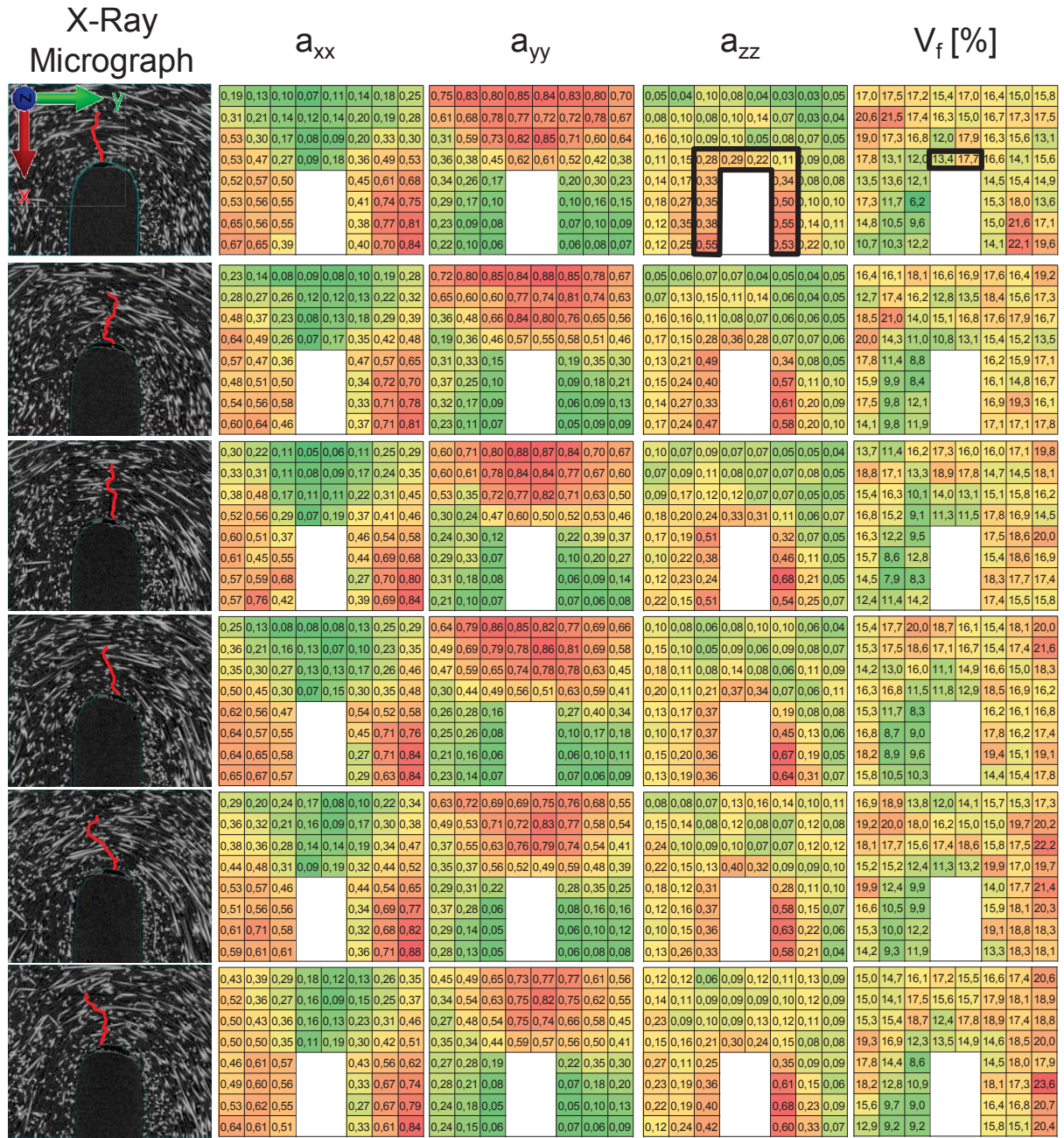
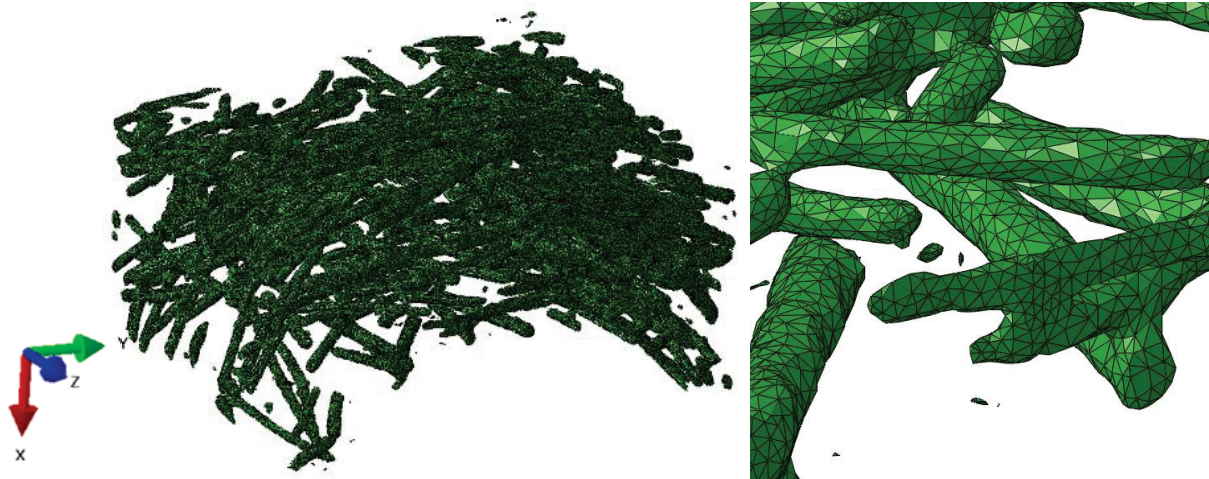


Figure 7.5. Analysis of the fiber orientation distribution and fiber content; 8 x 8 x 8 discretization.

## 7.3.2 Reconstruction of the material volume in the FEM Software ABAQUS

### 7.3.2.1. Geometry

A commercial software (Simpleware ScanIP [28]) was used for the automatic conversion of the X-Ray CT dataset into a solid mesh to import in a FEM software. Other examples of solid model generation from X-Ray CT datasets are reported in [29, 30]. In our case, this approach has shown some limitations illustrated in Figure 7.6. As reported in Section 7.2.2, the software for the analysis of the X-Ray CT dataset is based on the grey gradient. Artifacts in the X-Ray CT datasets likely due to material impurities which show a similar contrast as the fibers are included in the geometry creation (Figure 7.6 - right side). Moreover, if the fibers are close to each other, the software considers them as attached, leading to the formation of structures which are not characteristic of the real microstructure (Figure 7.6 – right side). Lastly, the shape of the fibers is not cylindrical but more irregular further complicating the geometry.



**Figure 7.6.** Reconstruction of the X-Ray CT data-set using the software Simpleware ScanIP.

Figure 7.7 illustrates why some fibers after reconstruction by the software are attached to each other. For example, if one looks at the fibers n°1 and n°2 in Figure 7.7a, they are really close to each other. Figure 7.7b shows the pixel distribution on the picture. Between the fibers and the matrix, the grey value varies gradually. If the fibers are too close to each other, the grey values of the pixels in the narrow space between the fibers may not be in matrix range. Hence,

the software cannot distinguish between two separated bodies. A possible solution of this problem would be the increase of the analysis resolution which is however not compatible with the available X-Ray CT.

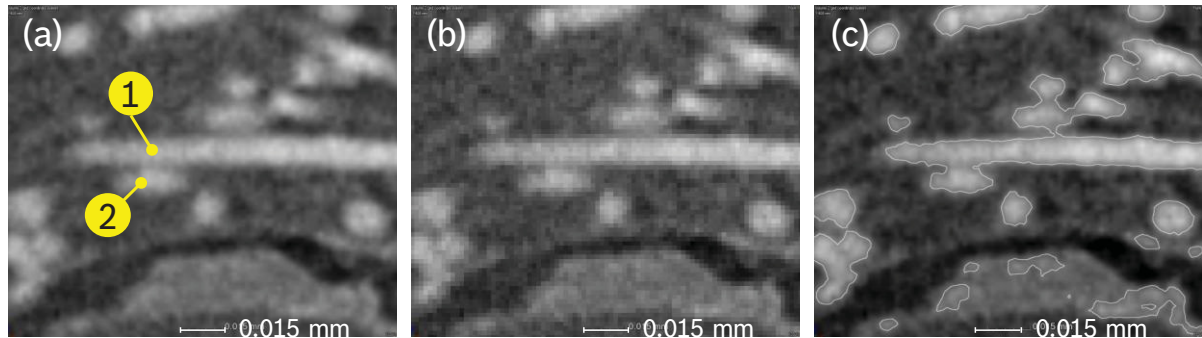


**Figure 7.7.** Detection of the fibers based on the grey values; (a) X-Ray CT picture; (b) Pixel distribution; (c) Grey gradient based fiber detection.

In order to overcome the limitations of the automatic reconstruction method, we propose just for this detailed investigation, a manual procedure to model the fibers. For each considered fiber, the operator identified the spatial coordinates of the fiber ends using the software dedicated to the analysis of the X-Ray CT dataset. Each fiber was modeled as a cylinder extruding a circle of diameter  $10\ \mu\text{m}$  (fiber diameter) along a straight path defined by the spatial coordinates of the fiber ends. The fibers showing a noticeable curvature were modeled by sweeping the circle along a spline joining multiple points extrapolated along the curved fiber axis. One example is the fiber n°5 in Figure 7.8. The numeration of the fibers shown in Figure 7.8 will be kept the same in the following pictures. To speed up the procedure, a python script was created. 50 fibers were modeled within the sub-volume of interest. The number of fibers in the material volume does not meet the requirements of the numerical homogenization but aims to describe and investigate the matrix stress distribution in the damaged zone. The matrix solid model was created extruding along the thickness a sketch including the notch profile and large enough to incorporate all the considered fibers. The two solid models (matrix and fibers) were merged together in ABAQUS/CAE retaining the intersecting boundaries. The reconstructed material volume does not represent an RVE because it does not meet the requirement of reproducing the effective material properties. From another perspective, the scale separation law is not respected; the average length of the fibers ( $l_f = 0.280\ \text{mm}$ ) is in fact almost equal to the notch radius ( $R_{\text{notch}} = 0.2\ \text{mm}$ ).



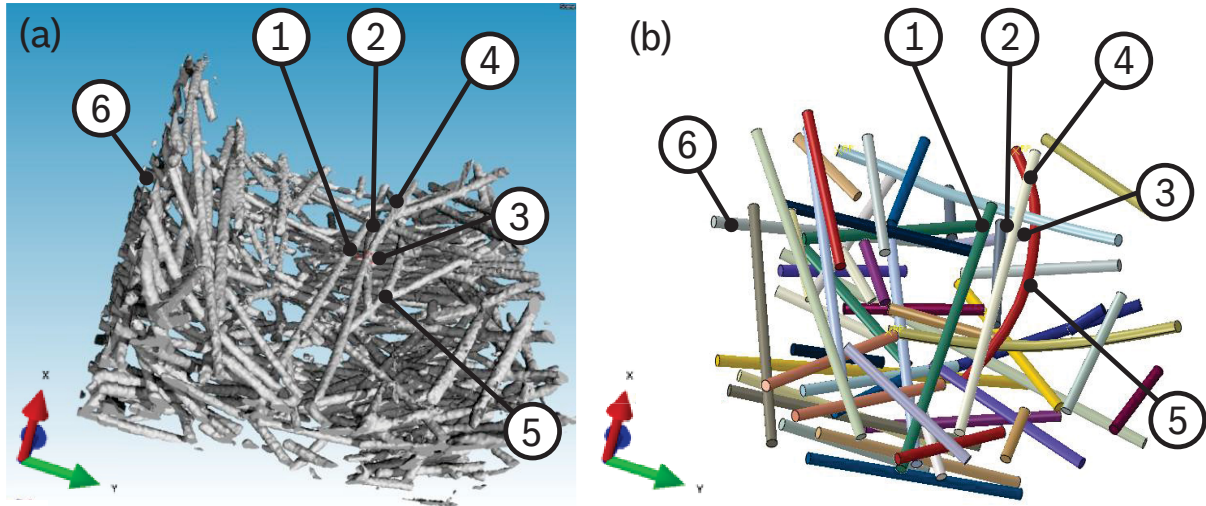


**Figure 7.8.** (a) Volume analyzed with X-Ray CT; (b) Volume reconstructed in ABAQUS/CAE.

### 7.3.2.2. Boundary conditions and mesh

The submodeling technique was used to assign the boundary conditions to the analyzed volume. A linear elastic simulation of the entire specimen was performed to calculate the global displacement distribution (Figure 7.9a). The software DIGIMAT-MF [31] was used to create a linear elastic material model homogenizing the elastic properties of glass fibers and pure resin. The material properties adopted for the constituents are reported in [9]. The software DIGIMAT-MAP [31] was used to map the FOTs calculated with the software MOLDFLOW [32] onto the structural mesh created in ABAQUS. The homogenized elastic properties depend on the local fiber orientation. The nodes on the bottom face of the specimen were constrained in all directions while uniform pressure, equal to 1 MPa was applied to the top surface. Because of the large dimension difference between the global model and the reconstructed volume, it was decided to add another submodel as intermediate step with the same material properties of the global model (Figure 7.9b). The displacements derived by the first sub-model were finally applied to the reconstructed volume. In this last step (Figure 7.9c), the constituents (fibers and matrix) were modeled as isotropic, linear elastic materials. It is worthwhile noting that the global model and the first sub-model are homogeneous while in the second sub-model is heterogeneous since fibers and matrix are explicitly modeled. In first approximation, perfect fiber-matrix bonding was assumed also between the fibers ends and the matrix where no adhesion is expected. In fact, during the

injection molding process, the fibers which are subjected to sizing treatment in order to improve the fiber-matrix adhesion, are broken up in shorter parts. The ends of these shorter fibers are new surfaces not covered by sizing. The mesh contains 60330 C3D8 elements for the global model, 528000 C3D8 elements for the first sub model and 1758635 C3D10 elements for the reconstructed volume. While mapped meshes with hexahedral elements were used for the global model and the first sub model, a mesh with tetrahedron elements was used for the reconstructed model due to the presence of the fibers in the material volume which lead to a more complex geometry. In the reconstructed model, the element size is 5.95E-003 mm.

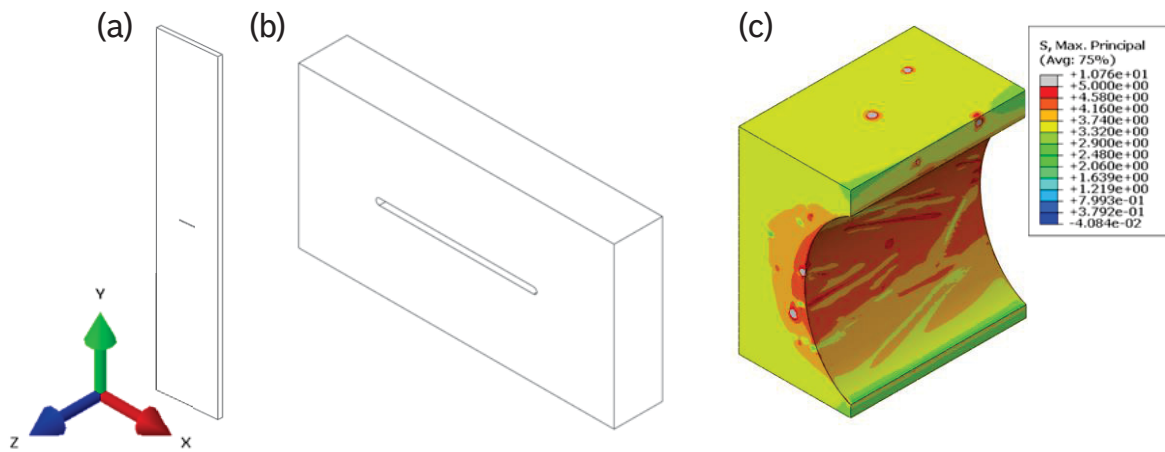
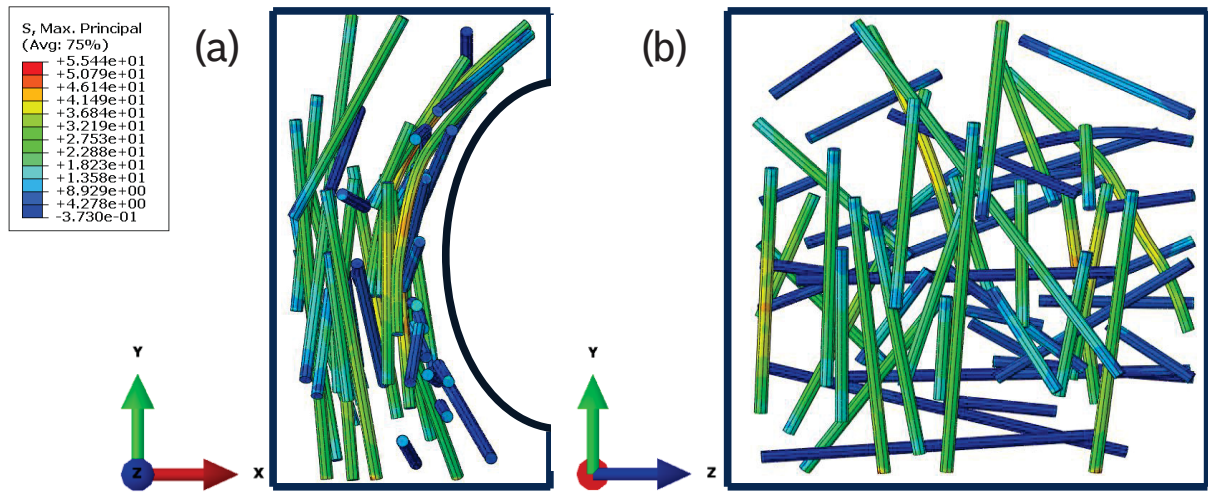


Figure 7.9. (a) Global model; (b) First sub model; (c) Reconstructed model.

### 7.3.2.3. Analysis of the results

Figure 7.10 shows the distribution of the maximum principal stress in the fibers. Fibers aligned in the loading direction (y-axis) undergo, on average, higher stresses than those aligned either to x- or z-axis. In fact, longitudinally oriented fibers carry the load transferred by the matrix leading to an increase of the Young's Modulus of the composite material.

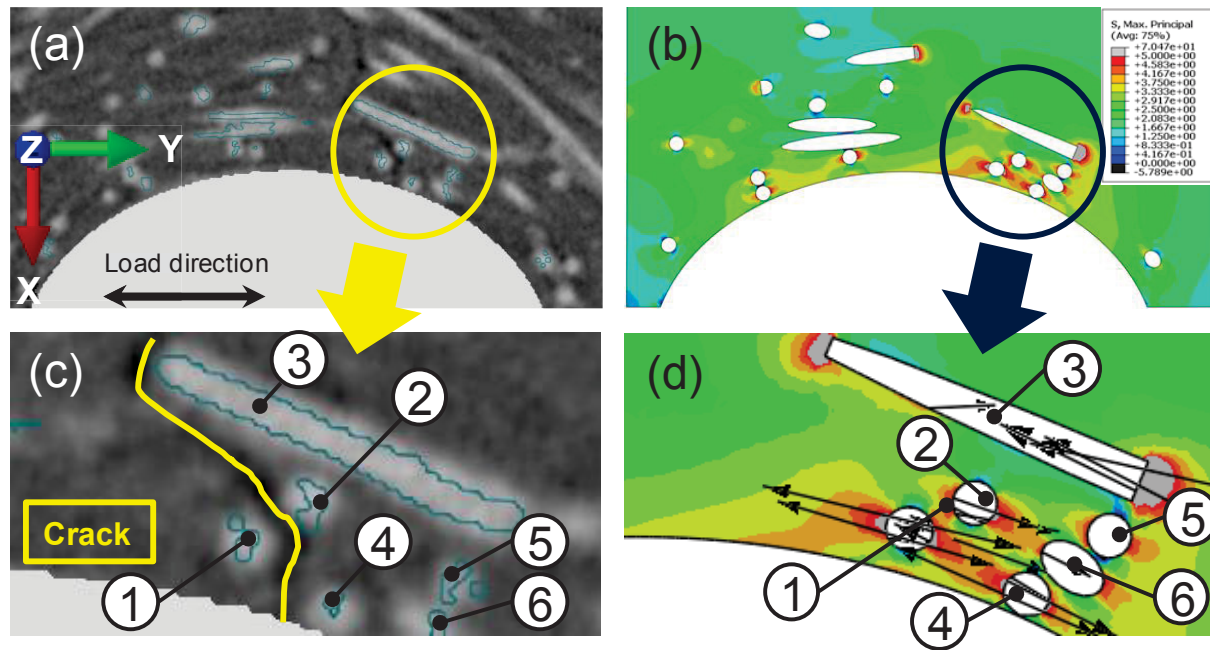


**Figure 7.10.** Stress distribution in the fibers of the reconstructed model (a) Front view, (b) Top view.

Figure 7.11 – 7.13 show a comparison between X-Ray CT micrographs and the corresponding contour plots of the maximum principal stress. In the contour plots, the fibers are hidden in order to highlight the matrix stress distribution. The direction of the maximum principal stress at the matrix hot-spots is also shown. Small discrepancies of the fiber positions between the FE model and the reality can be observed in Figure 7.11c-d. For example, fiber n°6 in the FE model is slightly moved from its reference position. That is essentially due to two reasons: Firstly, fiber n°6 is characterized by a large curvature being difficult to reproduce accurately. Secondly, in order to avoid any interference between the fibers, slight adjustments of the fiber positions were found to be necessary. Since the matrix stress concentrations are controlled by the mutual positions of the fibers, small microstructural variations lead to local variations of the stress field. For this reason, the stress analysis described in Figure 7.11 - 13 does not provide the absolute stress values in the matrix. Instead, it aims to figure out the local stress distributions around the notch. X-Ray CT micrographs reveal that crack initiates with little offset from the notch tip, in a fiber-rich region (Figure 7.11c). In this region, the highest matrix stress concentration occurs between through-the-thickness oriented fibers.

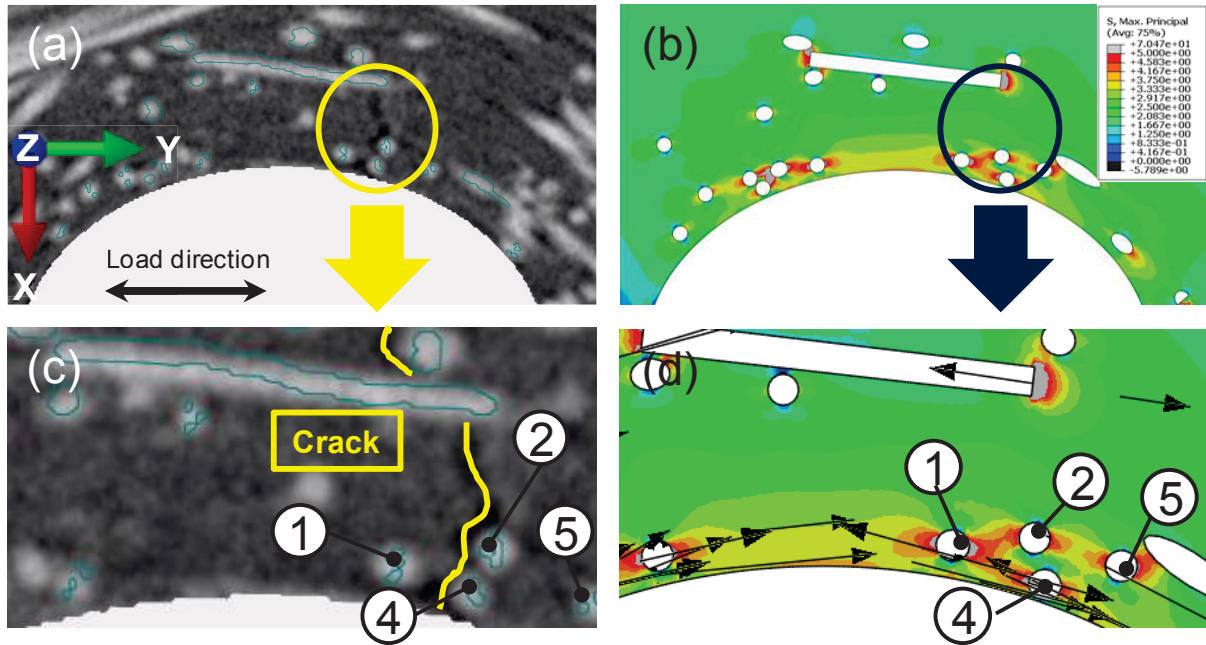
The direction of the local maximum principal stress is mostly perpendicular to the crack plane. In Figure 7.11, crack growths between the fibers n°1 and n°2 and it is forced to change direction due to the fiber n°3. The crack path develops between fibers in a typical fiber avoidance mode.





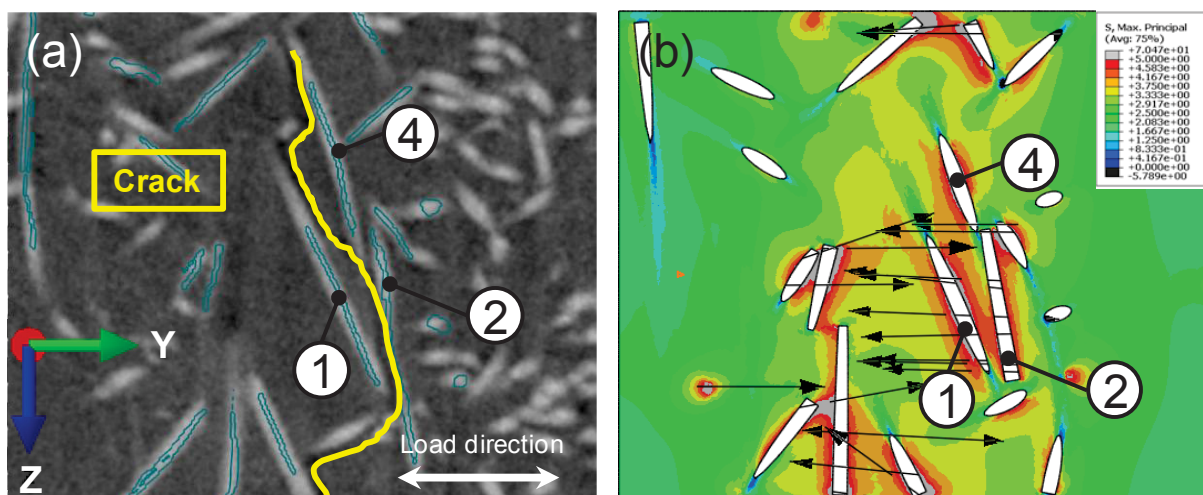
**Figure 7.11.** Comparison between X-Ray CT micrograph (a) and reconstructed model in the FEM code (b), front view; (c) Enlargement of Figure 7.11a; (d) Enlargement of Figure 7.11b. The arrows indicate the direction of the maximum principal stress.

Figure 7.12 shows another section along the thickness of the same sample analyzed in Figure 7.11. Two clusters of through-the-thickness oriented fibers are noticed. These clusters are located almost symmetrically about the x-z plane passing through the notch tip. However, there is only one crack on the right side of the notch. Concluding, there are multiple stress concentrations around the notch which are all potential sources of irreversibility. The combination of the weakest location due to local material morphology and the local stress state creates the condition for crack initiation. From this step on, the crack propagation is dominated by the singular stress field at the crack tip.



**Figure 7.12.** Comparison between X-Ray CT micrograph (a) and reconstructed model in the FEM code (b), front view; (c) Enlargement of Figure 7.12a; (d) Enlargement of Figure 7.12b. The arrows indicate the direction of the maximum principal stress.

Figure 7.13 shows the matrix stress distributions at crack initiation from a different perspective (y-z plane tangent to the notch tip). The fiber orientation is dominated by through-the-thickness oriented fibers. It is worthwhile noting that the matrix stress concentrations are influenced by the interfiber distance (see fiber n°1 and n°2).



**Figure 7.13.** Comparison between X-Ray CT micrograph (a) and reconstructed model in the FEM code (b), top view; The arrows indicate the direction of the maximum principal stress.

## **7.4. Conclusions**

An analysis of the fiber distribution at crack initiation for a short glass fiber reinforced polyamide (PA66-GF35) notched specimen was presented in this work. X-Ray CT was used for a quantitative description of the microstructure in a volume around the notch and for the reconstruction of the real fiber orientation distribution in the FEM software ABAQUS. Stress concentrations at the locations of crack initiation were also studied.

The insert within the mold used for creating the notch, leads to a perturbation of the melt flow during the injection molding process resulting in a three-dimensional fiber orientation distribution around the notch. At the close vicinity of the free surface of the notch, through-the-thickness oriented fibers were observed. Moreover, fiber clusters were found to be statistically distributed around the notch indicating that fiber content is not constant but varies significantly within the material. These local microstructural effects could be quantitatively captured by reducing the size of the elements where the FOT and the fiber content are measured.

The reconstruction of a material volume surrounding the notch in a FEM software had the objective to investigate the relation between the fiber distribution and the local stress concentrations in the matrix. With the use of the submodeling technique it was possible to study, from the qualitative point of view, the matrix stress distributions around the notch. The maximum matrix stress concentrations were found at clusters of through-the-thickness oriented fibers. The analysis of the stress concentrations is a preliminary step in investigating a crack initiation criterion.

## **References of Chapter 7**

- [1] E. Belmonte, M. De Monte, C. Hoffmann, M. Quaresimin, Damage mechanisms in a short glass fiber reinforced polyamide under fatigue loading, to appear.
- [2] E. Belmonte, M. De Monte, C. Hoffmann, M. Quaresimin, Influence of fiber loading on the fatigue damage mechanisms in short glass fiber reinforced polyamide, to appear.
- [3] K. Friedrich, Microstructure and fracture mechanical properties of short fiber reinforced thermoplastic P.E.T., Colloid and Polymer Science. 259 (1981) 808-811.

- [4] R.W. Lang, J.A. Manson, R.W. Hertzberg, Mechanisms of fatigue fracture in short glass fibre-reinforced polymers, *Journal of Materials Science*. 22 (1987) 4015-4030.
- [5] H. Voss, J. Karger-Kocsis, Fatigue crack propagation in glass-fibre and glass-sphere filled PBT composites, *Int. J. Fatigue*. 10 (1988) 3-11.
- [6] W.J. Evans, D.H. Isaac, K.S. Saib, The effect of short carbon fibre reinforcement on fatigue crack growth in PEEK, *Composites Part A: Applied Science and Manufacturing*. 27 (1996) 547-554.
- [7] Y. Zhou, P.K. Mallick, Fatigue performance of an injection-molded short E-glass fiber-reinforced polyamide 6,6. I. Effects of orientation, holes, and weld line, *Polymer Composites*. 27 (2006) 230-237.
- [8] A. Bernasconi, P. Davoli, A. Basile, A. Filippi, Effect of fibre orientation on the fatigue behaviour of a short glass fibre reinforced polyamide-6, *Int. J. Fatigue*. 29 (2007) 199-208.
- [9] M. De Monte, E. Moosbrugger, M. Quaresimin, Influence of temperature and thickness on the off-axis behaviour of short glass fibre reinforced polyamide 6.6 – Quasi-static loading, *Composites Part A: Applied Science and Manufacturing*. 41 (2010) 859-871.
- [10] M. De Monte, E. Moosbrugger, M. Quaresimin, Influence of temperature and thickness on the off-axis behaviour of short glass fibre reinforced polyamide 6.6 – cyclic loading, *Composites Part A: Applied Science and Manufacturing*. 41 (2010) 1368-1379.
- [11] S. Mortazavian, A. Fatemi, Effects of fiber orientation and anisotropy on tensile strength and elastic modulus of short fiber reinforced polymer composites, *Composites Part B: Engineering*. 72 (2015) 116-129.
- [12] S. Mortazavian, A. Fatemi, Fatigue behavior and modeling of short fiber reinforced polymer composites including anisotropy and temperature effects, *Int. J. Fatigue*. 77 (2015) 12-27.
- [13] P.J. Hine, R.A. Duckett, P. Caton-Rose, P.D. Coates, Fibre orientation structures and their effect on crack resistance of injection moulded transverse ribbed plate, *Plastics, Rubber and Composites*. 33 (2004) 43-53.

- [14] A. Bernasconi, P. Davoli, C. Armani, Fatigue strength of a clutch pedal made of reprocessed short glass fibre reinforced polyamide, *Int. J. Fatigue*. 32 (2010) 100-107.
- [15] C.M. Sonsino, E. Moosbrugger, Fatigue design of highly loaded short-glass-fibre reinforced polyamide parts in engine compartments, *Int. J. Fatigue*. 30 (2008) 1279-1288.
- [16] M. De Monte, E. Moosbrugger, K. Jaschek, M. Quaresimin, Multiaxial fatigue of a short glass fibre reinforced polyamide 6.6 – Fatigue and fracture behaviour, *Int. J. Fatigue*. 32 (2010) 17-28.
- [17] M. De Monte, E. Moosbrugger, K. Jaschek, M. Quaresimin, Multiaxial fatigue behaviour of a short-fibre reinforced polyamide 6.6 in the presence of notches. *ECCM - 13th European Conference on Composite Materials* (2008).
- [18] A. Bernasconi, F. Cosmi, E. Zappa, Combined Effect of Notches and Fibre Orientation on Fatigue Behaviour of Short Fibre Reinforced Polyamide, *Strain*. 46 (2010) 435-445.
- [19] A. Bernasconi, E. Conrado, P. Hine, An experimental investigation of the combined influence of notch size and fibre orientation on the fatigue strength of a short glass fibre reinforced polyamide 6, *Polym. Test*. 47 (2015) 12-21.
- [20] B. Mlekusch, E.A. Lehner, W. Geymayer, Fibre orientation in short-fibre-reinforced thermoplastics I. Contrast enhancement for image analysis, *Composites Sci. Technol*. 59 (1999) 543-545.
- [21] C. Eberhardt, A. Clarke, Fibre-orientation measurements in short-glass-fibre composites. Part I: automated, high-angular-resolution measurement by confocal microscopy, *Composites Sci. Technol*. 61 (2001) 1389-1400.
- [22] A. Bernasconi, F. Cosmi, P.J. Hine, Analysis of fibre orientation distribution in short fibre reinforced polymers: A comparison between optical and tomographic methods, *Composites Sci. Technol*. 72 (2012) 2002-2008.
- [23] F. Cosmi, A. Bernasconi, Micro-CT investigation on fatigue damage evolution in short fibre reinforced polymers, *Composites Sci. Technol*. 79 (2013) 70-76.

- [24] H. Rolland, N. Saintier, G. Robert, Damage mechanisms into short glass fibre reinforced thermoplastic during in situ microtomographic tensile tests. 16th European Conference on Composite Materials, ECCM16 (2014).
- [25] M.F. Arif, F. Meraghni, Y. Chemisky, N. Despringre, G. Robert, In situ damage mechanisms investigation of PA66/GF30 composite: Effect of relative humidity, Composites Part B: Engineering. 58 (2014) 487-495.
- [26] Abaqus Analysis User's Manual (Version 6.11), SIMULIA; 2011.
- [27] T. Riedel, Evaluation of 3D fiber orientation analysis based on x-ray computed tomography data. Proc. of Conference on Industrial Computed Tomography (2012).
- [28] Simpleware Ltd, exeter, United Kingdom.
- [29] M. Huang, Y. Li, X-ray tomography image-based reconstruction of microstructural finite element mesh models for heterogeneous materials, Computational Materials Science. 67 (2013) 63-72.
- [30] J.P. James, H.-. Choi, J.G. Pharoah, X-ray computed tomography reconstruction and analysis of polymer electrolyte membrane fuel cell porous transport layers, Int J Hydrogen Energy. 37 (2012) 18216-18230.
- [31] DIGIMAT, 2014, Software Platform for Nonlinear Multi-scale Modeling of Composite Materials and Structures, e-Xstream Engineering, Belgium and Luxembourg.
- [32] Autodesk, Inc., Moldflow 2014.





## **Chapter 8**

# **Multi-scale modeling of the fatigue behavior of short glass fiber reinforced polyamide notched specimens**

**Keywords:** Short Fiber Reinforced Composites, Fatigue, Polyamide, Multi-scale modeling

### **Abstract**

This paper presents a multi-scale strategy for the lifetime prediction, in terms of crack initiation, of short fiber reinforced polyamide specimens. Fatigue tests of specimens characterized by a central molded-in slit were carried out. In the first part of this work, the development of a two-dimensional geometric representation of the real microstructure around the notch is presented. The second part of the paper deals with the formulation of the criterion for the durability assessment. A local threshold stress which includes the microscopic matrix stress concentrations is used to summarize the fatigue data for different fiber volume fractions in a single scatter band. The strengths and the weaknesses of the proposed criterion as well as its possible extensions are also discussed.

### **8.1. Introduction**

The use of Short Fiber Reinforced Plastics (SFRPs) in the automotive sector is motivated by several reasons, among which: 1) Minimization of the vehicle weight; 2) Reduction of the manufacturing costs; 3) Design freedom. SFRPs exhibit high strength to weight ratio, high chemical and temperature resistance. Such characteristics make these materials ideal candidates for metal replacement in under-the-hood applications. Under-the-hood parts are exposed to cyclic loading due to vibrations, pulsating pressure, temperature variations. Approaches to durability become essential to predict the lifetime already in the design phase. In the literature, some phenomenological approaches for the lifetime prediction of SFRPs are available. Most of them are extensions of models originally developed for homogeneous, isotropic materials. Such approaches require test data to determine the phenomenological constants and do not provide the physical insight needed to improve the material performance. The Tsai-Hill criterion was extended by De Monte et al. [1, 2] to predict the influence of the

fiber orientation on the tensile and fatigue strength of PA66-GF35 plain specimens. The volume-based Strain Energy Density (SED) approach originally developed by Lazzarin et al. [3-5] quasi-brittle material and weld joints, was extended by De Monte and coworkers [6] in order to predict the lifetime of PA66-GF35 specimens with different notch geometries. The SED model was further extended by Schaaf and coworkers [7] for the lifetime prediction of a PBT-GF30 under thermomechanical loading. Recently, thanks to the increase of the computational power and the improvements of the experimental methods for the damage investigation, models able to take into account the microstructure have been proposed [8].

In this paper, a multi-scale model for the lifetime prediction up to crack initiation of SFRPs is presented. In certain components, the initiation of a crack corresponds to the component failure. An example is the fuel rail shown by Sonsino and Moosbrugger in [9]. In that case, the occurrence of a crack may lead to fuel leakage compromising the functioning of the component. According to Talreja [10], the first step of a durability approach is the stress analysis of the considered geometry under expected service environment using the assumed material model. SFRPs are heterogeneous materials. In addition to the macro stress concentrations at geometric discontinuities, microscopic stress concentrations emerge due to fiber-fiber and fiber-matrix interactions. The knowledge of the fiber distribution at crack initiation is thus of great interest since it enables the study of typical local stress concentrations. Analyzing the microstructure around a molded notch in a longitudinal injected specimen, the authors revealed the occurrence of through-the-thickness oriented fibers [11]. Building on these achievements, in Section 8.3 a geometric description of the microstructure around the notch is illustrated. In Section 8.4, a multi-scale modeling strategy is proposed. In order to study the effect of the fiber distribution on the fatigue material behavior, polyamides characterized by different fiber fractions were considered.

## **8.2. Experimental**

In this work, unreinforced and short glass fiber reinforced polyamides (PA66) were used. The material designations (PA66, PA66-GF15, PA66-GF25, PA66-GF35, PA66-GF50) correspond to 0 %, 15 %, 25 %, 35 %, 50 % weight fiber fraction respectively. Dog-bone plain specimens were tested under quasi-static loading to measure elastic and strength properties of the considered material systems. Notched specimens were tested under fatigue loading. The specimen geometries are shown in Figure 8.1. Both plain and notched specimens were longitudinally injected. The notch is created with an insert within the mold. Real

injection molded parts generally do not need any post-molding machining operation. All the geometric discontinuities are already within the mold.

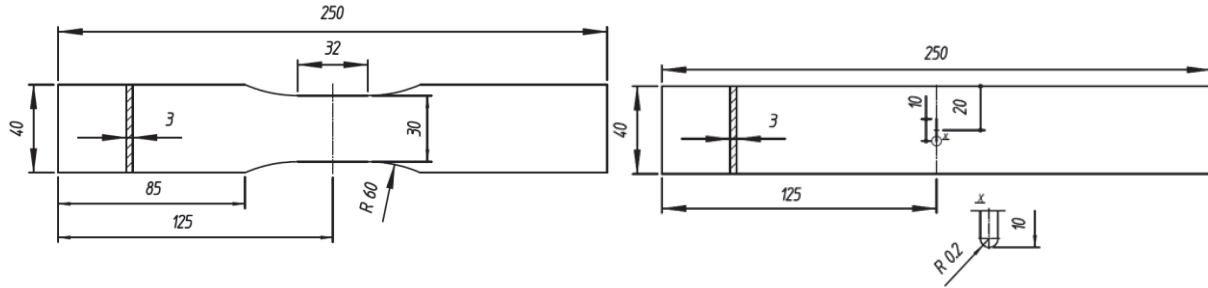


**Figure 8.1.** Specimen geometry and dimensions (in mm); plain specimen on the left; notched specimen on the right (see the enlargement of the notch tip at the bottom right of the figure).

Static and fatigue tests were carried out at room temperature without controlling the relative humidity of the room. Just after molding, the specimens were stored in drums containing a drying agent. Hence, we assume that all the specimens were tested in Dry-As-Molded (DAM) conditions. A Zwick/Roell Z050 was used to test plain specimens under quasi-static loading. The crosshead rate was kept slow for the measurement of the Young's modulus (1 mm/min) and accelerated (5 mm/min) in the second part of the test until specimen failure. The tensile properties for different fiber volume fractions are summarized in Table 8.1. Interestingly, while the Young's modulus ( $E$ ) and the Ultimate Tensile Strength (UTS) increase with increasing fiber fraction, the strain to failure ( $\epsilon$  at failure) of the reinforced materials is independent of the fiber content. Similar results were reported also by Bernasconi and Cosmi in [12]. Uniaxial fatigue tests were carried out on a servo-hydraulic testing machine, equipped with a load cell of 10 kN. Fatigue tests were performed under load control in tension-tension mode (load ratio  $R = 0$ ). The testing frequency was kept low in order to avoid the material self heating. In Figure 8.2b the fatigue results are reported by plotting the nominal net stress amplitude against the number of cycles to crack initiation (dotted line) and to failure (solid line). Fatigue data are represented in a double logarithmic diagram, plotting the net stress amplitude ( $\sigma_a$ ) against the number of cycles ( $N$ ) to crack initiation/failure. S-N curves with 50 % failure probability are plotted using eq. 8.1.

$$N \cdot \sigma_a^k = N_A \cdot \sigma_A^k \quad (8.1)$$

Where  $N_A = 1E6$  cycles and  $\sigma_A = \sigma_a(1E6)$ ,  $k$  is the inverse slope of the S-N line. For the crack initiation detection, an optical capturing method was used [13]. The fitting parameters used in the eq. 8.1 are reported in Table 8.1.

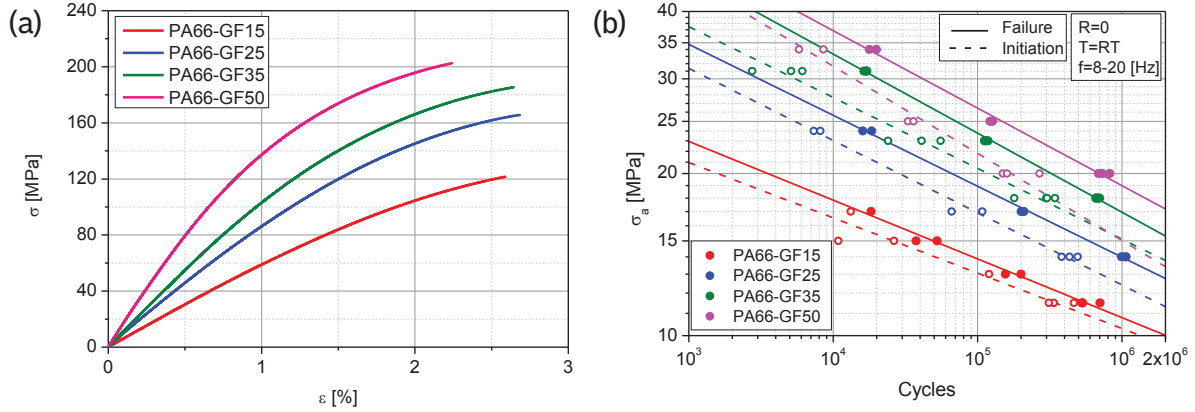


**Figure 8.2.** (a) Static tests of plain specimens for different fiber volume fractions; (b) Fatigue tests of notched specimens for different fiber volume fractions.

**Table 8.1.** Tensile properties of short glass fiber reinforced polyamides (PA66) having different fiber volume fractions.

Material	E [MPa]	UTS [MPa]	$\varepsilon$ at failure [%]
PA66-GF15	6176	120	2.50
PA66-GF25	8991	164	2.70
PA66-GF35	10899	184	2.60
PA66-GF50	16025	202	2.20

**Table 8.2.** S-N lines up to crack initiation and up to failure of short glass fiber reinforced polyamides (PA66) having different fiber volume fractions.

Material	Initiation		Failure	
	$\sigma_A$ [MPa]	k	$\sigma_A$ [MPa]	k
PA66-GF15	10.31	9.72	10.80	9.17
PA66-GF25	12.42	7.46	13.99	7.59
PA66-GF35	15.10	7.60	16.94	6.81
PA66-GF50	15.03	6.18	18.99	6.95

### **8.3. Equivalent description of the microstructure**

In this section, a statistical equivalency approach for the description of the fiber distribution at crack initiation is proposed. According to Pyrz [14], SFRPs can be described as statistically homogeneous materials. This means that the effective material properties can be obtained by averaging over a Representative Volume Element (RVE). Averaging is useful if the global elastic material properties have to be calculated. Instead, damage initiation is governed by local stresses. The mismatch between the elastic properties of fibers and matrix and the interaction between neighboring fibers lead to matrix stress concentrations which are preferred locations for crack initiation. Segurado and Llorca [15] studied the effect of particles spatial distributions in a RVE on the local stress distributions and the elastic global properties. They observed that the spatial arrangement of the particles (in particular the clusters of particles) influences the matrix stress peaks whereas it does not affect the effective material properties of the composite material. Bulsara and coworkers [16] investigated the RVE size with respect to the damage mechanisms matrix cracking and fiber-matrix debonding.

Figure 8.3 shows the statistical distribution of the maximum principal stress in the matrix in a real material volume around a molded-in notch tip. On the right of Figure 8.3, three contour plots represent the same distribution of the maximum principal stress but varying the lowest limit of the contour scale. For example, on the contour plot at the top-right of Figure 8.3 the stress from 2 MPa is plotted. The microscopic matrix stress concentrations occur either between through-the-thickness oriented fibers or at the ends of longitudinally oriented fibers and correspond to a small fraction of the total stresses. Through-the-thickness oriented fibers are restricted to a thin layer surrounding the notch, where damage is most likely to initiate.



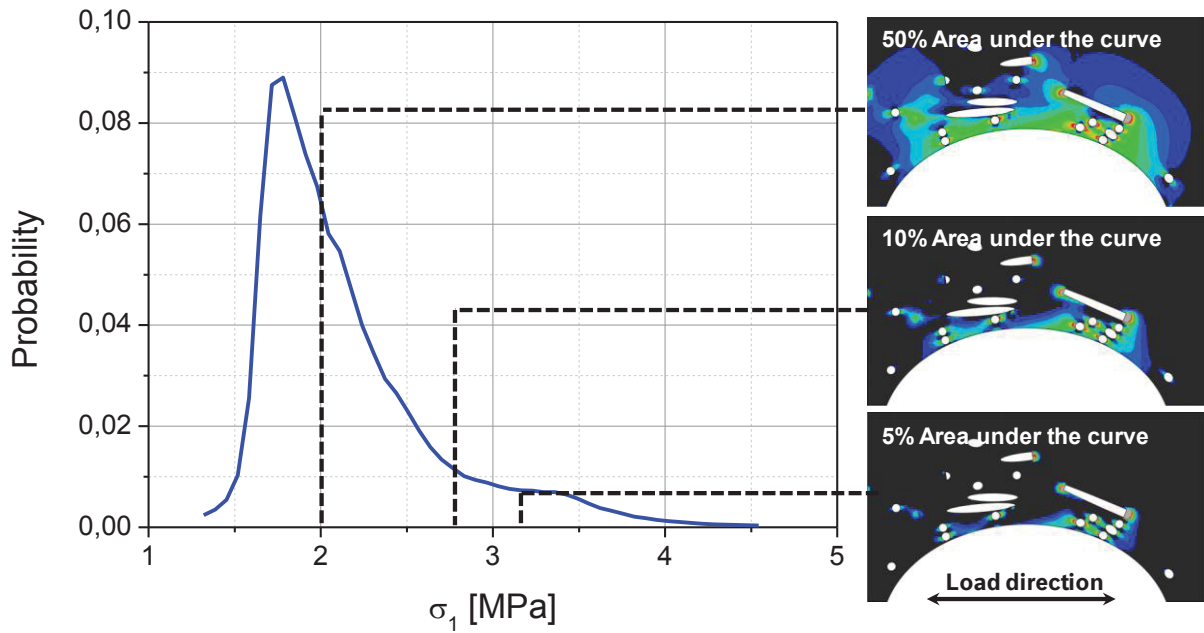


**Figure 8.3.** Max principal stress contours plots referring to percentage portions of the area under the stress distribution curve.

The microstructure shown in Figure 8.3 closely reproduces the fiber orientation distribution in the reality. However, the effort required for preparing and scanning the sample and for the analysis of the X-Ray CT datasets discourages the extension of this procedure for large experimental campaigns. The proposed strategy for the development of an equivalent geometric representation of the fiber orientation distribution aims to reproduce the typical observed matrix stress concentrations.

In a first approximation, the failure process in specimens weakened by molded-in notches can be divided into two parts. In a first phase, matrix cracking occurs in a zone characterized by clusters of through-the-thickness oriented fibers. From this point on, the crack propagates in a fiber avoidance mode leading to a zig-zag pattern mostly avoiding in-plane oriented fibers. Focusing on the damage initiation only, the microstructure was represented as a bi-dimensional layer surrounding the notch and containing a random distribution of through-the-thickness oriented fibers (Figure 8.4). The nominal fiber fraction was kept constant. The fiber diameter ( $d_f$ ) was kept constant and equal to  $10\ \mu\text{m}$ . A hard-core method was used by applying a uniform distribution for the fiber centers and considering a minimum permitted distance ( $\text{dist} = 1.05 \cdot d_f$ ) between any two centers. The size of the geometric representation of the microstructure is related to the layer within which through-the-thickness oriented fibers were observed. The layer width is set to 3.5 times the fiber diameter and indicates the distance

delimiting damage initiation area. The fiber-matrix interface was not modeled. Perfect fiber-matrix bonding was assumed. Plane strain elements were used in the simulation thus assuming that the fibers are endless. The element size was kept constant for various fiber fractions. The simplifications introduced in the geometric representation imply that the stress concentrations are only affected by the distance between neighboring fibers. Effects such the fibers overlapping as well as the influence of the fiber orientation were not taken into account. The boundary conditions of the microstructure were assigned using the submodeling technique. Two-dimensional homogeneous, isotropic, linear elastic simulations of the entire specimen were performed by only varying the Young's modulus depending on the fiber volume fraction (Figure 8.4a). The adopted values of the Young's modulus are summarized in Table 8.1. The nodes on the bottom face of the specimen were constrained in all the degrees of freedom while uniform pressure, equal to 1 MPa was applied to the top surface. Because of the huge size difference between the global model and the microstructure, an additional sub-model having the properties of the global model was simulated (Figure 8.4b). The displacement field resulting from the analysis of the first sub model model was finally assigned to the second sub-model (Figure 8.4c). In the second sub-model, fibers and matrix were explicitly modeled. In this case, the linear elastic material properties of fibers and matrix were adopted from [1].

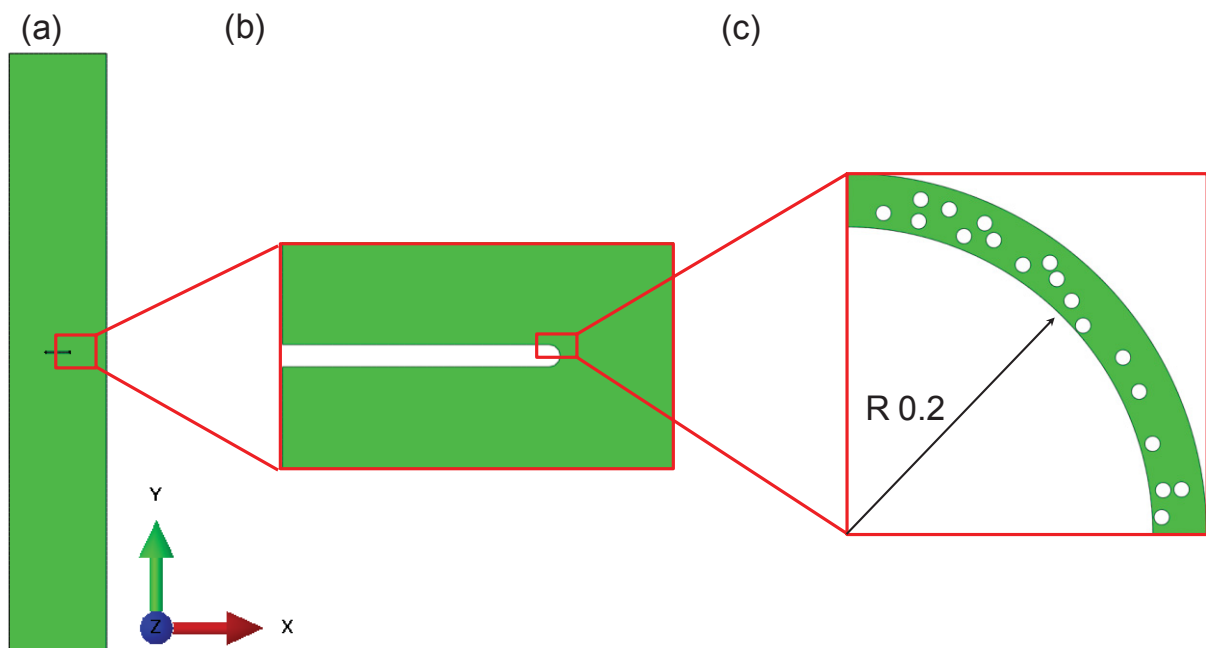


**Figure 8.4.** Description of the submodeling technique: (a) global model; (b) first sub model; (c) second sub model. One homogeneous material model was assigned to the global and the

first sub model while two different material models (fibers and matrix) were assigned to the second sub model.

#### 8.4. Formulation of the failure criterion and analysis of the results

Figure 8.5 shows the contours of the maximum principal stress in the matrix for different fiber fractions. For a given percentage area under the statistical stress distribution curve (Figure 8.3), the corresponding threshold stress is higher for lower fiber fractions. The reason is that the Young's modulus assigned to the global model influences the displacement distribution. A lower Young's modulus results in higher displacements transferred to the submodel. On the other hand, the interfiber distance decreases with increasing fiber volume fraction resulting in higher local stresses. The Young's modulus of the global model and the interfiber distance are the two factors which influence the matrix stress distribution in the microstructure.

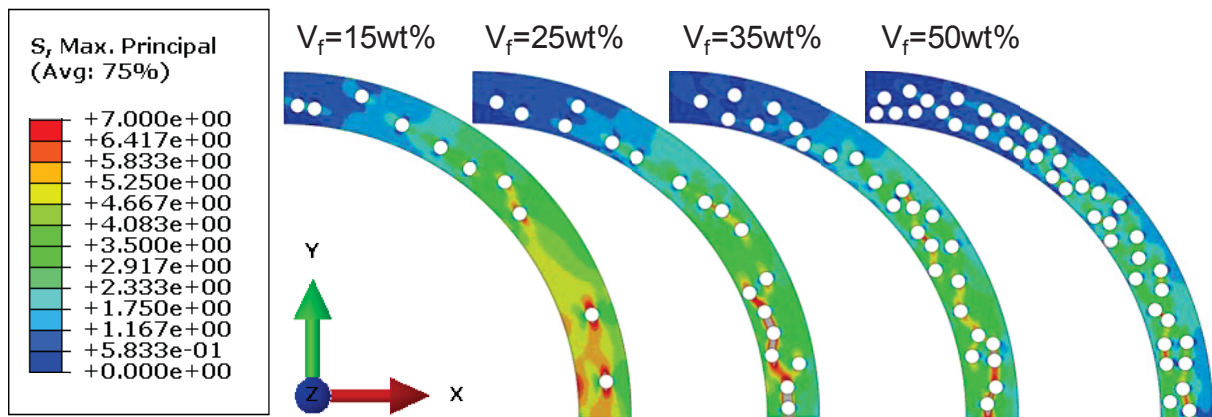


**Figure 8.5.** Contours of the microscopic matrix stress distributions varying the fiber volume fraction.

We followed a statistical approach for the derivation of a local, critical stress-based variable to be used in the multi-scale model. Taking as example the PA66-GF35 material, 20 random microstructures were generated. For each microstructure, the highest maximum principal stress and the stress thresholds referring to different portions of the total area under the stress distribution were calculated. For each stress threshold, the average value over the 20 microstructures and the standard deviation are reported in Figure 8.6. For a correct analysis of the scatter, the standard deviation was divided by the average value of the corresponding stress threshold. The high scatter shown by the highest maximum principal stress prevents its

use as failure variable in the multi-scale model. Instead, the threshold stress value referring to a specific portion of the total area under the curve exhibits a lower scatter. The standard deviation diminishes with increasing of the area under the stress distribution curve. However, if we take into account a large portion of the total area, we include stress regions which do not participate to the damage phenomenon (Figure 8.3). Following an engineering approach, the adopted stress threshold is the result of a trade-off between these two objectives. Finally, we found that the stress threshold referring to the 10 % of the area under the stress distribution curve exhibits a low scatter and identifies the stress concentrations which correspond to the potential sources of irreversibility in the microstructures (Figure 8.6).

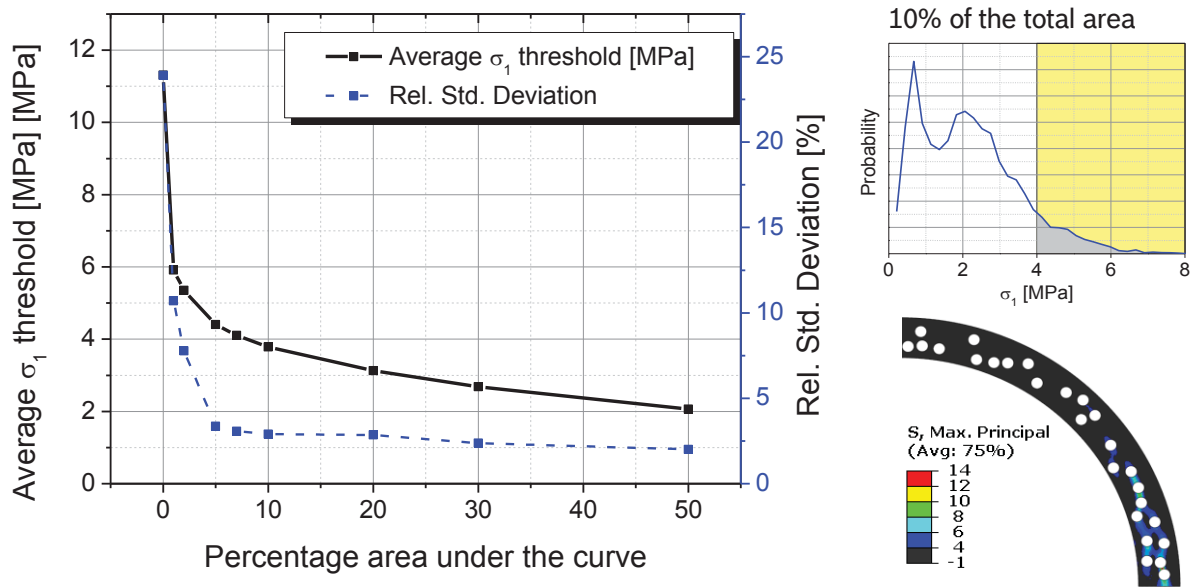


**Figure 8.6.** Evaluation of the average value and standard deviation of the local matrix threshold stress related to different percentage areas under the curve over 20 random microstructures.

The fatigue data were rearranged in terms of local matrix threshold stress amplitude  $\sigma_A^*$  according to the eq. 8.2.

$$\sigma_A^* = \sigma_A \cdot \sigma_I^* \quad (8.2)$$

Where  $\sigma_A$  is the nominal fatigue strength for a given number of cycles and  $\sigma_I^*$  is the concentration factor expressed as the threshold stress related to the 10 % of the area under the matrix stress distribution curve when a pressure equal to 1 MPa is applied to the global

model. The data represented in terms of local matrix threshold stress amplitude fall within a single band as shown in Figure 8.7. The scatter index  $T_\sigma$  is the ratio between the stress values at 90 % and 10 % failure probability.

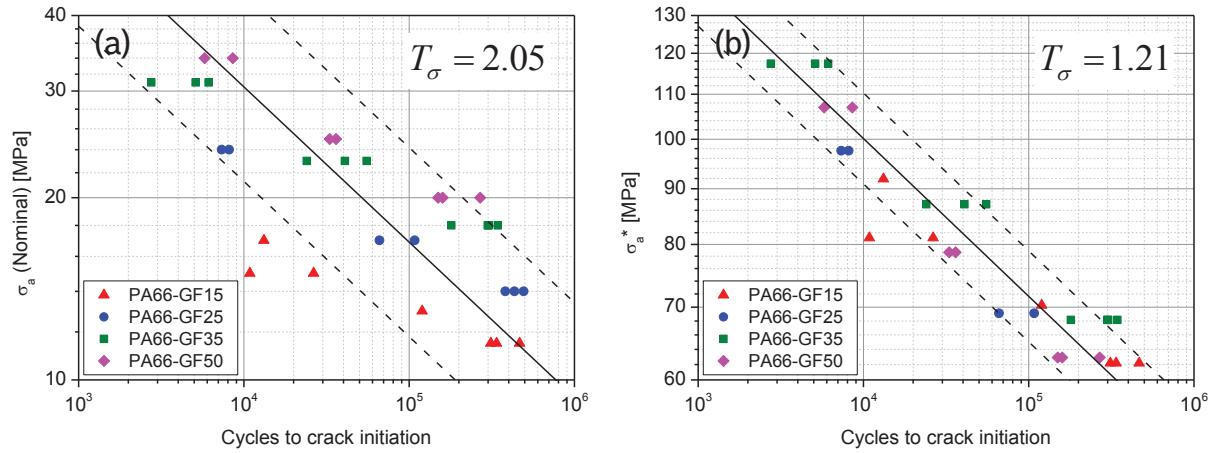


**Figure 8.7.** Fatigue data plotted in terms of nominal stress amplitude (a) and local matrix threshold stress amplitude against the number of cycles to crack initiation.

Assuming that  $\sigma_A^*$  is constant for each fiber volume fraction, the model enables the calculation of the nominal S-N curves for different fiber volume fractions basing on a single calibration curve. In fact the parameter  $\sigma_1^*$  can be calculated through a linear elastic FE analysis. Figure 8.8 shows the performance of the model reporting the experimental number of cycles against the estimated values using as calibration curve the S-N line referring to one of the considered fiber volume fractions. The dashed lines indicate the  $\pm 200\%$  error bands. Given a set of fatigue data for a specific fiber volume fraction, the relation between the stress amplitude ( $\sigma_a$ ) and the number of cycles to crack initiation ( $N$ ) is expressed by the eq. 8.1. The same equation is valid for the S-N line plotted in terms of local matrix threshold stress amplitude ( $\sigma_a^*$ ) against number of cycles to crack initiation ( $N$ ) (eq. 8.3).

$$N \cdot (\sigma_a^*)^k = N_A \cdot (\sigma_A^*)^k \quad (8.3)$$

The slope of the S-N line ( $k$ ) is kept constant. Given a value of the stress amplitude, it is possible to calculate the number of cycles to crack initiation for any other fiber volume fraction. For example, in the eq. 8.4, the calibration curve is the S-N line for PA66-GF35.

$$N_a = N_A \cdot \left( \frac{\sigma_A^*}{\sigma_a^*} \right)^k = N_A \cdot \left( \frac{\sigma_A^{GF35} \cdot \sigma_I^{*GF35}}{\sigma_A^? \cdot \sigma_I^{*?}} \right)^k \quad (8.4)$$

Where  $N_A = 1E6$  cycles,  $\sigma_A^{GF35}$  is the stress amplitude referring to 1E6 cycles,  $\sigma_I^{*GF35}$  the threshold stress limiting the highest 10 % of the stress distribution curve when a pressure equal to 1 MPa is applied to the global model. The appendix “?” indicates the fiber volume fraction of the outputted S-N line.

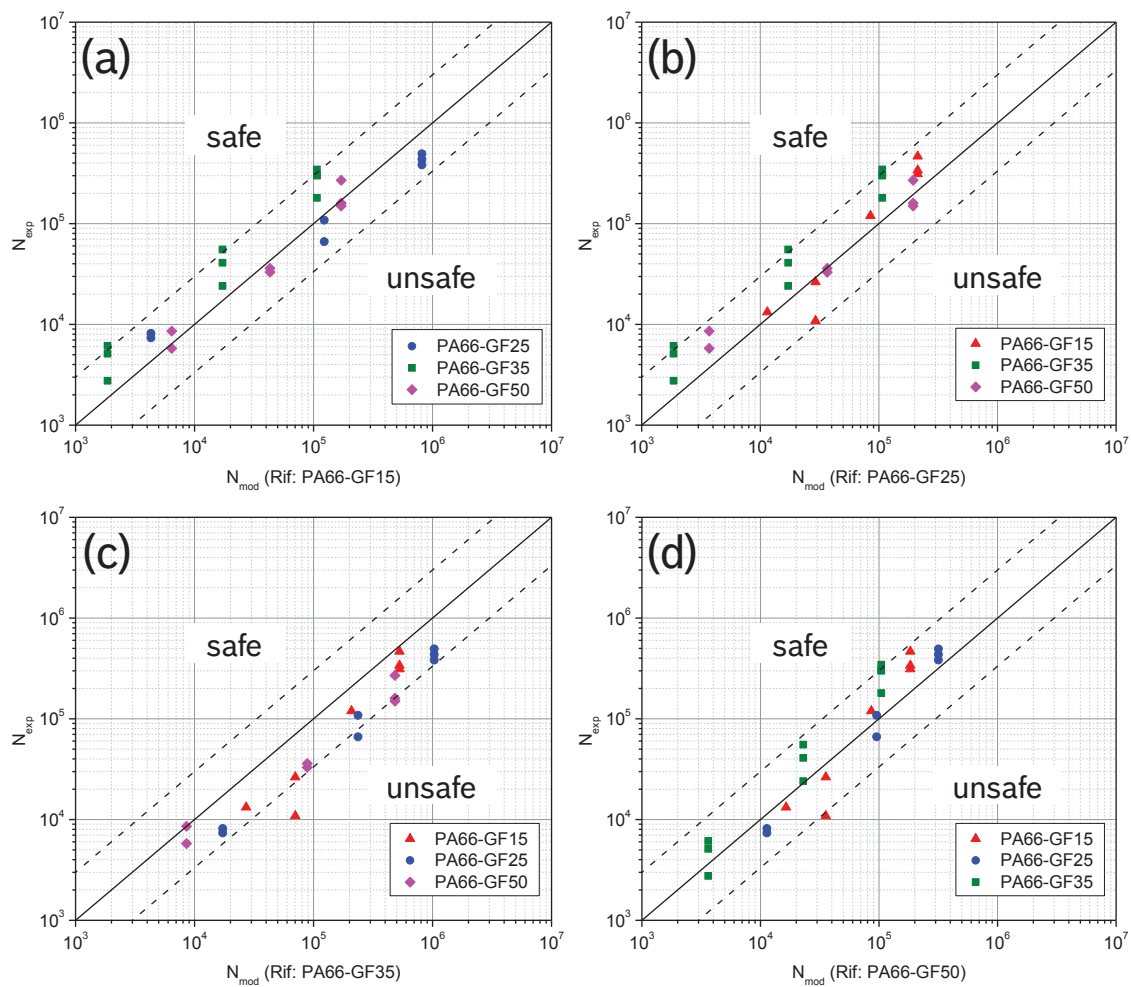


**Figure 8.8.** Performance of the criterion in terms of fatigue life considering as calibration curve the S-N curve of PA66-GF15 (a); PA66-GF25 (b); PA66-GF35 (c); PA66-GF50 (d); the dashed lines indicate the  $\pm 200\%$  error bands.



Despite the simplifications included in the model, the proposed multi-scale strategy gives acceptable results and in particular appears to be a rapid tool for the derivation of S-N lines for different fiber configurations.

## **8.5. Conclusions**

A multi-scale modeling strategy for the prediction of the lifetime up to crack initiation in notched specimens was presented. Despite its simplicity, the proposed multi-scale model gives good results requiring only one calibration curve. The approximations of the model (isotropic material model for the global model, bi-dimensional model, perfectly aligned fibers, absence of an interface model) could be removed without varying the proposed multi-scale strategy. The microstructure modeled in this work is representative of specimen weakened by a molded-in central notch. The fiber distribution should be investigated also for other specimen geometries and typical regions for crack initiation in real-world-components. In a future work, the fatigue data of plain specimens will be reanalyzed using the same multi-scale model.

## **References of Chapter 8**

- [1] M. De Monte, E. Moosbrugger, M. Quaresimin, Influence of temperature and thickness on the off-axis behaviour of short glass fibre reinforced polyamide 6.6 – Quasi-static loading, *Composites Part A: Applied Science and Manufacturing*. 41 (2010) 859-871.
- [2] M. De Monte, E. Moosbrugger, M. Quaresimin, Influence of temperature and thickness on the off-axis behaviour of short glass fibre reinforced polyamide 6.6 – cyclic loading, *Composites Part A: Applied Science and Manufacturing*. 41 (2010) 1368-1379.
- [3] P. Lazzarin, R. Zambardi, A finite-volume-energy based approach to predict the static and fatigue behavior of components with sharp V-shaped notches, *International Journal of Fracture*. 12 (2001) 275-298.
- [4] B. Atzori, F. Berto, P. Lazzarin, M. Quaresimin, Multi-axial fatigue behaviour of a severely notched carbon steel, *Int. J. Fatigue*. 28 (2006) 485-493.

- [5] P. Lazzarin, F. Berto, Some Expressions for the Strain Energy in a Finite Volume Surrounding the Root of Blunt V-notches, *International Journal of Fracture*. 135 (2005) 161-185.
- [6] M. De Monte, M. Quaresimin, P. Lazzarin, Modelling of fatigue strength data for a short fiber reinforced polyamide 6.6 based on local strain energy density. *Proceedings of ICCM16, 16th International Conference on Composite Materials (2007)*.
- [7] A. Schaaf, M. De Monte, E. Moosbrugger, M. Vormwald, M. Quaresimin, Life estimation methodology for short fiber reinforced polymers under thermo-mechanical loading in automotive applications, *Materialwissenschaft und Werkstofftechnik*. 46 (2015) 214-228.
- [8] N. Despringre, Y. Chemisky, M.F. Arif, G. Robert, Multi-scale viscoelastic damage model of short glass fiber reinforced thermoplastics under fatigue loading. *Proceeding of the 16th European Conference on Composite Materials (ECCM16) (22-26 June 2014)*.
- [9] C.M. Sonsino, E. Moosbrugger, Fatigue design of highly loaded short-glass-fibre reinforced polyamide parts in engine compartments, *Int. J. Fatigue*. 30 (2008) 1279-1288.
- [10] R. Talreja, Multi-scale modeling in damage mechanics of composite materials, *Journal of Materials Science*. 41 (2006) 6800-6812.
- [11] E. Belmonte, T. Riedel, M. De Monte, M. Quaresimin, Local microstructure and stress distributions at the crack initiation site in a short glass fiber reinforced polyamide under fatigue loading, to appear.
- [12] A. Bernasconi, F. Cosmi, Analysis of the dependence of the tensile behaviour of a short fibre reinforced polyamide upon fibre volume fraction, length and orientation, *Procedia Engineering*. 10 (2011) 2129-2134.
- [13] E. Belmonte, E. Moosbrugger, N. De Rossi, M. De Monte, M. Quaresimin, Life to crack initiation in notched specimens of unreinforced and short fiber reinforced polyamide under fatigue loading, to appear.
- [14] R. Pyrz, Microstructural Description of Composites, Statistical Methods, in: H.J. Böhm (Ed.), *Mechanics of Microstructured Materials*, Springer Vienna, 20014, pp. 173-233.

[15] J. Segurado, J. LLorca, Computational micromechanics of composites: The effect of particle spatial distribution, *Mech. Mater.* 38 (2006) 873-883.

[16] V.N. Bulsara, R. Talreja, J. Qu, Damage initiation under transverse loading of unidirectional composites with arbitrarily distributed fibers, *Composites Sci. Technol.* 59 (1999) 673-682.

## **Chapter 9**

### **Concluding remarks**

Engineering approaches to durability of SFRPs give accurate lifetime estimation when the damage mechanisms operating under the stress state conditions at critical locations are properly understood and incorporated in a lifetime prediction model. Currently, thanks to the improvements of the experimental techniques for the damage investigation and the explosion of the computational power, the time is ripe for the development of mechanism-based models. In this context, the damage initiation in a short glass fiber reinforced polyamide under fatigue loading has been investigated.

In Chapter 4, an optical method for the quantification of the lifetime to crack initiation in notched specimens has been presented. It was found that the contribution of the crack initiation / propagation phase to the total lifetime varies with the fiber volume fraction. For unfilled polyamide specimens, crack initiation corresponds to failure. The contribution of the crack propagation to the total lifetime increases with increasing fiber fraction. The accuracy of the method was validated by interrupting fatigue tests before specimen failure and measuring the real crack length on the polished side surface of the specimen by optical microscopy.

The initiation and progression of damage in plain and notched PA66-GF35 specimens have been studied in Chapter 5. Damage mechanisms discussed in literature were reviewed by reference to specific fractographic features: matrix fracture behavior (ductile / brittle), fiber failure / pull-out, degree of interfacial adhesion. The results of the literature review were used as basis for a comprehensive damage investigation on plain and notched PA66-GF35 specimens. High resolution Field Emission Scanning Electron Microscope (FESEM) was used to investigate the fractures surface of failed specimens and the side surface of specimens subjected to interrupted fatigue tests. Fibers on the fracture surface were found to be covered by a resin layer. This evidence suggests that damage occurs at a certain distance from the interface in form of matrix-cracking and not at the interface in form of fiber-matrix debonding. Cryogenic fracture of specimens previously tested until crack initiation revealed the occurrence of cavities on the cryo-fracture surface ahead of the crack tip. This evidence suggests that the mechanism of coalescence of voids in the matrix precedes the initiation of a crack. Analyzing the side surface of notched specimens subjected to interrupted fatigue test, it

was found the crack initiation position does not correspond to the notch tip as for homogeneous materials. Instead, the crack was found to initiate at clusters of through-the-thickness oriented fibers unevenly distributed around the notch.

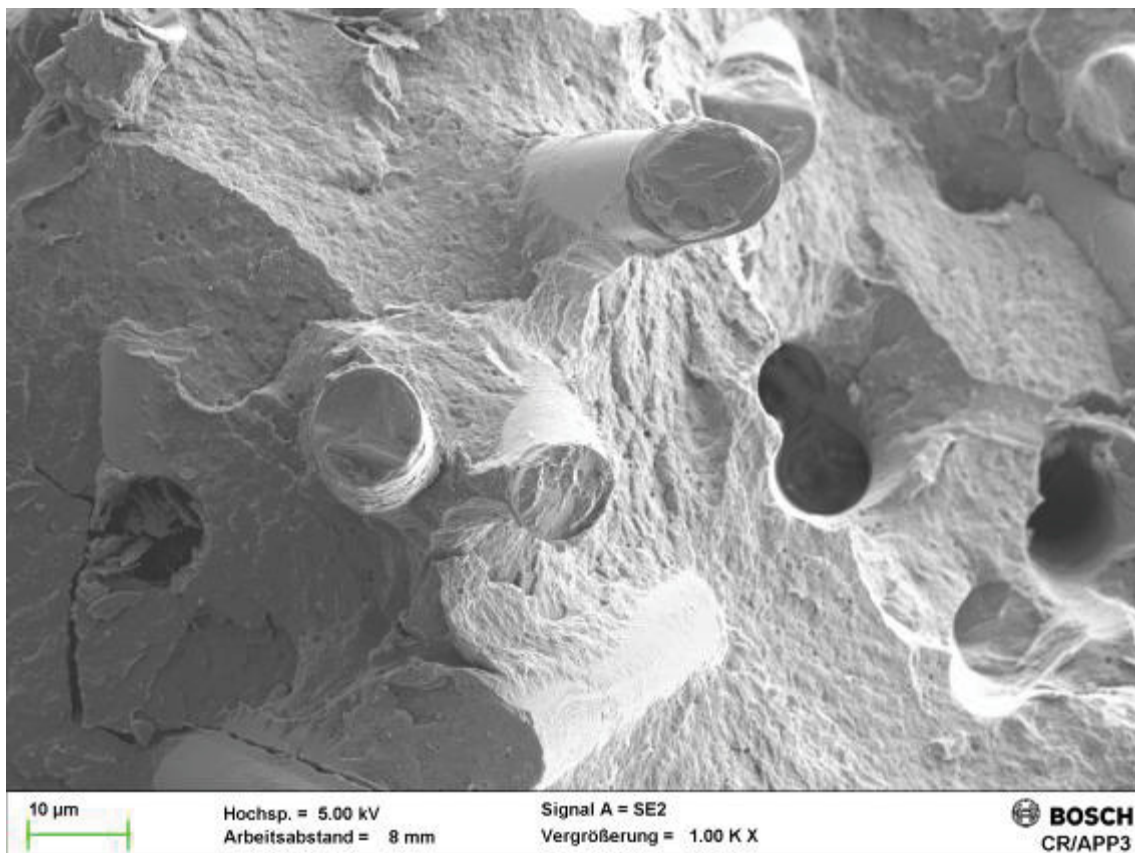
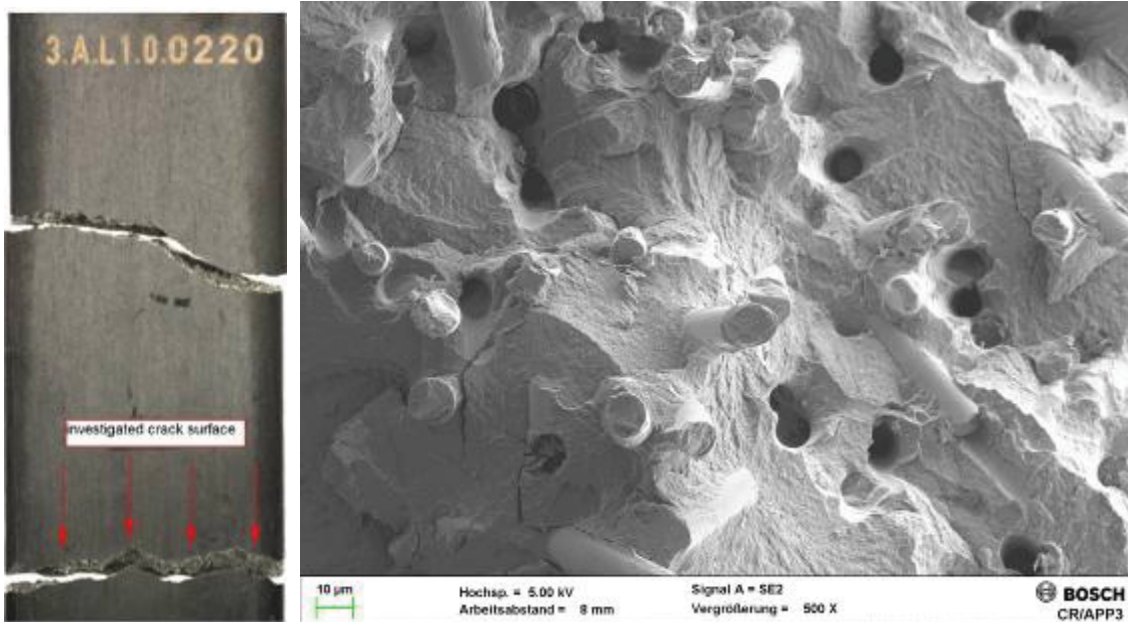
In Chapter 6, the damage investigation has been extended to consider the effect of the fiber volume fraction on the fatigue damage mechanisms in notched specimens. It was shown that the crack path is strongly affected by the fiber fraction. With high fiber fraction, fibers agglomerate forming clusters which force the crack to change continuously its propagation direction reducing the crack propagation rate. The analysis of the fracture surface showed that the fibers are covered by a resin layer thus indicating that damage occurs at a certain distance from the interface independently of the fiber content.

The effect of the fiber orientation on the local stress concentrations at crack initiation has been investigated in Chapter 7. For this purpose, a fatigue test of a notched specimen was interrupted at crack initiation and analyzed by means of X-Ray CT. The quantitative analysis of the fiber orientation distribution around the notch revealed the occurrence of through-the-thickness oriented fibers even though the specimen was injected in the longitudinal direction. The real fiber distribution around the notch was manually reconstructed and simulated with the FEM code ABAQUS. The combined effect of the notch and the fiber orientation distribution at crack initiation was studied. Highest matrix stress concentrations were found between through-the-thickness oriented fibers. This analysis is a preliminary step for the definition of a crack initiation criterion.

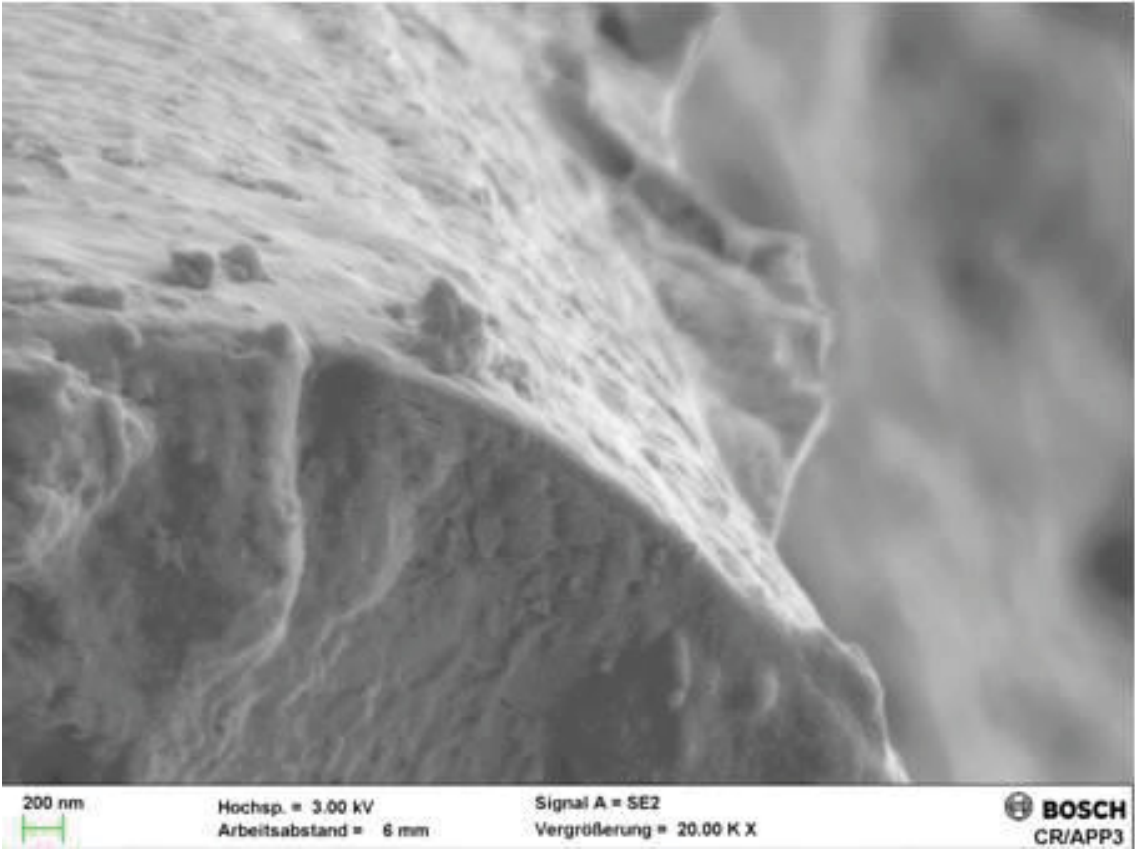
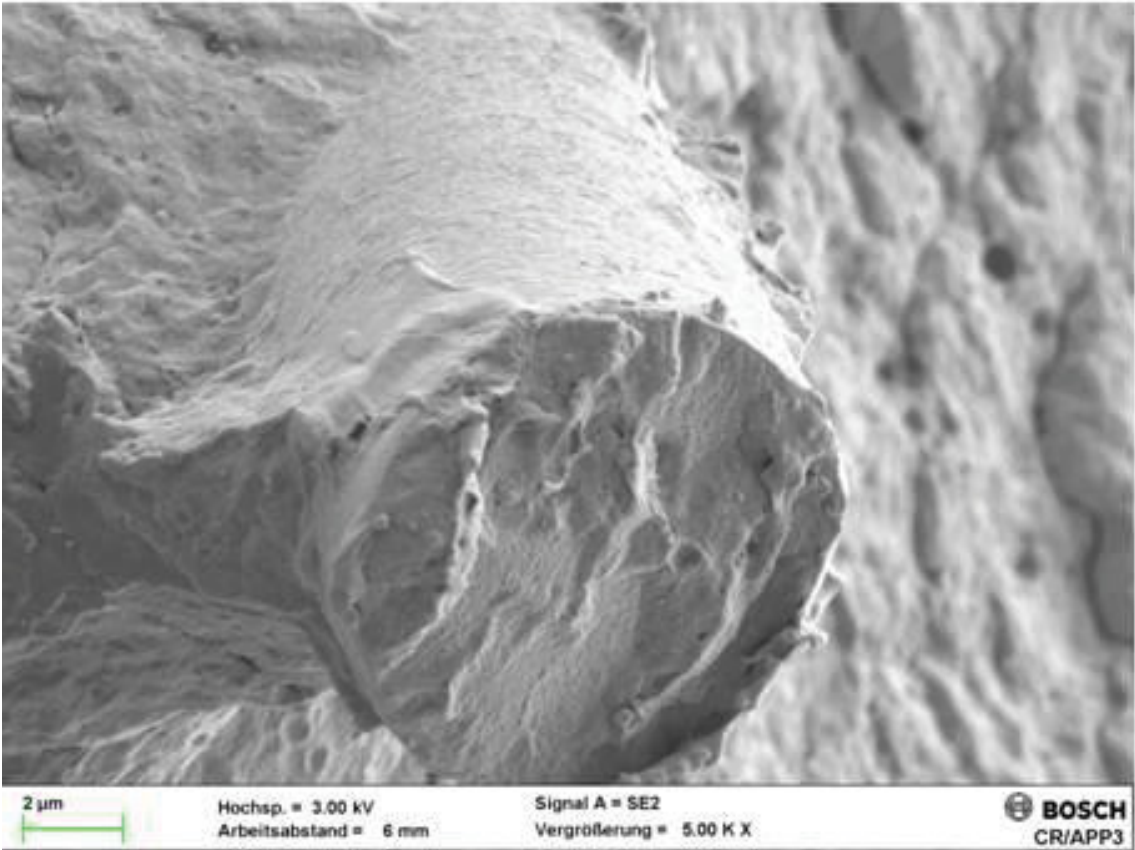
Finally, a multi-scale model for the crack initiation prediction of short glass fiber reinforced polyamide notched specimens has been presented in Chapter 8. In Chapter 5 and Chapter 7 it was found that in notched specimens, crack initiates mostly at clusters of through-the-thickness oriented fibers. Building on this experimental evidence, the microstructure was modeled as a bi-dimensional layer around the notch with a random distribution of through-the-thickness oriented fibers. The local stress distribution was studied with the submodeling technique. The global model was modeled at continuum level with the material properties of the composite. In the sub-model, fibers and matrix were explicitly modeled. This multi-scale strategy was used for the computation of the stress threshold which includes the highest 10 % of the stress distribution in the matrix. It was shown that this failure parameter was suitable for compress crack initiation data for different fiber fractions into a single scatter band relating the local matrix threshold stress amplitude to the number of cycles to crack initiation.

## Appendix A. Damage investigation

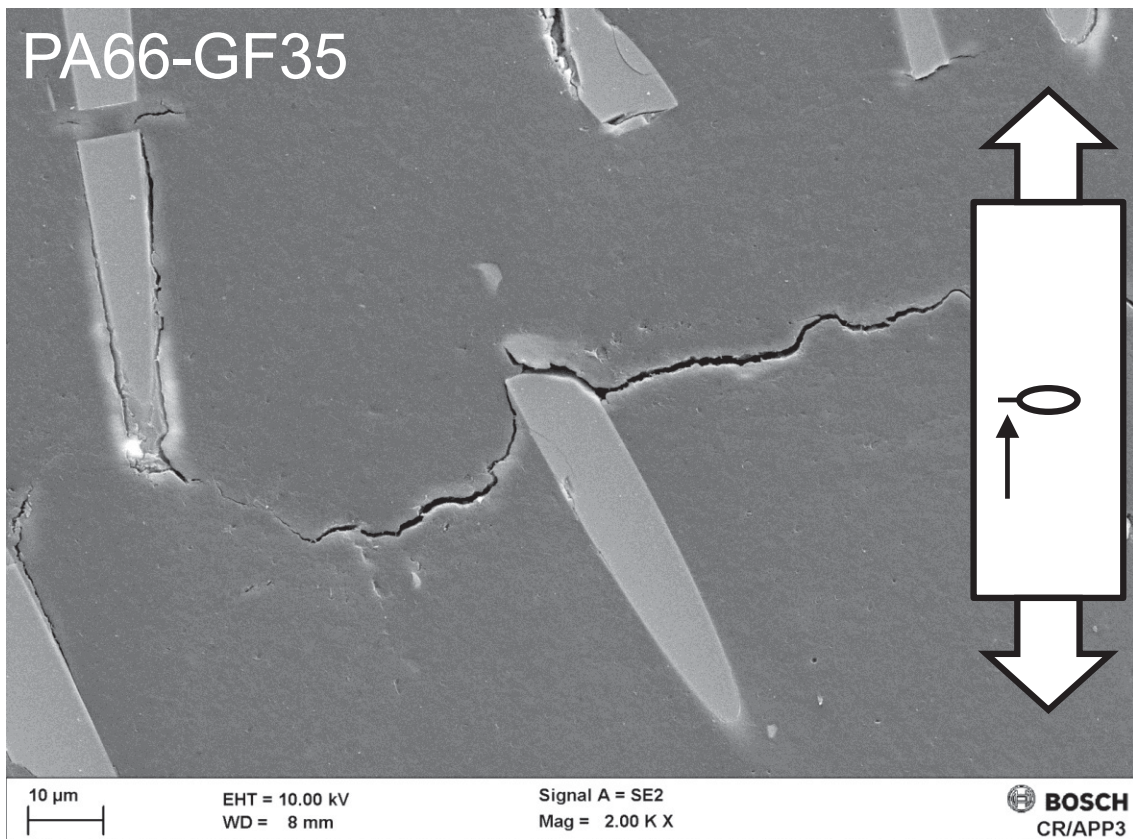
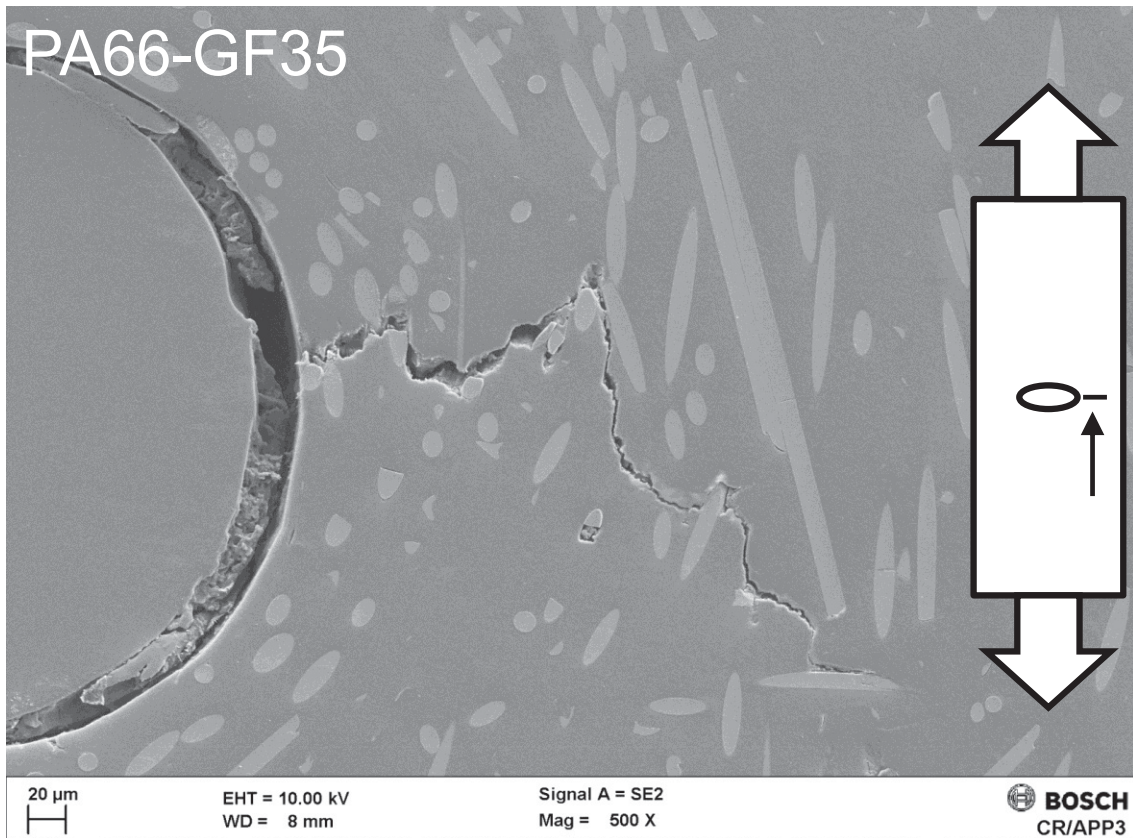
### 1. Analysis of the cryo-fracture surface of PA66-GF35 specimen





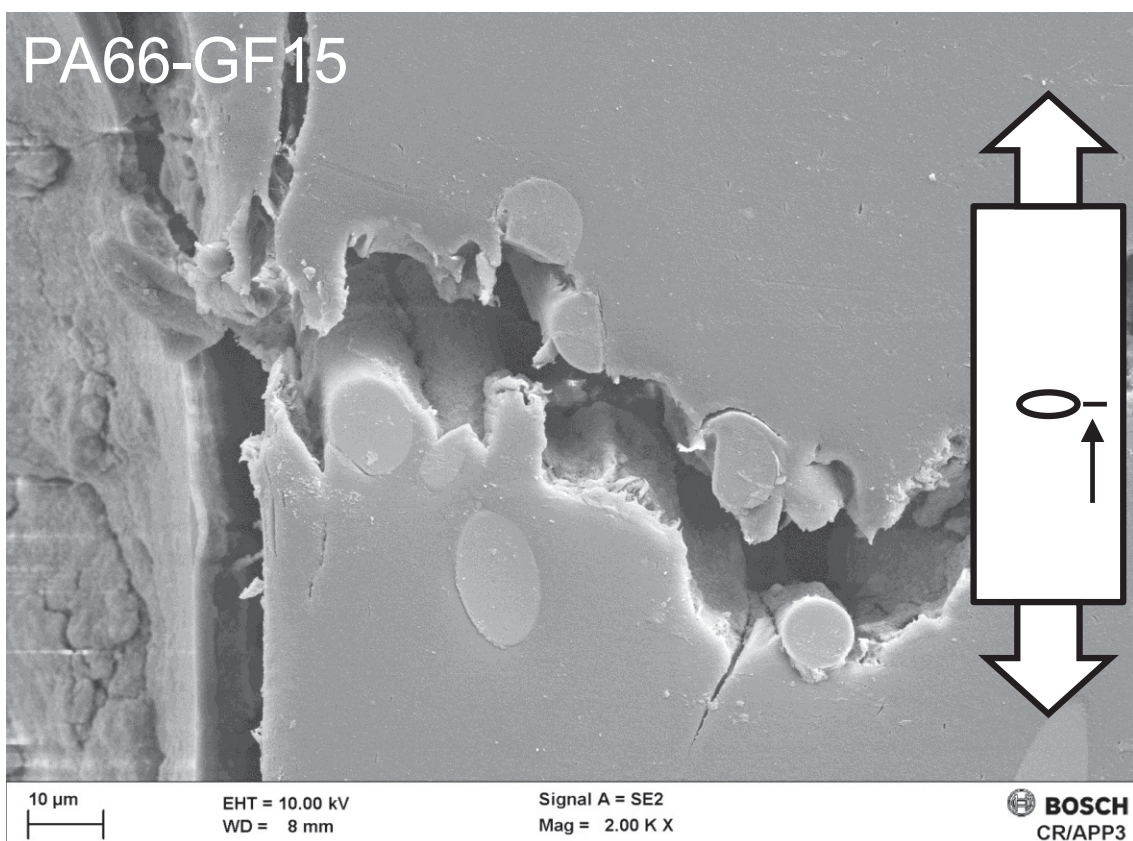
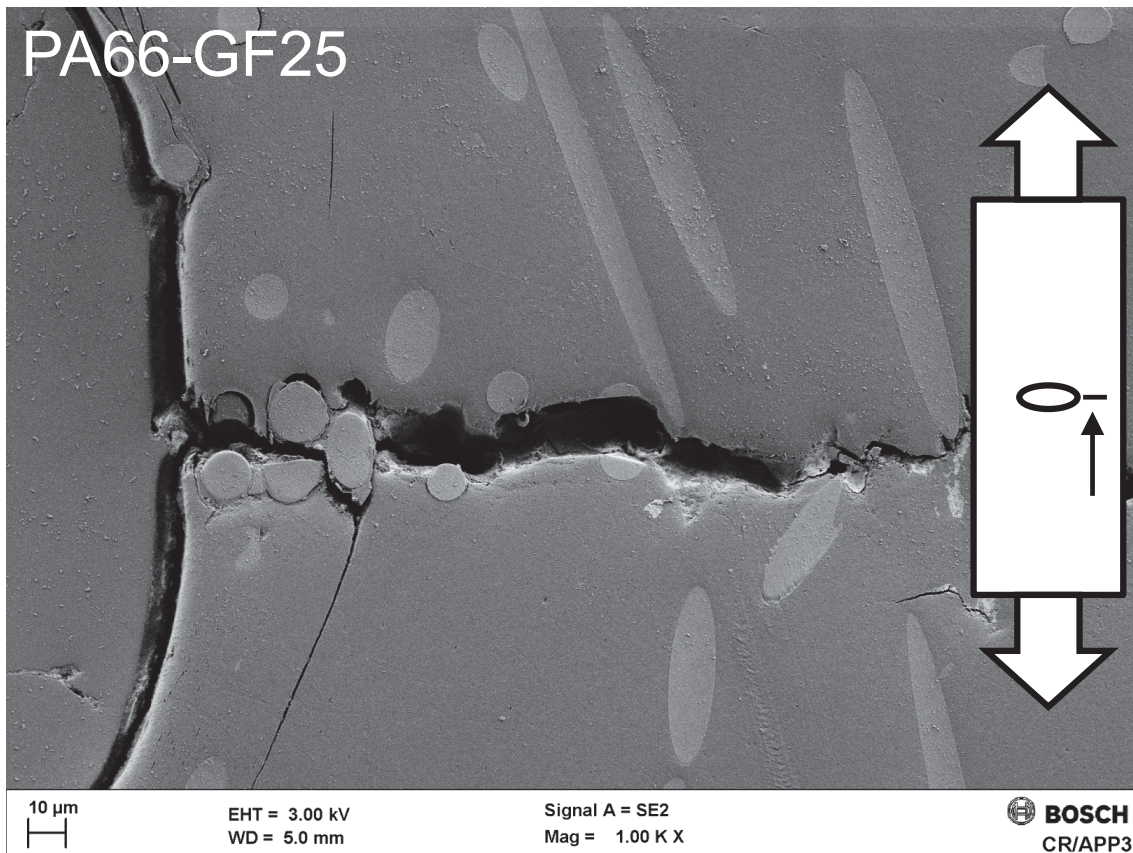


## 2. Fiber avoidance mode



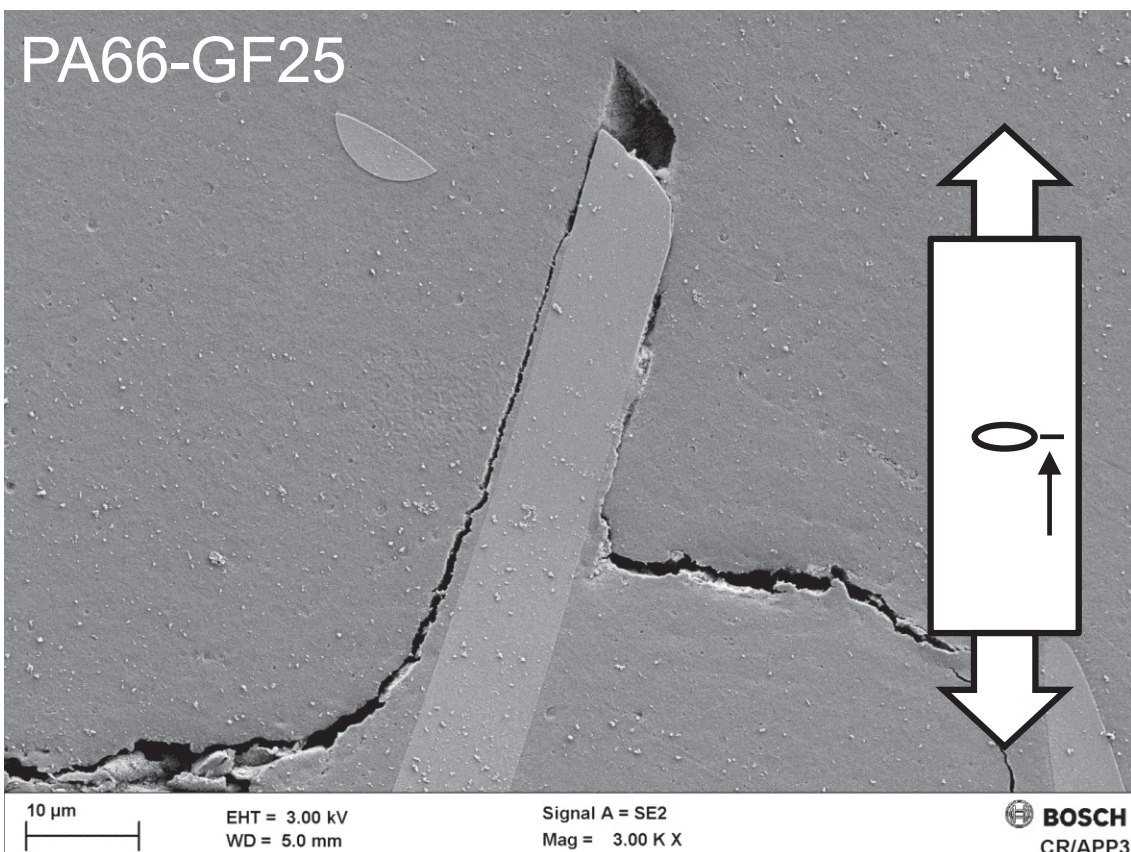
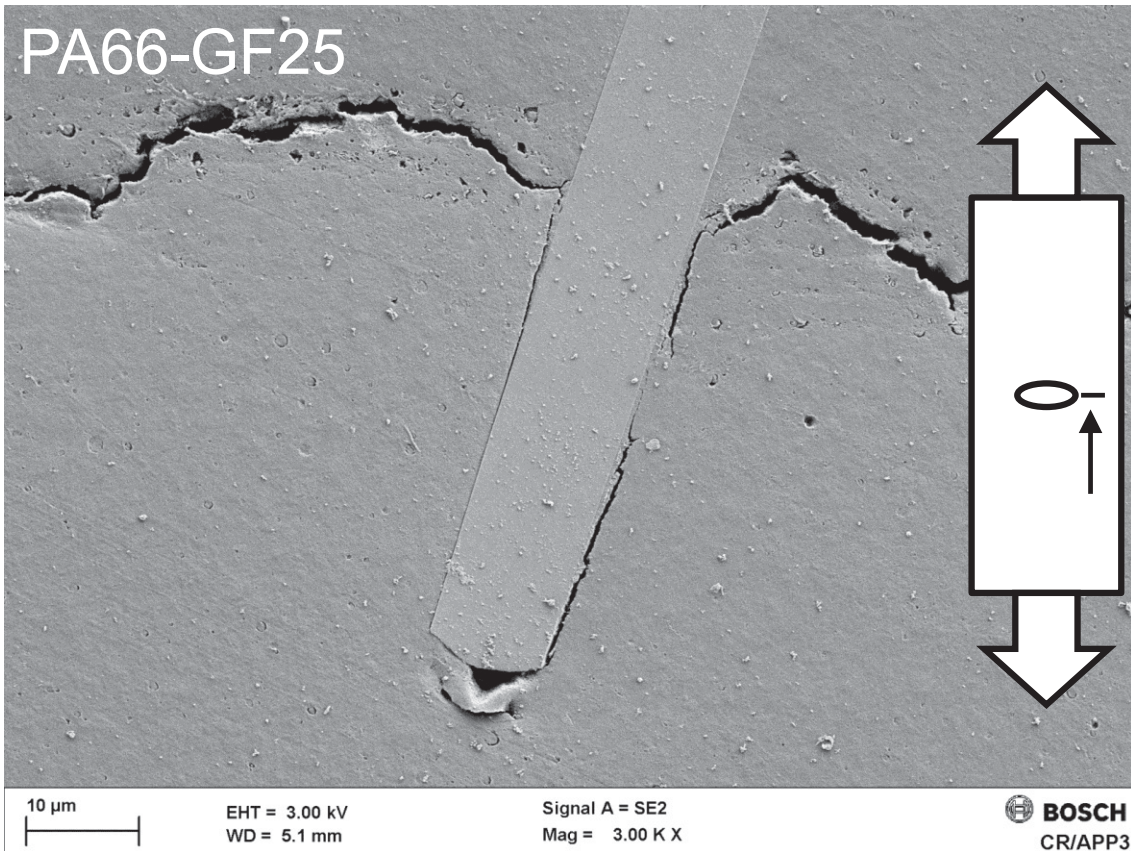


### 3. Clusters of through-the-thickness oriented fibers



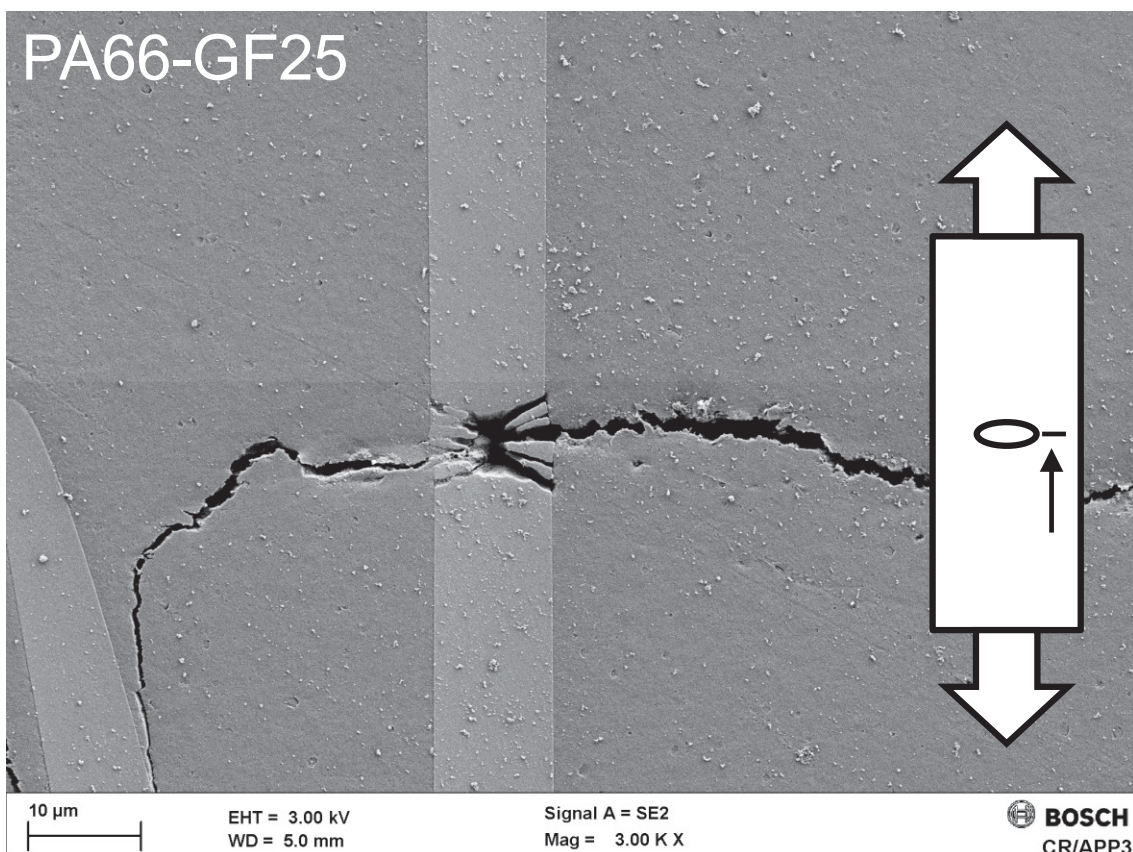
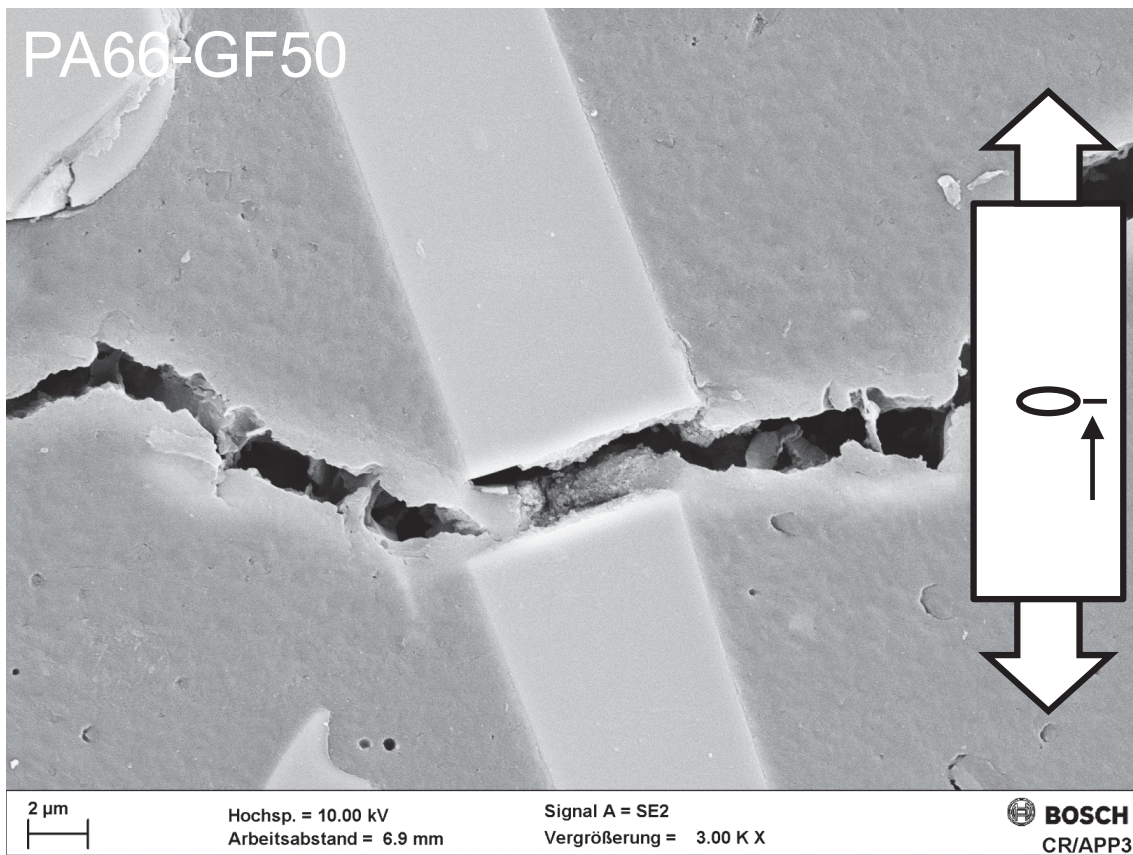


#### 4. Fiber pull-out



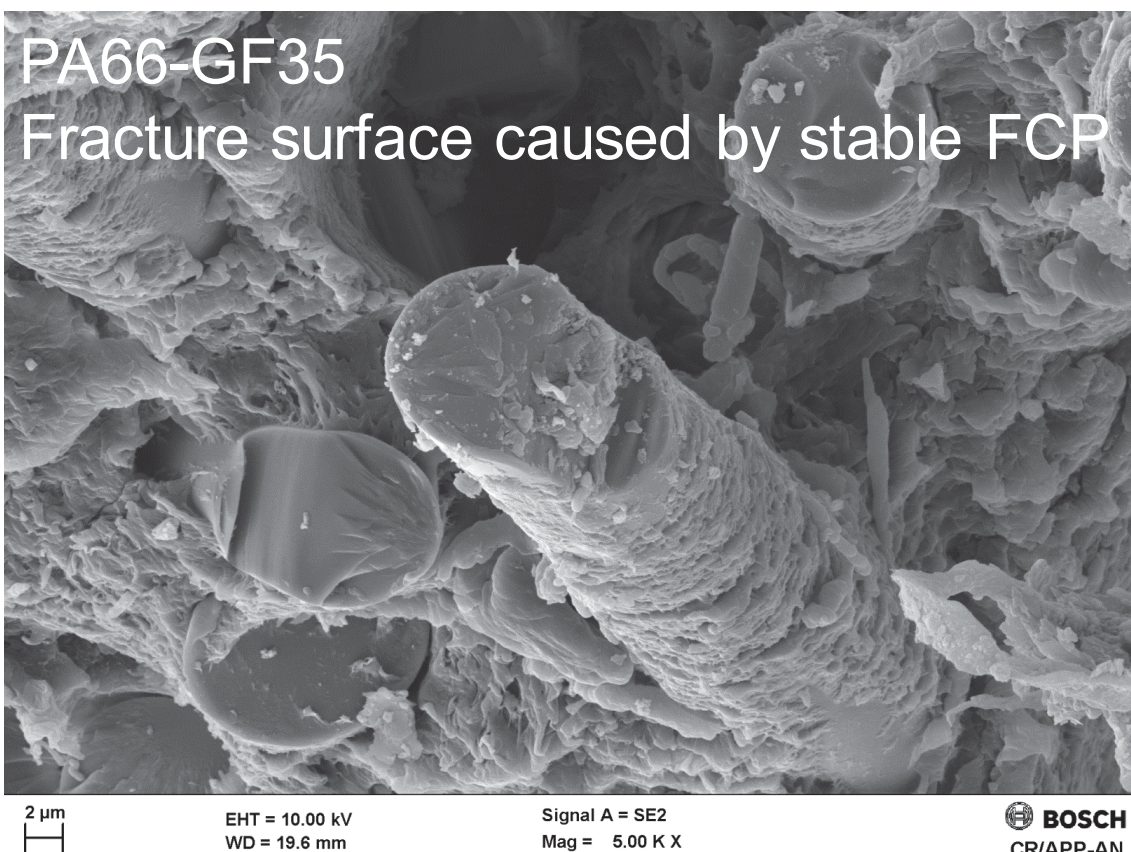
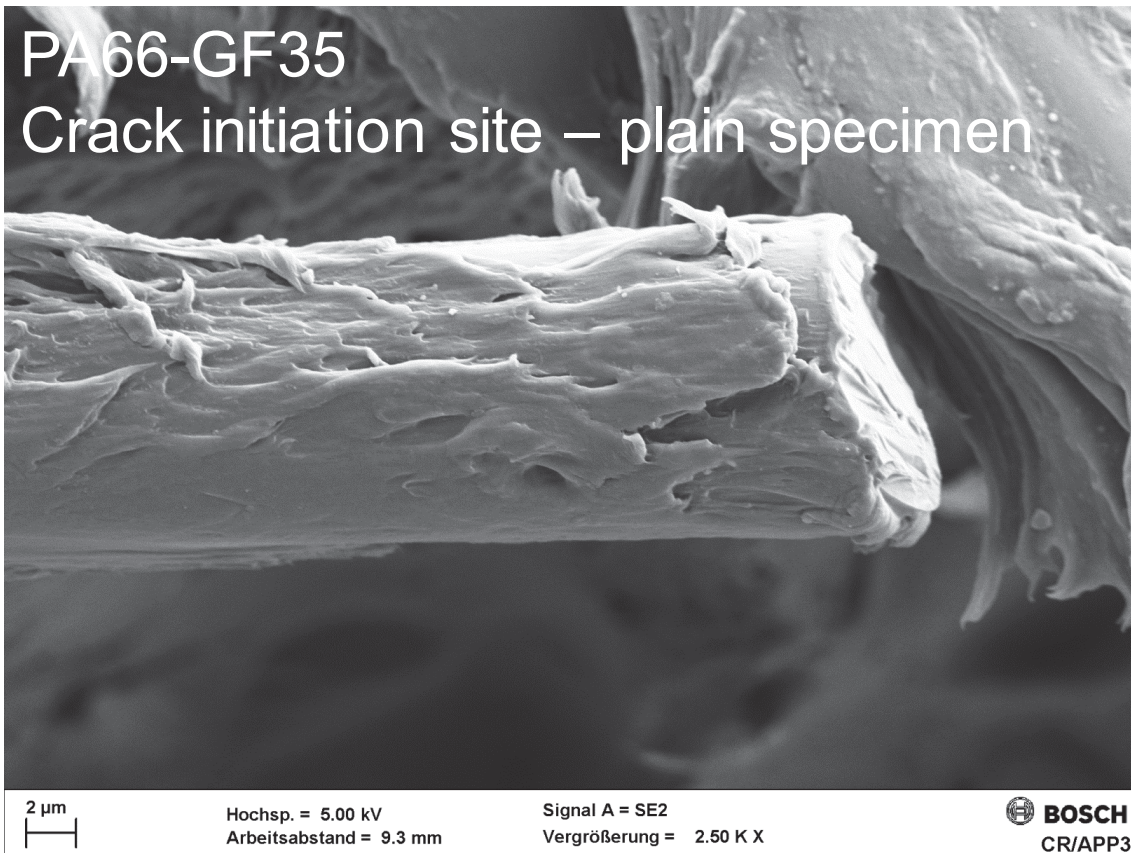


## 5. Fiber failure

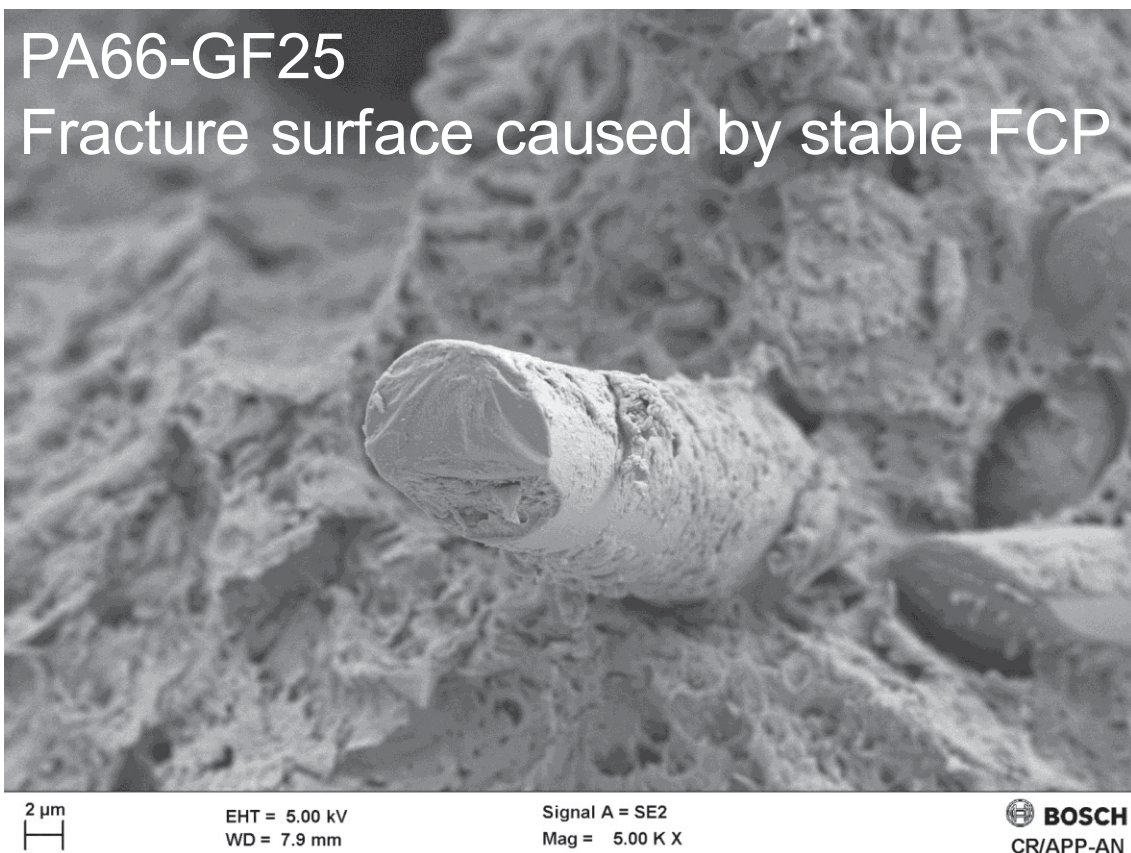
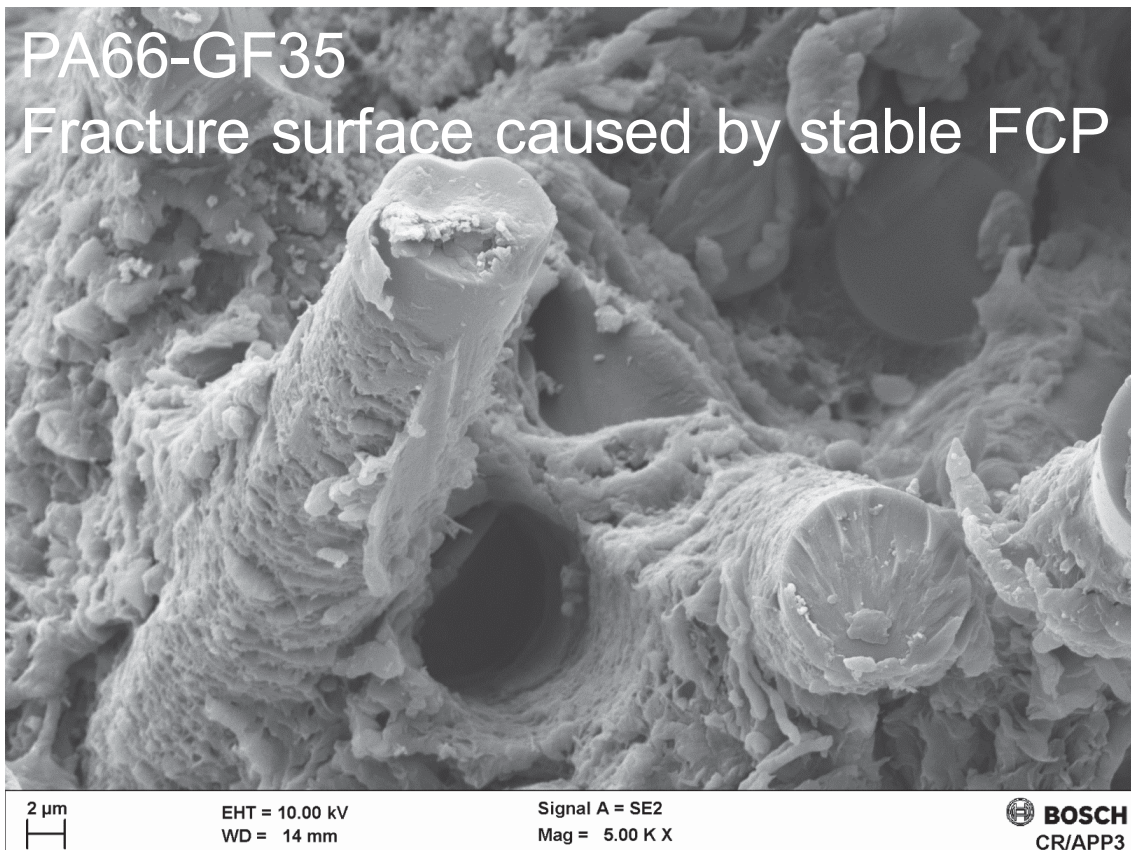




## 6. Degree of fiber-matrix adhesion



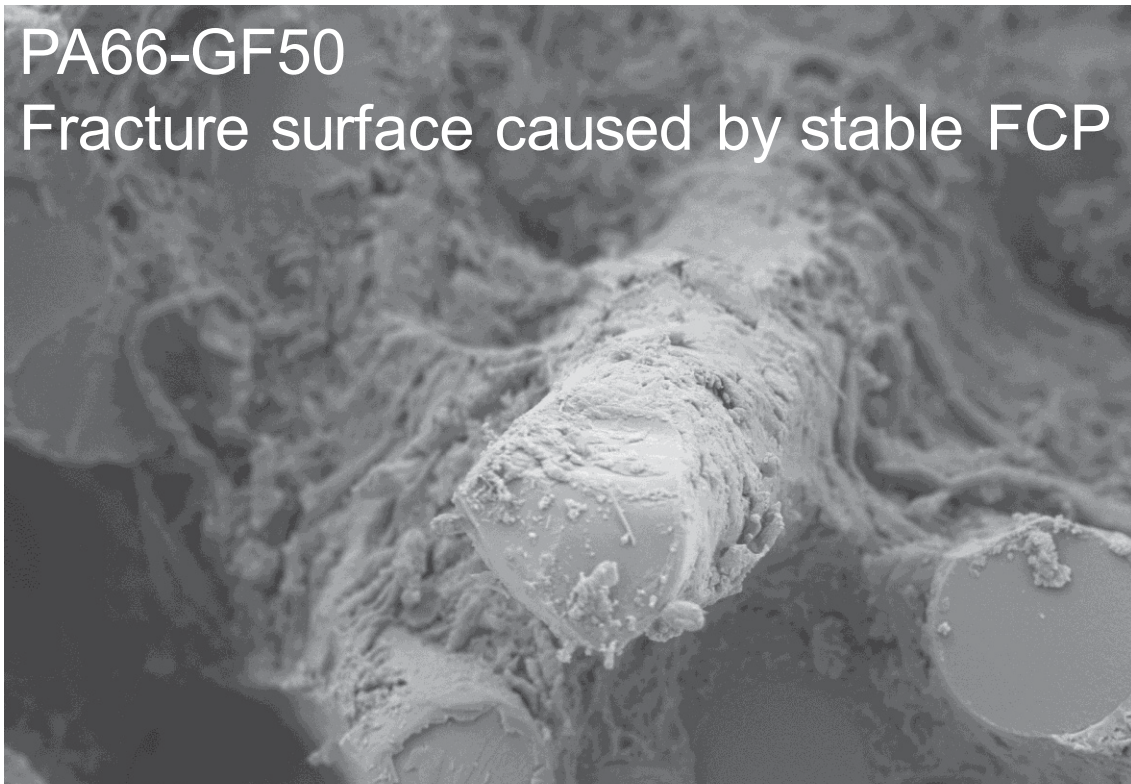






PA66-GF50

Fracture surface caused by stable FCP



2  $\mu$ m

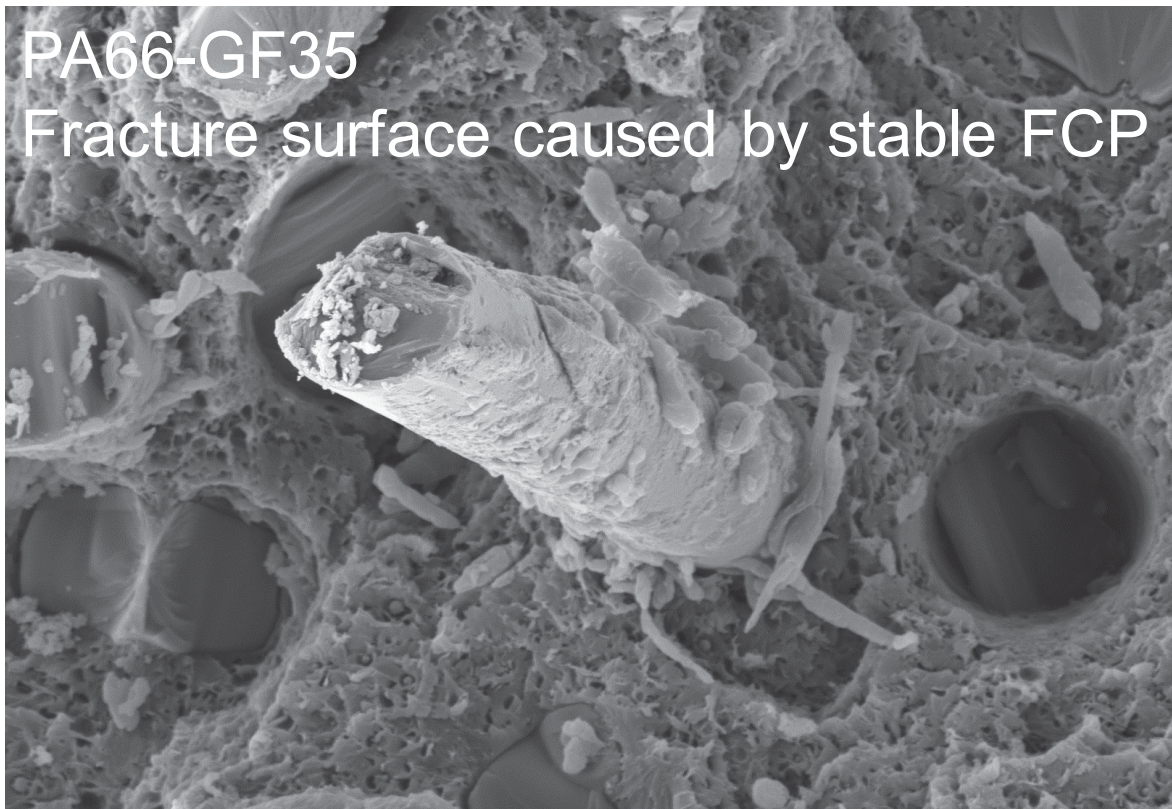
EHT = 5.00 kV  
WD = 9.6 mm

Signal A = SE2  
Mag = 5.00 K X

 **BOSCH**  
CR/APP-AN

PA66-GF35

Fracture surface caused by stable FCP



2  $\mu$ m

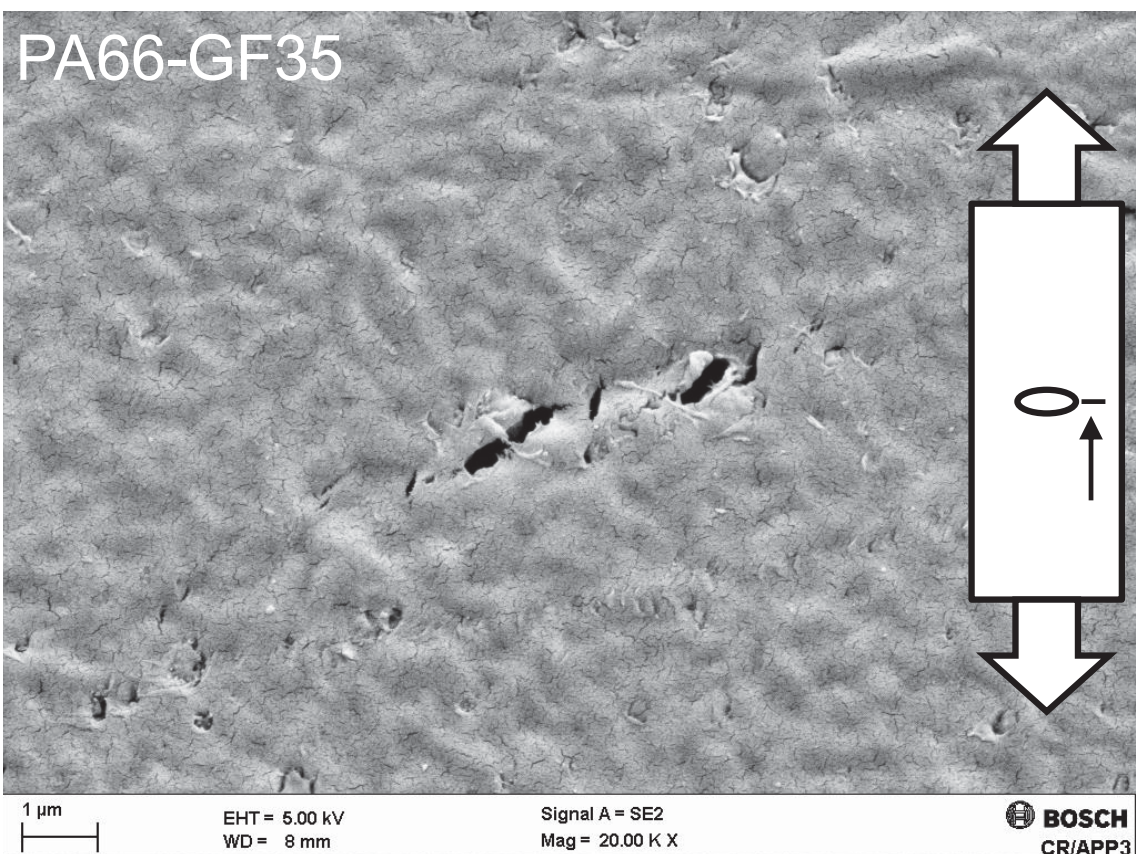
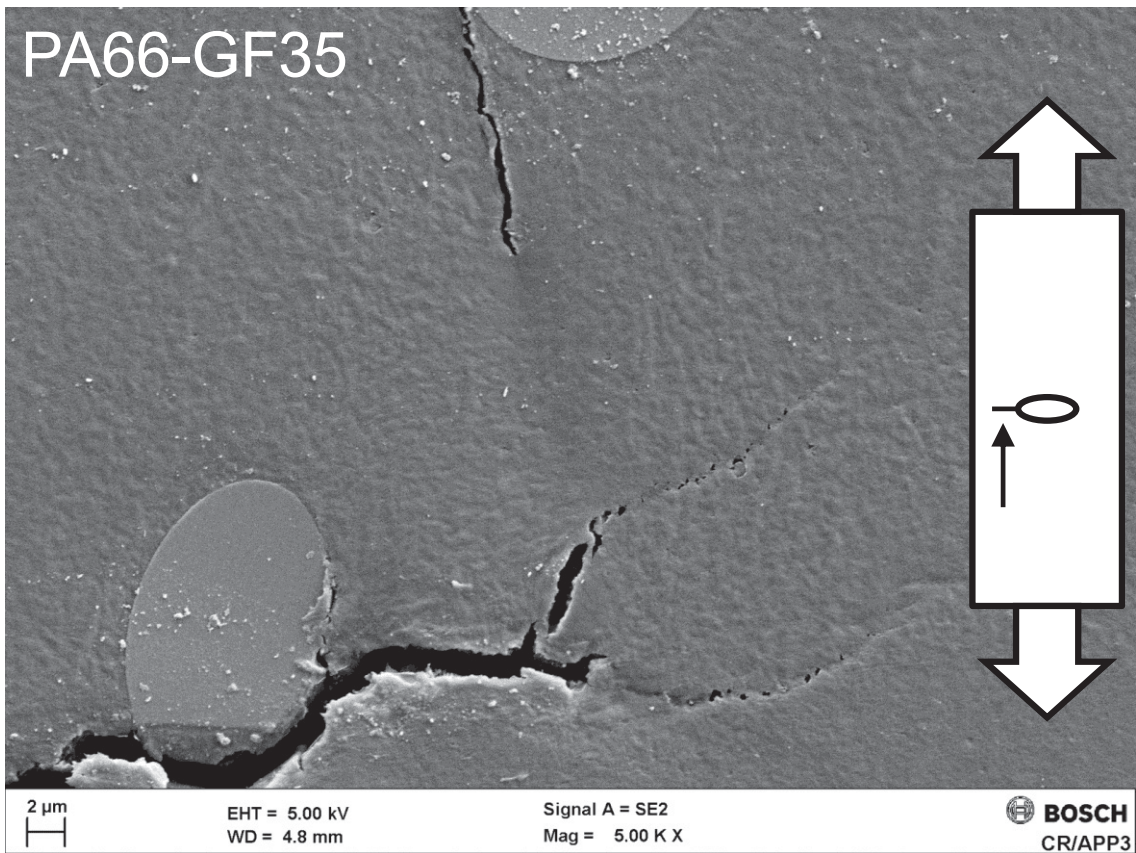
EHT = 10.00 kV  
WD = 20.3 mm

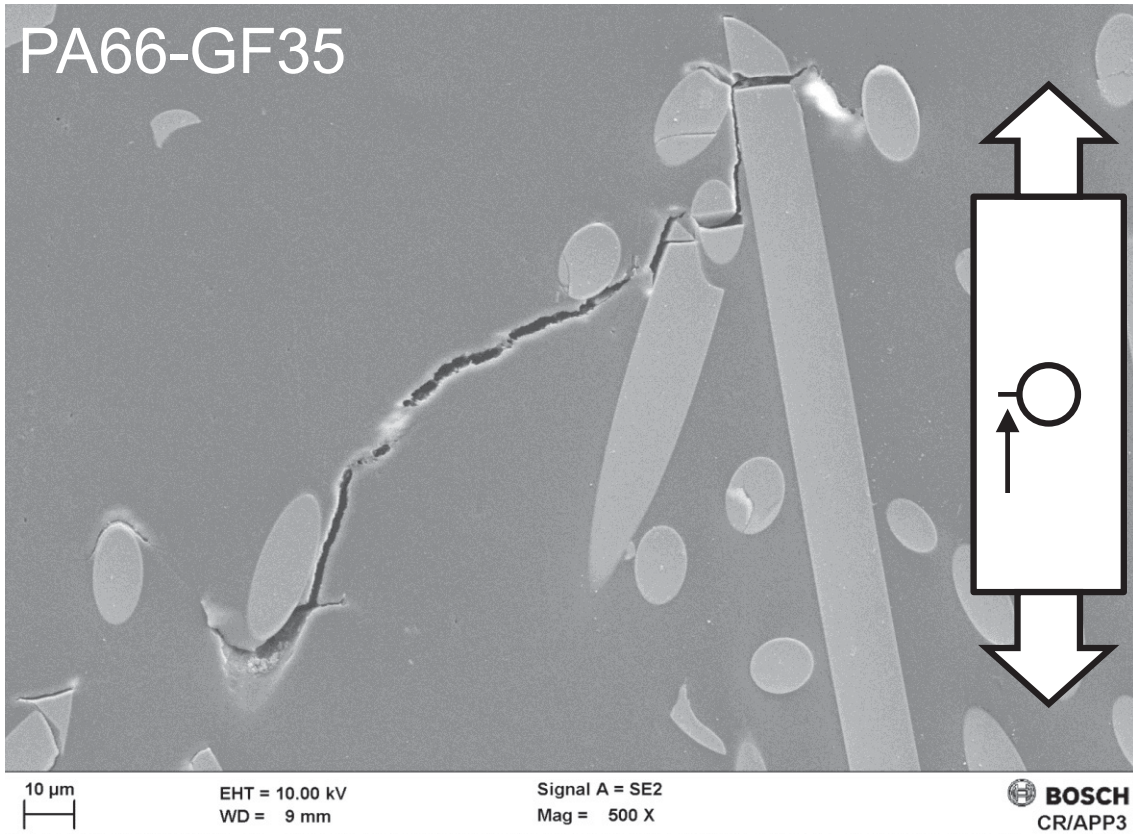
Signal A = SE2  
Mag = 5.00 K X

 **BOSCH**  
CR/APP-AN



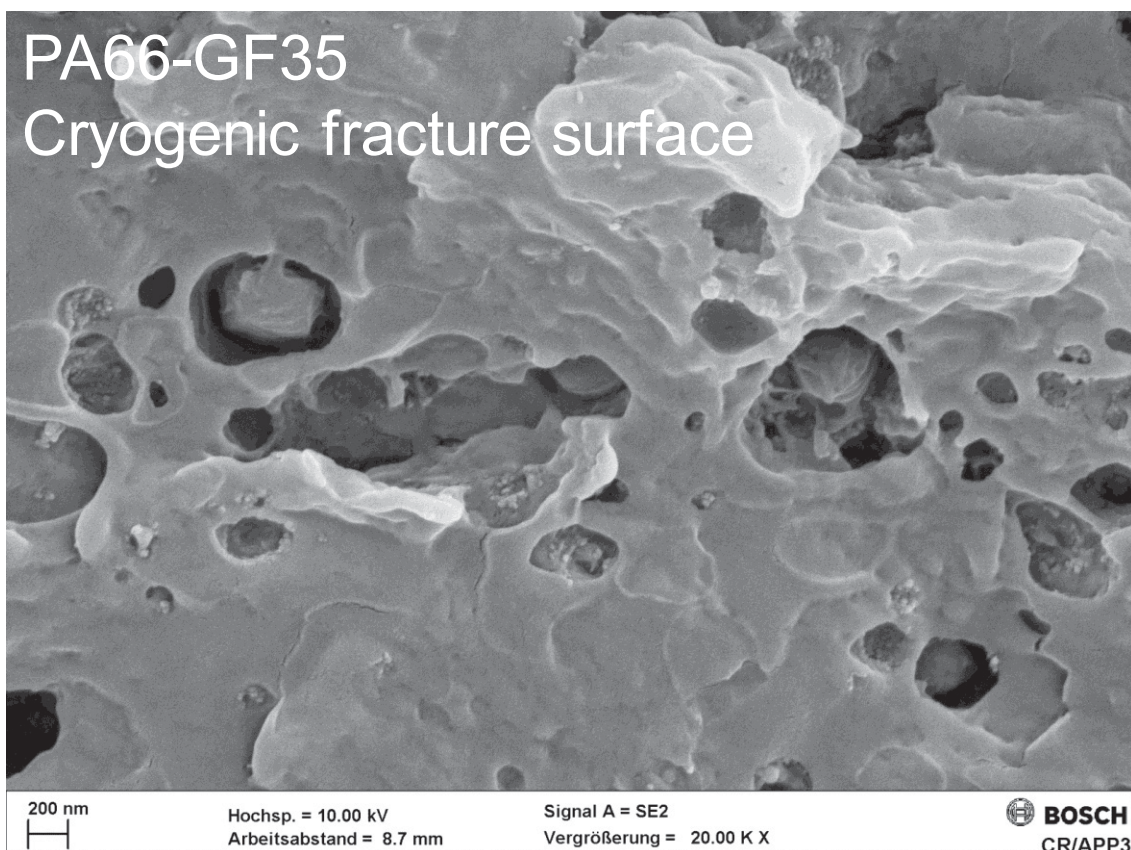
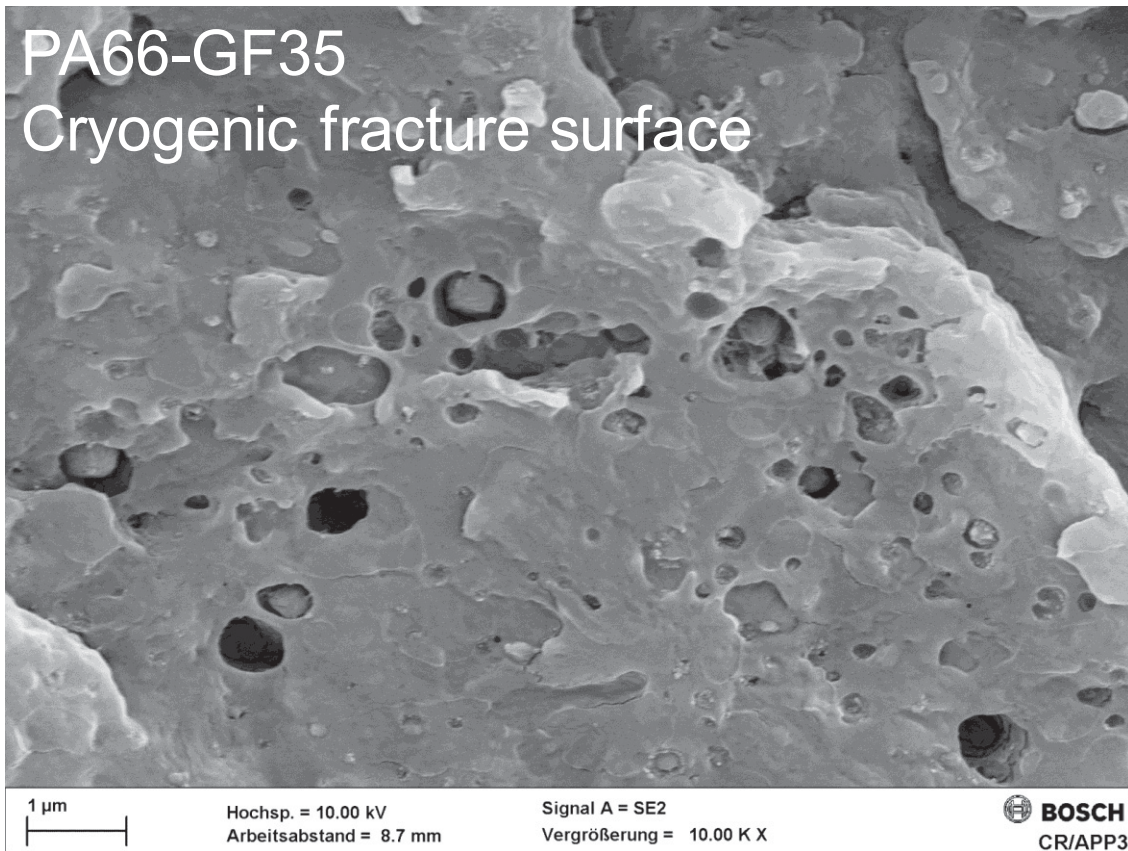
## 7. Matrix cracking



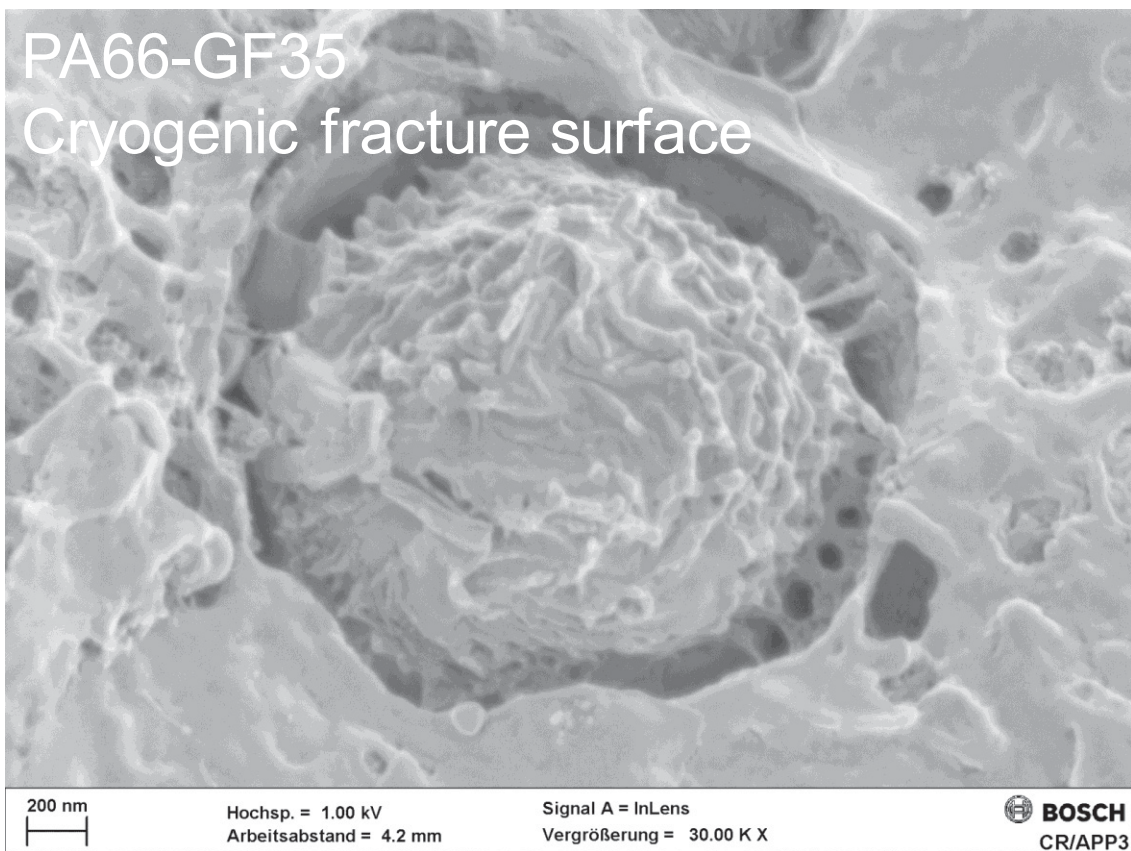
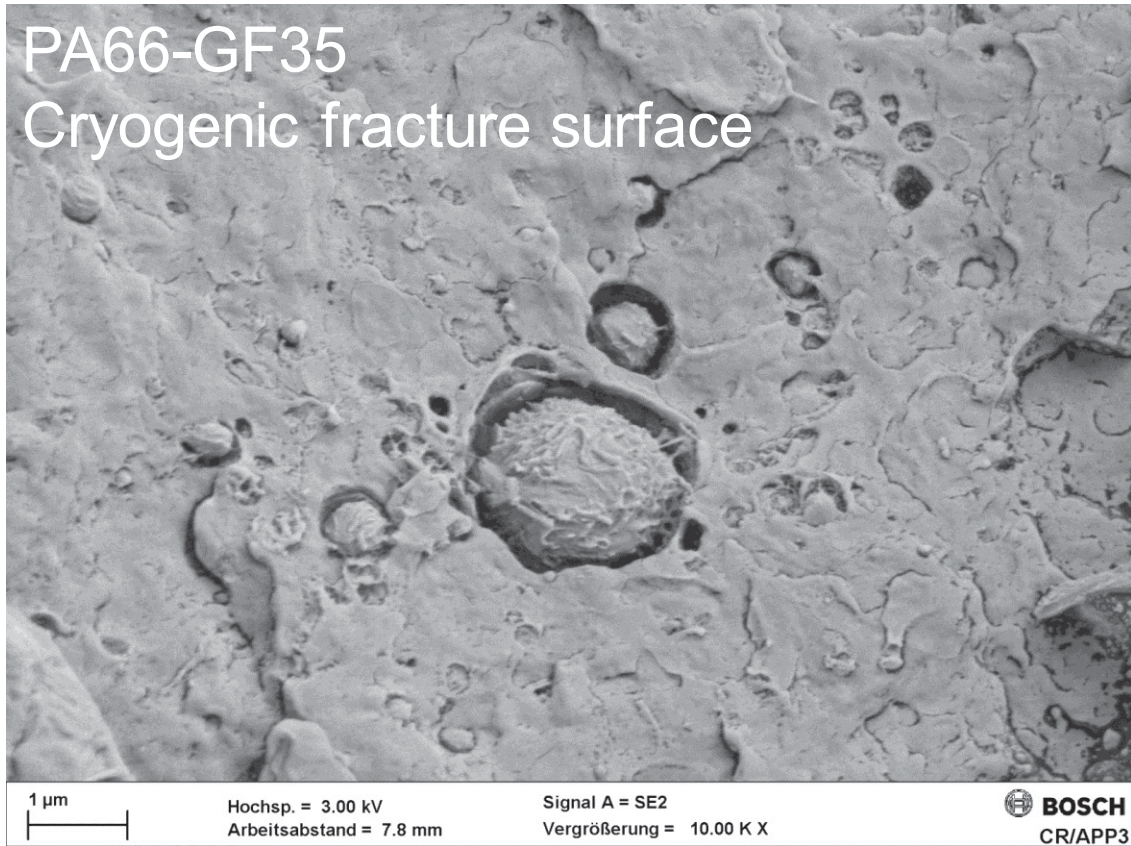




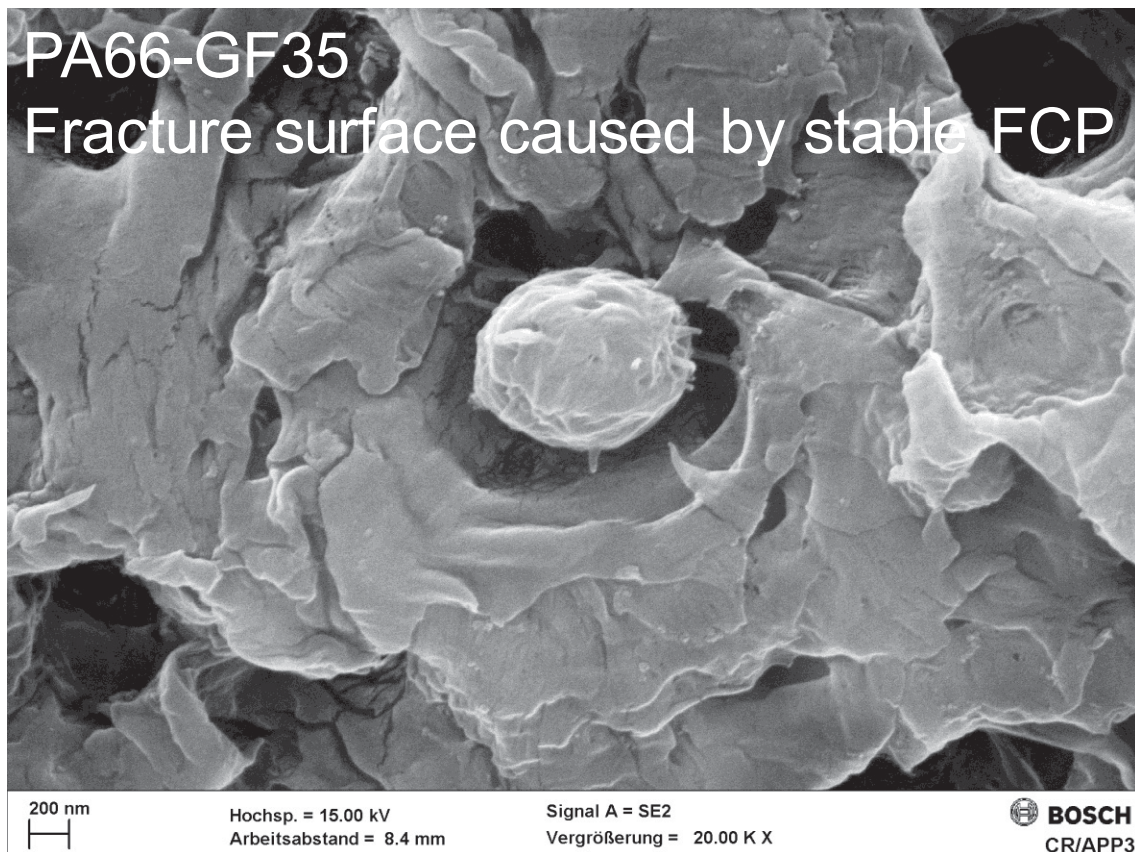
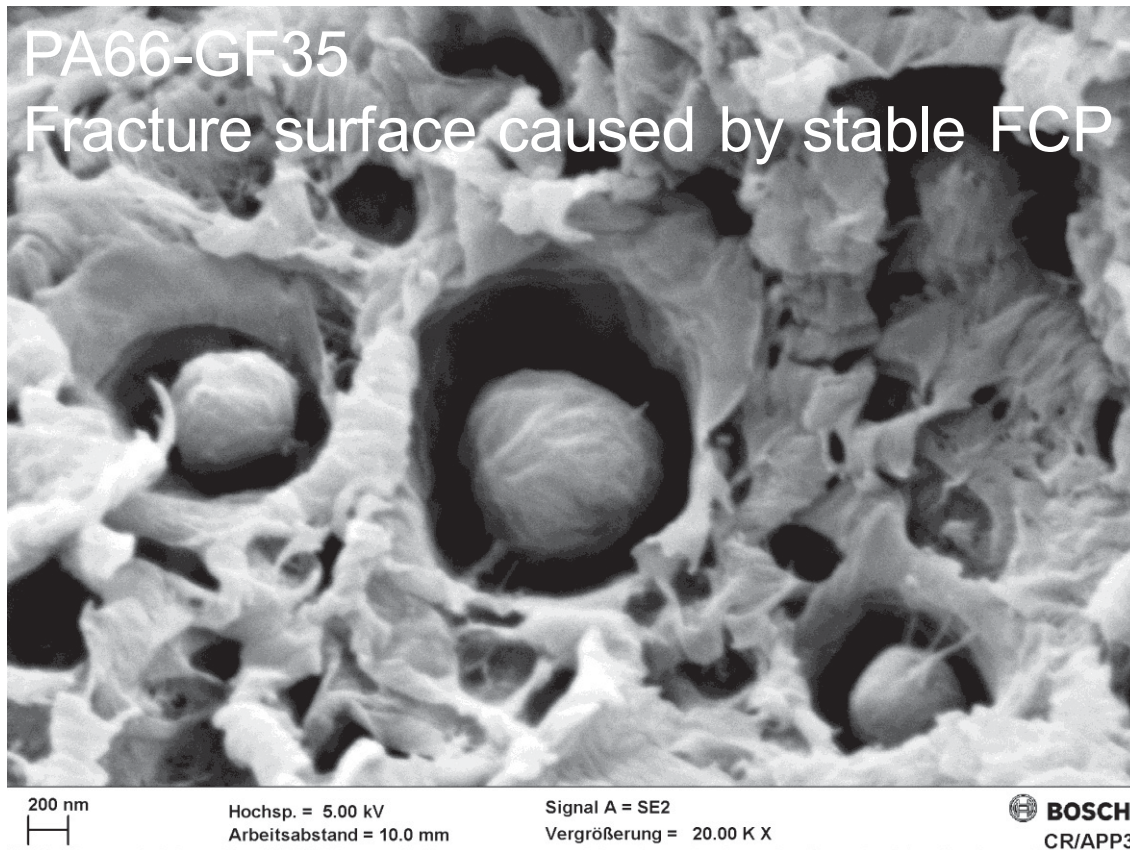
## 8. Voids and particles











## **Appendix B**

# **Use of Digital Image Correlation (DIC) for the crack initiation detection during fatigue tests of PA66-GF35 notched specimens**

## **1. Introduction**

Digital Image Correlation (DIC) was used for the crack initiation detection in short glass fiber reinforced polyamide notched specimens under fatigue loading. Bernasconi and coworkers [1] used DIC to study the strain field of notched specimens injected through different injection gates (longitudinal and lateral). They compared the local strain fields applying in a quasi-static manner a nominal stress corresponding to a lifetime of 1E6 cycles of the lateral injected specimen. They measured higher local strain values for the lateral injected specimen due a different fiber orientation distribution.

The aim of this work is to use the DIC as experimental method for the crack initiation detection in notched specimens of short fiber reinforced polyamide undergoing cyclic loading.

## **2. Experimental**

Uniaxial fatigue tests were carried out on a servo-hydraulic testing machine, equipped with a load cell of 10 kN under tension-tension loading (load ratio:  $R = 0$ ). Frequency was chosen in order to avoid the self-heating of the specimen and varies inversely with the load level. Temperature and humidity were not controlled during the tests. Fatigue tests were carried out until the separation of the specimen into two parts.

The material studied in the present investigation is a short fiber reinforced polyamide containing 35wt % glass fibers (designation PA66-GF35). Fibers have a diameter of 10  $\mu\text{m}$  and an average length of approximately 280  $\mu\text{m}$ . Notched specimens were used to facilitate the crack initiation detection. The dimensions of the specimen are shown in Figure 1.

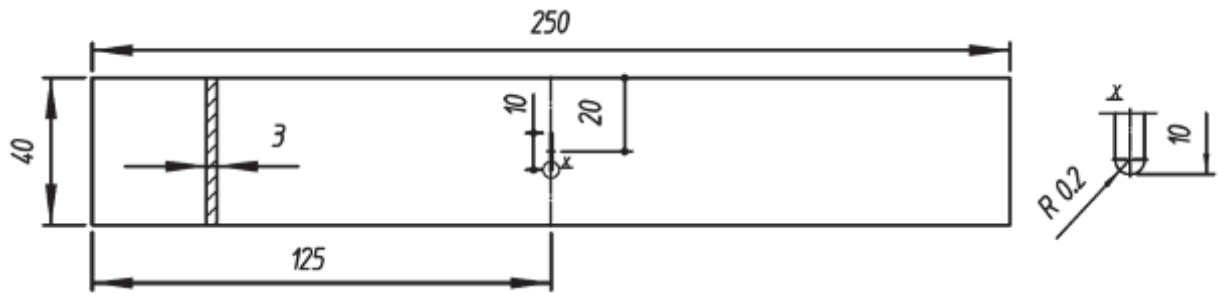


**Figure 1.** Specimen geometry and dimensions (in mm).

DIC analysis was performed using a commercial hardware and software package (ARAMIS) of the company GOM [2]. The image acquisition was performed using two digital CCD cameras with a resolution of 2 Megapixels (Figure 2a). Two high-performance LED lamps were mounted on the framework to illuminate the specimen surface resulting in a better image contrast (Figure 2a). The angle between the cameras and the angle between the lamps are set based on the size of the volume of interest. The image of the specimen surface is digitized on a pixel-by-pixel basis using the CCD digital cameras. Each pixel is characterized by a specific grey value. DIC is based on tracking the movement of a pixel subset (facet) over a series of images. Facets are therefore like strain gages which measure the strains at the local level on the specimen surface. For a better image contrast, the specimen surface was sprayed by means of a semi-gloss white spray (Figure 2b).



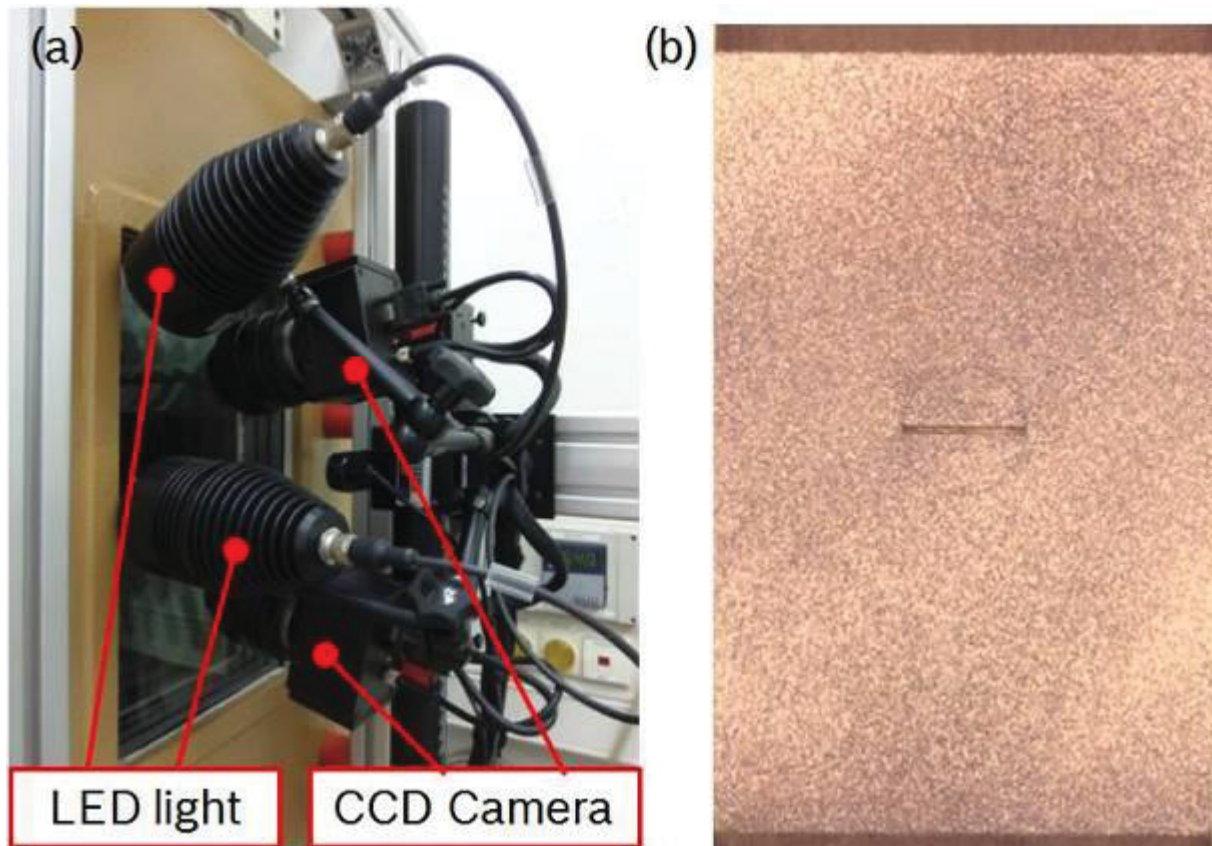


**Figure 2.** (a) Experimental set up; (b) Applied speckle pattern.

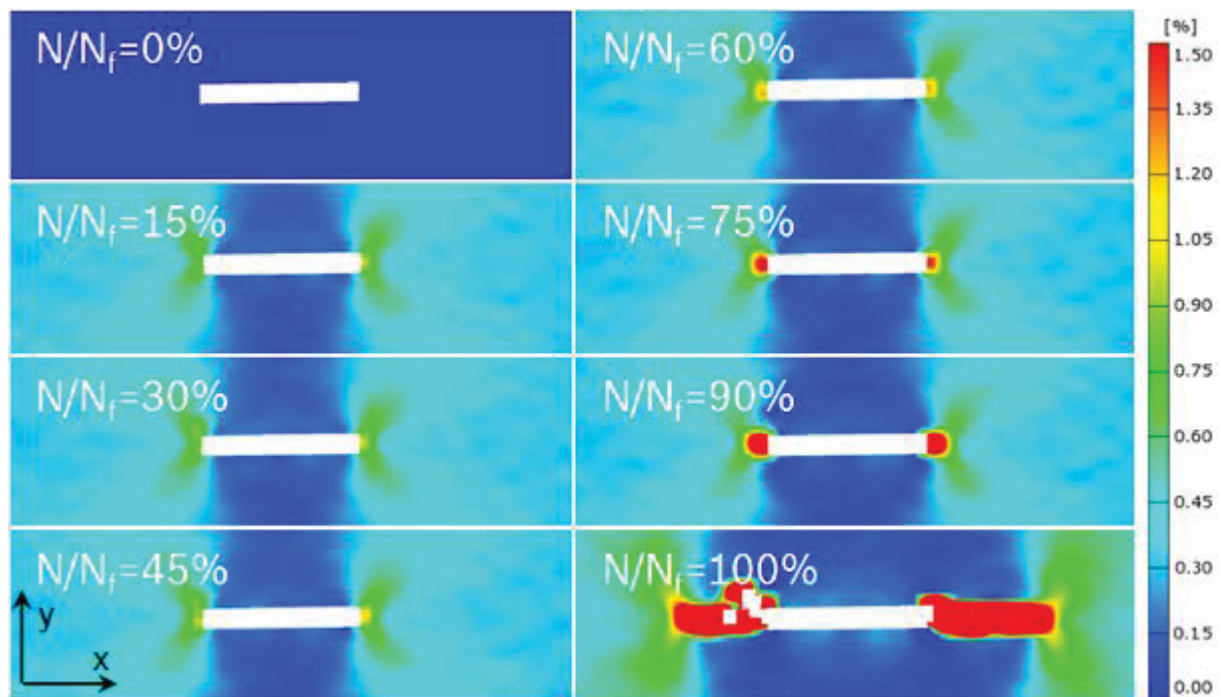
The grayscale histogram is a measure of the image contrast. The application of a speckle pattern to the specimen surface results in a more balanced distribution of the black and white pixels in the facets. In the present analysis, each facet has  $17 \times 13$  pixels. The image capture rate was adapted to the testing frequency. The image capture system was triggered with the cyclic loading. A picture was taken when the load reaches the 90 % of the maximum load. Data were post processed using the ARAMIS software. The filter option was used to reduce some of the experimental noise.

Some fatigue tests were interrupted before final failure in order to study a possible correlation between the strain evolution at the notch tips and the crack length. A sample surrounding the notch was machined from the specimen and prepared for the microscopic investigation. For the measure of the crack length, an optical microscope (Axio Scope.A1) was used.



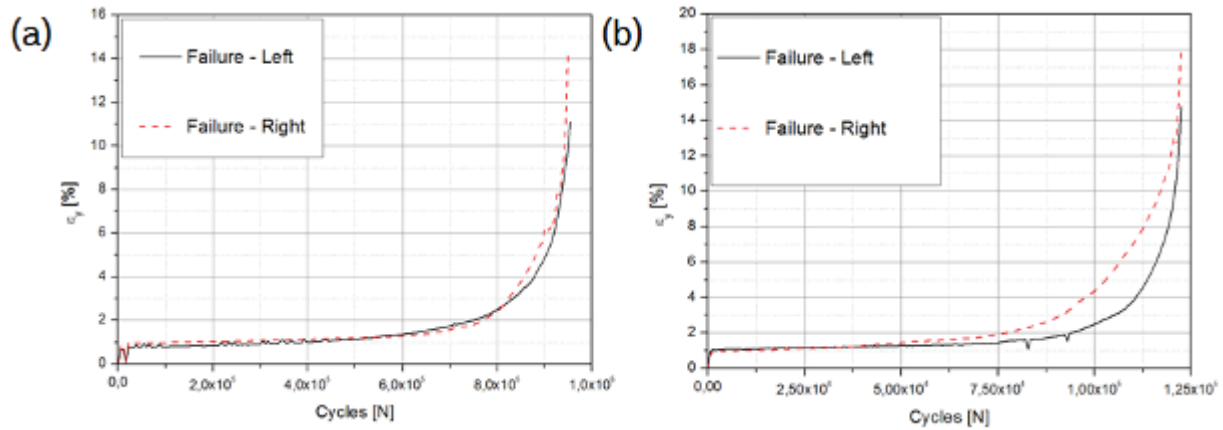
### 3. Results and discussion

Figure 3 shows the evolution of the normal strain  $\epsilon_{yy}$  during a fatigue test ( $\sigma_a = 18$  MPa;  $N_f = 954241$  Cycles). The U-form of the notch leads to a butterfly-shaped strain distribution. Strain peaks are located at the notch tip. No significant variation of the normal strain at the notch tips was observed for approximately half of the fatigue test. Thereafter, two local strain spots at the notch tips occur.



**Figure 3.** Evolution of the normal strain  $\epsilon_{yy}$  at the notch tips during a fatigue test.

The strain evolution shown in Figure 3 is graphically reported in Figure 4a. The maximum strain values at left and right side of the notch are plotted against the number of cycles. The strain profiles can be divided into two stages. At the beginning, the strain increases linearly. Before the specimen failure, a non linear trend of the maximum strain profile is noted. The two strain profiles almost coincide indicating that the crack propagation at left and right of the notch is almost equal. That is not true for all the performed tests. Figure 4b shows the strain evolution in another fatigue test carried out at the same load level. During the first part of the fatigue test, the maximum normal strain  $\epsilon_{yy}$  does not show any significant discrepancy between the left and the right of the notch. A gap opens when the curves develop a nonlinear trend. That occurs when one of the two cracks becomes dominant over the other.



**Figure 4.** Maximum strain profile at the notch tips during the fatigue tests. (a) Strain profiles almost coincide throughout the whole fatigue test. (b) A gap between the strain profiles is observed in the non-linear part of the curves.

In Figure 5, the maximum strain profiles are plotted for different tests characterized by the same load level. The trend of the strain profiles is similar. However, a significant scatter of the absolute strain values in the first stage of the fatigue tests can be appreciated (Figure 5b).

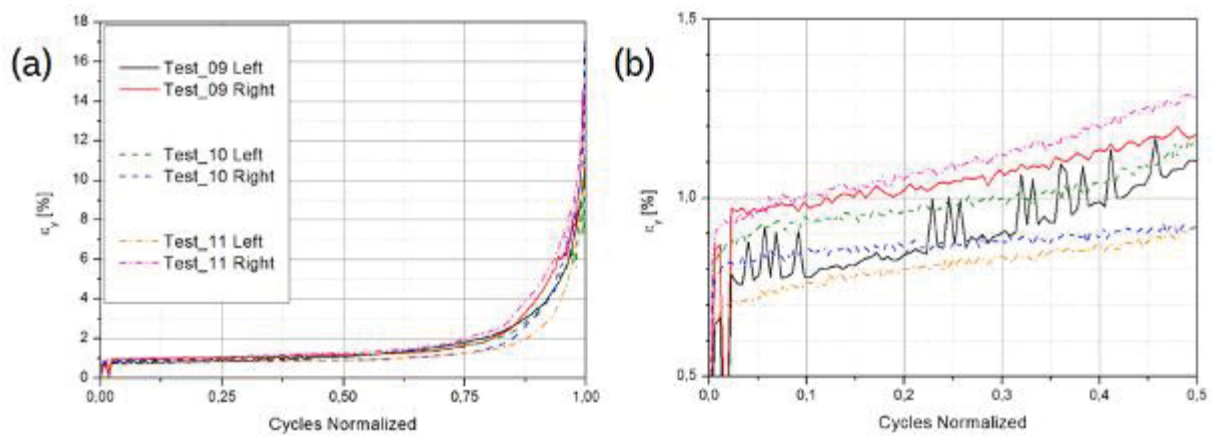


**Figure 5.** Strain profiles plotted against the normalized lifetime. The fatigue tests are characterized by the same load level: (a) Strain profiles throughout the tests; (b) Strain profiles until 50% of the total lifetime.

Due to the data scatter, the maximum strain cannot be used for the crack initiation detection. Another criterion is that a crack occurs when the strain profile develops a nonlinear trend. In Figure 6, the profiles of the maximum strain at the both sides of the notch are plotted for a fatigue test carried out until failure and for a interrupted fatigue test, for the same load level ( $\sigma_a = 18$  MPa). The fatigue test was stopped at half of the expected total lifetime of the

specimen. No variation of the strain profile can be appreciated before interrupting the test. Figure 6c and Figure 6d show that when the test fatigue test was interrupted, two macro cracks were already propagating from the notch tips.

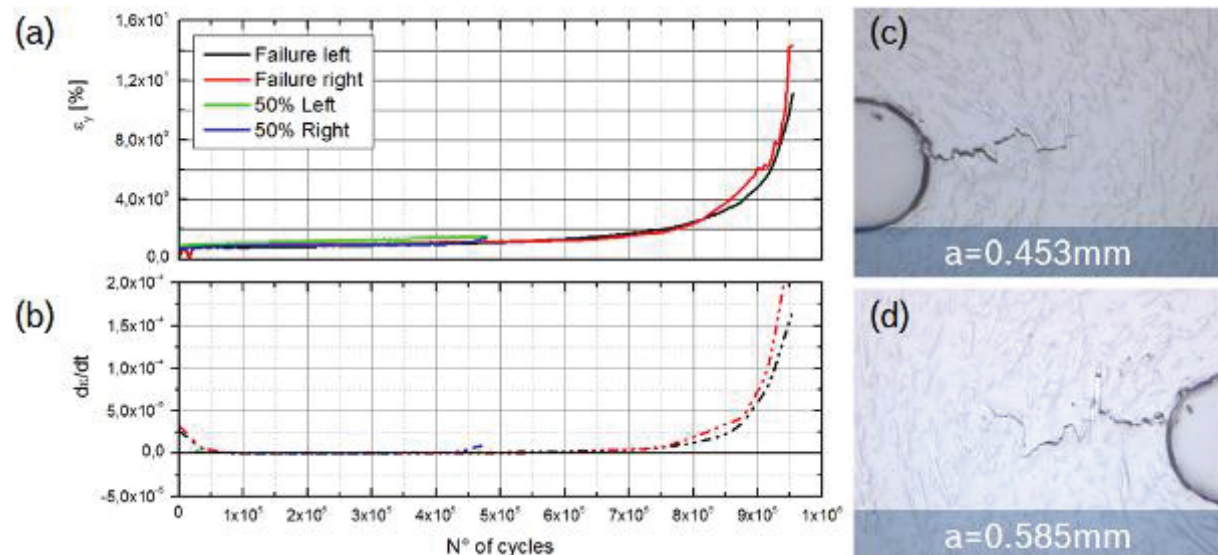


**Figure 6.** Interrupted fatigue test ( $N / N_f = 50 \%$ ) and microscopic analysis of the crack length: (a) Profile of the maximum strain over the lifetime; (b) Profile of the maximum strain rate over the lifetime; (c) Micrographs at the right of the notch; (d) Micrographs at the left of the notch;

Another fatigue test was interrupted for  $N/N_f = 70 \%$  (Figure 7). The length of the cracks is almost twice of the crack measured in Figure 6. At the left of the notch, where the longer crack is measured, the strain profile has just overcome the linear part of the diagram. The analysis of the interrupted fatigue tests gives an idea of the method accuracy. With the DIC based method, it is not possible to measure cracks shorter than 0.7 mm.

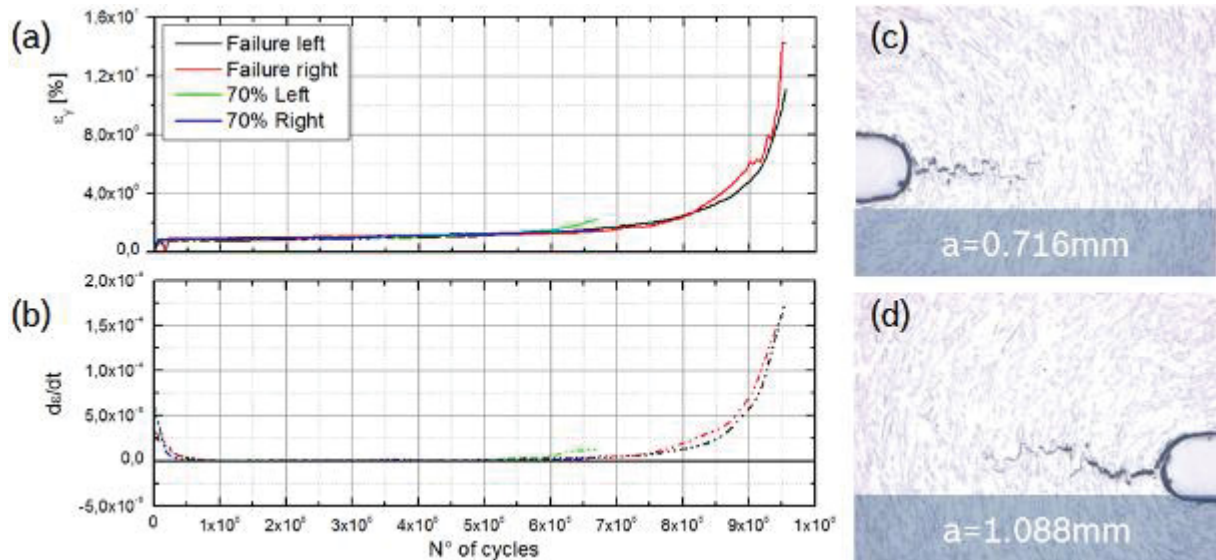


Figure 7. Interrupted fatigue test ( $N / N_f = 70 \%$ ) and microscopic analysis of the crack length

#### 4. Conclusions

DIC was used for the crack initiation detection in notched short glass fiber reinforced polyamide specimens under fatigue loading. The profile of the maximum normal strain at the notch tips during a fatigue test can be divided into a linear and a non-linear part. Two variables were investigated for the crack initiation detection. 1) The maximum normal strain; 2) The maximum strain rate. The maximum normal strain has high scatter. Therefore it cannot be used for the crack initiation detection. It was found that the maximum strain rate is non zero when a macro crack is already propagating. Concluding, for the set-up presented in this work, DIC enables the detection of macro cracks longer than 0.7 mm. Improvements in terms of resolution and accuracy are under investigation.

#### References of Appendix B

[1] A. Bernasconi, F. Cosmi, E. Zappa, Combined Effect of Notches and Fibre Orientation on Fatigue Behaviour of Short Fibre Reinforced Polyamide, *Strain*. 46 (2010) 435-445.

[2] ARAMIS, User Manual by GOM GmbH. Germany, Braunschweig, 2011, version.





## List of publications

### International Journals

1. Belmonte E. Moosbrugger E. Quaresimin M. De Monte M. Life to crack initiation in notched specimens of unreinforced and short fiber reinforced polyamide under fatigue loading. To appear.
2. Belmonte E. De Monte M. Quaresimin M. Hoffmann C. Fatigue damage mechanisms in a short glass fiber reinforced polyamide 6.6. To appear.
3. Belmonte E. De Monte M. Quaresimin M. Hoffmann C. Damage evolution in short fiber reinforced polyamide under fatigue loading: influence of the fiber volume fraction. To appear.
4. Belmonte E. De Monte M. Riedel T. Quaresimin M. A study of the matrix microscopic stress concentrations at crack initiation in a short fiber reinforced polyamide under fatigue loading. To appear

### International Conferences

5. Belmonte E. De Monte M. Quaresimin M. Multi-scale modeling of the fatigue behavior of short glass fiber reinforced polyamide notched specimens, 20<sup>th</sup> International Conference of Composite Materials, Copenhagen (Denmark), July 19-24 (2015).
6. Cruz C.A, Belmonte E. Lux A. De Monte M. Quaresimin M. Multi-scale analysis of the ageing of a reinforced polyamide 66 in ethanol-based fuels, 20<sup>th</sup> International Conference of Composite Materials, Copenhagen (Denmark), July 19-24 (2015).
7. Belmonte E. Moosbrugger E. Quaresimin M. De Monte M. Detection of crack initiation in notched specimens of unreinforced and short fiber reinforced polyamide under fatigue loading, 6<sup>th</sup> International Conference on Fatigue of Composite, Paris (France), March 25-27 (2015).
8. Belmonte E. De Monte M. Riedel T. Quaresimin M. A study of the matrix microscopic stress concentrations at crack initiation in a short fiber reinforced polyamide under fatigue loading, 6<sup>th</sup> International Conference on Fatigue of Composite, Paris (France), March 25-27 (2015).

9. Belmonte E. De Monte M. Quaresimin M. Hoffmann C. Damage mechanisms of short glass fiber reinforced polyamide 6.6 under fatigue loading, 16th European Conference on Composites Materials, Seville (Spain), June 22-26 (2014).

## **National Conferences**

10. Belmonte E. De Monte M. Quaresimin M. Hoffmann C. Damage evolution in short fiber reinforced polyamide under fatigue loading: influence of the fiber volume fraction. 43° Convegno Nazionale AIAS, Rimini, (2014).
11. Belmonte E. De Monte M. Quaresimin M. Hoffmann C. Matrix stress distributions at the crack initiation site in a short fiber reinforced polyamide under fatigue loading. 43° Convegno Nazionale AIAS, Rimini, (2014).

